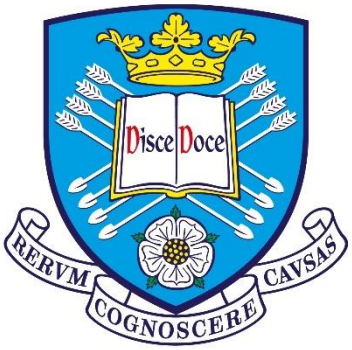

The University Of Sheffield.

Effect of a Terminal Overdeepening on Glacier Hydrology and Flow

William James Higson

A dissertation submitted to the University of Sheffield in accordance with the requirements for award of the degree of Doctor of Philosophy in the Faculty of Social Sciences

Department of Geography

8th October 2021

ABSTRACT

Overdeepenings in the bedrock topography beneath glaciers are commonplace. Despite this, the subglacial processes associated with them remain poorly understood. It has been hypothesized that adverse bed gradients can reduce the efficiency of the drainage system and therefore encourage basal sediment to accumulate. To determine to what extent an overdeepening might influence ice flow and the drainage system, a terminal overdeepening at Findelengletscher, Switzerland was targeted. Nine Uncrewed Aerial Vehicle (UAV) surveys were carried out, spread across late August and early September 2016, early July 2017 and early September 2017 along with two Ground Penetrating Surveys (GPR) in February and July 2017. An overdeepening with a bed-to-surface slope ratio above the threshold for glaciohydraulic supercooling with basal sediment layers on its adverse slope was present. Up-glacier ice flow velocities and spatial ice loss patterns across the melt season were consistent with drainage system evolution, whilst a less efficient system was present longer across the overdeepening. Findings indicate that drainage, and thus ice flow, at the terminus of Findelengletscher are strongly influenced by the adverse slope. The presence of a more inefficient distributed system at the terminus leads to a reduction in energy and decreases sediment transport in this location. Furthermore, a more evolved drainage system was considered to hasten the formation of cauldron like features along main subglacial flow paths. It is recommended for glacial and geological modellers that bed topography be given consideration when estimating rates of sediment erosion and transportation.

AUTHOR'S DECLARATION

I declare that the work in this dissertation was carried out in accordance with the requirements of the University's Regulations and Code of Practice for Research Degree Programmes and that it has not been submitted for any other academic award. Except where indicated by specific reference in the text, the work is the candidate's own work. Work done in collaboration with, or with the assistance of, others is indicated as such. Any views expressed in the dissertation are those of the author.

William Higson

8th October 2021

ACKNOWLEDGMENTS

Although I am the author of this work, compiling it was not a solo effort by any means and involved considerable time and sacrifices of many people who I will attempt here to outline, where I can, those who contributed to this work.

Firstly, I would like to thank everyone involved in the fieldwork and data collection side of this work both in the UK and Switzerland. Those who had advice and supplied it willingly at the AGM in Zurich. Thanks to Gwen and Andreas Vieli for the generous use of GPR equipment their patience in explaining to me the rudiments of a MALA GPR. Thanks to Owen McAree for his help with the basics of UAV flying and more importantly all the laws. Thanks to everyone who helped out on fieldwork in varying capacities: Ruth, Kaylee, Saskia, Guy, Simon, Marie and special thanks to my good friend Steve who volunteered to help drag a GPR up a mountain in February and also drove me to and from Zermatt.

I wish to extend my thanks and acknowledge the efforts of Daniel Farinotti, who couldn't have done more to help support my fieldwork and make me feel welcome within the cryospheric community, the lending of equipment from VAW, his help and knowledge for fieldwork including a very impromptu crash course on crevasse safety late one evening when I'm sure he'd have been wanting to do anything else!

I wish to thank my friends within the geography department at Sheffield, all who have helped in some small way but particularly Tom and Rob who offered support coffee and burritos where needed.

I wish to thank my supervisory team Darrel Swift and Robert ‘Robbo’ Bryant who have been through it all with unwavering patience and support and countless lunches in the pub. I really don’t know how I would have got as far as I have without them both and I can’t think of a way to adequately repay their generosity.

Finally, but by no means least I’d like to thank my partner Lucy for believing in me, supporting me and making me smile every step of the way through thick and thin, two house moves and one baby.

CONTENTS

ABSTRACT ..... **i**

AUTHOR'S DECLARATION ..... **ii**

ACKNOWLEDGMENTS ..... **iii**

CONTENTS ..... **v**

LIST OF TABLES ..... **xii**

LIST OF FIGURES ..... **xiii**

1. INTRODUCTION TO THE RESEARCH **1**

1.1 INTRODUCTION AND RATIONALE 1

1.1.1 Structure of chapter 4

1.2 KEY CONCEPTS OF GLACIAL HYDROLOGY 5

1.2.1 Sources of glacial meltwater 5

1.2.2 Distributed and Channelised Subglacial Drainage 6

1.2.3 Studying sub/englacial drainage systems 16

1.3 CORE PRINCIPLES OF GLACIER DYNAMICS 22

1.3.1 Seasonal scale glacier dynamics 22

1.3.2 Influences on glacier dynamics 26

1.3.3 The effects of hydrology on basal sliding 29

1.3.4 Spatial coupling (stress gradients) 34

1.3.5 Summary of glacier dynamics 35

1.4 GLACIER-BED TOPOGRAPHY AND ITS INFLUENCE ON ICE FLOW 35

1.4.1 Influence of subglacial topography on glacier flow 35

1.4.2 The role of overdeepenings 36

1.4.3 The role of supercooling 41

1.4.4 The role of ponding 43

1.4.5 Cauldrons 47

1.5 RESEARCH QUESTIONS 48

1.5.1 Research Question 1 49

1.5.2 Research Question 2 49

1.5.3 Research Question 3 50

1.6 THESIS OUTLINE 51

2. METHODS 52

2.1 INTRODUCTION 52

2.1.1 Structure of the Chapter 52

2.2 FIELD SITE IDENTIFICATION 52

2.2.1 Using the ice thickness inversion technique 56

2.2.2 Field site: Findelengletscher 65

2.3 GPR 73

2.3.1 A review of GPR in glacial studies 73

2.3.2 Field collection of GPR 75

2.3.3 Post processing & interpretation 83

2.3.4 GPR uncertainties 94

2.3.5 Summary of GPR 97

2.4 UAVs 97

2.4.1 The potential for UAVs in glacial environments 97

2.4.2 UAV Equipment Selection 98

2.4.3 Field collection of UAV images 100

2.4.4 Processing imagery 108

2.4.5 Summary of UAV work carried out 114

2.5 COSI-CORR 115

2.6 CREATING A BASELINE MODEL 118

2.6.1 Creating Baseline Velocities 120

2.7 SUMMARY OF METHODOLOGY 122

3. BASAL TOPOGRAPHY AND PROCESSES AT FINDELENGLETSCHER 124

3.1 CHAPTER OVERVIEW 124

3.1.1 Importance of understanding basal topography 125

3.1.2 Structure of chapter 127

3.2 BED TOPOGAPHY MODELS 128

3.2.1 Model creation 128

3.2.2 Results (Models A to D) 132

3.2.3 Model intercomparison results 137

3.3 INTERNAL ICE STRUCTURE AND FEATURES DISCOVERED 142

3.3.1 Overview 142

3.3.2 Results 142

3.4 BED MORPHOLOGY SIGNIFICANCE 152

3.4.1 Overview 152

3.4.2 Bed morphology of Findelengletscher 153

3.4.3 Subglacial water flow: routing and system morphology 157

3.5 ELEVATION CHANGE 164

3.6 SUMMARY 167

4. SPATIAL VARIATION IN FLOW VELOCITY AT FINDELENGLETSCHER 169

4.1 INTRODUCTION 169

4.1.1 Rationale 170

4.1.2 Structure of Chapter Four 171

4.2 ICE FLOW BEHAVIOUR AT FINDELENGLETSCHER 172

4.2.1 Areas of Interest (AOIs) 172

4.2.2 Feature Tracking 175

4.3 SUMMARY 185

5. TEMPORAL PATTERNS OF FLOW VELOCITY AT FINDELENGLETSHER 187

5.1 INTRODUCTION 187

5.1.1 Structure of the chapter 187

5.1.2 Importance of understanding temporal flow patterns 188

5.2 EXPECTED GLACIER REACTION TO CLIMATIC CONDITIONS 189

5.2.1 Climatic Influences on Dynamics 190

5.2.2 Comparing Findelengletscher Data to Baseline Expectations 197

5.3 TEMPORAL VELOCITIES AT AREAS OF INTEREST 202

5.3.1 Areas of Interest 1-3 204

5.3.2 Areas of Interest 4-7 207

5.3.3 Area of Interest 8 211

5.4 ICE LOSS OVER TIME AT FINDELENGLETSCHER 212

5.5 SUMMARY 216

6. DISCUSSION 218

6.1 INTRODUCTION 218

6.2 VELOCITY PATTERNS 218

6.2.1 General velocity patterns in temperate valley glaciers 219

6.2.2 Velocity patterns at Findelengletscher 222

6.2.3 Residual Data 230

6.3 HYDROLOGY PATTERNS 235

6.3.1 Hydrological routing 235

6.3.2 Temporal evolution of the drainage system at Findelengletscher 237

6.4 THE EFFECTS OF OVERDEEPENINGS 238

6.4.1 The effects of overdeepenings on glaciers and ice sheets 239

6.4.2 Basal sediment and supercooling at Findelengletcher 241

6.4.3 The effects of an overdeepening on Findelengletscher 248

6.4.4 Velocity changes across the overdeepening 250

6.5 ICE LOSS 252

6.5.1 Patterns of ice loss Findelengletscher 253

6.5.2 Interpreting Seasonal and annual elevation change 254

6.5.3 Ice loss vs ice flow 257

6.6 CAULDRONS AT FINDELENGLETSCHER 262

6.6.1 Development and Analysis of Cauldrons 263

6.6.2 Future Cauldron development at Findelengletscher 267

6.7 SUMMARY OF DISCUSSION 268

7. CONCLUSION AND WIDER IMPLICATIONS 269

7.1 Introduction 269

7.2 Answering the Research Questions of the Thesis 269

7.2.1 Research Question 1 269

7.2.2 Research Question 2 270

7.2.3 Research Question 3 271

7.3 Limitations 271

7.4 Wider implications 272

7.5 Further Research Suggestions 272

8. REFERENCES 274

LIST OF TABLES

TABLE 2.1: CRITERIA FOR SUITABLE FIELD SITES. 53

TABLE 2.2: SUMMARY OF THE FIVE MOST SUITABLE GLACIERS FOR FURTHER RESEARCH AND GROUND TRUTHING. OD = OVERDEEPENING, SC = SUPERCOOLING AND P = PONDING. 60

TABLE 2.3: MALA SETTINGS FOR FEBRUARY FIELDWORK, TAKEN FROM ZEKOLLARI ET AL. (2013) 78

TABLE 2.4: PULSEEKKO SETTINGS FOR JULY FIELDWORK. 82

TABLE 2.5: DIFFERENCES BETWEEN INDIVIDUAL TRANSECT DEPTHS AT CROSS-SECTIONAL POINTS FOR FINDELENGLETSCHER DURING FEBRUARY GPR FIELDWORK. 91

TABLE 2.6: DIFFERENCES BETWEEN INDIVIDUAL TRANSECT DEPTHS AT CROSS-SECTIONAL POINTS FOR FINDELENGLETSCHER DURING JULY GPR FIELDWORK. 92

TABLE 2.7: BEDROCK ESTIMATIONS AT INTERSECTIONS OF GPR TRANSECTS BETWEEN FEBRUARY AND JULY FIELDWORK. 93

TABLE 2.8: COMPARISON OF TYPES OF UAV. 98

TABLE 2.9: SPECIFICATIONS FOR THE DJI PHANTOM 4 99

TABLE 2.10: UAV FLIGHT STATISTICS AT FINDELENGLETSCHER. 100

TABLE 2.11: MEMORY CONSUMPTION REQUIRED IN THE CREATION OF AGISOFT SFM MODELS. FIGURES ARE BASED ON 12-MEGAPIXEL IMAGES. TAKEN FROM (AGISOFT 2018). 101

TABLE 2.12: IMAGE RECORDING AND QUALITY RESULTS. 111

TABLE 2.13: AGISOFT PHOTOSCAN MODEL STATISTICS. 113

TABLE 3.1: *DESCRIPTIONS OF THE VARIOUS BED MODELS GENERATED* 134

TABLE 4.1: DESCRIPTIONS OF THE SEPARATE AOIS FOR ICE FLOW VELOCITY AND DIRECTION ANALYSIS AT THE FIELD SITE. 174

TABLE 4.2: ESTIMATES OF AVERAGE ICE FLOW VELOCITY PER YEAR VIA MANUAL AND COSI-CORR FEATURE TRACKING FOR BOTH WINTER (6/9/16 – 5/7/17) AND SUMMER (7/7/17 – 3/9/17) WITHIN THE AREAS DENOTED IN FIGURE 4.5. 179

TABLE 5.1: *MODEL ORTHOMOSAIC PAIRS AND THEIR TIME SPANS.* 190

LIST OF FIGURES

FIGURE 1.1: ILLUSTRATION OF HYDROLOGICAL PROCESSES AND PATHWAYS BENEATH A GLACIER. IMPORTANT FEATURES OF THE HYDROLOGICAL TRANSPORT SYSTEM ARE AS FOLLOWS: 2) – FIRN MELTING AND REFREEZING (DENSIFICATION). 3) – SUPRAGLACIAL TO SUBGLACIAL CONNECTIONS. 4) – SUPRAGLACIAL DRAINAGE CAUSING MOULIN AND CREVASSE WIDENING. 6. BASAL SEDIMENT DEPOSITION. 7) – BASAL MELTING ON ADVERSE SLOPES (TAKEN FROM NIENOW ET AL., 2017). 9

FIGURE 1.2: *PLAN VIEW OF AN EXAMPLE OF (A) AN EFFICIENT ARBORESCENT SYSTEM LIKELY SEEN AT THE END OF A MELT SEASON AND (B) AN INEFFICIENT, NONARBORESCENT DRAINAGE SYSTEM, LIKELY SEEN AT THE BEGINNING OF A MELT SEASON (TAKEN FROM FOUNTAIN & WALDER, 1998).* 9

FIGURE 1.3: ENGLACIAL CONDUITS FLOWING PERPENDICULAR TO EQUIPOTENTIAL SURFACES AS PROPOSED BY SHREVE 1985 (TAKEN FROM GULLEY ET AL., 2009, ADAPTED FROM SHREVE 1985) 11

FIGURE 1.4: DIFFERENT FORMS OF SUBGLACIAL DRAINAGE, GROUPED INTO EFFICIENT AND INEFFICIENT. C-CHANNELS CAN BE CLASSED AS EITHER BASED ON THE EFFICIENCY OF THEIR OPENING AND CLOSING PROCESSES (TAKEN FROM FLOWERS 2015). 14

FIGURE 1.5: VELOCITY (TAKEN FROM VARIOUS CENTRE LINES STAKES), DISCHARGE AND TEMPERATURE RECORDED FROM HAUT D'AROLLA GLACIER OVER THE MELT SEASON OF 1998. DASHED LINES ON ALL OF THE GRAPHS INDICATE 'SPRING EVENTS' TAKEN FROM MAIR ET AL. (2003). 19

FIGURE 1.6: VELOCITY RATES ACROSS MULTIPLE SEASONS AT STORGLACIAREN (TAKEN FROM HOOKE ET AL., 1989). 24

FIGURE 1.7: *PATTERNS OF VELOCITY SPEED-UP ACROSS THE MELT-SEASON IN YEARS OF HIGH (1995, 1998 (ORANGE)) AND LOW (1993, 1996, 1997 (BLUE)) MELTING BASED ON POINT DATA FROM 6 GLACIERS (TAKEN FROM SUNDAL ET AL. 2011). ERROR BARS SHOW ONE SD OF UNCERTAINTY, COLOUR REPRESENTS ESTIMATED DAILY SURFACE RUNOFF RATES.* 25

FIGURE 1.8: SURFACE, INTERNAL AND BASAL VELOCITIES AT FOUR SITES AT HAUT D'AROLLA GLACIER MEASURED OVER THE SPRING, SUMMER, AND AUTUMN/WINTER SEASONS (TAKEN FROM WILLIS ET AL., 2003). 28

FIGURE 1.9: LONGITUDINAL SECTION OF STORGLACIÄREN, SWEDEN SHOWING LOCALISED CREVASSING ZONES PRIOR TO OVERDEEPENINGS. (TAKEN FROM HOOKE ET AL., 1991, P1106). 39

FIGURE 1.10: A THEORISED GRAPH OF BASAL WATER PRESSURE AND SLIDING VELOCITY OVER A MELT SEASON FOR OVERDEEPENED AND NON-OVERDEEPENED BED MORPHOLOGIES. A) SHOWS BASAL MELTING AND SURFACE RUN OFF B) SHOWS WATER PRESSURE AND SLIDING RATE. (TAKEN FROM COOK AND SWIFT, 2012). 40

Figure 1.11: A cartoon showing subglacial ponding in an overdeepening at D). (Taken from Cook and Swift, 2012). 46

Figure 1.12: Overdeepenings (red) and potential ponding based on Shreve's (1972) threshold (blue) beneath Jakobshavn Isbrae and Recovery Glacier (taken from Patton et al., 2015) 46

Figure 1.13: Cauldron depression forming at the tongue of Sulztalferner, Austria (taken from Stocker-Waldhuber et al., 2017). 48

Figure 2.1: Looking up glacier, a modelled estimate of glacial bedrock topography and overlying ice surface DEM of Haut d'Arolla, Switzerland. Contours are shown every five metre. Model created by author. 55

Figure 2.2: Validation of Farinotti's (2009a) inversion method, based on comparison to GPR measured transects of Unteraar Glacier (taken from Farinotti et al., 2009b). GPR transects show a strong similarity to the bedrock inversion approach, more so towards the terminus. 55

Figure 2.3: *Mass conservation of a portion of ice along a longitudinal profile of a glacier. Where dx is length and h is height, b and b^L are the rates of mass gain or loss (mass balance), $\partial h/\partial t$ is the rate of ice-thickness change, q is the specific mass flux, height length (Taken from Farinotti et al. 2009b).* 56

Figure 2.4: Two images automatically generated by the Farinotti et al. (2009a) ice-thickness inversion model. Left: Oberaar Glacier. Right: Zmutt Glacier. 57

Figure 2.5: Image of the estimated bedrock topography using Farinotti et al. (2009a) model of Findelengletscher from nadir. Contours are recorded every 5 m, with coloured contours showing DEM altitude every 100 m from 2600-2800 m. 58

Figure 2.6: *Flow chart of the processes required to find a suitable field site.* 59

Figure 2.7: An Ice thickness estimate of Oberaargletscher from Farinotti et al. (2009a) inversion model. 61

Figure 2.8: Bedrock surface: ice surface slope ratio compared to the supercooling threshold for five potential field sites. Bedrock and ice surface altitudes are shown too on the primary y axis. 62

Figure 2.9: Longitudinal transect of ice-surface and bedrock-ice interfaces (shown in blue and black respectively) and their relative slope angle ratios (red line is the ponding threshold, orange and purple lines are the supercooling threshold – 1.2-1.7). The red shaded area represents the glacier's retreat from 2000 to 2016, and red circles highlight the locations of overdeepenings, so it was key that the predicted overdeepenings were sufficiently far away from the terminus so as not to have been exposed by the glacier's retreat. 64

Figure 2.10: Bedrock estimate of the terminus of Findelengletscher from Feiger et al. 2018, using GPR data from VAW, (2015). Contours are every 10 m. 65

Figure 2.11: Current glacier extent of Findelengletscher (NASA, 2009) the steady retreat of the snout of Findelengletscher is highlighted in red, taken and digitised from Swiss aerial imagery (swisstopo, 2018). 67

Figure 2.12: Cumulative front variation of Findelengletscher (1885-2016). (Glaciological Reports 1881-2017, www.glamos.ch). 67

Figure 2.13: Annotated Proglacial Area of Findelengletscher. 68

Figure 2.14: Above: Findelengletscher proglacial area with highlighted previous and current meltwater channels. Below: terminus of Findelengletscher, September 2004 (Midgley, 2004 unpublished). 69

Figure 2.15: Retreat of Findelengletscher terminus 1982-2015 (taken from aerial imagery from Swisstopo, (2018)). 70

Figure 2.16: Lateral moraine colapse at Findelengletscher. Top Left: Contours represent altitude every 10 m. Top Right: Looking due North at the collapse. Bottom: Looking East up the glacier. 72

Figure 2.17: Debris covered ice and its insulating affects against down-wasting. Image looking East, up-glacier, July 2017. 72

Figure 2.18: Comparison of 100 (top), 50 (centre) and 25 (bottom) MHz traces along similar longitudinal transects at Griesgletscher 30/06/17 (works carried out by the author). 75

Figure 2.19: GPR transect 14 from July Findelen fieldwork. Red circles show where the GPR travelled over a supraglacial stream. Other similar but less defined features can be seen where the GPR was positioned close to a supraglacial stream. 77

Figure 2.20: MALA GPR device with 25 MHz Antenna coil - Findelengletscher February 2017. 79

Figure 2.21: A) proposed transects to be measured on February GPR fieldwork. Note the red shaded areas were considered unsafe due to crevasses or steep terrain. Priorities were given to transects red being high, amber medium and green low. B) actual transects measured (red dots) and the route taken (blue line). C) Start and end points of each transect. 80

Figure 2.22: Pulse Ekko GPR set up at Findelengletscher. 81

Figure 2.23:. Red and blue lines represent GPR transects from February and July respectively. Location on steep slope angles across Findelengletscher are indicated by shaded areas. 83

Figure 2.24: Flow diagram of the processing steps taken for GPR traces in ReflexW. 84

FIGURE 2.25: TWO TRACES SHOWING THE BEFORE AND AFTER EFFECT OF STATIC CORRECTION WHEREBY THE ZERO TIME IS CALIBRATED. 85

FIGURE 2.26: BEFORE (ABOVE) AND AFTER (BELOW) EDITING TRACES OF GPR DATA THROUGH REFLEXW (RED ARROWS INDICATE TIME PERIODS WHERE TRACES WERE BEING RECORDED WHILST STATIONARY). 86

FIGURE 2.27: A LONGITUDINAL TRANSECT (TRANSECT 15, JULY 2017) WITH AN APPLIED 3D TOPOGRAPHY CORRECTION. THE SURFACE SLOPE OF THE GLACIER CAN BE SEEN CLEARLY - MOVING UP GLACIER FROM LEFT TO RIGHT. 87

FIGURE 2.28: IMAGE SHOWING JULY 2017 FINDELENGLETSCHER TRANSECTS AND PICKED BED. (BLACK SHOWS SECTIONS THAT HAVE BEEN SUCCESSFULLY PICKED. RED SHOWS LACK OF CLEAR BED REFLECTOR.) 88

FIGURE 2.29: A COMPARISON OF TWO REFLECTORS ALONG THE SAME TRACE, THE LOWER REFLECTOR IS ASSUMED TO BE THE BEDROCK AND DISPLAYS A NORMAL POLARITY WHIST THE UPPER REFLECTOR SHOWS A REVERSED POLARITY WHICH COULD SUGGEST AN AIR CAVITY, PERHAPS A RELIC FROM A CLOSED CREVASSE (EXAMPLE TAKEN FROM DATA COLLECTED BY AUTHOR AT GRIESGLETSCHER 30/6/17). 89

FIGURE 2.30: *HYPERBOLA FITTING FOR TRANSECTS 17 AND 21. CONSIDERED TO BE AIR FILLED VOIDS* 90

FIGURE 2.31: ABOVE: LOCATION OF ALL GPR TRANSECT INTERSECTIONS. BELOW: BOX PLOT OF CROSS COMPARISON GPR POINTS BETWEEN DIFFERENT FIELDWORK. FROM ALL POINTS AN ERROR LEVEL OF 4.8 ± 1.27 M WAS CALCULATED. 93

FIGURE 2.32: DJI PHANTOM 4 99

FIGURE 2.33: LEFT: IMAGE LATERAL OVERLAP RIGHT: IMAGE SIDE OVERLAP AS CALCULATED BY UAVPHOTO (2014) UAV AND CAMERA PARAMETERS WERE INPUT ACCORDING TO FLIGHT PARAMETERS. SIDE OVERLAP WAS REPLICATED BY FLIPPING THE X AND Y SIZE AND ALTERING THE VELOCITY TO '8' AND IMAGE INTERVAL TO '5' TO SIMULATE THE APPROXIMATE 40 M GAP BETWEEN LATERAL FLIGHT PATHS OF THE UAV. 102

FIGURE 2.34: TYPICAL LATERAL OVERLAP BETWEEN TWO IMAGES (RED AND YELLOW OUTLINE). (IMAGE FROM FLIGHT 2, 27/8/16). 102

FIGURE 2.35: DIFFERENT GCPS SHAPES AND SIZES USED BETWEEN 2016 (LEFT) AND 2017 (RIGHT). 105

FIGURE 2.36: SHADOW EFFECT ON DEM ESTIMATES. TOP LEFT: FLIGHT 030917. TOP RIGHT: FLIGHT 070917. BOTTOM LEFT: FLIGHT 030917 WITH DEM LOSS OVERLAY. 106

FIGURE 2.37: LEFT: LOW LYING CLOUD CONDITIONS ON 30/08/17 LOOKING SOUTH ACROSS GRIESGLETSCHER. RIGHT: LOW FOG AT FINDELENGLETSCHER LOOKING EAST UP VALLEY 6/9/16. 107

FIGURE 2.38: FOUR INDIVIDUAL FLIGHTS THAT MAKE UP AN ORTHOMOSAIC (SHOWN BENEATH). INDIVIDUAL DOTS REPRESENT THE LOCATION OF IMAGES CAPTURED, AND PINK TRIANGLES REPRESENT TAKE OFF/LANDING POINTS. (6/9/17). 108

FIGURE 2.39: CREATION OF 3D STRUCTURE USING MULTIPLE VIEWPOINTS FROM A MOVING CAMERA (FIGURE TAKEN FROM WESTOBY ET AL., 2012). 109

FIGURE 2.40: AGISOFT PHOTOSCAN WORK-FLOW DIAGRAM. 109

FIGURE 2.41: DIFFERENCE IN DEM RESOLUTION BETWEEN 'LOW', 'MEDIUM' AND 'HIGH' PROCESSING OPTIONS IN AGISOFT PHOTOSCAN (**A**: 3D IMAGE OVERLAY OF THE DEM. **B**: CREVASSES AT 'LOW' QUALITY. **C**: CREVASSES AT 'MEDIUM' QUALITY. **D**: CREVASSES AT 'HIGH' QUALITY)..... 112

FIGURE 2.42: AREA IN F1 WHERE AN UNSUITABLE LEVEL OF IMAGE OVERLAP IS RECORDED. 114

FIGURE 2.43: WORKFLOW PROCESS FOR CALCULATING GLACIER VELOCITIES USING COSI-CORR SOFTWARE. (MODIFIED FROM JAWAK ET AL., 2018). 115

FIGURE 2.44: BIRDSEYE VIEW (LEFT) AND SIDE VIEW (RIGHT) OF TYPICAL GLACIER FLOW PATTERNS (TAKEN FROM HUDLESTON, (2015)). 119

FIGURE 2.45: A VELOCITY SOLUTION FOR A PARABOLIC CROSS-SECTION USING THE ADJUSTED SLIDING LAW AS PROPOSED BY HARBOR (1992). THE MAXIMUM ICE DEPTH IN THIS CASE WAS 310 M AND THE SURFACE WIDTH 1240 M, THE APPROXIMATE DIMENSIONS OF THE ATHABASCA GLACIER, CANADA. 119

FIGURE 2.46: *CORRELATION OF DIURNAL ICE SPEED AND WATER STORAGE (TAKEN FROM BARTHOLOMAUS ET AL., 2008).* 120

FIGURE 2.47: SMOOTHING OF BASELINE VELOCITIES. 121

FIGURE 2.48: INTERPOLATED/SMOOTHED BASELINE OF GLACIER VELOCITIES (TOP) MADE FROM AVERAGING VELOCITIES OF TWO LATE MELT SEASON PERIODS A YEAR APART (MIDDLE AND BOTTOM). 122

FIGURE 3.1: MULTI-FACETED APPROACH UNDERTAKEN IN THIS CHAPTER TO UNDERSTAND GLACIAL CONDITIONS AT FINDELENGLETSCHER. 125

FIGURE 3.2: DIFFERENCES IN ESTIMATING GLACIER BOUNDARIES FOR FINDELENGLETSCHER. TOP LEFT: SATELLITE IMAGE (GOOGLE MAPS, 2018). TOP RIGHT: MAP SWISSTLM (SWISSTOPO, 2018). BOTTOM: BOTH OVERLAID AND ANNOTATED TO SHOW DIFFERENCE IN BOUNDARIES, BLACK LINE REPRESENTS VISIBLE BOUNDARY, BLUE AREAS REPRESENT SEDIMENT LADEN DEAD ICE. RED LINE REPRESENTS THE ESTIMATED CENTRAL FLOW LINE. 131

FIGURE 3.3: FEIGER ET AL. (2018) BEDROCK TOPOGRAPHY ESTIMATE, 10 M CONTOURS OVERLAID ON UAV DERIVED IMAGE OF FINDELENGLETSCHER (5TH JULY 2017), NON-DEBRIS COVERED GLACIER OUTLINE SHOWN IN BLUE. 132

FIGURE 3.4: OUTLINE OF THE TERMINUS OF FINDELENGLETSCHER FOR CLEAR ICE AND OVERLYING DEBRIS-COVERED ICE OVERLAIN ON ORTHOMOSAIC IMAGE TAKEN ON 27TH AUGUST 2016. 132

FIGURE 3.5: *MAP OF THE FEBRUARY 2017 (TOP), JULY 2017 (MIDDLE) AND VAW APRIL 2015 (BOTTOM) GPR TRANSECTS SHOWING ICE THICKNESS WHERE A CLEAR BED REFLECTOR COULD BE OBTAINED (ALTITUDE OF DEM MINUS ALTITUDE OF BEDROCK). DEM OF THE ICE SURFACE IN GREYSCALE AT 20 M INTERVALS FROM 5TH JULY 2017.* 133

FIGURE 3.6: *FOUR BED MODELS OF FINDELENGLETSCHER, CREATED VIA RADIAL BASE FUNCTION WITH CONTOURS EVERY 10 M. (SEE TABLE 3.14 FOR A DESCRIPTION OF HOW EACH WAS DERIVED)* 136

FIGURE 3.7: A RADIAL BASE FUNCTION CALCULATION OF THE BED TOPOGRAPHY (BED MODEL A) OF FINDELENGLETSCHER. AN ESTIMATED FLOW LINE BASED ON MAXIMUM LONGITUDINAL DEPTH IS DEPICTED BY A GREEN DASHED LINE. 137

FIGURE 3.8: COMPARISONS OF DIFFERENCES BETWEEN BED MODEL B AND A, C AND D. 140

FIGURE 3.9: 10 M CONTOUR MAPS OF THE BED OF FINDELENGLETSCHER FROM FEIGER ET AL. (2018) (ABOVE) AND GRAB ET AL. (2021) (BELOW). GPR TRANSECTS USED IN THESE CALCULATIONS ARE COLOURED BASED ON THE ALTITUDE OF BED ESTIMATES. OVERDEEPENINGS FROM THESE ESTIMATIONS ARE SHOWN IN RED AND ORANGE RESPECTIVELY TO MATCH THAT OF FIGURE 3.10. 141

FIGURE 3.10: THE LOCATION OF THREE BED MODEL OVERDEEPENINGS AND ESTIMATES AS TO WHERE THE OVERDEEPENING IS SITUATED. CONTOURS ARE EVERY 1 METRE. 141

FIGURE 3.11: (TOP) COMPARING THE PICKED TRACES FROM THE JULY AND FEBRUARY GPR TRANSECTS. (MIDDLE) UNANNOTATED VIEW OF THE GPR TRACES WITH GREY BEING FEBRUARY AND PURPLE BEING JULY. (BOTTOM) ANNOTATION OF THE BASAL ICE FEATURE AS SEEN USING REFLEXW. 145

FIGURE 3.12: IMAGE OF WHERE THE BASAL ICE IS EXPECTED TO REACH THE SURFACE IF ITS ANGLE UP THROUGH THE ICE REMAINS CONSTANT (RED CIRCLE) AND WHERE THE TRACE DENOTING BASAL ICE IN THE TRANSECTS FROM BOTH FEBRUARY AND JULY 2017 WAS RECORDED, WITH THE ORIGIN POINT OF THIS BASAL ICE LAYER AT THE VERY EDGE OF THE IMAGE (BLUE LINE). GREEN LIGHT DENOTES THE EXTENT OF THE OVERDEEPENING IN FIGURE 3.10. 146

FIGURE 3.13: (A) ILLUSTRATION SHOWING THE FORMATION OF SEDIMENT-RICH ENGLACIAL THRUSTING AND HUMMOCKY CONTROLLED-MORAINES AT KVÍÁRJÖKULL, ICELAND TAKEN FROM COOK & SWIFT, 2012. (B) AERIAL IMAGE OF FINDELENGLETSCHER TERMINUS SHOWING DEBRIS-RICH BASAL ICE BEING DEPOSITED ON THE RIGHT SIDE LOOKING UP GLACIER (IMAGE TAKEN 7/9/17). 146

FIGURE 3.14: ABOVE) TRANSECT 20 (TAKEN ON 6TH JULY 2017) SHOWING VARIOUS NEAR SURFACE CREVASSE FEATURES HIGHLIGHTED IN RED. BELOW) LOCATION OF THE TRANSECT AND FEATURES ON THE GLACIER FOR TWO DIFFERENT TIME PERIODS OVER THE COURSE OF THE MELT SEASON. 148

FIGURE 3.15: LEFT: TRANSECT 2 & 20 TRANSECTS OVERLAIN OVER A CAULDRON FEATURE FROM AN ORTHOMOSAIC DATED 7TH SEPTEMBER 2017. RIGHT: REFLEXW GPR FOR TRANSECT 2 TAKEN IN FEBRUARY SHOWING CREVASSE FEATURES OF THE CAULDRON PRIOR TO SURFACE CREVASSING OCCURRING. 148

FIGURE 3.16: A) HILLSHADE OF 7TH SEPTEMBER 2017 DEM ANNOTATED SHOWING ESTIMATED SUBGLACIAL FLOW PATH (SEE CHAPTER 3.4.1) AND CAULDRON LOCATIONS. THE DATE REFERS TO WHEN CREVASSES WERE FIRST NOTED TO FORM RATHER THAN THE COLLAPSE. B) IMAGE FROM SUMMER 2019 SHOWING SEDIMENT MORAINE. C & D) FIELD IMAGES SHOWING COLLAPSE OF CAULDRONS. N.B. IMAGES B-D TAKEN FROM HTTPS://WWW.YOUTUBE.COM/WATCH?V=KGYXJEGOC78 149

FIGURE 3.17: GPR TRACE OF TRANSECT 16 HIGHLIGHTING FEATURES RELATED TO THE DEVELOPMENT OF A CAULDRON. GPR SURVEY DATED 6TH JULY 2017. 150

FIGURE 3.18: (A) TRANSECT 15 SHOWING THE EXTENT TWO REFLECTORS ONE ON TOP OF THE OTHER, RUNNING LONGITUDINALLY (RED LINE). (B) AN ANNOTATED CLOSE UP OF THE TRACE HIGHLIGHTED BY THE BLUE RECTANGLE WITH WIGGLE-WINDOW TO SHOW THE POLARITY OF THE TRACE. (C) A HILLSHADE DEM WITH THE EXTENT OF THE FEATURE IN RED AND ESTIMATED SUBGLACIAL FLOW PATHS (BLUE). (D) A TOPOGRAPHICALLY CORRECTED VIEW OF THE TRACE LEFT TO RIGHT BEING EAST TO WEST WITH THE TWO REFLECTORS OUTLINED BY THE TWO RED LINES. 152

FIGURE 3.19 – *A LONGITUDINAL TRANSECT (TRANSECT 24) SHOWING THE PRESENCE OF ADVERSE SLOPE OF AN OVERDEEPENING ALONG WITH A BASAL DEBRIS LAYER RECORDED 5TH SEPTEMBER 2017.* 154

FIGURE 3.20: TOP) BED MODEL B FLOW PATHWAYS AND LOCATION OF THE ESTIMATED CENTRAL FLOW LINE. BOTTOM) SUPERCOOLING AND PONDING THRESHOLDS WHEN CALCULATING SLOPE ANGLES ALONG THE MAIN HYDROLOGICAL FLOW LINE. SLOPE ANGLE IS MEASURED BASED ON THE ALTITUDE OF POINTS ALONG THIS LINE 2 M APART. 156

FIGURE 3.21: AVERAGE DAILY DISCHARGE RATES (M3/S) FOR FINDELENGLETSCHER SUMMER 2017. ORANGE LINE INDICATES WHEN THE GPR SURVEY WAS CARRIED OUT OVER THAT SUMMER. 157

FIGURE 3.22: SUBGLACIAL FLOW PATHWAYS FOR FOUR BED MODELS OUTLINED IN..... 158

FIGURE 3.23: GLACIAL FLOW PATH DERIVED BY EQUATION (1) USING FEIGER ET AL. 2018 DATA FOR FINDELENGLETSCHER (BELOW). CLOSE UP OF FLOW PATHS AT SNOUT (RED RECTANGLE) OVERLAID WITH ORTHOMOSAIC FROM 5TH JULY 2017. (ABOVE).... 160

FIGURE 3.24: FIELD PHOTO SHOWING THE EMERGENCE OF A LATERAL HYDROLOGICAL FLOW PATH FROM BENEATH THE GLACIER. THE WATER CONTINUES TO FLOW DOWN HILL BACK INTO THE DEPTHS OF THE GLACIER OFF-CAMERA TO THE LEFT (JULY 2017)... 161

FIGURE 3.25: LEFT) FLOW PATHS (BLUE), OVERDEEPENING (BLACK) AND TRANSECT 21 & 22 TRANSPOSED ONTO AN ORTHOMOSAIC IMAGE OF FINDELENGLETSCHER (7TH SEPTEMBER 2017). RIGHT) 3D IMAGE OF SAME DATA ON THE BED MODEL WITH CONTOURS EVERY 5 M LOOKING EAST UP VALLEY FROM ABOVE SNOUT OF FINDELENGLETSCHER.

FIGURE 3.26: HYPERBOLA LOCATED ABOVE BEDROCK AT TRANSECT 21 TAKEN 6TH JULY 2017. 163

FIGURE 3.27: POSSIBLE SUBGLACIAL CHANNEL AT TRANSECT 22, TAKEN 6TH JULY 2017. 164

FIGURE 3.28: SUBGLACIAL FLOW PATHWAYS (BLUE COARSE DATA FROM FEIGER ET AL. (2018), BLACK DATA FROM BEDROCK MASK CREATED BY THIS STUDY) COMPARED TO ANNUAL ELEVATION CHANGE. 166

FIGURE 3.29: SUBGLACIAL FLOW PATHWAYS (BLUE COARSE DATA FROM FEIGER ET AL. (2018), BLACK DATA FROM BEDROCK MASK CREATED BY THIS STUDY) COMPARED TO SUMMER ELEVATION CHANGE. 166

FIGURE 3.30: RETREAT OF FINDELENGLETSCHER 2016-19. OUTLINES OF 2016 AND 2017 EXTENTS OVERLAIN OVER PLANET IMAGERY (2020) FROM LATE SUMMER 2019. WORLD IMAGERY - SOURCE: ESRI, MAXAR, GEOEYE, EARTHSTAR GEOGRAPHICS, CNES/AIRBUS DS, USDA, USGS, AEROGRID, IGN, AND THE GIS USER COMMUNITY. 167

FIGURE 4.1: WORKFLOW DIAGRAM OF DATA AVAILABLE AND WHAT WILL BE ACHIEVED IN CHAPTER 4 (AND 5)..... 172

FIGURE 4.2: INDIVIDUAL AREAS OF INTEREST AT FINDELENGLETSCHER..... 174

FIGURE 4.3: WINTER AND SUMMER ICE FLOW VELOCITIES AT FINDELENGLETSCHER. AOI GRID IS OVERLAIN FOR REFERENCE..... 177

FIGURE 4.4: ICE THICKNESS OF FINDELENGLETSCHER TERMINUS (AREAS OF DEAD ICE HAVE BEEN EXCLUDED). A DENOTES A SHALLOWER AREA JUST PRIOR TO THE OVERDEEPENING AND B SHOWS THE LOCATION OF THE OVERDEEPENING (FROM GPR SURVEYS CONDUCTED 7/2/17 & 6/7/17 – SECTION 2.3.2. DEM FROM 5/7/17 UAV FLIGHTS – SECTION 2.4.3)..... 177

FIGURE 4.5: AVERAGE VELOCITY RATES BETWEEN 27TH AUGUST AND 6TH SEPTEMBER 2016. 178

FIGURE 4.6: TOP) CENTRAL AND 15 M NORTH AND SOUTH FLOW LINE OF FINDELENGLETSCHER TERMINUS. MIDDLE) VELOCITIES ALONG AND 15 M EITHER SIDE OF THE CENTRAL FLOW LINE OF FINDELENGLETSCHER BETWEEN AUGUST 27TH – SEPTEMBER 6TH, 2016. BOTTOM) SUPERCOOLING/PONDING RATIO SMOOTHED OVER A 6 M AREA. 178

FIGURE 4.7: BOX PLOTS OF MEANS AND STANDARD DEVIATIONS FOR ALL AOIS FROM BOTH WINTER AND SUMMER PERIODS FOR BOTH MANUAL AND COSI-CORR DERIVED VELOCITY..... 180

FIGURE 4.8: MANUAL ESTIMATION LOCATIONS AND AREAS FOR TABLE 4.2. 180

FIGURE 4.9: INDIVIDUAL AREAS OF INTEREST AT FINDELENGLETSCHER (DEPICTED IN FIGURE 9) SHOWING VELOCITIES AND DIRECTION OVER THE SUMMER 2017 (RED) AND WINTER 2016/17 (BLUE) SEASONS..... 182

FIGURE 4.10: SURFACE VELOCITIES FROM AUGUST 27TH – 6TH SEPTEMBER 2016 ALONG THE CENTRAL FLOWLINE THROUGH THE OVERDEEPENING AT THE TERMINUS OF FINDELENGLETSCHER. 185

FIGURE 5.1: *TEMPERATURE (°C) (ABOVE) AND DISCHARGE (M^3 S) (BELOW) OF FINDELENGLETSCHER OVER THE SUMMER MELT SEASONS OF 2016 AND 2017.*..... 191

FIGURE 5.2: *HOURLY TEMPERATURES AND DISCHARGE AT FINDELENGLETSCHER OVER THE 2017 MELT SEASON. DATES OF UAV SURVEYS ARE VISIBLE IN LIGHT BLUE.* 194

FIGURE 5.3: *GRAPH OF ICE FLOW VELOCITIES PER AREA AND AVERAGE TEMPERATURES FROM TIME PERIODS THAT DATA WAS COLLECTED.* 195

FIGURE 5.4: *ATMOSPHERIC CONDITIONS (PRECIPITATION, DISCHARGE AND TEMPERATURE) AND MEAN VELOCITIES (BLACK ERROR BARS SHOW 1 AND 2 STANDARD DEVIATIONS, GREEN LINE REPRESENTS AVERAGED VELOCITY BETWEEN ORTHOMOSAICS) AT FINDELENGLETSCHER OVER THE STUDY PERIOD.* 196

FIGURE 5.5: AVERAGE DISCHARGE (M^3/S) FOR SUMMER MELT SEASONS OF FINDELENGLETSCHER (2016 & 2017). 197

FIGURE 5.6: *RESIDUAL DATA FROM WINTER (6TH SEPTEMBER – 5TH JULY).* 199

FIGURE 5.7: *RESIDUAL DATA FROM SPRING (5TH JULY – 7TH JULY).* 200

FIGURE 5.8: *RESIDUAL DATA FROM SUMMER MELT SEASON, BOTH VELOCITY DIFFERENCE (M/YR) AND PERCENTAGE CHANGE FROM THE BASELINE (7TH JULY – 3RD SEPTEMBER).* 202

FIGURE 5.9: INDIVIDUAL AOI AND ORTHOMOSAIC PAIRS GRID. 203

FIGURE 5.10: *BOXPLOTS OF AOI1 TEMPORALLY FROM ORTHOMOSAIC PAIRS STRETCHING FROM 27TH AUGUST 2016 – 7TH SEPTEMBER 2017.* 204

FIGURE 5.11: *BOXPLOTS OF AOI2 TEMPORALLY FROM ORTHOMOSAIC PAIRS STRETCHING FROM 27TH AUGUST 2016 – 7TH SEPTEMBER 2017.* 205

FIGURE 5.12: *BOXPLOTS OF AOI3 TEMPORALLY FROM ORTHOMOSAIC PAIRS STRETCHING FROM 27TH AUGUST 2016 – 7TH SEPTEMBER 2017.* 206

FIGURE 5.13: SURFACE VELOCITY AT FINDELENGLETSCHER OVERDEEPENING IN LATE SUMMER 2016 AND 2017. 207

FIGURE 5.14: *BOXPLOTS OF AOI4 TEMPORALLY FROM ORTHOMOSAIC PAIRS STRETCHING FROM 27TH AUGUST 2016 – 7TH SEPTEMBER 2017.* 208

FIGURE 5.15: *BOXPLOTS OF AOI5 TEMPORALLY FROM ORTHOMOSAIC PAIRS STRETCHING FROM 27TH AUGUST 2016 – 7TH SEPTEMBER 2017.* 209

FIGURE 5.16: *BOXPLOTS OF AOI6 TEMPORALLY FROM ORTHOMOSAIC PAIRS STRETCHING FROM 27TH AUGUST 2016 – 7TH SEPTEMBER 2017.* 210

FIGURE 5.17: *BOXPLOTS OF AOI7 TEMPORALLY FROM ORTHOMOSAIC PAIRS STRETCHING FROM 27TH AUGUST 2016 – 7TH SEPTEMBER 2017.* 210

FIGURE 5.18: *LOCATION OF VELOCITY INCREASE AT AOI6 (3RD – 6TH SEPTEMBER 2016).* 211

FIGURE 5.19: *BOXPLOTS OF AOI8 TEMPORALLY FROM ORTHOMOSAIC PAIRS STRETCHING FROM 27TH AUGUST 2016 – 7TH SEPTEMBER 2017.* 212

FIGURE 5.20: *BOX AND WHISKER PLOTS SHOWING ICE LOSS TO TWO STANDARD DEVIATIONS AT FINDELENGLETSCHER. THE RED LINE REPRESENTS AVERAGE 24 HR TEMPERATURES BETWEEN ORTHOMOSAIC PAIR IMAGES.* 214

FIGURE 5.21: *TEMPORAL ICE LOSS AT FINDELENGLETSCHER FOR WINTER (6TH SEPTEMBER TO 5TH JULY), SPRING (5TH-7TH JULY) AND SUMMER (7TH JULY – 7TH SEPTEMBER). VALUES REPRESENT THE RATE OF ICE LOSS PER YEAR IF VALUES PERSISTED AT THESE RATES.* 215

FIGURE 5.22: *SOUTHERN LATERAL CAULDRON DEVELOPMENT (HIGHLIGHTED IN RED) IN AOI4, LOOKING NORTH-EAST.* 216

FIGURE 6.1: LONGITUDINAL VELOCITIES OF A & B: HAUT D'AROLLA, SWITZERLAND ACROSS THE 1994 AND 1998 MELT SEASONS (MAIR ET AL., 2001; SWIFT ET AL., 2005), C: WORTHINGTON GLACIER, ALASKA 1994 (PFEFFER & WELCH, 1996 P45), D: STORGLACIAREN, SWEDEN 1982-85 (HOOKE ET AL., 1989). 221

FIGURE 6.2: TEMPORAL AND SPATIAL PATTERNS OF ICE FLOW VELOCITY OF LIRUNG GLACIER, NEPAL IN 2013 SUMMER AND 2013-14 WINTER. (KRAAIJENBRINK ET AL., 2016)..... 221

FIGURE 6.3: VELOCITY AND RUNOFF RATES AT GREENLAND ICE SHEET (DAVISON ET AL., 2019). 222

FIGURE 6.4: VELOCITY MEASUREMENTS OF THREE POLES PLACED ALONG THE CENTRE LINE OF FINDELENGLETSCHER 1979-1994 (TAKEN FROM IKEN & TRUFFER, (1997)). 223

FIGURE 6.5: *LINE GRAPH OF MEAN VELOCITIES TEMPORALLY (ORTHOMOSAIC PAIRS) AND SPATIALLY (AOIS).* 227

FIGURE 6.6: CARTOON SHOWING HOW MASS LOSS CAN AFFECT THE ACCURACY OF FLOW DIRECTION AND VELOCITY. 230

FIGURE 6.7: *NON-RESIDUAL ICE FLOW VELOCITIES FOR THE SPRING (F6F7) ORTHOMOSAIC PAIR. DASHED AND DOTTED LINE REPRESENT POTENTIAL SUBGLACIAL FLOW PATHS CREATING LOCALISED MELT.* 234

FIGURE 6.8: *DIFFERENCES IN PROGLACIAL STREAM EXTENTS. LEFT – 5TH JULY 2017, RIGHT – 7TH JULY 2017.* 234

FIGURE 6.9: ICE FLOW VELOCITIES OVER A SUBGLACIAL LAKE, WESTERN ANTARCTICA (ROSS ET AL., 2011)..... 240

FIGURE 6.10: ENGLACIAL CONDUITS ACROSS AN OVERDEEPENING AT RHONEGLETSCHER (CHURCH ET AL., 2019). 240

FIGURE 6.11: BASAL ICE AND SUBGLACIAL SEDIMENTS FOUND ON AN ADVERSE SLOPE AT MUIR GLACIER, ALASKA (ALLEY ET AL., 2003A). 242

FIGURE 6.12*: TOP: FIELD PHOTO OF BASAL DEBRIS FACIES BAND NEAR THE MAIN EGRESS POINT OF FINDELENGLETSCHER, AUGUST 2016. BOTTOM: FRAZIL ICE IN THE PROGLACIAL ZONE OF FINDELENGLETSCHER, 1 KM FROM THE GLACIER TERMINUS 28TH AUGUST 2016.* 246

FIGURE 6.13: FIELD PHOTO OF THE COLLAPSED CAULDRON AT THE TERMINUS OF FINDELENGLETSCHER FACING SOUTH, TAKEN 3RD SEPTEMBER 2017. 247

FIGURE 6.14: DEBRIS ENTRAINMENT AT A GLACIER BASE BASED ON VARIATIONS IN BEDROCK TOPOGRAPHY AND SUBSEQUENT TRANSPORTATION TO THE ICE SURFACE (TAKEN FROM MONZ ET AL., 2021). 247

FIGURE 6.15: LONGITUDINAL VARIATION OF VELOCITY ACROSS AN OVERDEEPENED BED AT STORGLACIÄREN IN JULY 1983. TAKEN FROM HOOKE ET AL. (1989). 252

FIGURE 6.16: SUMMER 2017 MASS LOSS ACROSS THE CAULDRON FEATURE AT FINDELENGLETSCHER, ALSO CONSIDERED TO BE THE AREA OF PROMINENT HYDROLOGICAL FLOW. ABOVE SHOWS MASS LOSS ACROSS THE ENTIRE SUMMER FROM 5TH JULY TO 7TH SEPTEMBER. BOTTOM LEFT SHOWS PATTERNS OF LOSS PER DAY AT THE BEGINNING OF THE SEASON. BOTTOM RIGHT SHOWS THE PATTERNS OF LOSS AT THE END OF THE SEASON. 256

FIGURE 6.17: ATMOSPHERIC TEMPERATURES ACROSS THE 2017 MELT SEASON WITH HIGHLIGHTED DATA COLLECTION DAYS AT FINDELENGLETSCHER. WEATHER STATION IS LOCATED (LAT 46.00036, LON 7.8727036) APPROX. 2 KM UP GLACIER AND AT AN ALTITUDE 300 M HIGHER THAN THE FIELD SITE. THEREFORE, ACTUAL FIELD SITE TEMPERATURES ARE LIKELY TO BE UNDERESTIMATED HERE. 257

FIGURE 6.18: *A) ICE LOSS FOR SUMMER PERIOD BETWEEN 5TH JULY AND 7TH SEPTEMBER 2017. B) STATE OF THE TERMINUS OF FINDELENGLETSCHER, 2019. C & D) ICE FLOW VELOCITY OVER SAME PERIOD AND COMPARISON WITH THE 2019 GLACIER EXTENT. INSET IN D SHOWS A CLOSE UP OF THE CAULDRON WITH ICE FLOW VELOCITY AND DIRECTION. YELLOW LINES DEPICT AOIS WITH CAULDRON DEVELOPMENT OCCURRING WITHIN AOI3.* 260

FIGURE 6.19: FIELD IMAGE OF COLLAPSED CAULDRON AND DISTINCTIVE CIRCULAR CREVASSING AT FINDELENGLETSCHER LOOKING SOUTH (3RD SEPTEMBER 2017). 263

FIGURE 6.20*: CAULDRON COLLAPSE AND SUBGLACIAL CHANNEL AT D'OTEMMA GLACIER. A) ORTHOMOSAIC WITH ABLATION STAKES (BLACK DOTS) AND GPR SURVEYS (BLUE STIPPLES). B) CHANGE IN SURFACE ELEVATION BETWEEN 7TH – 23RD AUGUST 2018 (TAKEN FROM EGLI ET AL. 2021A)* 266

FIGURE 6.21: RETREAT OF FINDELENGLETSCHER FROM 2009 TO 2019. 266

1. INTRODUCTION TO THE RESEARCH

1.1 INTRODUCTION AND RATIONALE

This thesis is concerned with subglacial topography and its effects on glacial hydrology and glacial dynamics at Findelengletscher, a mid-sized temperate alpine glacier situated on the border of Switzerland and Italy. Previous works have highlighted variability in subglacial hydrological conditions seasonally (Nienow *et al.,* 1998; Irvine-Fynn *et al.,* 2006; Nanni *et al.* 2019) and how this has a clear and significant effect on glacier flow velocities (Bartholomaus *et al.,* 2007). However, bedrock topography also plays a role in the hydraulic behaviour and therefore dynamics of glaciers, and, although this role is often highlighted (Glasser, 1995; Siegert *et al.,* 2005; Herman *et al*., 2011; Zhang *et al*., 2021), detailed studies of its role are rare.

Better understanding the drivers for glacial dynamics is important, as evidenced by the extreme rates of retreat in historical evidence. This shows that glacier retreat in the Alps has been exceptional since the middle of the 19th century (Schaefli *et al*., 2018). From 1980 – 2010 the trend amongst glaciers within the Alps has been one of extensive and accelerating mass loss with an overall ice volume loss over this time of −22.51 ± 1.76 km^3 (Fischer *et al*., 2015). Since the turn of the century, mass loss rates are higher than at any time since observational records began (Zemp *et al.,* 2015). It is predicted that within the Alps, and globally, this trend will continue through the current century with further glacier mass loss "far beyond historical precedent" predicted (Zemp *et al*., 2015; Zekollari *et al.,* 2019).

Understanding glacial dynamics is a complex issue (Clark, 1997) that is of prime importance for understanding contribution of ice sheet and glacier melt to sea level (Huybrechts, 2002). The more we understand the factors affecting the movement of glaciers, the better and more accurately we can use glaciers as a tool for understanding the effects of climate change on the planet (Oerlemans, 1994; Hock *et al.,* 2005; Gerbaux *et al.,* 2005; Liu *et al.,* 2019). Field studies and modelling have shown that glacier length fluctuations are a reflection of variations in summer temperatures (Vincent, 2002) and are therefore an accurate proxy record for temperature in the last 500 years (Oerlemans, 2005). In addition, understanding how glacial retreat and meltwater production is affected by climatic conditions is important for hydroelectric power applications particularly in Alpine areas (Fountain and Walder, 1998, Frey *et al.,* 2010) and more specifically the continuance of these power sources (Schaefli *et al.*, 2018).

The numerous interacting factors that dictate glacier flow mechanisms and dynamics have mostly been well-studied, including, for example, climate (Kääb, 2005; Magrani *et al*., 2022), volume and routing of meltwater (Joughlin *et al.,* 2008), and the presence of basal debris (Iverson *et al.,* 2003). However, less is known concerning the influence of bedrock overdeepenings on glacier flow (Cook and Swift, 2012). Overdeepenings are potentially important because they give rise to phenomena that have significant capacity to affect glacial dynamics such as the thrusting of ice (Moore *et al*., 2011), the supercooling of subglacial waters (Alley *et al*., 1998), and also the ponding of subglacial waters (Scambos *et al*., 2011). Such phenomena are of importance due to smaller scale glaciers having a shorter response time to a changing environment (Oerlemans and Fortuin, 1992). In addition, a greater understanding of the influence of glacier bed topography on hydrological processes is of importance to the prediction of changes in glacier hydrological regime (Huss *et al.,* 2008), the

formation and location of future pro-glacial lakes (Frey *et al.,* 2010; Viani *et al*., 2017), and glacier evolution in response to changing climate (Schneeberger *et al.,* 2001).

In recent years the development of uncrewed aerial vehicles (UAVs) has become important in many geographical fields from small scale water pollution (Zang *et al.,* 2012) to landslide displacement mapping (Lucieer *et al.,* 2011) and, more recently, glacial feature tracking (Immerzeel *et al.,* 2014). The rise in the use of UAVs is due to their potential to record land surface data in more precise detail (both in terms of resolution and temporal regularity) than available satellite and this combined with their relative low cost provides the potential for reconnaissance within the field that is as yet unrivalled (Rango *et al.,* 2009). In addition, the much-improved resolution and quality of data available from UAV studies today does not require significant time expenditure in the field (e.g., Dugdale, 2007). Because glacier bed topographies are increasingly well-known from radar studies and inversion methods (Fountain & Jacobel, 1997), detailed study of glacier dynamics using UAVs could be targeted at areas where the glacier bed is overdeepened and this could provide useful insight into glacier-bed dynamic effects. For example, there is potential to obtain independent evidence to support processes such as supercooling (Hooke, 1991; Alley *et al.,* 2003b; see Section 1.4.3) and subglacial ponding.

This study combines UAV monitoring of glacier dynamics with the application of ground penetrating radar (GPR) to the study of subglacial and englacial processes to constrain how an overdeepening affects hydrological and ice flow processes at a temperate Alpine glacier. Nonetheless, some of the more traditional remote sensing methods remain complimentary to UAV technology as there has been a considerable amount data recorded using these methods (Kulkarni *et al.,* 2007; Berthier *et al.,* 2007; Nick *et al.,* 2009) such as ice velocities,

surface characteristics and glacier facies (Hagen *et al.,* 2003). An Alpine glacier was chosen because smaller Alpine glaciers offer easier access than the outlet glaciers of large ice sheets. Nonetheless, it is clear from many previous studies that some of the essential features of Alpine glacier hydrology and dynamics are also characteristic of the ice sheets (e.g., Davison *et al*., 2019), meaning hydraulic and ice dynamic influences of glacier bed topography observed at valley glaciers should at least also have some applicability at ice sheet scales. There are some instances where ice sheets glacier characteristics can differ significantly. For example, ice sheets operate on larger scales to glaciers with in general, thicker ice which can cause creep closures to occur more rapidly (Burke *et al.,* 2012; Beaud *et al.,* 2018), or the lack of ice surface melt from Antarctica when compared to valley glaciers due to extreme atmospheric conditions.

This Introductory chapter seeks to review relevant findings in the fields of glacier hydrological, ice dynamic and subglacial geomorphological process and concludes by introducing the aims and objectives of the work presented within this thesis.

1.1.1 Structure of chapter

Section 1.2 explains the various ways in which meltwater is created, from what sources and how they travel through a glacier, finishing with how these processes are measured and recorded. For a more detailed and thorough review on glacial hydrology, particularly in the context of overdeepenings, see Cook & Swift (2012), Hooke (2005), and Paterson (2016). Section 1.3 discusses some of the observations of the dynamics of glacier ice and how and why these dynamics are affected and controlled. Section 1.4 describes the ways in which subglacial topography can affect the overlying ice dynamics (Section 1.4.1) and in particular reviews hydrological behaviour (Section 1.4.1, 1.4.2, 1.4.3, and 1.4.4) and its effect on ice

dynamics and, briefly, sediment export by the glacier drainage system. Sections 1.5 and 1.6 then explain the principle aims and outline of the thesis respectively.

1.2 KEY CONCEPTS OF GLACIAL HYDROLOGY

1.2.1 Sources of glacial meltwater

Meltwaters predominantly egress from the terminus of glaciers via a limited number of streams that follow the ice-bed interface. However, in the summer months, waters originate mostly from supraglacial (rather than subglacial) sources (Malard *et al.,* 1999), with basal melt, precipitation and groundwater sources making up a relatively small proportion of glacier runoff.

The origins of glacial meltwater can be split into one of three categories; supraglacial from above or at the surface of the glacier; englacial, from within the glacier; and subglacial, where water melts from the base of the glacier at the ice-bed interface. Supraglacial melt may originate from firn and snow. However, in the summer the amount of supraglacial melt dramatically increases due to higher atmospheric temperatures and a steady reduction in glacier surface albedo as the surface snow melts and exposes bare glacier ice (Oerlemans, 1989; Trusel *et al.*, 2012). Englacial melt is produced by heat generated from frictional dissipation of the potential energy of flowing water in englacial channels (Paterson 2016) as well as heat advection from flowing water upstream (Benn *et al.*, 2009). Both will increase through the melt season as melt and channel efficiency increase, adding to velocity (friction) and volume (heat advection). Subglacial melt can be generated by the same methods as englacial melt; however, due to the complexities in the interaction of ice with the bed, there are further potential sources of meltwater to consider. Notably, meltwater can be generated

by frictional heating from ice flow (Persson, 2015), geothermal heat (van der Veen *et al.,* 2007), as well as regelation (Cuffey & Paterson, 2010), although subsequent refreezing of basal melt may occur where melt encounters undulations in basal topography (Cook & Swift, 2012).

The most important and influential source of meltwater in the ablation zone of glaciers in the summer is supraglacial melt in the form of surface ice melt. Surface ice melt has high seasonal variability (Muthyala *et al.* 2020), with the majority being produced in summer, and the rate of melt production from this source can be up to 100 times more than that by any other source (Cuffey & Paterson, 2010). Subglacial and englacial melt happens on a much smaller scale and subglacial melt in particular demonstrates less seasonal variation (Seaberg *et al.,* 1988). Supraglacial melt is thus a significant driving force behind much of a glacier's dynamic behaviour, with many temperate glaciers showing velocity increases during the melt season (Armstrong *et al.,* 2017) that coincide closely with increases in supraglacial melt (Langley *et al.,* 2016).

1.2.2 Distributed and Channelised Subglacial Drainage

As the melt season begins, supraglacial runoff is initially low due to the presence of overlying snow and firn layers which can slow or refreeze any surface water. As the melt season progresses, however, the snowline retreats up-glacier and exposes bare glacier ice, which increases runoff dramatically (Jansson *et al.,* 2003). Runoff either drains to lateral streams or enters the englacial or subglacial system through crevasses (often running perpendicular to flow) or moulins (Hooke *et al.,* 1991). An example of the multitude of different routes of meltwater can be seen in Figure 1.1. The englacial conduit system and the equipotential

contours that direct englacial (and subglacial flow) are described in the following section (1.2.2.1).

The types of subglacial drainage can be split into two main categories: distributed systems and channelised (or localised) systems (Hewitt & Fowler, 2008). Distributed systems tend to dominate subglacial transmission of melt in the early melt season (Hooke 1989; Nienow *et al.,* 1998) and are characterised as being slow and inefficient, with lots of small drainage pathways branching off in a 'vein-like' structure in various directions (Figure 1.2), which may be remnants of previous flow paths that have not fully closed in winter months, or 'linked cavity' systems created by uneven bedrock (Kamb, 1987). Channelised systems tend to become more ubiquitous later in the melt season as certain flow paths enlarge and become large channels that are, hydraulically, a much more efficient means of drainage (Seaberg *et al.,* 1988). Channelised systems carry meltwater at higher velocities, have larger diameters, and are more direct. The splitting of flow paths into two categories is down to their hydraulic efficiencies and therefore their effect on subglacial water pressures and thus glacier dynamics.

Subglacial drainage systems thus have the ability to change considerably through the melt season. If enough melt occurs, the system will tend towards more efficient drainage over the course of a melt season (Fudge *et al*., 2008), as shown in Figure 1.2. Nonetheless, drainage systems considered to be channelised or distributed typically coexist (Simkins et al. 2021) within the glacial system, with channelized systems existing in summer in addition to the distributed system, and therefore lowering subglacial water pressures within the distributed system. The changing nature of these meltwater flow paths thus directly affects friction at the ice-bed interface and therefore rates of glacier flow (Mejia et al. 2021). Englacial flow systems

are less important in terms of their effects on glacier flow, although englacial flow paths are necessary for surface melt to access the glacier bed (Church et al 2019).

Early in the melt season, water pressures will be high in distributed systems as the glacier adapts to the increased melt water present (Clyne *et al*., 2022), which promotes higher glacial sliding speeds by reducing the ice-bed mechanical coupling (Nani *et al*., 2021). Over the melt season, channelised systems develop which lower water pressures and therefore increase effective pressure, which is the difference between normal stress at the bed and water pressures (Rada & Shoof, 2018). Increases in effective pressure can lead to a decrease in the drainage activity in distributed drainage systems that surround more channelised areas (Rada & Shoof, 2018). Low water pressures are maintained by the melting of channel walls caused by the heat created by viscous dissipation from the melt water (Young *et al.,* 2022). Towards the end of the melt season meltwater inputs decrease and channel sizes are reduced due to creep-closure (Vijay *et al*., 2021) which reverts the hydrological system back to a distributed system with high water pressure over the winter (Fountain and Walder, 1998; Sugiyama *et al.,* 2019).

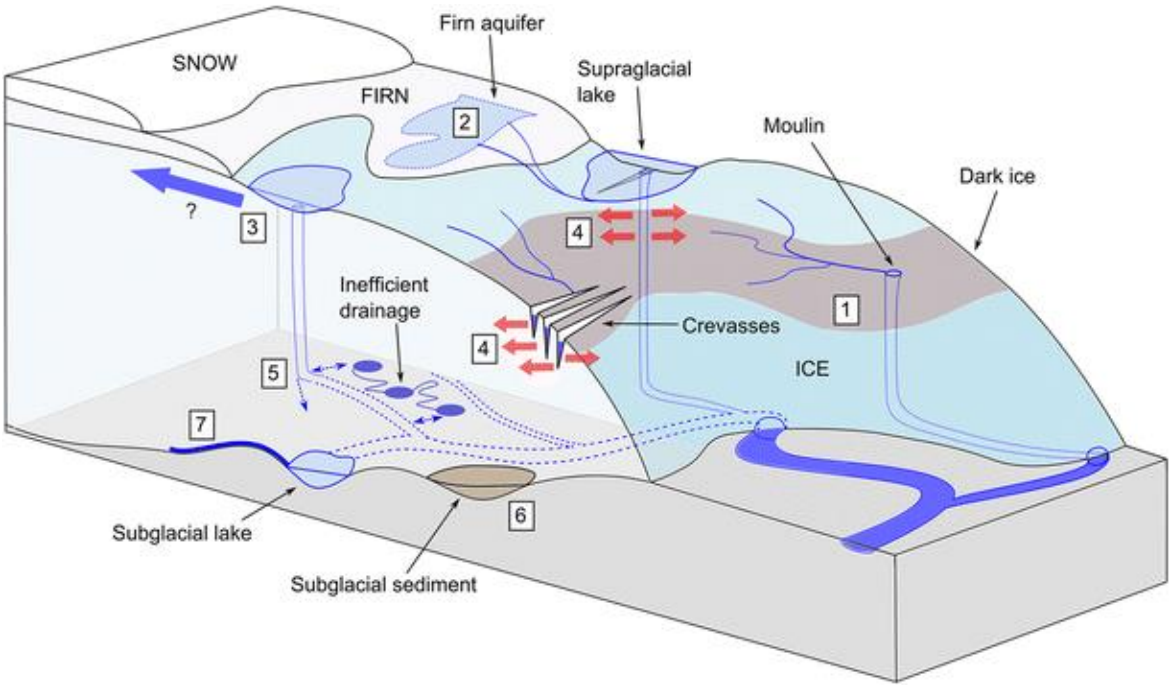

Figure 1.1: *Illustration of hydrological processes and pathways beneath a glacier. Important features of the hydrological transport system are as follows: 2) – firn melting and refreezing (densification). 3) – supraglacial to subglacial connections. 4) – supraglacial drainage causing moulin and crevasse widening. 6. Basal sediment deposition. 7) – basal melting on adverse slopes (Taken from Nienow et al., 2017).*

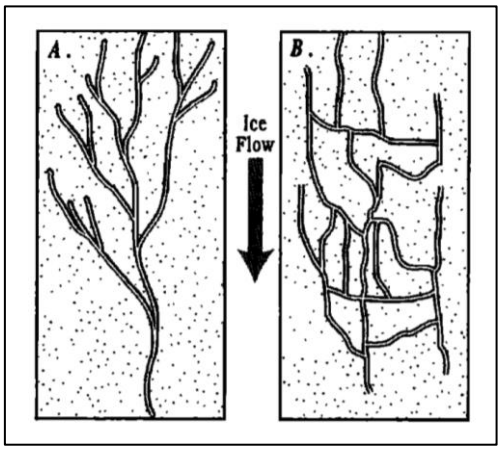

Figure 1.2: *Plan view of an example of (a) an efficient arborescent system likely seen at the end of a melt season and (b) an inefficient, nonarborescent drainage system, likely seen at the beginning of a melt season (taken from Fountain & Walder, 1998).*

1.2.2.1 Englacial drainage

Englacial flow paths can be formed by different processes. Firstly, the incisions made by supraglacial streams into the glacier due to dissipation of frictional heat may be followed by roof closure by either viscous creep or coverage by snow and ice in a process known as 'cut and closure' (Gulley *et al.,* 2009). Secondly, hydrofracturing enables crevasses to extend downward into the ice if there is a suitable supply of meltwater. Without meltwater, crevasses do not penetrate more than several 10s of metres into the glacier because the tensile stresses that open crevasses are 'cancelled out' at depth by ice pressures that cause closure (van der Veen 1998). The expansion of crevasses and moulins due to supraglacial meltwaters can allow direct access of surface meltwater to the ice bed at concentrated localised points where crevassing is occurring. However, crevasses and moulins have also been observed to intersect englacial conduit networks (e.g., Copland *et al*. 1997). Conduits that drain meltwater from the bottom of crevasses and moulins will increase in size during the melt season as flowing water dissipates frictional heat (Röthlisberger, 1972; Shreve, 1972).

Although englacial conduit formation is classically assumed to occur as a result of the 'primary permeability' of ice, which arises because of free space for water existing between the crystal structure (Lliboutry, 1971), englacial conduit formation can also occur by means of 'secondary permeability' as described by Gulley & Benn (2007). Here, permeability can be provided by sediment-filled thrusts or sediment deposits within previously eroded supraglacial runoff streams (Gulley & Benn, 2007). It should be noted that the latter process is much more prevalent at debris covered glaciers (Benn *et al*., 2012).

The likelihood of englacial conduits reaching the bed is increased nearer to the terminus where ice is usually thinner (and therefore less ice penetration is required) and surface melt

rates are highest, although it is reasonable to assume that englacial conduit networks exist in any location in a glacier where ice is temperate. The ability of englacial flow paths to connect to subglacial channels is an important factor in influencing the behaviour of the subglacial drainage system and subglacial water pressures, and therefore rates of basal sliding that are strongly influenced by the latter. Englacial conduits flow perpendicular to planes of equal water pressure (equipotential surfaces) as stated by Shreve (1972) and can be seen in Figure 1.3. Equipotential surfaces dip up-glacier with a slope ~11 times that of the ice surface (Shreve, 1972) with conduits forming normal to this (Gulley *et al*., 2009) with water flowing from regions of high to low potential following the steepest gradient.

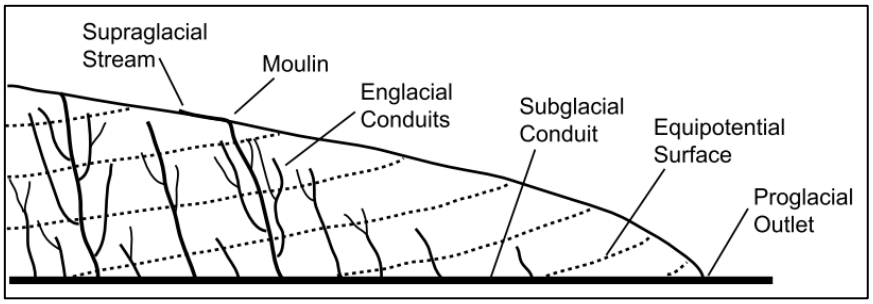

Figure 1.3: *Englacial conduits flowing perpendicular to equipotential surfaces as proposed by Shreve 1985 (Taken from Gulley et al., 2009, adapted from Shreve 1985)*

1.2.2.2 Subglacial drainage

The directions and pathways of subglacial water flow are constrained by numerous factors including the locations of meltwater sources, bed topography, substrate type, and ice mass geometry. Distributed drainage systems typically dominate when melt sources are low in volume and relatively constant, and a system dominated by distributed drainage pathways can characterise the 'winter' hydrological system (Section 1.2.1). Large contributions of melt that encourage the development of hydrologically efficient channel systems tend to be either

seasonal, arising from surface melt, or episodical, arising from release of glacially stored water as a jökulhlaup.

When a layer of either rock or sediment is present at the basal interface, meltwaters may flow in a 'film' of liquid at the ice-bed interface Weertman (1972) or as a network of small canals (Walder and Fowler, 1994). Water at the ice-bed interface in general flows perpendicular to contours of equal hydraulic potential (Shreve, 1972), though subglacial water in distributed systems may, locally, flow between cavities created in the lee of protrusions (Kamb, 1987). Melt water flow pathways can also be influenced by glaciological structures such as crevasses or moulins (Benn *et al*., 2009; Gulley, 2009). All distributed systems are characterised by slow water flow speeds (Flowers, 2015) and behave oppositely to efficient channel systems in that water pressure in distributed systems increases with increasing discharge (Flowers, 2015), although the link between water pressure and discharge is generally based on steady state assumptions that do not take into account seasonal conditions (Feinstein *et al*., 2020).

Because maintenance of subglacial channels requires large and sustained discharges, subglacial channels typically originate at the glacier bed where discrete inputs of supraglacial melt are present. Similar to distributed subglacial drainage, many different types of channelised subglacial flow have been suggested (Figure 1.4). R-channels (Röthlisberger channels) are semi-circular in shape and cut up into the ice from a flat bedrock base and probably the most widely used within the theoretical literature on subglacial flow paths in valley glaciers (Damsgaard *et al.,* 2017). N-channels (Nye channels) are channels incised into the bedrock, usually with a flat or convex ice roof. H-channels have been proposed by Hooke et al. (1990) as being more plausible than R-channels due to higher creep closure rates than Röthlisberger's model suggesting that these H-channels are a better match with their

measurements of basal water pressure. These systems are efficient because, in contrast to the behaviour of distributed systems, water pressures within them decreases as discharge increases. This behaviour arises because water pressures in englacial conduits and subglacial channels are determined by the balance between melting of channel walls through dissipation of frictional heat generated by the flowing water and inward creep of surrounding ice, meaning that, as discharge increases, the additional heat dissipated means melting of the channel walls increases, thus enlarging the channel (or conduit) system.

Water pressures in temperate valley glaciers entering winter are initially low due to low melt volumes, before a repressurisation of the system occurs due to closure of channels and background basal melt. Water pressures then increase during the beginning of the melt season as increased surface melt encounters inefficient subglacial drainage pathways (Hooke 1989; Nienow *et al.,* 1998). Later, in summer, when the subglacial drainage system becomes channelised, subglacial water pressures tend to decrease (Shoof, 2010; Cowton *et al*., 2013; Rada & Schoof, 2018). Finally, in autumn, when discharge reduces, pressures in channels will increase as inward ice-creep reduces the flow path size. The shape of the channel will influence how quickly these channels will close due to overburden pressures. For example, H-channels are likely to close faster than an N or R channel due to it having higher proportions of ice making up its perimeter (Hooke *et al*., 1990; Meyer *et al*., 2015).

Therefore, in order to better understand the relationship between ice flow velocity and meltwater, an understanding of how the drainage system changes over the season is needed.

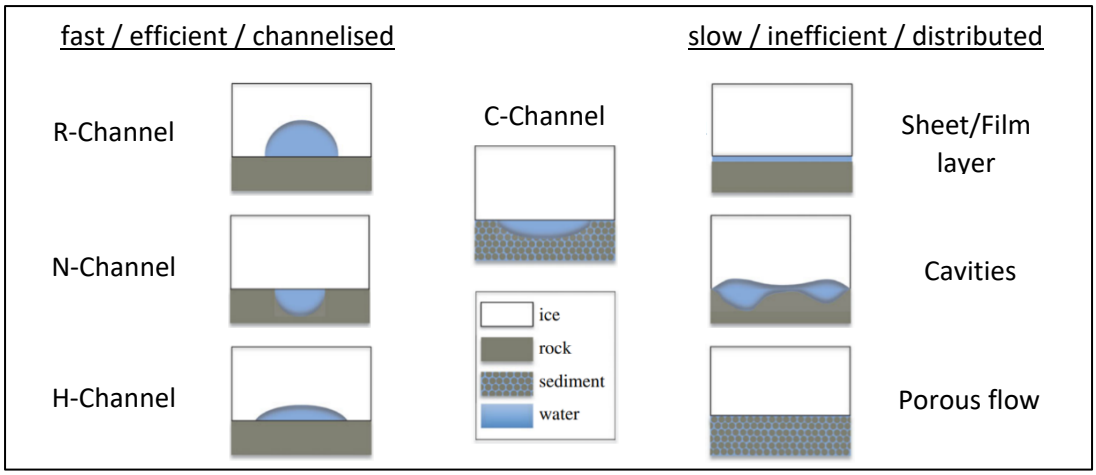

Figure 1.4: *Different forms of subglacial drainage, grouped into efficient and inefficient. C-channels can be classed as either based on the efficiency of their opening and closing processes (Taken from Flowers 2015).*

1.2.2.3 Seasonal drainage system evolution

A trend towards fewer englacial channels with larger diameters is prevalent due to a positive feedback loop whereby larger conduits attract increased water flow which operates at a lower pressure gradient to its surroundings. This in turn generates more heat in the flowing water which causes the ice of the conduit wall to melt at an accelerated rate, further enlarging the conduit (Walder, 1982; Lliboutry, 1983). Brief increases in melt water supply that occur for example, during a strong diurnal melt cycle, are accommodated by the drainage system through short term spikes in water pressure and lead to ice velocity increases (Schoof, 2010). As the melt season progresses towards the late summer, the snowline will retreat up-glacier and continue to thin. Along with this, the channelised system will also expand up-glacier as higher altitude crevasses and moulins are uncovered and melt further into the glacier's interior. Channelised growth is likely to be more extensive closer to the terminus due to the ever-increasing amounts (up until the Equilibrium line altitude (ELA)) of meltwater generated

up-glacier (Hooke *et al.,* 1989; Sharp *et al.,* 1993; Cook *et al.,* 2006). A network of sub and englacial channels will have formed intersecting the distributed system.

With the onset of winter, meltwater from supraglacial and englacial sources all but cease, low atmospheric temperatures cause reduced melting and precipitation falls as snow clogging moulins and crevasses and allowing overburden pressures to close these and any other conduits to the glacier's interior. Subglacial channels also close due to a lack of supply of meltwater.

1.2.2.4 The significance of water pressure and discharge for glacier flow

The relationships between discharge and water pressure in channelised and distributed systems, as described above, are of paramount importance for glacier movement. In distributed systems, high inputs of meltwater will cause high water pressures, which reduces ice-bed friction and leads to faster rates of basal sliding, although it can also destabilise such systems (Kamb, 1987; Flowers, 2015). For channelised systems, water pressure, being inversely related to discharge, means higher discharges leads to lower basal water pressures and thus greater ice-bed friction and slower glacier flow (e.g., Meyer *et al.,* 2016). This will be covered in more detail in Section 1.3.3 where core principles of glacier dynamics are discussed.

1.2.2.5 Transference of meltwater between different drainage systems

When differences in pressure is present, it is possible that both channelised and distributed systems interact with each other in transferring water between systems (Hubbard *et al*., 1995; Meyer *et al.,* 2015; Cowton *et al*., 2016). This is apparent towards the start of the melt season in what has been coined as a 'spring event' (Fenn & Gomez, 1989; Swift *et al*., 2005a; Bingham *et al*., 2006), where embryonic subglacial channels are not yet efficient enough to transport

the large amounts of meltwater (usually from supraglacial melting) suddenly present at this time (discussed in more detail in Section 1.3.3.1). This creates an increase in basal water pressure, reducing friction between ice and the bed, and therefore increasing glacier velocities through increased basal sliding rates (Gimbert *et al*., 2016). Water transfer also occurs when channels are fully established in the summer as a result of diurnal variation in discharge volumes within channels (Jansson, 1996). First, at the time that discharge reaches a peak in the mid- to-late afternoon, channel capacities may be inadequate to transport the discharge, this is due to channels not being able to adjust diurnally because melt rates are too slow. Instead, channels tend to be adjusted to the mean discharge over several days prior. Therefore, water pressures in channels may increase to exceed overburden pressures, and this will drive water from channels into the surrounding distributed system (Hubbard *et al.,* 1995; Bingham *et al.,* 2005). Transfer of meltwater then occurs in the opposite direction (distributed to channelised) in the early evening through to the morning (Schuler *et al*., 2004) as the discharge within channels declines and the pressure gradient between channels and the distributed system reverses.

1.2.3 Studying sub/englacial drainage systems

Investigating how glacier drainage systems evolve and interact is particularly difficult due to the inherent difficulty in accessing the internal structure of a glacier (Sharp, 2006). With the exception of limited locations where direct field observations (Section 1.2.3.1) can be made, such as the glacial terminus and at crevasses and moulins, glacial drainage structure must often be inferred, ideally by application of several independent methods. These methods might include clast measurements or other geomorphological evidence from the proglacial

area (Section1.2.3.2), and remote sensing techniques such as ground penetrating radar and dye tracing (Section 1.2.3.3).

1.2.3.1 Direct observation methods

There are few locations where direct observations of englacial, or subglacial drainage are possible. It is possible to access some larger channels in winter when glacial meltwaters are at their minimum (Kamb & LeChapelle, 1964; Benn *et al*., 2009; Gimbert *et al*., 2016; Benn *et al*., 2017). In addition, access holes can be drilled into the glacier mechanically, via steam drilling (Fountain *et al*., 2005; Tsutaki & Sugiyama, 2009) to provide access for video cameras, thermometers, turbidity sensors etc.

Difficulties arise in extrapolating direct observations to the scale of whole glaciers due to the low spatial resolution of such data (Lindbäck *et al*., 2015). Such observations usually cover a few sparse points due to the labour-intensive and difficult nature of creating artificial access (Harper *et al*., 2010) or opportunistic nature of natural locations. For example, locations used are most likely to be close to the margins of a glacier (Hubbard & Nienow, 1997), where conditions are likely to be different from other parts of the glacier system. It is important to consider also that the process of accessing englacial and subglacial conduits will have an effect on local conditions such as water pressure and temperature (Engelhardt & Kamb, 1997). Naturally occurring locations where the englacial/subglacial hydrological system can be accessed can also be considered not wholly representative of the system due to their access to outside air pressures not being general of the wider glacier.

1.2.3.2 Studies of proglacial locations

Previous subglacial flowpaths can be inferred by examining the hydrographs of proglacial streams (Willis *et al.,* 1996; Covington *et al*., 2012; Miles *et al*., 2019). Plume analysis has been

used to infer flow path characteristics at tidewater glaciers (Slater *et al*., 2017) and might also be usefully applied to proglacial lakes. In terms of geomorphological evidence, N-channels and former subglacial canals exposed by glacier retreat have been examined to infer previous glacial drainage pathways and their conditions (Sharp *et al*., 1989; Clerc *et al.,* 2013; Greenwood *et al*., 2016). The presence of eskers offers the most abundant evidence of water flow left behind ice sheets and glaciers (Burke *et al*., 2012; Butcher *et al*., 2021)

A drawback with these methods is the detail that can be obtained because information is lacking on when such features were active. In addition, such methods are only really useful at retreating glaciers where such evidence is relatively 'fresh'.

The measurement of subglacial discharge at the terminus of the glacier is also an important method. The shape of the hydrograph, when twinned with atmospheric factors such as temperature or precipitation can show information such as the lag time and evolution of the drainage system (Hannah *et al*., 1999); lower lag times mean a more efficient, channelised drainage system (Willis, 1995). Hydrographs oscillate diurnally (Hooke *et al*., 1990) as can be seen in Figure 1.5. The amplitude of this oscillation can show us the evolution of the system as well with higher peaked readings denoting a more channelised system. For example, Swift *et al. (*2005b) found hydrograph peaks occurring earlier in the day as the melt season progressed. Turbidity and electrical conductivity are other tools that can be used when measuring terminal outlet streams (Gurnell & Warburton 1990; Engel *et al*., 2018). A sudden spike in turbidity can represent a sudden drainage of previously ponded basal water which has also drained with it the basal substrate (Stone *et al.,* 1993).

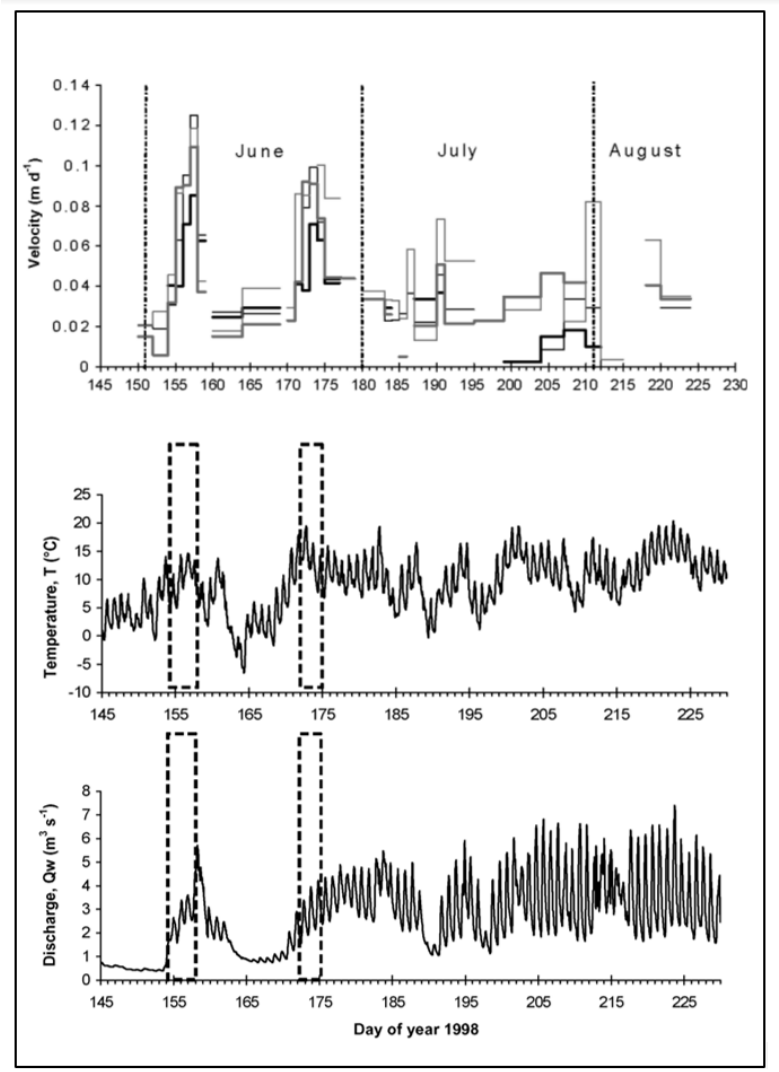

Figure 1.5*: Velocity (taken from various centre lines stakes), discharge and temperature recorded from Haut d'Arolla Glacier over the melt season of 1998. Dashed lines on all of the graphs indicate 'spring events' taken from Mair et al. (2003).*

1.2.3.3 Remote/secondary methods

Both methods mentioned in Sections 1.2.3.2 and 1.2.3.3 have considerable limitations in terms of how well they represent current or wider glacial conditions. Therefore, the development of alternate means to estimate glacial flow paths have been developed namely ground penetrating radar (GPR), dye-tracing and remote sensing techniques.

Ground penetrating radar has long been used in glaciological studies to show the topography of the underlying bedrock (Collins *et al.,* 1989; Saintenoy *et al*., 2013; Fischer & Kuhn, 2013) and to investigate glacier thermal regime (Reinardy et al. 2019). It is a particularly effective method of showing the bedrock depth and morphology due to ice having a low attenuation of electromagnetic waves (Rutishauser *et al*., 2016). This is important for glaciologists because subglacial topography directly affects glacier behaviour (Scherler *et al.,* 2011), including the development of the channelised drainage system (as discussed further in Section 1.4.1). Notably, GPR has been used successfully to measure englacial water movement in glaciers (Jacobel & Raymond, 1984); GPR has also been able to distinguish voids within glaciers (Nobes, 2015), which may represent relic channelised features partly closed by ice-creep during the winter season; and basal water can help the identification of the ice-bed interface (Zirizzotti *et al*., 2010). Nonetheless, the scatter on GPR traces from englacial and surface meltwater means it is not an ideal medium for application to glaciers (Murray *et al.,* 2007). GPR is therefore most effectively applied in the winter months when liquid water is less present within the glacier (Rutishauser *et al*., 2016).

Dye tracing techniques have been used for investigating glacial systems for over a century (Hubbard & Nienow, 1997) and can be used to estimate the likely drainage paths taken beneath a glacier (Nienow *et al*., 1996a), whether they are channelised or distributed, and how these systems change seasonally (Nienow *et al*., 1998; Cowton *et al*., 2012; Sharp & Tranter, 2017) as well as diurnally (Schuler *et al*., 2004). Tracers are typically fluorescent dyes which are highly soluble in water that are 'injected' into a glacier, usually via a crevasse, moulin or supraglacial lake (Werder & Funk, 2009; Werder *et al*., 2010; Dahlke *et al*., 2015; Fyffe *et al*., 2019), or via a borehole (Kamb *et al*., 1985; Hock & Wrangler, 1999; Gordon *et al.,* 2001). The dye thus follows the glacier drainage system before being discharged in one (or

multiple) outflows, where the dye concentration can be measured using fluorometry (Chandler *et al.,* 2013).

A good example of a novel remote sensing method would be via seismic array studies such as that of Nanni et al. (2021) who have been able to establish two-dimensional mapping of the subglacial drainage system. In studies where dye has been injected into boreholes, transit times through a glacier tend to be measured in days or weeks with long dispersal times (Gulley *et al.,* 2012), whereas dye injected into moulins that feed hydraulically efficient channels are transmitted through the glacier system at rates that are roughly one order of magnitude faster (Nienow *et al*., 1998). This is due to boreholes being unlikely to be installed in close proximity to conduits or channels, which occupy only a small area of the glacier, meaning dye is likely to initially enter an inefficient distributed system. In contrast, moulin-based dye injections, particularly in the summer, are likely to lead to dye directly entering the channelised system (Gulley *et al.,* 2012). Because longer travel times and distributed drainage morphologies lead to greater dye dispersion, highly dispersed dye 'return curves' are representative of inefficient distributed systems, whereas shorter and more peaked return curves are more representative of channelised systems (Chandler *et al.,* 2013).

All these remote methods of estimating and understanding glacial hydrology have different limitations in their application. It is therefore most prudent to employ a multifaceted approach which incorporates a selection of these methods in tandem to estimate subglacial and englacial hydrology.

1.3 CORE PRINCIPLES OF GLACIER DYNAMICS

Glacier dynamics are ruled by a complex set of processes which combine to provide the fluctuating rates of horizontal and vertical glacier movement that are seen on a daily/seasonal/annual level. The motion of glaciers is broadly via two distinct processes: (a) basal sliding, which is the horizontal movement of a glacier across the bedrock or substrate by means of simple shear (i.e., slip) or deformation of the substrate itself; and (b) the internal deformation of englacial ice, which is also known as 'creep' (Krabbendam, 2016). Both processes are discussed in further detail in Section 1.3.2. It should be noted however that whilst basal sliding is considered to vary temporally, internal deformation changes very little across a year and as such will provide a limited impact on any daily/seasonal/annual changes to glacier dynamics (Hewitt & Fowler, 2008). It is therefore inferred that basal sliding is the main driving force behind inter- and intra-annual changes in glacier flow.

For longer term changes in glacier movement to be adequately measured and understood, glaciers must be observed over longer timescales such as over the course of a melt season or multiple melt seasons. Numerous studies have attempted to do this (Hooke *et al*., 1989; Iken & Bindschadler, 1896; Swift *et al.,* 2002, 2005; Johnston *et al.,* 2005; Vijay *et al*. 2021) with the aim of better understanding how the hydrological system evolves temporally and how this affects dynamics. This section will outline and highlight the findings and theories from these studies into seasonal fluctuations in glacial dynamics

1.3.1 Seasonal scale glacier dynamics

From previous studies, it has been made clear that glacier dynamics vary considerably over temporal scales as well as spatially (e.g., Mair *et al*., 2001). temporal changes are more likely

due to temporal changes in hydrology at the glacier bed (Nienow *et al*., 1996b; Cowton *et al*., 2013) whereas variability in spatial motion is likely to be due a combination of the underlying topography (Ng et al., 2018), ice surface slope (driving stress) (Kaushik *et al*., 2022) and bed substrate (Rippin, 2013).

Notably, higher glacial velocities are typically recorded during the summer melt season than in winter (**Figure *1.6***) when no melt is present (Willis, 1995) (Figure 1.7). Further, vertical uplift has been shown to more likely to occur in the early melt season, when subglacial drainage is inefficient and surface melt is increasing and is less likely to occur as the melt season progresses as a result of the development of efficient subglacial channel networks (Anderson *et al.,* 2004; Iken & Bindschadler, 1986; Vincent *et al.,* 2022). Horizontal velocities also may be observed to peak in the early melt season (**Figure *1.6***) when vertical uplift is also at a maximum, and this behaviour has become known as a 'spring event' (Section 1.3.3.1). Both the vertical and horizontal velocities are linked in that they both are dependent on increased water pressures, and therefore usually increase and decrease at the same time (Andreasen 1985; Iken & Bindschadler, 1986). Seasonal velocities follow a distinct pattern as can be seen in **Figure *1.6*** with a sudden increase in velocity in the early melt season due to high levels of meltwater, an adaptation by the glacier in processing this meltwater efficiently which steadily reduces the velocity until winter where, due to accumulation from snow and limited meltwater, velocities remain relatively constant and low.

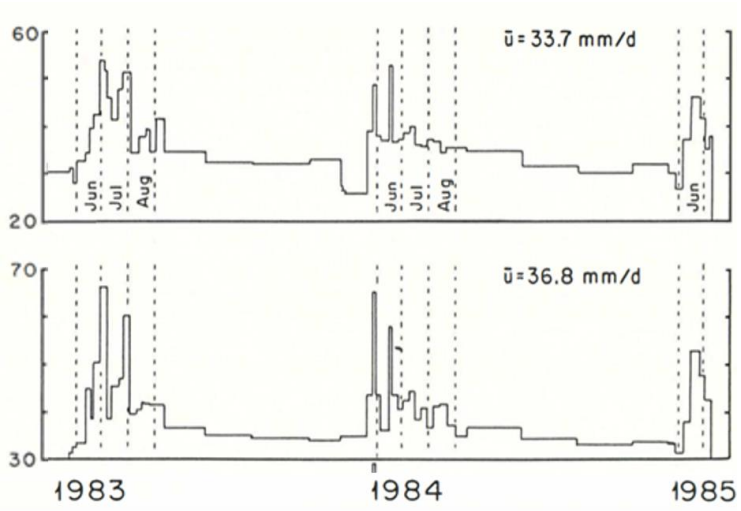

Figure 1.6*: Velocity rates across multiple seasons at Storglaciaren (taken from Hooke et al., 1989).*

On shorter timescales, diurnal velocity variation has been observed during summer as a result of over-pressurisation of channels at peak melt causing transfer of water into the adjacent distributed system (Alley *et al.,* 1997; Kehew *et al.,* 2012; Swift *et al*., 2021).

As stated above, spatial variations in glacier velocity flow is, in part, controlled by topography. For instance, higher velocities are observed along the centre line at the surface of glaciers due to ice depths being highest towards the centre and therefore more internal deformation and greater rates of basal sliding. Velocities are slower at the margins of glaciers due to frictional drag and lower driving stresses from thinner ice (Bamber & Layberry, 2001). Surface velocities are not uniform, consisting of 'sticky spots' where localised areas of ice move slower than the rest of the ice around them (Alley 1993; Stokes *et al*., 2007; Seddik *et al.,* 2019). Quite why these areas are more resistant is not fully understood but likely due to the underlying hydrological system and the state of the substrate and its topography beneath (Stokes *et al*., 2007).

Another phenomenon associated with seasonal changes in the glacial hydrological drainage system is the occurrence of kinematic waves within the glacier, where an uplift in the glacier creates a 'bulge' or 'wave' that travels down glacier at approximately 5 times the ice velocity (Hodge 1974; Iken *et al*.1983; Iken & Bindschadler 1986; Hewitt & Fowler 2008; Riel *et al.,* 2021). Especially noticeable to glacier motion during the winter is precipitation. Where little to no surface melt is occurring and there is less water within the system, heavy rainfall events lead to short-term velocity peaks, likely due to their lubricative effects subglacially (Anandakrishnan & Alley, 1997; Purdie *et al.,* 2008; Wendleder *et al*., 2018).

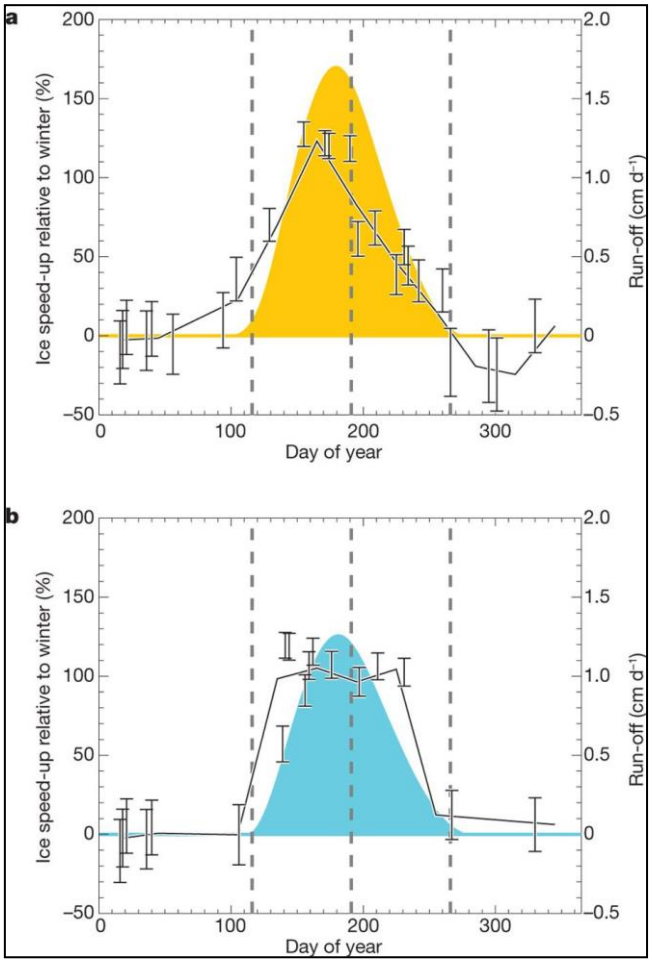

Figure 1.7: *Patterns of velocity speed-up across the melt-season in years of high (1995, 1998 (Orange)) and low (1993, 1996, 1997 (Blue)) melting based on point data from 6 glaciers*

(taken from Sundal et al. 2011). Error bars show one SD of uncertainty, colour represents estimated daily surface runoff rates.

1.3.2 Influences on glacier dynamics

As previously mentioned in Section 1.3, out of the two main factors responsible for movement in glaciers (basal sliding and internal deformation), the key influence in variations of velocities is basal sliding (Echelmeyer & Zhongxiang, 1987; Hooke *et al*., 1992), whilst internal deformation is considered to remain constant annually (Hewitt & Fowler 2008). However, studies have shown increases of internal deformation at the start of the melt season (Willis *et al*., 2003; Brzozowski & Hooke, 1981). The following will discuss the findings and assumptions of studies into these two main factors.

Glacier ice deforms slowly due to individual ice crystals moving relative to one another in response to gravity or other applied stresses (Cuffey & Paterson, 2010). This is a relatively constant process occurring in glaciers regardless of seasonal conditions; however, it is suggested that there may be a slight increase in this internal deformation in the summer due to increased supraglacial meltwater affecting ice deformation by enabling the alteration of adjoining crystals displaying opposing orientations across intergranular boundaries (Cuffey & Paterson, 2010). Spatial velocity variations from this effect alone are not responsible for the differences in surface velocities seasonally or diurnally. It is predominantly the variations in basal motion that causes this.

Basal motion is made up of basal sliding – the horizontal movement of the glacier along the bedrock, and sediment deformation – where loose or unstable sediment comprising of the basal layer are deformed (Boulton *et al*., 2001). Whilst it is difficult to access the bed directly,

borehole studies have been carried out in some instances that show the differences in velocities between basal motion and internal deformation by measuring both surface velocity and borehole measurements (Willis *et al*., 2003). However, inferring the contribution to velocity caused by basal sliding versus sediment deformation is more difficult due to the difficulties inherent in reaching the ice-bedrock interface. Lab experiments have been carried out to show how debris laden bedrock can alter the behaviour of glacier motion. For example, Zoet *et al.* (2013) suggest that in sediment-rich areas a 'stick-slip' alternation occurs, whereby due to the high friction and therefore heat, generated by sediment and clasts in the ice, higher meltwaters are created which increases glacier velocity (slip). Low initial lubrication of these areas and the heightened friction from substrates cause an initial 'sticky-spot' (stick). Studies widely agree that the rates of basal motion are generally enhanced in the summer months (seasonally) and during the daytime, when atmospheric conditions are at their warmest (diurnally) (Hooke *et al.,* 1990; Alley *et al.,* 1997; Nienow *et al*., 1998; Schuler *et al*., 2004; Kehew *et al.,* 2012; Cowton *et al*., 2012; Sharp & Tranter, 2017). Boulton *et al*., (2001) suggest that glacial coupling between the bed and glacier, and therefore basal sliding or sediment deformation, is predominantly determined by the state of consolidation of the till, which in turn, is reliant on variations in water pressure.

When surface velocities and basal velocities have been measured concurrently, it has been noted that basal motion made up 50-70% of surface velocities at the centreline (Willis *et al*., 2003), and much more nearer the glacier margins (Harbour *et al.,* 1997) where ice thickness was shallower. It can also be seen from Figure 1.8 that the spatial distribution of surface dynamics is not uniform due to changes to the stress gradient (longitudinal and transverse) from elsewhere in the glacier, often due to bed features such as isolated bedrock bumps and riegels (Rippin *et al.,* 2011), as will be covered below (Section 1.4.1). Therefore, changes in

the basal motion at one location can have a direct effect on dynamics at another location through extensional or compressive strain (Howat *et al.,* 2008).

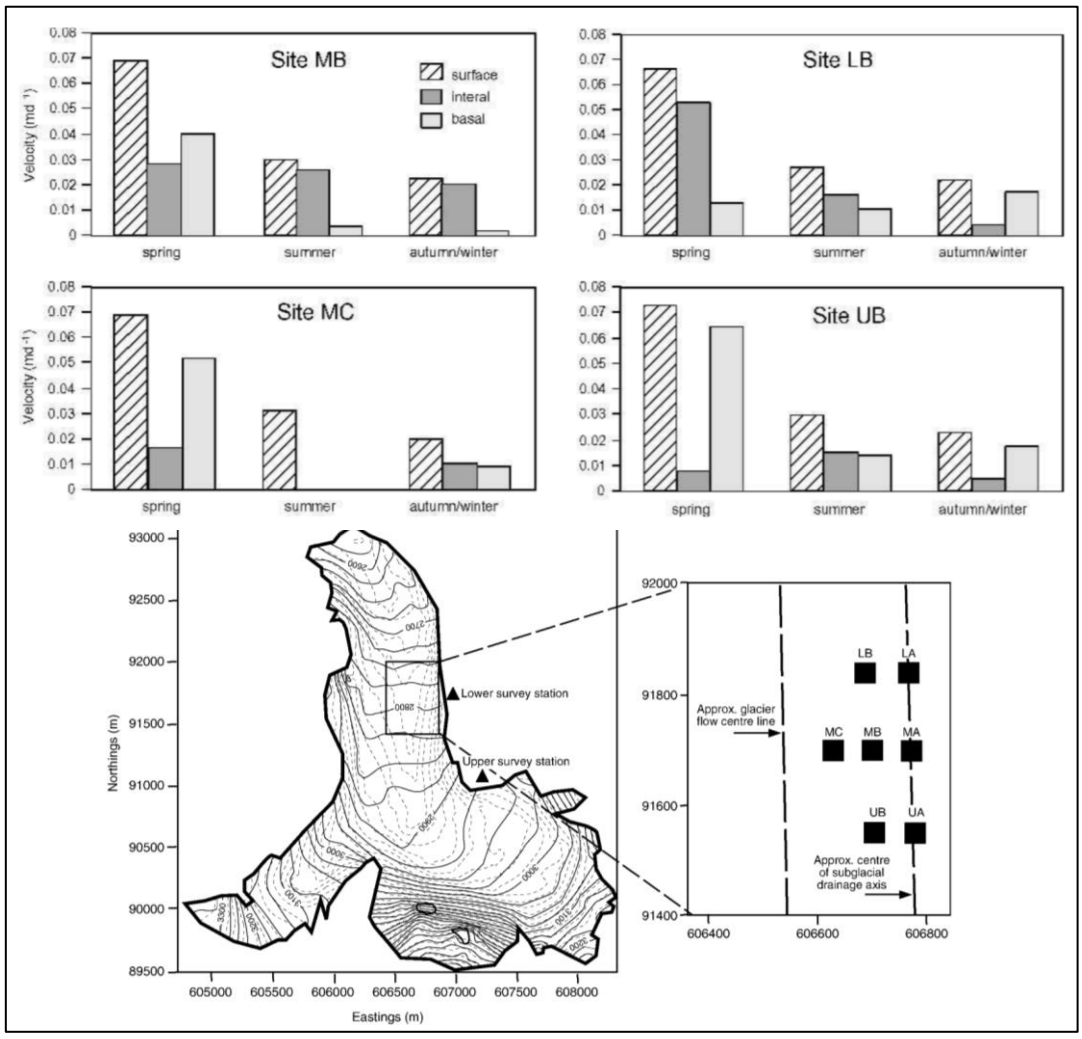

Figure 1.8*: Surface, internal and basal velocities at four sites at Haut d'Arolla glacier measured over the spring, summer, and autumn/winter seasons (taken from Willis et al., 2003).*

Findings from previous studies regarding seasonal variations of glacial dynamics have tried to correlate temporal differences in glacier dynamics with temporal changes in the hydrology whilst accounting for the effects of the wider stress gradient differences across the glacier.

The following two sections (1.3.3 & 1.3.4)) will highlight the effects of subglacial hydrology and longitudinal stresses on spreading variations in basal sliding to the ice surface.

1.3.3 The effects of hydrology on basal sliding

Among the literature there is a consensus that a correlation between horizontal glacial velocities and elevated water storage subglacially (Iken & Bindschadler, 1986; Bell, 2008; Bartholomaus *et al.,* 2008; Benn *et al*., 2017). It has also been suggested that this is due to increased localised water pressures reducing friction and encouraging basal sliding (Hubbard *et al.,* 1995; Bartholomew *et al*., 2010; Hoffman & Price, 2014). The combination of increased storage and increased water pressures often occur together (Iken *et al*. 1983; Iken & Bindschadler, 1986) because both conditions arise from the same cause, namely the inefficiency of the drainage system in coping with the levels of meltwater at that moment in time. This therefore shows the importance of the state of the hydrological drainage system and its direct effect on both spatial and temporal patterns of glacial dynamics, chiefly velocities (Moon *et al*., 2014). Furthermore, the evolution of this glacial drainage system in meeting the needs of the seasonally fluctuating meltwater conditions, has a clear effect on differences in seasonal dynamics (Nienow *et al.,* 1998; Mair *et al.,* 2002; Davison *et al*., 2020) and cause certain phenomena as will now be discussed.

1.3.3.1 Spring events

As touched upon previously (Section 1.2.2.5), a phenomenon labelled as a ‘spring event’ occurs when subglacial and englacial transport pathways are not efficient enough to transport the sudden high levels of meltwater through its system. The abundance of meltwater entering the system faster than it can be expelled leads to increases in water pressure and thus, increased basal sliding and therefore increased horizonal velocities across the glacier.

Combined with this, vertical uplift also known as 'jacking' (Hooke *et al.,* 1989; Werder *et al.,* 2013) can occur in response to high water pressures, and may occur over the course of a few hours to several days (Iken & Bindschadler 1986; Mair *et al.,* 2003; Bingham *et al.,* 2006), particularly close to the terminus (Bingham *et al.,* 2006) where maximum meltwater is located due to the cumulative effects of melting the further down-glacier travelled.

Before a spring event occurs (usually at the beginning of a melt season), distributed channel systems dominate (Section 1.2.2.5). As atmospheric temperatures increase and supraglacial snow and firn melt at increasing rates, they produce too much meltwater for the system to effectively deal with and expand quick enough to deal with the high levels of melt. Figure 1.5 shows how increasing temperatures link to discharge and can encourage these events to occur. High water pressures can force melt into adjacent subglacially distributed drainage systems, or water can directly reach the distributed system. If water pressure becomes high enough in relation to the mass of ice above, the friction between the glacier and the bed can be significantly reduced due to the glacier essentially becoming 'flooded' by the subglacial water beneath (Cook & Swift, 2012) causing basal sliding and vertical uplift ('jacking') and therefore horizontal and vertical velocity increases. These conditions will persist either until either (*a*) the hydrological drainage system adapts to become efficient enough to cope with the increased levels of meltwaters or, (*b*) the levels of meltwater themselves decrease, perhaps due to reduced melting from higher atmospheric temperatures or precipitation.

1.3.3.2 Jökulhlaups

A Jökulhlaup refers to a flood of water 'bursting' from a glacier (Maizels, 1997) usually from an ice dammed lake within or adjacent to the glacier (Tweed & Russell, 1999). Jökulhlaups can be representative of seasonal consistency, whereby occurrences arise during very similar

times each year (Bjornsson, 2009; Mernild & Hasholt, 2009). When the damming wall of the glacier retreats to a critical threshold and the weight of the dammed water cannot be supported, the lake will drain. If drainage is subglacial in nature then, like a 'spring event', meltwater levels will be too high for the glacier to effectively deal with and increased 'jacking' and basal sliding can occur in the same way as outlined in Section 1.3.3.1. Once the lake has drained and discharge is no longer enough to maintain the channels against the effects of ice-creep, the channels will close again allowing the lake to build-up once more (Tweed & Russell, 1999). In this way, Jökulhlaups can be part of the seasonal drainage patterns of glaciers. These ice-dammed lakes are not specific to any region or size of glacier, instead they occur across a multitude of different locations (Tweed & Russell, 1999).

1.3.3.3 Kinematic waves

Waves on a glacier (known as 'kinematic waves') have been observed for over 100 years (Hewitt & Fowler, 2008). The theory explaining such waves was developed by Weertman (1958) and Nye (1959; 1960). These waves, which are noticeable by their vertical uplift and above average horizontal velocities, approximately 5-8 times that of the surrounding horizontal glacier velocities (Van de Wal & Oerlemans, 1995; Hewitt & Fowler, 2008), are caused by variations in basal sliding (Van de Wal & Oerlemans, 1995).

Kinematic waves occur when ice flux into a section of a glacier is greater than the flux out of it, such as a large accumulation of mass. Because the ice flux and velocity are both greater (rarely less more than 10% (Hooke p368; Van de Wal & Oerlemans, 1995) than in the thinner ice immediately up and down glacier of it, the resulting wave moves faster than the surrounding glacier ice (Hooke, 2005 p368). These kinematic wave velocities are distinct from spring events (Hewitt & Fowler 2008).

1.3.3.4 Late melt season velocity oscillations

Towards the end of the melt season, the drainage system will consist of an arborescent efficient channel system made up by fewer channels with wider diameters, with an inefficient distributed system occupying areas beyond the efficient system (Section 1.2.2). Over the course of the melt season this system has evolved towards a more efficient construct to help evacuate supraglacial meltwaters as quickly as possible through the system to the terminus. Due to the high efficiency of the system now present, low subglacial water pressures and thus decreased basal motion will occur when compared to early in the melt season (Cowton *et al.,* 2016). The system will also be more able to deal with significant increases in meltwater, be that from high temperatures causing an increased supraglacial melt or high precipitation (Meierbachtol *et al*., 2013) a reason why spring events do not occur at the end of the melt season. However, drastic increases in hydrological input (such as jökulhlaups) can still produce velocity and uplift peaks (Russell *et al*., 2006; Einarsson *et al*., 2016). On a seasonal scale, velocities are likely to decrease towards the end of the melt season due to the efficiency of the drainage system, however, diurnal variations may be at their most variable (Hooke *et al.,* 1990; Hubbard *et al.,* 1995; Bartholomew *et al*., 2012) due higher atmospheric temperatures in the daytime, creating more melt and therefore higher subglacial water pressures. During autumn and winter, velocities can drop below background levels, before slowly recovering.

Where considerable diurnal oscillation occurs (also known as the diurnal variation ratio, i.e., the maximum melt divided by the minimum melt for the day (Bartholomaus *et al*., 2011)), even the efficient drainage system may not be able to cope with evacuating the meltwater subglacially in the system at its peak, in this case water may be diverted into the distributed system that transects the channelised system. This can lead to meltwater migration into neighbouring distributed systems (Hubbard *et al*., 1995; Andrews *et al*., 2014) where high

pressures can induce increased basal motion adjacent to the main channelised system in peak melt time diurnally. These diurnal velocity cycles are most likely to occur only on days where substantial meltwater inputs occur in the system (Nienow *et al*., 2005). As meltwater volumes are tied strongly to air temperature (Mair *et al*., 2003; Andrews *et al.,* 2014) melt rates are reduced nocturnally when temperatures are low which allows water pressure in channelised systems to drop and meltwaters to flow through channelised systems again rather than distributed systems (Schuler *et al*., 2004) leading to a decrease in basal motion at areas away from main channelised drainage routes (Iken and Bindshadler, 1986).

1.3.3.5 Non-uniform drivers of basal sliding

Section 1.3.3.4 above suggests a causality between subglacial hydrology and glacier motion over the course of a melt season. The interconnectivity of drainage pathways beneath a glacier as well as the spatial differences at the basal interface plays a big part in this relationship being observed.

A distributed drainage system contains numerous interconnected cavities and areas where the basal interface is isolated (Figure 1.4, Section 1.2.2.2). The latter of these can create 'sticky spots', defined as individual areas of high basal drag and constant water pressures surrounded by well lubricated areas with access to meltwater (Alley 1993). Cavities in sticky spots will not experience the same changes in water pressure brought on by intra-annual variability due to their relative isolation from the rest of the system and will behave far more uniformly across a melt season with respect to velocities caused by basal sliding. Glaciers with numerous sticky spots will present more irregular dynamics as these locations will behave contrary in their basal motion to interconnected areas of high pressure and therefore high basal motion (Alley, 1993; Stokes *et al*., 2007). The locations of sticky spots due to isolated

drainage can change due to the fluctuating nature of hydrological drainage as well as basal motion events intra-annually. The association of basal water pressures with glacier dynamics may therefore be due to how the interconnected or isolated drainage system changes (Mair *et al*., 2001; Stokes *et al*.,2007).

The make-up of the subglacial substrate may also play an important role on basal motion at localised levels. For example, areas with a waterlogged sediment may have different levels of basal drag to that of bare rock creating a nonuniform pattern to basal motion (Christoffersen & Tulaczyk, 2003; Walter *et al.,* 2014). Again, the levels of sediments in the basal interface can vary over time too (Alley *et al*., 2003; Cook & Swift 2012) affecting the potential basal motion not just spatially but temporally too.

1.3.4 Spatial coupling (stress gradients)

As previously mentioned, (Section 1.3.2) basal sliding is considered a key driver of velocity variations temporally across a glacier, yet the localised differences in basal sliding have a wide impact across the glacier as a whole due to spatial coupling. Spatial coupling is the interrelationship between basal processes and surface motion based on the internal stress gradients of the glacier. An example would be at a location down-glacier where basal drag is low and basal sliding rates high, the increased velocities would cause a 'pulling' stress on ice up-glacier. It is possible that in this way, events considered to be localised basal sliding could in fact be due to spatial coupling of the stress gradient from elsewhere on the glacier. Based on this affect, it is important not to judge surface characteristics such as velocities, direction of flow or features such as crevassing by the basal conditions directly below alone, but as a part of a wider area around that point (Howat *et al*., 2008; Scott *et al*., 2009; Pimentel &

Flowers, 2010; Cuffey & Paterson, 2010), their affects lessening with distance travelled away from that point (Kamb & Echelmeyer, 1986).

1.3.5 Summary of glacier dynamics

Glacier dynamics are complicated owing to the myriad of different factors that affects them. Overall, however, they largely represent the variations in everchanging hydrological conditions at a glacier. The key factors affecting localised changes in basal sliding are the basal water pressures which are determined by the efficiency and isolation/interconnectivity of the drainage system as well as supraglacial melt rates. Gross variations in basal sliding velocities are roughly reflected in variations in surface velocities; however, spatial stress-gradient coupling may affect velocities at a wider level.

1.4 GLACIER-BED TOPOGRAPHY AND ITS INFLUENCE ON ICE FLOW

1.4.1 Influence of subglacial topography on glacier flow

The topography beneath a glacier is an important consideration when understanding variations of the glacier dynamics regarding direction and velocity. For example, driving stresses are directly affected by the slope angle at a particular point, whereby ice on steeper gradients will travel faster than flatter gradients (Rippin *et al*., 2011). This causes differences in the stress gradient throughout the glacier especially due to the common undulating shape of bedrock beneath overstep glaciers (Cook & Swift, 2012; Swift & Jones, 2018). This can lead to features such as crevasses forming in the vicinity of rough bed terrain which can have significant impacts on the hydrological inputs intra-annually (Iverson 1991; MacGregor *et al.,* 2000; Poiner *et al*., 2019).

Not only does the underlying topography affect driving stresses, but it also affects the morphology of the drainage system, which itself directly affects the ways in which water travels subglacially and thus subglacial water pressures (Mair *et al*., 2001). This is discussed in more detail below. Valley glaciers are defined entirely by their topography and will flow down-valley at its lowest point. Schoof (2004) and Lovell *et al.* (2018) suggests glacial surging behaviour can be strongly influenced by the underlying bedrock topography.

1.4.2 The role of overdeepenings

Overdeepenings are a basin-like feature of the topography beneath a glacier system that are typically of a magnitude of 10-10^2 m deep and 10-10^3 m long (Cook & Swift, 2012). Their importance is predominantly due to the different forces at play when ice and subglacial water is required to flow uphill (i.e., along the adverse slope of the overdeepening). This can create specific behavioural changes in subglacial drainage hydrology, as well as stress gradients within the ice, which will be discussed below.

1.4.2.1 How overdeepenings form

The glaciological term 'overdeepening' has been around for over 100 years, being used in the early 20th Century to describe hanging valleys in the lower region of Ticino Valley, Switzerland (Garwood, 1902). The term 'overdeepening' was initially used to describe the deepening of any valley by ice because glacial valleys appear to incise more deeply into the landscape than would be expected if the landscape was shaped by fluvial processes.

Currently many aspects of overdeepening formation remain inadequately understood (Cook & Swift, 2012). However, it is theorised that they develop either due to lithological weaknesses in the bedrock where glacial erosion is thus more active (Preusser *et al.,* 2010; Steinemann *et al.,* 2021) or by hydrological and glacial erosion feedbacks that amplify small

bed irregularities (Hooke, 1991). Further, it has been proposed that these mechanisms should cause all glacier beds to evolve toward an equilibrium overdeepened bed geometry over time (Alley *et al*., 2003; Cook & Swift 2012). Overdeepenings are a common part of the geological landscape and are present beneath many types of ice masses, including valley and outlet glaciers (Hooke, 1991; Alley *et al.,* 2003b; Swift *et al.* 2021), ice caps (Flowers *et al.,* 2005; Marshall *et al.,* 2005; Evans *et al.,* 2018), and ice sheets (Schoof, 2007; Durand *et al.,* 2009; Patton *et al.,* 2015, 2016).

There is an ambiguity in the identification and classification of overdeepenings due to there being no minimum depth threshold; only that, to be considered to have been 'overdeepened', glaciers need to exceed the natural limits of fluvial erosion, leading to the formation of a basin with an adverse slope (Hooke 1991). Patton *et* al., (2015) do attempt to determine objectively the outer limits as to where an overdeepening should be drawn. Hooke suggests that there is very little difference between overdeepenings and cirques and that there may be a common causality for the two features as they are both caused by the same erosional processes, namely, abrasion and quarrying (Embleton and King, 1968; Alley *et al*., 2019). Alley *et al.* (2003a) however notes that overdeepenings in cirques largely appear to reflect a rotational movement of ice that is characteristic of cirque-glacier flow (Grove, 1958), meaning cirque overdeepenings are likely fundamentally different in their origin to their down-glacier counterparts. Indeed, Cook and Swift (2012) noted that, as well as being formed in cirques, overdeepenings are found beneath glacial termini and at confluences (the latter is also noted by Garwood, 1902).

It is possible that overdeepening formation is the result of a multitude of factors, such as variations in basal friction, water pressure, bedrock strength, and initial bedrock topography.

However, a novel process of overdeepening formation was proposed by Hooke (1991) and this has been widely accepted as a leading hypothesis by subsequent literature (Alley *et al.,* 1998; Cook *et al.,* 2006; Antoniazza & Lane, 2021). Hooke (1991) explains that, as a glacier flows down-valley, it will naturally encounter resistance from the valley floor itself, and not necessarily in a uniform manner. Occasionally the glacier will be forced to flow over bedrock steps where the bedrock is more resistant to erosion (in a similar manner to water flowing over a knickpoint in the bed of a river). When this occurs, the increase in flow velocity caused by the localised steepening of the bed initiates surface crevassing (Figure 1.9). These crevasses then direct surface melt to the bed, allowing these locations to experience strong basal water pressure fluctuations (Iverson 1991; MacGregor *et al.,* 2000) that enhance the quarrying rate. Such fluctuations occur because supraglacial melt has strong diurnal variability (Hooke *et al*., 1990). Quarrying of the bed in turn increases the initial gradient of the slope and this furthers the surface crevassing. The increase in sliding velocities created by the steeper slope may also lead to increased erosion by means of quarrying and abrasion (e.g., Herman *et al.,* 2011).

Overdeepenings are possibly therefore more prevalent down-glacier in the ablation region of glaciers because here there is an increased amount of surface melt available (Hooke *et al.,* 1989; Cook *et al.,* 2006). Furthermore, a steeper ice surface slope increases the potential for water and sediment to be transported out of the overdeepening (Cook & Swift, 2012), permitting more rapid erosional processes than if sediment was permitted to accumulate as a subglacial till layer (Herman *et al.,* 2011).

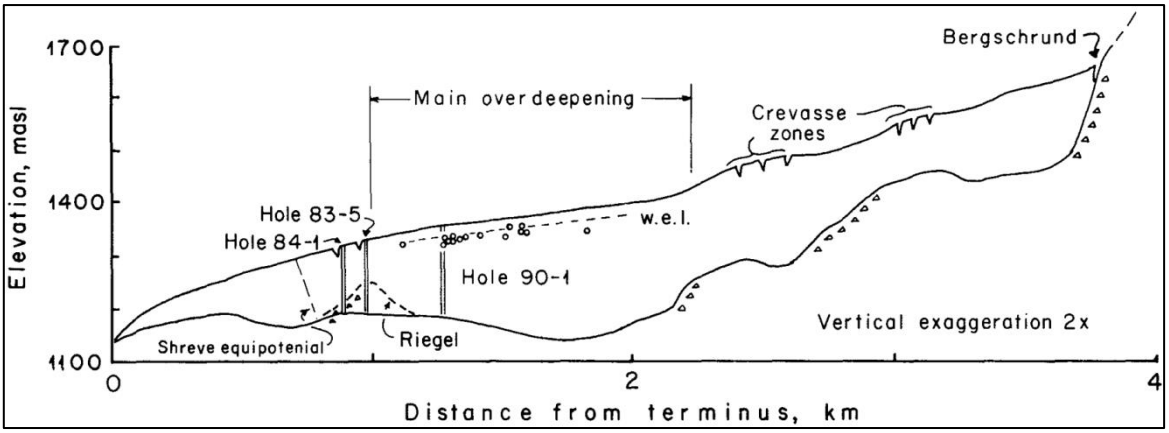

Figure 1.9*: Longitudinal section of Storglaciären, Sweden showing localised crevassing zones prior to overdeepenings. (Taken from Hooke et al., 1991, p1106).*

1.4.2.2 Overdeepenings and the drainage system

Fountain and Walder (1998) found that the water discharge of glaciers in summer was approximately two orders of magnitude higher than in winter which suggests that there is a great deal more water available beneath a glacier in summer months and this will increase glacial flow velocities due to the decreases in basal friction. This sudden increase in flow velocity was termed a 'spring event' suggesting an annual recurrence, backed up by the findings of Swift *et al.* (2005) from work on the same glacier; Haut d'Arolla, Switzerland. When a 'spring event' occurs at a temperate glacier with an overdeepening, it is likely that the amount of water suddenly subglacially present would greatly decrease friction between the glacier and the bed, decreasing basal stress and therefore increase the local velocity across this overdeepening via basal sliding as described in Section 1.3.3.1. This should be evidenced by an increase in crevassing up-glacier from the overdeepening as well as increased rates of velocity across the overdeepening, particularly at the deepest point of the overdeepening where ponding is more likely to occur.

Once meltwaters have flowed into the subglacial system, it is rare for them to flow back into the englacial system again. However, overdeepenings can affect the meltwater drainage system due to the energy required to flow up an adverse slope being used up and refreezing therefore occurring. These slopes will cause substantial lateral diversions in the drainage system (Sharp, 2006; Swift *et al.,* 2021), which can redirect subglacial water into englacial systems (Clason *et al*., 2015; Swift *et al.,* 2021).

Figure 1.10 shows how an overdeepening may delay the onset of channelisation from a more distributed form of hydrological system due to an increase in sliding velocities of a glacier attributable to higher basal water pressure because of a reduced transmissivity of the subglacial flowpaths. In this way a very real change to glacier dynamics is theorised by topography's effect on the drainage system.

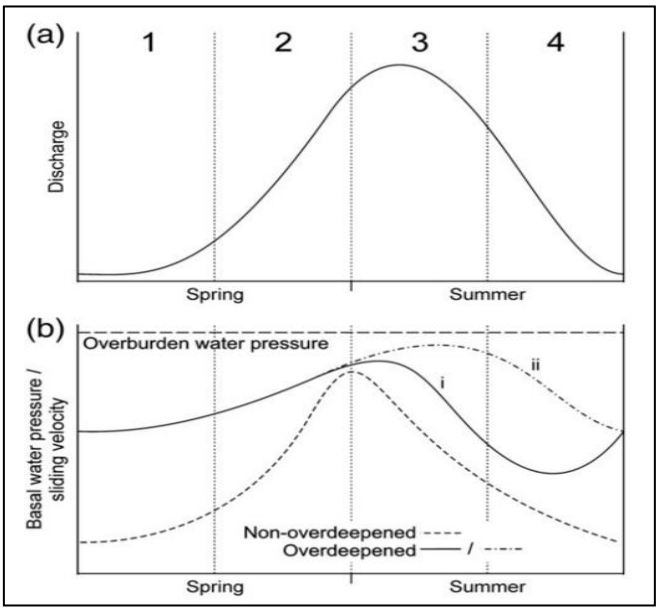

Figure 1.10*: A theorised graph of basal water pressure and sliding velocity over a melt season for overdeepened and non-overdeepened bed morphologies. A) shows basal melting and surface run off B) shows water pressure and sliding rate. (Taken from Cook and Swift, 2012).*

1.4.3 The role of supercooling

As water moves subglacially along an adverse slope within an overdeepening, energy is expended due to the movement of water against gravity. In turn this reduces the amount of energy available to be expended as heat (Cook *et al.,* 2006; Alley *et al.,* 2019). This causes subglacial water channels to constrict due to refreezing of water to the inside of conduits which, in turn, increases the water pressure within these conduits. The ice surface to bedrock slope angle ratio is crucial to this refreezing as will be discussed shortly. The reduction in energy also decreases water velocity and, with it, sedimental transport (Alley *et al.,* 2003a; Swift *et al.,* 2018). This is why, as Hooke (1991) suggested, sediment may be deposited on the adverse slope of an overdeepening. The freezing of water as it traverses an adverse slope is known as glaciohydraulic supercooling. Supercooling is essentially an antonym of melting, where all energy is used up to warm the melt water.

Within the literature it is commonly cited that the threshold for supercooling to occur is when the adverse bed slope is between 1.2-1.7 (Alley *et al.,* 1998) times the angle of the ice-surface slope (Hooke and Pohjola, 1994; Alley *et al.,* 2003a; Cook and Knight, 2009; Swift *et al.,* 2018). When this occurs, the thermal energy produced and the rate at which the water temperature is increased (due to viscous dissipation of heat by the flowing water) will not be sufficient enough to match the change of the pressure melting point as water rises from the overdeepening, and this leads to supercooling. When this occurs, subglacial transport pathways will become restricted and transport of sediment by water will be reduced. Werder (2016) further suggests that variations in basal water pressure will influence this threshold by adding a term that corrects for water pressures below overburden at the downstream end of the overdeepening.

Supercooling is clearly an important factor to consider in the change in dynamics of the glacier, indeed Cook *et al.* (2006, p581) consider the process to have a "fundamental implications for the behaviour of glaciers" due to its effect on sediment transport and its potential to alter the morphology of the glacier bed through sediment deposition and transport (Alley *et al.,* 2003a). Alley goes on to hypothesise that supercooling causes glacier flow velocity to increase due to water pressures increasing and thus basal friction decreasing (Sugiyama and Gudmundsson, 2004). Nonetheless, it has also been suggested that the prevalence of supercooling and its importance may have been exaggerated (Knight, 2003); for example, to explain basal ice sequences in unsuitable situations. Supercooling appears mostly prevalent (due to observations only) within Iceland (Roberts *et al.,* 2002, Tweed *et al.,* 2005) and Alaska, specifically at Matanuska Glacier (Alley *et al.,* 1998; 2003b; Baker *et al.,* 2003; Alley *et al.,* 2019), which is considered to have the most complete evidence for this process (Cook *et al.,* 2006).

From work at Storglaciären (Hooke *et al.,* 1988; Hooke and Pohjola, 1994) it is suggested that as subglacial pathways become less efficient, more water is transported across an overdeepening englacially, thus bypassing the adverse slope and making it a more efficient transport method. Cook and Swift (2012) consider it possible that this process is relatively common and that the diversion of water englacially through will reduce the amount of supercooling occurring within an overdeepening. This might go some way to explaining why the process is not widely evident outside of a few examples in Iceland and Alaska.

As the overdeepening is eroded up-valley a protective till layer is formed on the adverse slope as the glacier erodes the bed (Hooke, 1991; Alley *et al.,* 2003b; Cook *et al.,* 2006; Egholm, 2012). It has been suggested that such sediment layers can only be as a result of

overdeepenings (Lawson *et al.,* 1998; Strasser *et al.,* 1996). It has been further suggested that the ice-surface will tend towards the horizontal at these areas due to a substantial decrease of basal drag and thus increase in efficiency of ice flow, with Haeberli *et al.* (2016b) indicating a slope angle of <5-10° (Cook and Swift, 2012). This would increase the likelihood of supercooling or ponding thresholds being reached. The more that the ice-surface is flattened, the further the pressure-melting point is reduced within the overdeepening, causing hydrological transport channels to constrict further and therefore reduce the efficiency of sediment removal (Alley *et al.,* 2003b). If this negative feedback loop continues, it would lead to a state of supercooling becoming commonplace at areas of overdeepening (Creyts *et al*., 2013).

1.4.4 The role of ponding

When the adverse slope of an overdeepening is ~11 times the gradient of the ice-surface slope water cannot escape the overdeepening and a subglacial lake must form, as proposed by Shreve (1972) (see Figure 1.11). From the literature it appears there is little evidence of ponding within valley glaciers (Cook and Swift, 2012). Evidence for ponding has been predominantly found at larger ice masses such as in Greenland (Palmer et al., 2013; Bowling *et al.,* 2019) and Antarctica (Siegert, 2018; MacKie et al., 2020). Werder (2016) suggests that this may be due to the depth of overdeepenings stabilising at supercooling thresholds (1.2 – 1.7) due to reduced basal water pressure variations, reduced sediment evacuation and increased sediment deposition, which forms a protective layer inhibiting further down erosion of the bed, thus stabilising the depth and making further deepening unlikely (Livingstone *et al.,* 2012).

At overdeepenings exhibiting ponding, basal friction is greatly reduced as ponding will cause the ice to be buoyant because basal friction will approach zero (Patton *et al.,* 2015) and the ice-surface slope should flatten considerably. It may be possible to identify ponding locations using remote sensing from analysis of glacier slope but also by elevation changes due to lake filling or emptying. For example, Scambos *et al.* (2011) inferred subglacial lakes beneath Crane Glacier, Antarctica by matching elevation changes to similar response characteristics such as the raising of the surface at the downstream area of the ponding location, similar to the work of Wingham *et al*. (2006) at subglacial lakes in East Antarctica.

In situations where the ponding threshold has not been reached, it is still likely that basal water pressures will approach the ice-overburden pressure and thus provide a similar buoyancy force (Iverson *et al.,* 1995; Clarke, 2005). This is known as 'decoupling' of ice from the bed, and means effective pressure decreases, basal friction (drag) decreases, and sliding of ice across the bed increases. The decoupling is a response to the high basal water pressures and is supported by confined subglacial hydraulic requirements due to an adverse slope acting as a confinement layer (Buechi *et al*., 2017). Cook & Swift, (2012) suggest that, whilst likely rare, due to the fluctuations of melt diurnally, there must be periods of time where ponding does occur within valley glaciers, as long as the ice mass is sufficiently thin so as to remain buoyant.

Such basal water pressures have been shown to occur at valley glaciers within the Alps (Sugiyama and Gudmundsson, 2004) and therefore a drastic reduction in basal drag (Cook and Swift, 2012) is likely to significantly affect glacial dynamics by increasing the sliding velocity in these areas (Iken, 1981). Cook and Swift (2012) suggest that the 'standard model'

of the drainage system suggests that basal water pressure will most closely approach the overburden water pressure in early summer (Figure 1.10).

Overdeepenings exhibiting adverse slopes that exceed 11 times the ice surface slope reduce sediment transport to virtually nil due to the inability for water and sediment suspended within this water, to be flushed out of the depression. In order for sediment to be transported out of the basin, a retreat of the glacier is necessary which steepens the ice surface slope and increases the ponding threshold, enabling the subglacial water to be flush out (Jordan *et al*., 2010; Scambos *et al*., 2011).

Evidence of valley glacier ponding is scarce in the literature (Scambos *et al.,* 2011), whilst overdeepenings are considered commonplace (Fiebig *et al.,* 2010; Cook & Swift, 2012). From Figure 1.12, areas of potential ponding are rare in relation to the number of overdeepenings, even in these examples (Greenland Ice Sheet and a large Antarctic glacier). Ponding is less prevalent in valley glaciers due to the steeper reliefs leading to a higher ponding threshold from the bed. How common ponding is in valley glaciers and what the effects might be, are yet to be adequately discussed within the literature. Quite what effect ponding has upon glacial dynamics is uncertain; however, findings from Pattyn et al. (2004) found that ice velocities over a subglacial lake at Vostok increased due to the drag-free basal boundary conditions. As a glacier retreats the slope angle of the ice-surface above the ponded area is increased which may lead to a "flushing out" of ponded water from an overdeepening which can lead to noticeable changes in localised glacier elevation (Scambos *et al.,* 2011).

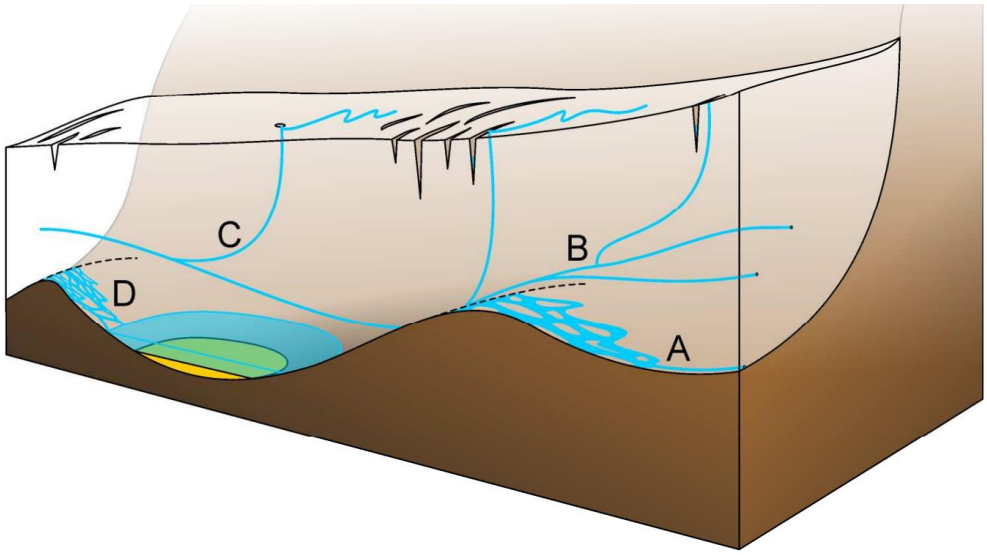

Figure 1.11*: A cartoon showing subglacial ponding in an overdeepening at D). (Taken from Cook and Swift, 2012).*

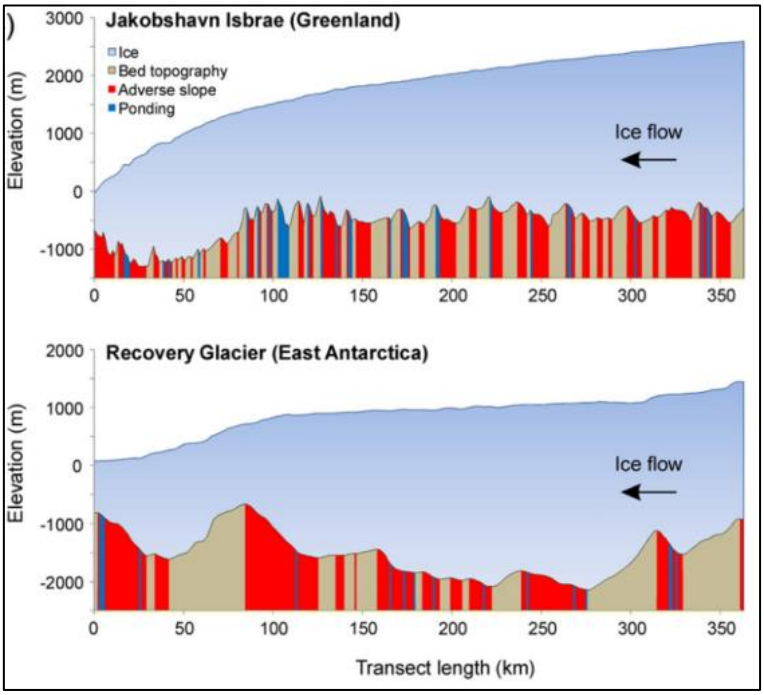

Figure 1.12*: Overdeepenings (red) and potential ponding based on Shreve's (1972) threshold (blue) beneath Jakobshavn Isbrae and Recovery Glacier (taken from Patton et al., 2015)*

1.4.5 Cauldrons

Cauldrons, also known as funnel-shaped surface depressions are a glacial feature that occur generally at the terminus of glaciers undergoing extreme retreat (Stocker-Waldhuber, 2017; Keller-Pirklbauer & Kulmer, 2018). They are characterised by concentric crevasses that appear on the ice surface in the early stages of development (Egli *et al*., 2021b), at the centre of which the ice is seen to be depressed into a bowl-like feature (see Figure 1.13). These features have been observed widely, with the most prominent at Vatnajökull, Iceland where a cauldron has formed above a subglacial lake (Magnusson *et al.*, 2007). Large subglacial hydrology paths or lakes can influence the stress and strain field of a glacier in a way that leads to supraglacial depressions with circular crevasses (Stocker-Waldhuber, 2017; Egli *et al*., 2021a). The presence of significant subglacial water is vital to their development and subsequent collapse as the amount of water travelling through these channels cause local ablation rates to increase substantially (Kellerer-Pirklbauer *et al.* 2019). Indeed, Stocker-Waldhuber et al. (2017) posited that the thermal heat supplied by these subglacial channels cause higher melt rates from below leading to further surface depression in the centre of the features until eventually collapsing under its own weight leaving a near circular funnel at the glacier surface (Stocker-Waldhuber et al., 2017). These features tend to follow the subglacial flow paths up-glacier, Egli *et al*. 2021 finding localised surface depressions occurring up to 600 m up glacier along these flow paths. Cauldron features have a significant impact on glacier retreat and mass loss and can be considered indicative of nonlinear increased response of glacier to climate change (Stocker-Waldhuber et al., 2017). Indeed, Xu *et al*. (2022) reported that changes in volume due to these observed collapsing events comprises 28% and that a single ice collapse event may exceed the interannual level of volume change.

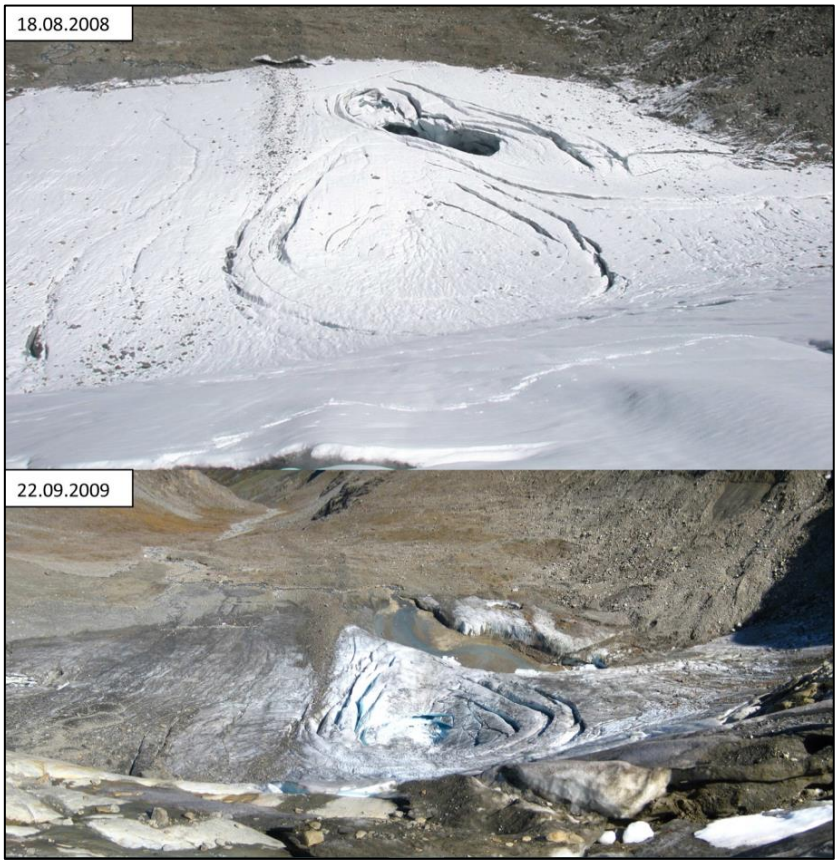

Figure 1.13: *Cauldron depression forming at the tongue of Sulztalferner, Austria (taken from Stocker-Waldhuber et al., 2017).*

1.5 RESEARCH QUESTIONS

As reviewed in this chapter, bedrock topography and glacial hydrology are key drivers of the intra-annual dynamics of a glacier. Both these drivers influence each another; the underlying topography of a glacier significantly influences the drainage patterns that occur within and beneath it and hydrology influences erosion and deposition rates. This insight can be upscaled to larger ice masses too. As subglacial environments are inherently inaccessible, one approach to this problem is for hydrological conditions to be inferred from surface movement. Currently

there is a lack of knowledge as to the glacier response to certain characteristics such as overdeepenings and cauldron features. Therefore, it is crucial to determine whether and how, topography and by extension the specific subglacial hydrology can affect glacial dynamics both spatially and temporally. The key aim of this work was to examine topographic controls on glacier dynamics at Findelengletscher, a moderate sized valley glacier located in the Valais Canton, Switzerland. The specific research questions of this thesis are:

1.5.1 Research Question 1

How is the seasonal development of a drainage system influenced by subglacial topography, namely due to the presence of an overdeepening?

In order to answer this question, firstly it is necessary to identify a suitable field site with an overdeepening. To get an idea of the subglacial drainage system and how this develops seasonally, a multifaceted methodological approach will be taken involving numerous UAV surveys to compare elevation changes and surface dynamics at different seasons to build a picture of the temporal development of the hydrological system. Ground-penetrating radar surveys will also be carried out in order to identify the extent of the overdeepening and to gain a better understanding of sub/englacial features that might provide clues to the drainage system. Finally atmospheric conditions and discharge data will be used in conjunction with these methods to provide a complete picture of the drainage system both temporally and spatially.

1.5.2 Research Question 2

How does the drainage system influence glacial dynamics such as flow velocities and elevation change?

A digital elevation model (DEM) and glacier bed model will be developed from the data collected to answer Research Question 1. This will be used to calculate the glaciohydraulic potential of the glacier and provide estimated hydrological flow routing. Elevation changes and ice velocities can be compared to these routes to form an answer to this question

1.5.3 Research Question 3

Is it possible to identify cauldron features before they present on the ice surface and what influences do these features have on elevation change and glacial retreat?

GPR data will be analysed and cross referenced with estimated flow routing, elevation changes from DEM differencing, and feature tracking to inform how and where cauldron features may form and whether any early signs of them can be identified before they present supraglacially.

In order to answer these research questions, field studies were carried out at Findelengletscher during the summers of 2016 & 2017 as well as the winter of 2017. Subglacial topography was inferred by a series of GPR surveys, and a time-series data set of glacier dynamics was recorded over the course of a year spanning two melt seasons using photogrammetry from multiple UAV flights. Second-hand data in the form of discharge, atmospheric conditions and previous GPR surveys have also been gathered and can be compared with glacier motion to give a more complete view of the glacial processes at play. This multifaceted approach aims to provide an empirical framework for studying topographic and hydrological controls of glacier dynamics.

1.6 THESIS OUTLINE

This thesis is comprised of seven chapters. The following chapter (Chapter 2) comprises a review of how a suitable field site was chosen and the various field methods and techniques used in the gathering of suitable data. The findings from this data will be expanded upon in Chapters 3 – 5. In this way the first two chapters represent an essential knowledge background for the understanding of the following three.

Chapter 3 will be concerned with findings from the ground penetrating radar (GPR) fieldwork carried out in both February and July 2017. Chapter 4 will proffer an analysis of the intra-glacial dynamics of the glaciers spatially whilst Chapter 5 will contrast and compare flow patterns between fieldwork data gathered and previous scientific data temporally.

Chapter 6 will tie in the conclusions made from the previous three chapters in order to present a multifaceted analysis of glacier dynamics and their relationship with topographic and hydrological drivers.

It should be noted here that the author was involved in the Swift *et al*. (2021) works that looked at evacuated basal sediment across the late melt season in 2016 as an indicator of the drainage system present beneath the glacier which dovetails well with this work.

2. METHODS

2.1 INTRODUCTION

2.1.1 Structure of the Chapter

This chapter presents the methods required to address the research aim and key questions outlined previously in Chapter 1. Section 2.2 will focus on the creation of a small inventory to identify an appropriate field-site for in-depth study based on ease of access and the presence of overdeepened subglacial topography. The most suitable field-site will then be chosen and an extensive review on its history and current state will be carried out. Section 2.3 will take a closer look at ground-penetrating radar (GPR) methods used in gathering subglacial radio-echo data from both MALA (February 2017) and Pulse Ekko (July 2017) hardware systems and post-processing of the data. Section 2.4 will describe uncrewed aerial vehicle (UAV) imagery techniques that will be utilised to create geo-rectified topographic information for the field site such as digital elevation models (DEM) and high resolution (~4 cm) orthomosaics. These two data sets (Section 2.3 & 2.4) will be combined to create a 3D model of the glacier surface and subsurface topography in Chapter 3. Finally, Section 2.5 will provide a summary of the key steps taken in gathering and processing the data.

2.2 FIELD SITE IDENTIFICATION

The lack of any extensive databases regarding overdeepened glacier basins made it necessary to utilise a remote-sense based technique to quickly identify suitable sites. In order to find an appropriate field site where overdeepenings and their associated glacial responses are present, it was necessary to use a tool to estimate what the underlying bedrock topography of a glacier might look like. The biggest issue to overcome with investigating subglacial processes is that access is virtually impossible, and conditions have to either be estimated or measured remotely by techniques such as dye tracing or probes. A suitable site needs to fulfil multiple criteria (Table 2.1).

Table 2.1: *Criteria for suitable field sites.*

Issue	Criteria
Significant overdeepening	Exhibiting one or more overdeepenings modelled to be comfortably exceeding supercooling thresholds.
Easy access	Glaciers should be accessible without too much walking (<5km) to maximise data collection in the field.
Previous scientific work	A past record of growth/retreat and previous scientific investigations and data such as GPR data to validate (ground truth) modelled bedrock topography.

Firstly, and of prime importance, is the likelihood of overdeepenings, particularly where the overdeepening has a high chance of exceeding the supercooling or ponding threshold.

Ice thickness estimates such as GlabTop (Linsbauer & Haeberli, 2012; Haeberli *et al*., 2013) or ITEM (Farinotti *et al.*, 2009a) present an approximation of bedrock topography, and can be used as a tool for locating areas where overdeepenings occur (Grabiec *et al*., 2012). To locate these overdeepening features as efficiently as possible, the bed-inversion method (Farinotti *et al*., 2009a) was used, which calculated the estimated ice thickness from Shuttle Radar Topography Mission (SRTM) data. Being able to estimate subglacial topography and subtracting it from the Digital Elevation Model (DEM) the inversion technique enables the calculation of ice thickness and the glacier's bedrock morphology as can be seen in Figure 2.1. Further to this, by taking a transect through the central flow line of the glacier a comparison of the slope angle of the bedrock-ice and ice-surface interfaces can be made, which is necessary to find areas of potential supercooling and ponding. Validation of Farinotti's inversion method (2009a), is produced by Farinotti *et al.* (2009b) by way of GPR sounding at 82 cross- profiles showed that there was a deviation of approximately 25% between the model projections and the GPR data and that on average the cross-sectional areas differ by less than 20%. Figure 2.2 shows that measurements tend to be more accurate closer to the terminus and that bedrock profiles are smoothed more than their GPR counterparts. A similar method of ground-truthing by GPR comparison can be found in Linsbauer *et al.* (2016). This approach is only compatible with SRTM data from 2000 which covers an area between 60°N and 60°S (Jarvis *et al.,* 2004) and therefore excludes higher or lower latitude areas such as Iceland, Antarctica, and parts of Scandinavia. The resolution of SRTM data is approximately 30m (Slater *et al.,* 2006) however, as overdeepenings are typically hundreds or thousands of metres in size in temperate ice valleys alone (Cook & Swift, 2012), the resolution will be suitable to identify these overdeepenings, making this approach an effective remote research tool. The Alps has thorough and the longest running information on the spatial distribution

and variation of glaciers in the world (Haeberli *et al*., 1989), with Switzerland specifically providing many comprehensive long-term data series (Gärtner-Roer et al. 2019) and therefore fulfils the need for a study area with records of growth/retreat and previous scientific investigation. Furthermore, the infrastructure available in developed countries such as Switzerland, Austria and France provide a higher likelihood of easier access.

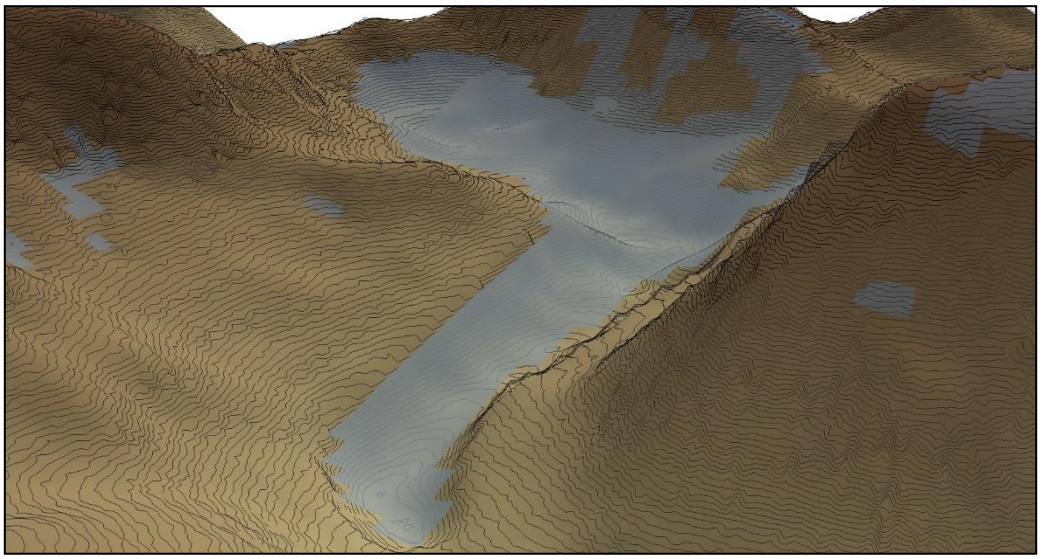

Figure 2.1: *Looking up glacier, a modelled estimate of glacial bedrock topography and overlying ice surface DEM of Haut d'Arolla, Switzerland. Contours are shown every five metre. Model created by author.*

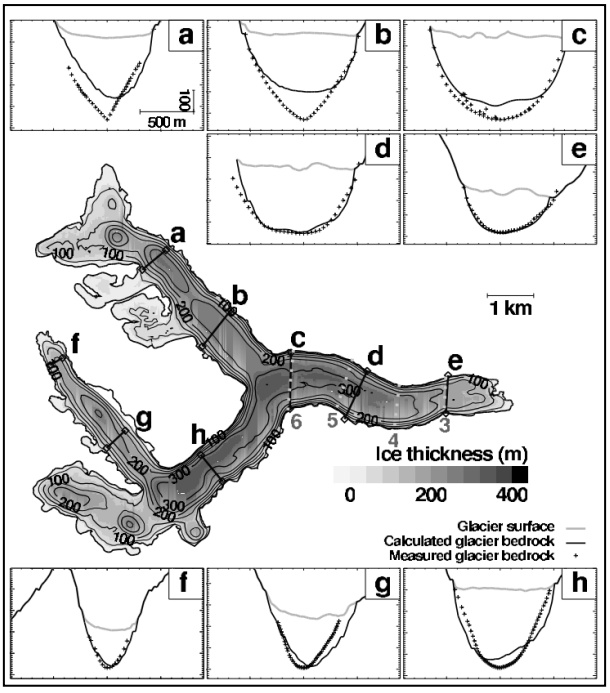

Figure 2.2: *Validation of Farinotti's (2009a) inversion method, based on comparison to GPR measured transects of Unteraar Glacier (taken from Farinotti et al., 2009b). GPR transects show a strong similarity to the bedrock inversion approach, more so towards the terminus.*

2.2.1 Using the ice thickness inversion technique

The method developed by Farinotti *et al.* (2009a) estimates the glacier's ice mass and its distribution in the form of ice-thickness based on the surface topography. Based on the principles of mass conservation, outlined in (Figure 2.3), the distribution of the mass-balance should be in equilibrium with differences in the ice-flux and the resultant variations in the elevation of the ice-surface. As a result, the thickness of the ice can be estimated from these ice fluxes (Farinotti *et al*., 2009a). This ice thickness is then subtracted from the surface DEM which provides an estimate of the bedrock topography (Overeem *et al*., 2017). This method has been shown to be effective by comparing the findings to that of GPR transects carried out as a form of ground-truthed comparison (Farinotti *et al*., 2009b; Linsbauer *et al*., 2012; Farinotti *et al*., 2017).

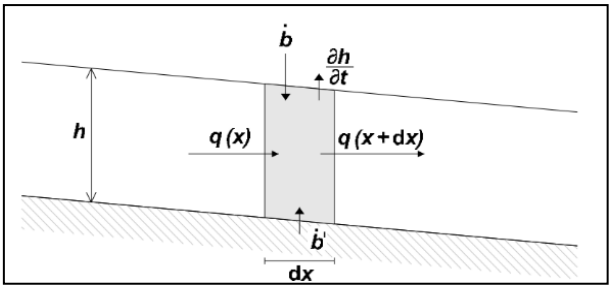

Figure 2.3: *Mass conservation of a portion of ice along a longitudinal profile of a glacier. Where dx is length and h is height, b and b^{l} are the rates of mass gain or loss (mass balance)57, ∂h/∂t is the rate of ice-thickness change, q is the specific mass flux, height length (Taken from Farinotti et al. 2009b).*

The process required to run the script developed by Farinotti *et al*. (2009) run in IDL consists of a sequence of inputs and simplifications. The distributions of mass balance are, in general, not known (Farinotti *et al*., 2009) and therefore a variable is introduced known as the "apparent mass balance" identified at any point as the variance between the ice surface mass balance and the ice thickness rate of change. This assumed mass balance is considered to change linearly with altitude for both the ablation and accumulation areas respectively (Farinotti, *et al*., 2009). How this apparent mass balance is distributed across the glacier is used to calculate a cumulative ice volume flux which is then converted into an ice thickness using a combination of Hutter's (1983) shallow ice approximation and Glen's (1955) flow law. The resultant ice thickness is interpolated over the glacier by using the glacier outlines from the GLIMS glacier database.

It is uncertain quite how much erosion/deposition will have occurred beneath a glacier from the time of these satellite missions to present day, however the bedrock is likely to be in a similar shape. As this ice-thickness inversion model is being used as an information retrieval tool, to locate potential overdeepenings, it is not vital that the data used is current as it is

highly unlikely that any overdeepenings present in 2000 will not be present beneath the glacier today, except in the instance of considerable glacier retreat.

Data created by the ice-thickness inversion method automatically generated ice thickness maps of the specific area measured, which was useful for giving a sense of the bedrock topography (Figure 2.4 & Figure 2.5).

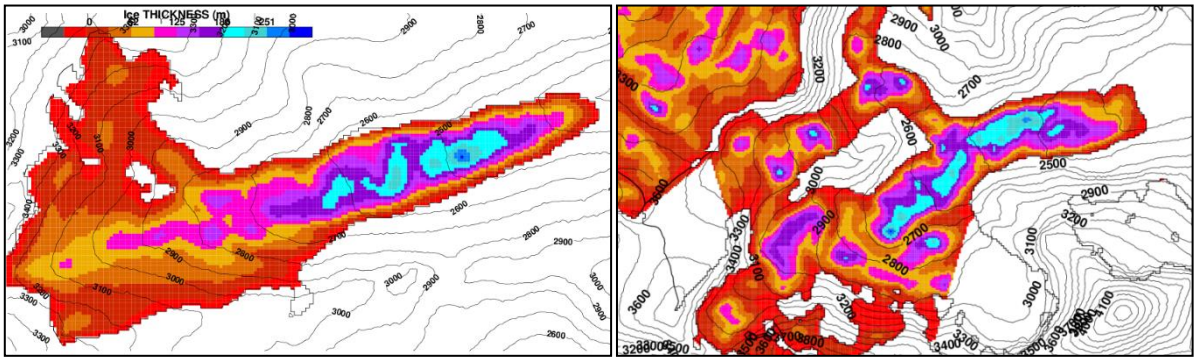

Figure 2.4: Two images automatically generated by the Farinotti et al. (2009a) ice-thickness inversion model. Left: Oberaar Glacier. Right: Zmutt Glacier.

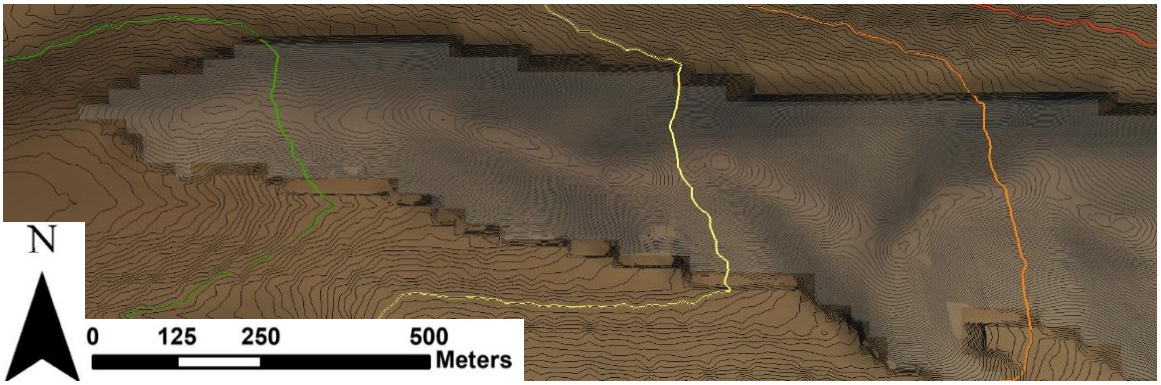

Figure 2.5: Image of the estimated bedrock topography using Farinotti et al. (2009a) model of Findelengletscher from nadir. Contours are recorded every 5 m, with coloured contours showing DEM altitude every 100 m from 2600-2800 m.

2.2.1.1 Applying parameters to narrow the search

The Alps has 712 glaciers (WGMS, 2016). To produce a bed inversion, and create centreline transects for each of these would be too arduous a task. The method was initially applied to 112 glaciers across the Alps which was considered by the author to be enough of a pool to then be narrowed down to the five most suitable glaciers (Table 2.2) using the flow chart (Figure 2.6).

Hooke (1991) suggests there to be little difference between cirques and overdeepenings. Whilst this may be true, cirque glaciers are of similar size to the overdeepening. So that the impacts of an overdeepening can be observed it is best that a direct comparison of conditions such as glacial velocity at the overdeepening with those away from the overdeepening can be made. With cirque glaciers it is much less likely that this will be the case as opposed to typical valley glaciers. Cirque glaciers will therefore be discounted from the Alpine overdeepening inventory as indicated in the flowchart (Figure 2.6).

Due to the ambiguity in minimum depth required for classification, any glacier presenting an adverse slope was recorded. However, difficult to access glaciers were excluded due to the difficulties arising in ground-truthing these sites. An ideal glacier should be as straight as possible, so as not to complicate flow lines and no less than 3km^2 (in keeping with Farinotti *et al.* 2009a) so that a suitable sized ablation zone can be analysed. Glaciers presenting high supraglacial debris cover will also be excluded due to the shielding effect they impose on melt/mass loss, as well as the added difficulty in producing clear GPR results when ground-truthing (this will be covered in more detail in Section 2.3 GPR).

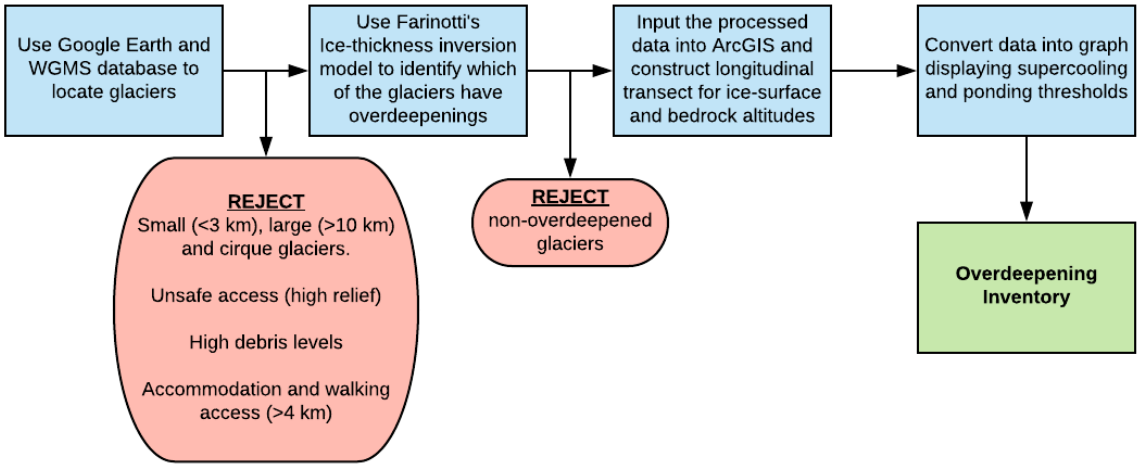

Figure 2.6: *Flow chart of the processes required to find a suitable field site.*

From an in-depth investigation of 112 glaciers, the aforementioned factors were considered along with centreline transects of the estimated bedrock and ice surface slope angle using the ice-thickness inversion method set forth by Farinotti *et al.* (2009a). The results for the most suitable glaciers are summarised in Table 2.2, and can be seen in Figure 2.7 & Figure 2.8. Table 2.2 shows that multiple glaciers exist, at least in theory, where supercooling and/or ponding may be present.

An important issue to consider here is what length of overdeepening is needed to influence the drainage system of a glacier. The work of Hooke *et al.* (1989) on Storglaciaren shows the overdeepening of less than 1 km has an effect on the drainage system. Lawson *et al.* (1998) show effects on the drainage system at Matanuska glacier, with a basin depth of 25 m (Cook & Swift 2012). The resolution of the SRTM data already being ~30 m (Smith & Sandwell, 2003), smaller overdeepenings than this may be missed anyway and, in this way, the minimum bounds of an overdeepening were set to >30 m. It was considered that this was a large enough area for processes pertaining to overdeepenings to occur and for the glacier to be affected by them. With regard to minimum accepted depth of an overdeepening, Patton *et al*. (2015)

rejected depths lower than 40 m for their identification of overdeepenings beneath contemporary ice sheets. Alpine valley glaciers are significantly smaller in scale (at least an order of magnitude) and therefore the minimum depth of an overdeepening should be likewise so any adverse slope above 4 m will be considered to be an accepted overdeepening.

Table 2.2: Summary of the five most suitable glaciers for further research and ground truthing. OD = Overdeepening, SC = Supercooling and P = Ponding.

No.	Region	Country	Name	(km) Length	(km) Area	(m) Min. Alt	(m) Max. Alt	Type	OD	SC	P	Distance to (km) Accom.	Distance to (km) Road	Relief	Debris	Previous OD work/estimates
1	Alps	Switz	Mont Mine	5.4	9.8	2023	3711	Valley	6	6	0	3	3	Low	Low	Haeberli et al., (2016a)
2	Alps	Switz	Findelen	6.9	12.9	2500	3937	Valley	11	10	2	3	2	Low	Low	Haeberli et al., (2016)
3	Alps	Switz	Stein	4.2	7.2	2021	3455	Valley	3	3	0	1	0.5	Low	Low	Haeberli & Hohmann (2008)
4	Alps	Switz	Oberaar	4.7	3.7	2310	3388	Valley	7	7	0	3	3	Low	Low	No
5	Alps	Switz	Trift	6.4	14.6	1753	3381	Valley	3	3	0	3	3	Low	Low	Haeberli et al., (2016b)

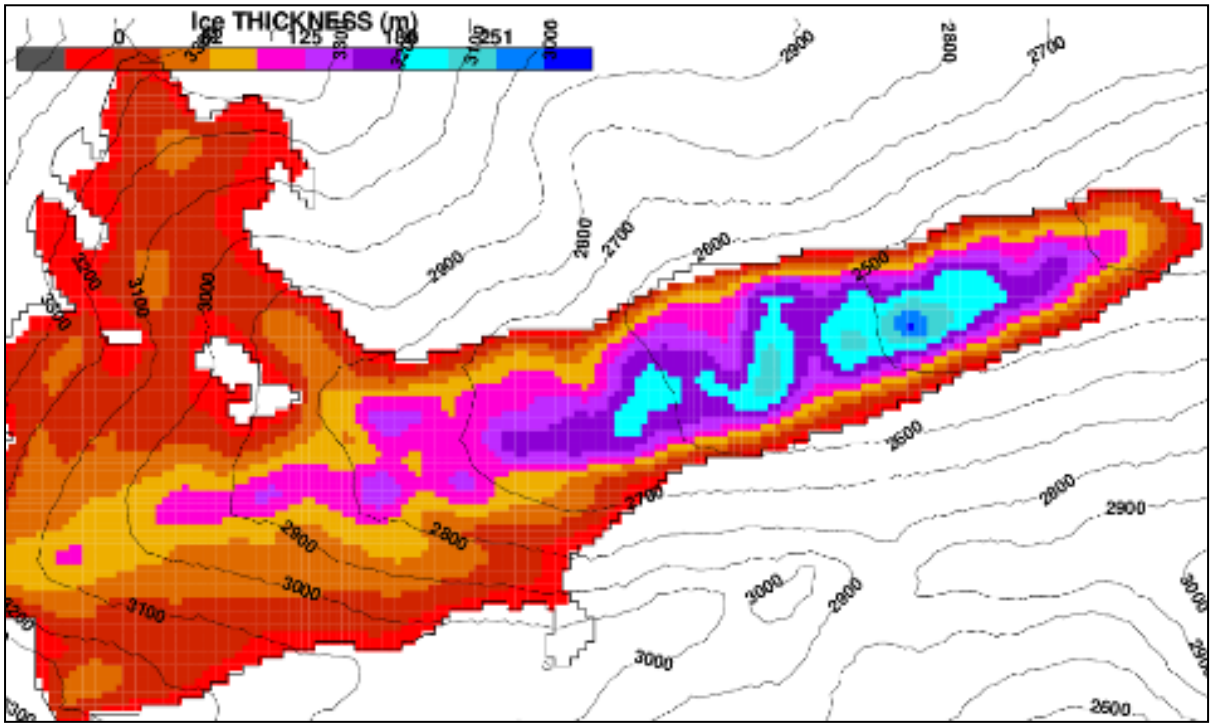

Figure 2.7: An Ice thickness estimate of Oberaargletscher from Farinotti et al. (2009a) inversion model.

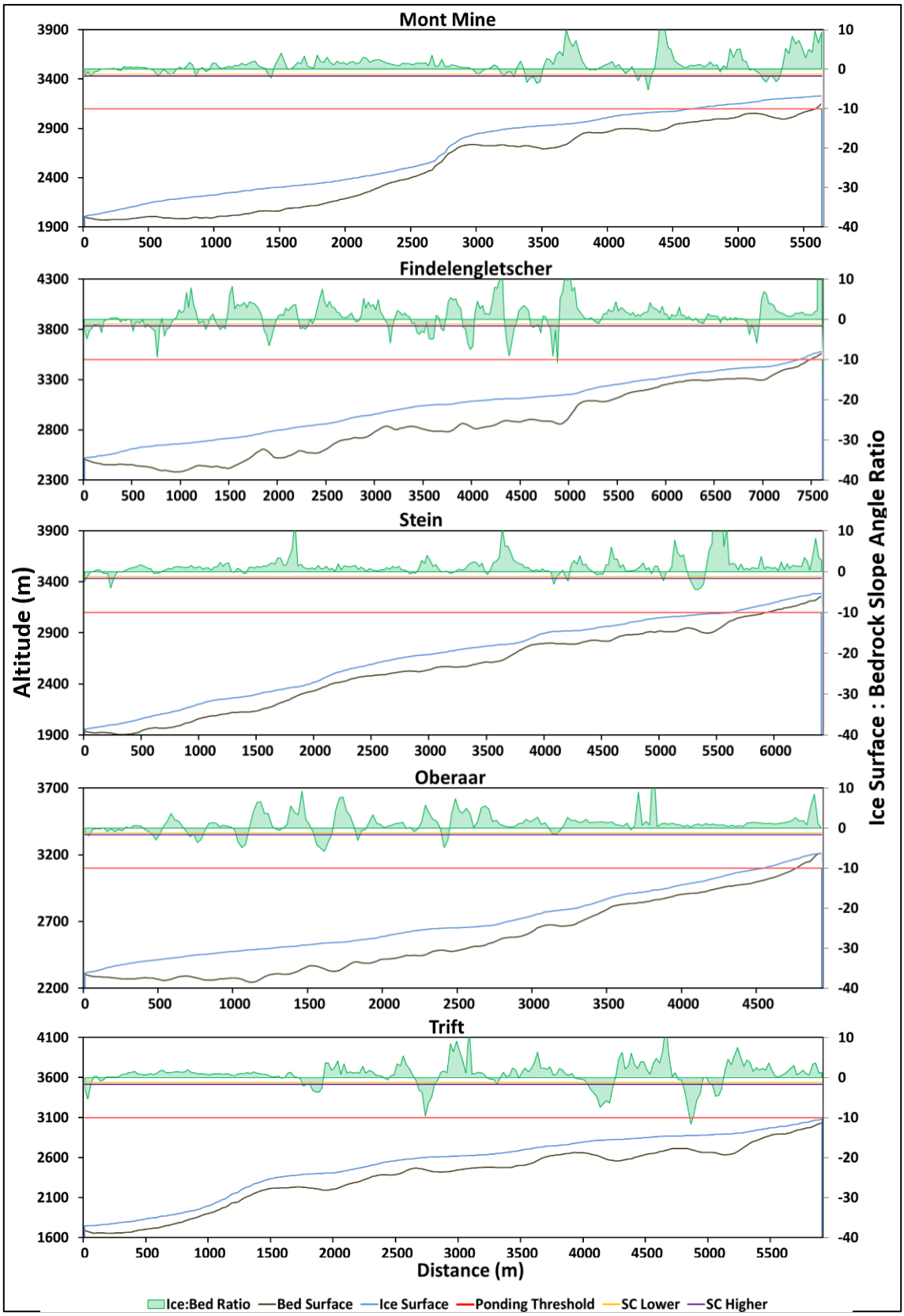

Figure 2.8: Bedrock surface: ice surface slope ratio compared to the supercooling threshold for five potential field sites. Bedrock and ice surface altitudes are shown too on the primary y axis.

Taking into account all of the parameters above, Findelengletscher in the South of the Valais Canton of Switzerland was chosen, having two significant overdeepenings near the terminus (Figure 2.9) and numerous previous GPR works carried out by Wächter (*unpublished*), Machguth *et al*. (2006); Sold *et al*. (2015); Sold *et al*. (2016). The flatness of the ice-surface at the glacier terminus is also important, as it promotes the likelihood of processes such as supercooling and ponding being present due to the ice-surface/bed surface slope angle being directly related to the occurrence of these processes. Figure 2.9 shows the centre line for the tongue of Findelengletscher and the relationship between the estimated bed and ice-surface slope angle. Even with an allowance of ± 30% in the bed, to take into account the standard error of estimate (SEE) of ice-thickness in Farinotti's (2009a) study, the supercooling threshold is being met at numerous locations.

It is important to consider however, that since 2000, the glacier has receded ~600 m (see red area in Figure 2.9 which will affect the slope angle of the ice surface therefore altering the supercooling threshold over the overdeepening which is a drawback of this approach. However, it is unlikely that the overdeepenings will have changed significantly in that time and therefore this method for locating overdeepenings is considered to be robust. Indeed, as discussed in Section 1.4.4, glacial retreats lead to increased ice-surface slope angles at the terminus which can "flush out" sediment that was previously deposited due to supercooling (Scambos *et al.,* 2011). This, if anything, can amplify the depth of the overdeepening. A comparison of Figure 2.9 with current supercooling threshold levels can be made once an accurate DEM and bed estimate have been established using the methods outlined in this chapter.

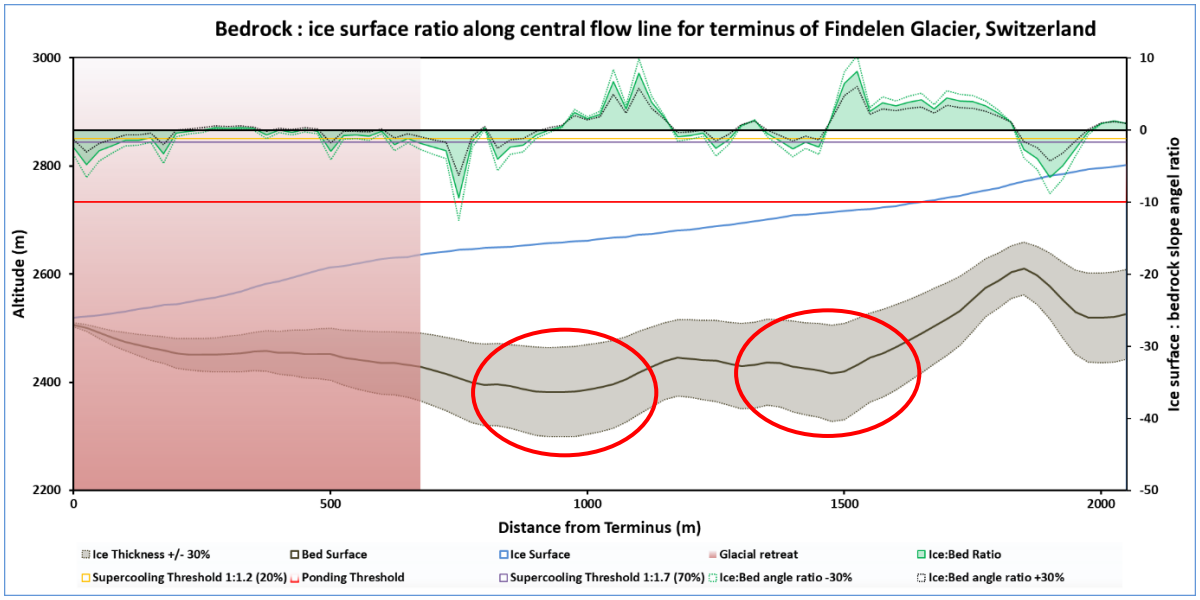

Figure 2.9: Longitudinal transect of ice-surface and bedrock-ice interfaces (shown in blue and black respectively) and their relative slope angle ratios (red line is the ponding threshold, orange and purple lines are the supercooling threshold – 1.2-1.7). The red shaded area represents the glacier's retreat from 2000 to 2016, and red circles highlight the locations of overdeepenings, so it was key that the predicted overdeepenings were sufficiently far away from the terminus so as not to have been exposed by the glacier's retreat.

2.2.1.2 Ground truthing field-site using previous data

As shown in the previous section, the bed inversion method shows overdeepenings to be present in the ablation zone of Findelengletscher. This is further backed up by Haeberli *et al*. (2013) who also postulated two overdeepenings at the glacier tongue despite using a different ice thickness calculation (GlabTop).

Previous works from VAW, (2015) in the form of subglacial radio-echo data were used to validate the findings from Farinotti's bed inversion method. Figure 2.10 shows bed contours every 10 m from Feiger *et al*. (2018) using this data set. Several sub-basins of the overdeepening here are present at the terminus of Findelengletscher. Now that the presence

of an overdeepening at the terminus has been substantiated by secondary methods (see Section 1.2.4.3) such as GPR, this glacier can be accepted as a suitable field site.

-.

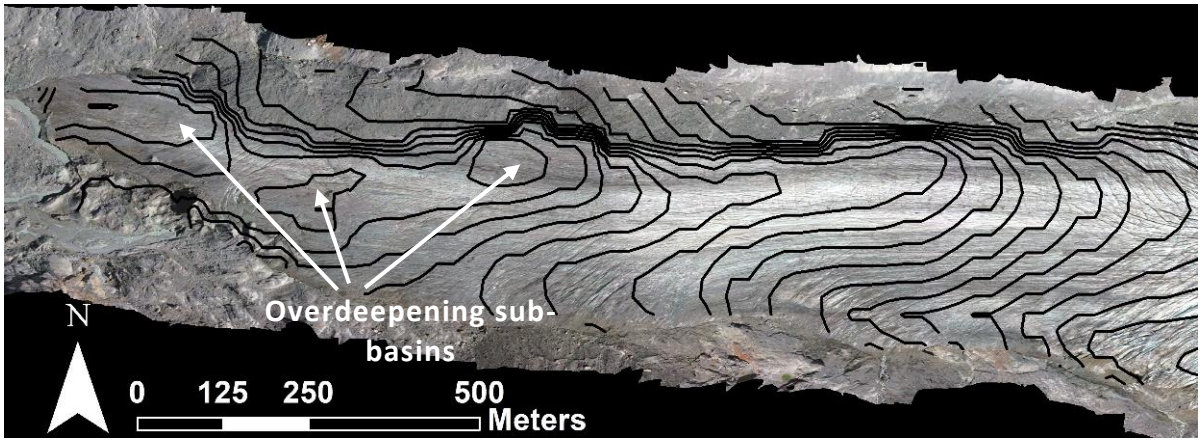

Figure 2.10: Bedrock estimate of the terminus of Findelengletscher from Feiger et al. 2018, using GPR data from VAW, (2015). Contours are every 10 m.

2.2.2 Field site: Findelengletscher

2.2.2.1 Introduction

Findelengletscher is a moderately sized valley glacier located in the Valais Canton in the southwest of Switzerland. The glacier is situated approximately 5 km to the East of the small town of Zermatt. The glacier itself flows in a west-north-westerly direction in its accumulation area before changing direction to a more true-westerly direction in its ablation area (Figure 2.11). According to the World Glacier Monitoring Service (WGMS, 2018) it has a current area of 12.9 km^2, with a length of 6.9 km and is 3.6 km wide at its widest point. With an altitude range of between 2500-3600 m, the average downhill slope angle can be approximately calculated as roughly 9.1°, although Linsbauer & Haeberli, (2012) suggest mean slope angle across the glacier to be 14.9°. From Farinotti's (2009a) work, the terminus, or lower 1.3 km has a low slope angle of 7.7°. The terminus has limited crevassing and is therefore easily

accessible (Pelto, 2016), is nearly completely free of debris (Joerg *et al*., 2012) and an overdeepening is situated within this area too (Haeberli *et al*., 2013). Recent estimates predict average ice thickness to be 55.4 ±13.3 m across the glacier (Feiger *et al.*, 2018).

2.2.2.2 History

Since glacial measurement records began in Switzerland in 1885 (Glaciological Reports (1881-2017)) the general trend has been one of retreat (Figure 2.11). Findelengletscher itself follows this trend (Figure 2.12). The WGMS (2018) estimates retreats of 2528 m from 1885-2016. Findelengletscher was in approximate equilibrium for at least 35 years, until 1920, after which, year on year retreat occurred. Apart from six years of advance in the early 1980s, Findelengletscher has steadily retreated for 95 years. Since records of this glacier began, it has lost 27% of its total length, with a present-day length of 6.9 km (Glaciological Reports 1881-2017). From 2009 to 2016 the glacier snout has retreated a further 365m. The total area of Findelengletscher has reduced in size by approximately 2% (0.27 km^2) from October 2005 to September 2010 (Joerg et al., 2012) and the average ice thickness change from 2005 to 2010 was -3.18 m, with maximum ice thickness loss at the terminus of -35 m (Joerg et al., 2012).

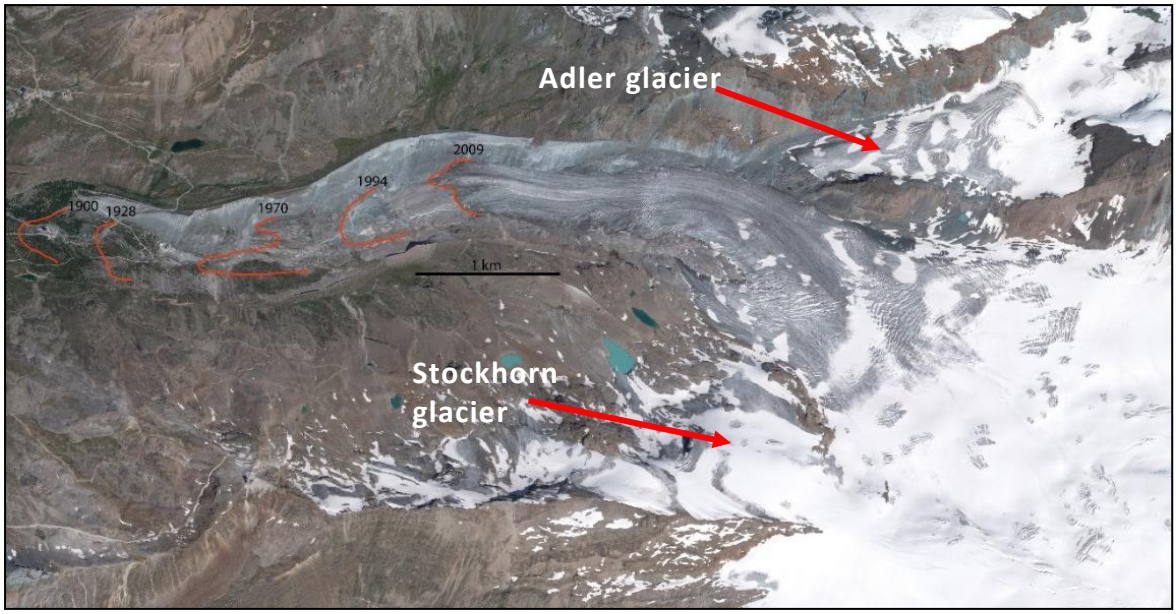

Figure 2.11: Current glacier extent of Findelengletscher (NASA, 2009) the steady retreat of the snout of Findelengletscher is highlighted in red, taken and digitised from Swiss aerial imagery (swisstopo, 2018).

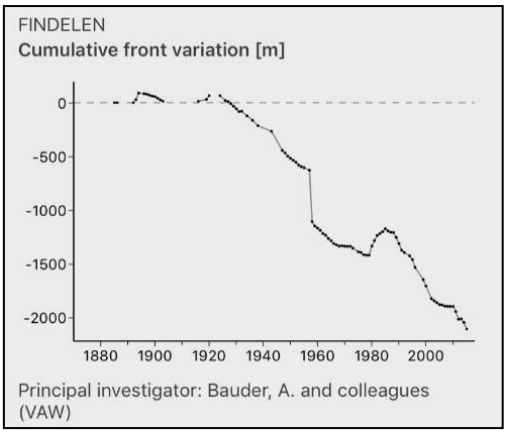

Figure 2.12: Cumulative front variation of Findelengletscher (1885-2016). (Glaciological Reports 1881-2017, www.glamos.ch).

2.2.2.3 Proglacial area and notable features

Findelengletscher is situated in an area dominated by granite and basalt, both physically strong rock types, and therefore more resistant to glacial erosion and there are high amounts of moraine debris surrounding the glacier laterally and terminally. (Swisstopo, 2018).

The immediate proglacial area of Findelengletscher currently consists of an area of thrusted debris and dead ice in the south with the main subglacial river flowing out from here (Figure 2.13) and snaking north across the glacier's northern terminus before cutting into and through a large mound of debris (Figure 2.14). The topography flattens out creating a braided river approximately 900m^2 at the end of which sits the hydroelectricity and gauging station. Between 2000 and 2002 when the terminus of the glacier extended to this flatter area, the current braided river area was instead a small proglacial lake (see Figure 2.15, '1999' image).

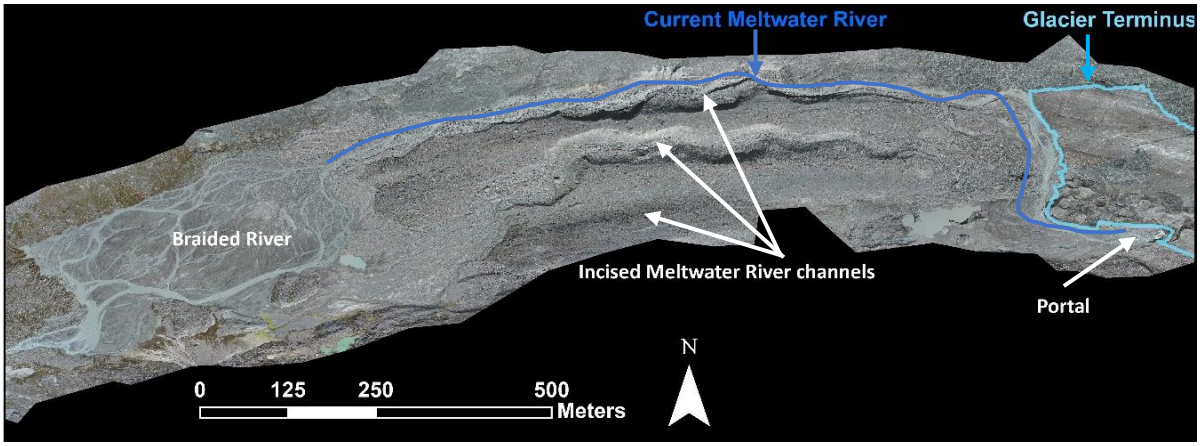

Figure 2.13: Annotated Proglacial Area of Findelengletscher.

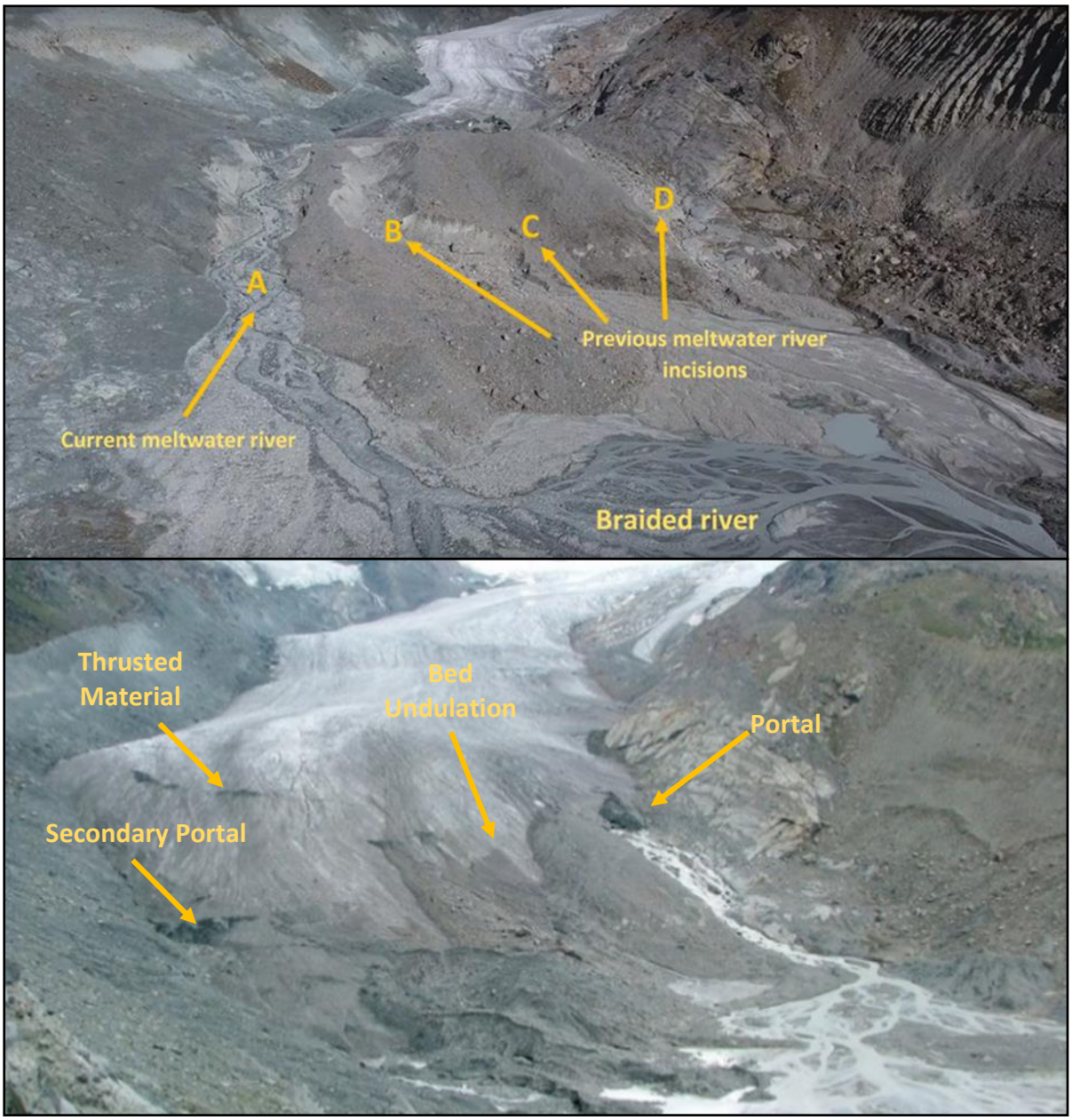

Figure 2.14: Above: Findelengletscher proglacial area with highlighted previous and current meltwater channels. Below: terminus of Findelengletscher, September 2004 (Midgley, 2004 unpublished).

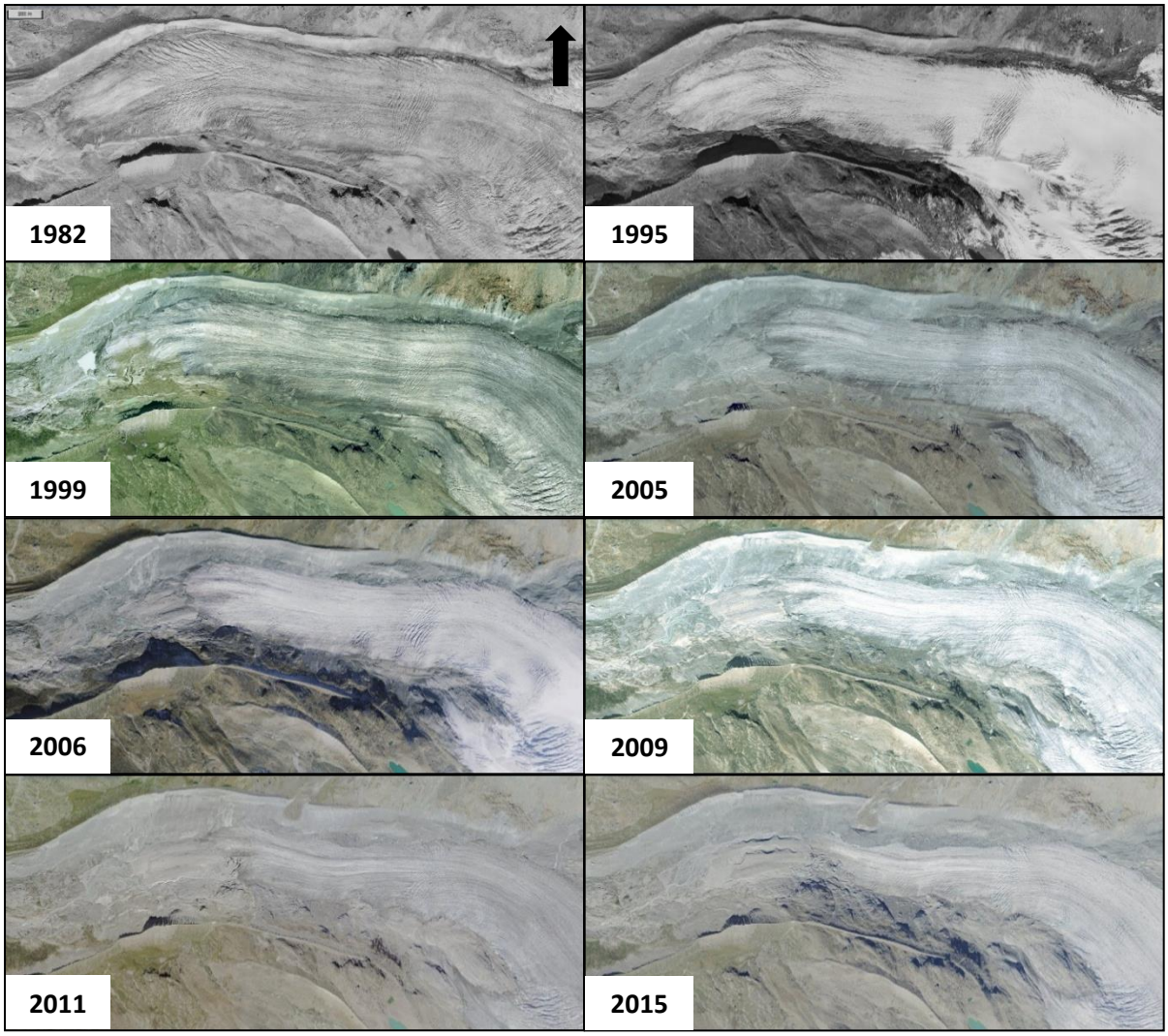

Figure 2.15: Retreat of Findelengletscher terminus 1982-2015 (taken from aerial imagery from Swisstopo, (2018)).

The meltwater from Findelengletscher drains into the Vispa river and passes through Zermatt and carrying on down the valley until it joins with the larger Rhone River (Pelto, 2016). The main meltwater stream egressing from Findelengletscher has altered its course over previous years. This is likely due to the changes in the size and shape of the glacier such as where the main portal occurs.

As can be seen from Figure 2.14, the proglacial moraine feature shows four distinct indentations labelled A-D. Looking East to West it is clear that A is the current meltwater

channel, and it is quite pronounced with significant incisions being made into the proglacial debris. Previous imagery of the proglacial area (Figure 2.15) shows that D used to be the main river channel - with A a much smaller tributary - in 2012, however at some stage between then and 2015 the location of the main channel switched to A (Figure 2.14). From observed satellite imagery, channel B appears to transport a small amount of meltwater however, nothing near the volume required to produce the level of moraine incision from 2012 to 2015. Incision C seems unlikely to be made by any significant river based on the shape of the incision and lack of images of rivers running through this area since the glacier has retreated. The 2004 image (Figure 2.14) shows this shape being present as the ice retreats. It is believed, based on the smoothness of the incision that this has been caused by glacial erosion alone.

As can be seen from Figure 2.16, a recent landslide from the northern lateral moraine occurred at some stage between 2006 and 2009. The debris from this moraine covers the surface of the glacier in this area which led to a shielding against melt. Whilst some down-wasting has occurred, it can be seen from Figure 2.17 that the glacier has thinned considerably compared to that of the debris covered area. The depth of debris varied considerably, but on average was estimated to be approximately 1 m. In some areas the ice sits just beneath a thin layer of fine sediment, on other, large metre scale boulders are present. This debris layer is likely protecting this area of now dead-ice from thinning (Dobhal *et al*., 2013). This debris covered area, whilst still being connected with the rest of the glacier, will not be suitable for GPR surveying.

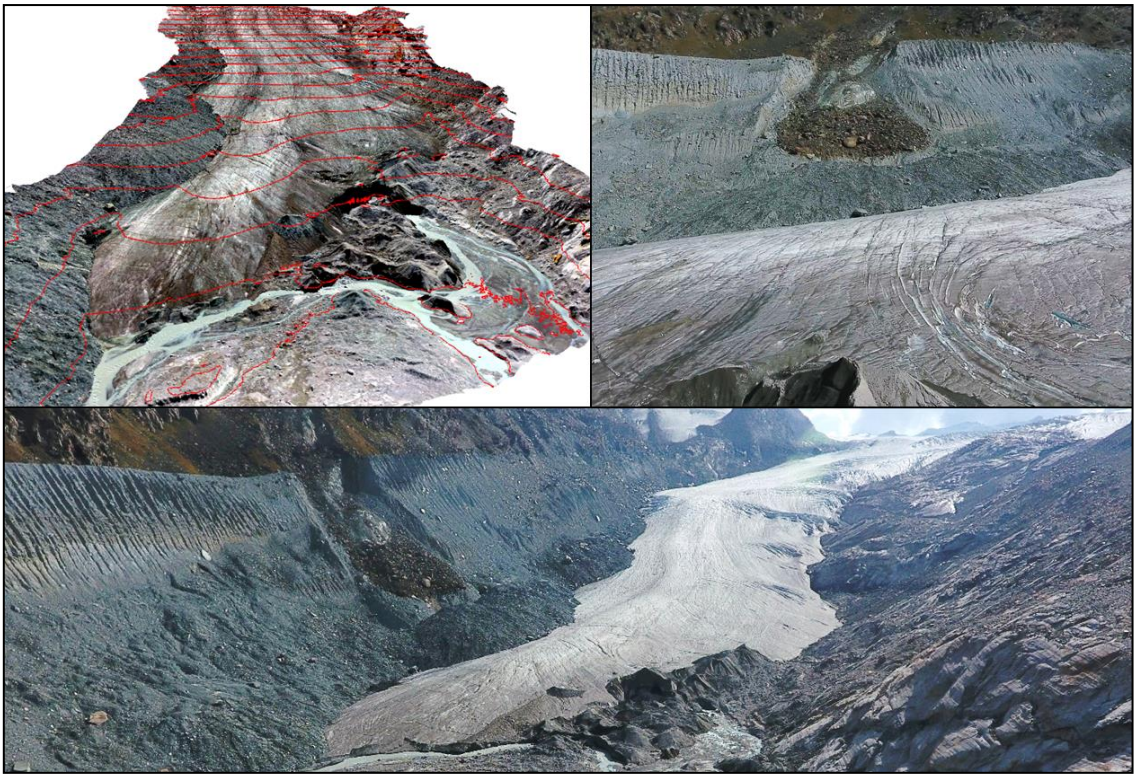

Figure 2.16: Lateral moraine colapse at Findelengletscher. Top Left: Contours represent altitude every 10 m. Top Right: Looking due North at the collapse. Bottom: Looking East up the glacier.

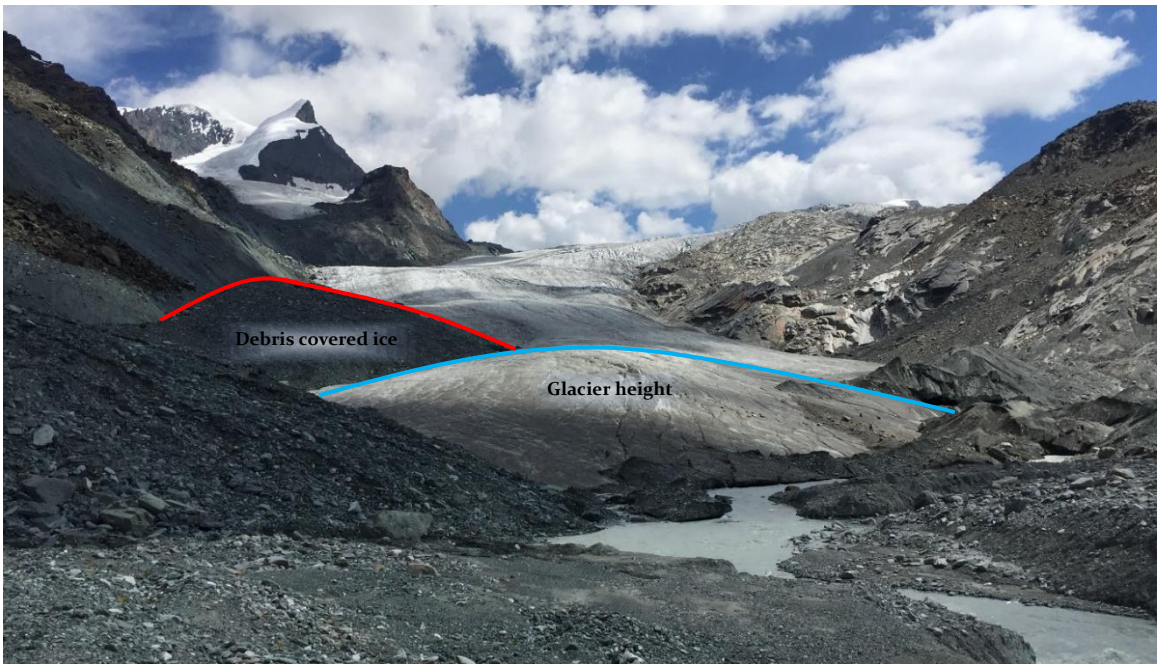

Figure 2.17: Debris covered ice and its insulating affects against down-wasting. Image looking East, up-glacier, July 2017.

Where once part of the greater Findelengletscher, due to recent retreats, the glaciers of Adler and Stockhorn are now separate glaciers, albeit ones that share the same drainage catchment and whose meltwaters still drain through and beneath Findelengletscher. Located to the north and south of Findelengletscher respectively (Figure 2.11) and comprising of an area of 2 km^2 and 0.1 km^2, meltwater from these glaciers still have an important role to play in the subglacial hydrology of Findelengletscher. Adler glacier became disconnected from Findelengletscher in 1993 and has since steadily retreated and thinned also (WGMS, 2018).

2.3 GPR

2.3.1 A review of GPR in glacial studies

Ground Penetrating Radar (GPR) is a method that has been used in many different cold region locations such as the Greenland Ice Sheet (Forster *et al.*, 2014), Antarctica (Spikes *et al.*, 2004) and valley glaciers (Binder *et al.*, 2009). However, applications to determine the ice thickness of temperate valley glaciers are rare (Rutishauser *et al*., 2016). Ice is a very transparent material to radio wave signals (Arcone, 1996) which makes the use of GPR on glaciers suitable.

Electromagnetic waves are fired into the ice through a transmitter and are rebounded back to the surface where they are recorded by a receiver. Depending on the depth and properties of subsurface structures, a signal of the shape of these reflectors can be detected and inferred due to the dielectric differences in the density and composition of various media (Urbini *et al.,* 2001).

The frequency of these wavelengths affects the depth of ice they can penetrate, with lower frequencies able to pierce further into the ice (Smith & Jol, 1995). However, the lower the

frequency used, the lower the resolution of the recorded data (Jol, 1995). Therefore, it is important to be able to predict the approximate depths of the ice beforehand so that an appropriate transmitter can be used. For example, when measuring the bed of ice sheets (where ice depths are relatively large) transmitters of between two and six MHz are used (Le Gall *et al.,* 2008). Whereas when measuring valley glaciers, typical depths are around 20-200 m and therefore a more appropriate transmitter of 25-100 MHz is required (Moorman & Michel, 1998, Pälli *et al*, 2002, Machguth *et al.,* 2006, Bælum & Benn, 2011,).

A comparison of the same transect using three different transmitters is shown in Figure 2.18. Here frequencies of 25, 50 and 100 MHz were used when measuring the bed surface at Griesgletscher. As can be seen, the 100 MHz transmitter does not penetrate all the way to the bed in the deeper area where the bedrock is estimated at >110 m. However, the 50 and 25 MHz transmitters were able to reach to the bottom of the glacier where the ice-bed interface is located.

A GPR survey had been carried out by VAW at Findelengletscher in the month of April 2015, areas containing adverse slopes were found to be present. The fieldwork aimed to remeasure these transects in order to add some reliability to these interpretations.

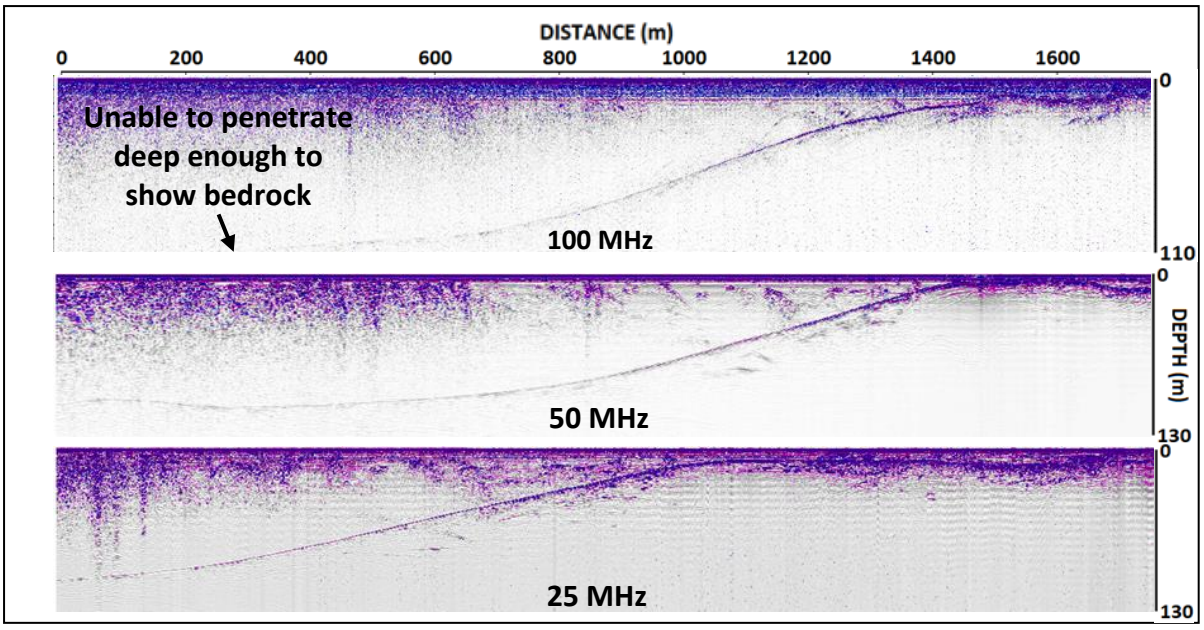

Figure 2.18: Comparison of 100 (top), 50 (centre) and 25 (bottom) MHz traces along similar longitudinal transects at Griesgletscher 30/06/17 (works carried out by the author).

2.3.2 Field collection of GPR

GPR was successfully collected over the course of 2 field seasons in February and July 2017 respectively. For the glacier measured in this study, and as mentioned previously in Section 2.2.1 Using the ice thickness inversion technique. Farinotti's (2009a) approach was used as an initial approximate guide as to how thick the ice would be and therefore what antenna would proffer the best results. Based on availability, across this study two different GPR systems were used; MALA and PulseEKKO. Whilst both devices carried out the same job, there were some differences in how they worked and could be used in the field.

2.3.2.1 General fieldwork planning and issues

A GPR survey was planned for February 2017 due to there being as relatively low levels of meltwater present at this time of the year. A drawback to conducting the survey during these winter months was the severe accessibility issues due to inclement ground and atmospheric

conditions. Meltwater can affect the attenuation of the radar signal through the glacier causing a lack of clarity in the trace of the bedrock reflector (Murray *et al*, 2007). Of course, meltwater reflectors can tell us a lot about the internal state and structure of the glacier (Irvine-Fynn *et al.,* 2006) such as transport regimes through englacial or subglacial conduits. However, as the primary aim is to reconstruct the glacier's bedrock to identify the location of overdeepenings, February was considered the ideal time to gather GPR data due to the temperatures being cold enough that much of the meltwater is frozen englacially (Gulley *et al.,* 2009).

In the days immediately prior to the planned fieldwork a large amount (15 cm) of fresh snow fell which made the journey to the field site unsuitable due to the increased risk of avalanche. Due to these adverse weather conditions and consequent difficulty accessing the glacier, a helicopter was required to reach and return from the field site. This significantly increased the cost and reduced the amount of time that could be spent in collecting data. GPS data for transects was recorded using a backup Garmin eTrex 10 device which offered an accuracy of < 3 m (Garmin eTrex series 2016, Oderwald & Boucher, 2003). A fault with the GPS receiver, discovered in the field, prevented more accurate dGPS data from being recorded directly from the MALA device. Route waypoints were logged on the device prior to use to ensure that the glacier tongue was measured as evenly as possible. Known crevassed areas were avoided due to the high risk of injury they presented, and individuals were tethered together with rope at all times to further mitigate this risk. Two researchers operated the machine in single file to keep the Kevlar tube containing both antennas as straight as possible along the transect and also for ease of using the same snow tracks as the lead researcher to reduce fatigue. The lead researcher kept a check on the display and trace recordings whilst the second researcher directed based on the GPS waypoint plan. The antenna and receiver were separated by a rope

that is dragged along in a line behind the monitor. The work of Langhammer *et al.* (2017) suggests that bedrock reflections are considerably clearer when antenna-receiver alignments were in parallel to the direction of glacier flow for valley constrained glaciers. However, the design of the MALA meant it was not possible to carry the rope in a parallel fashion to glacier flow when recording transects across the width of the glacier particularly considering the amount of loose snow on the ground.

Carrying out the fieldwork in July it was expected that a considerable amount of supraglacial, englacial, and subglacial meltwater would be picked up by the sensors, creating a 'busier' transect. It is also highly possible that due to the increased levels of meltwater, characteristics such as the bedrock could be slightly obscured or in some instances obscured completely. This effect can be seen in Figure 2.19 which shows how supraglacial streams can obscure other features in the trace. It was noted when recording data on site that there was a noticeable 'blur' to traces when the PulseEkko transmitter and receiver passed over a supraglacial meltwater stream.

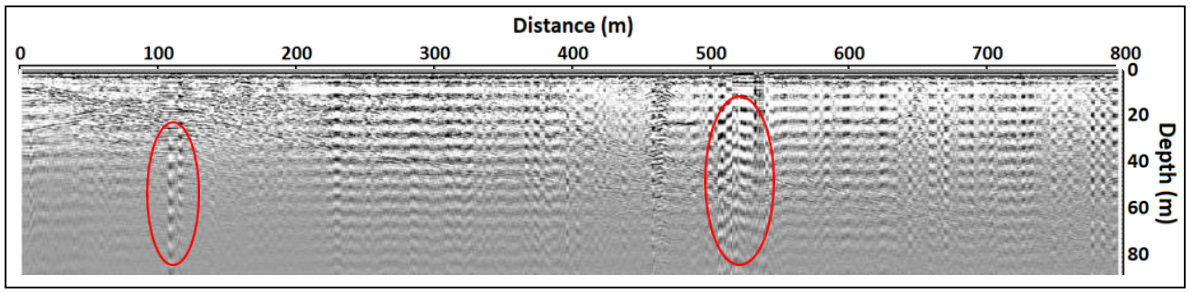

Figure 2.19: GPR transect 14 from July Findelen fieldwork. Red circles show where the GPR travelled over a supraglacial stream. Other similar but less defined features can be seen where the GPR was positioned close to a supraglacial stream.

2.3.2.2 Fieldwork February 2017

During the February 2017 fieldwork at Findelengletscher a MALA Ground Explorer GPR was used with a 25 MHz shielded Antenna (Figure 2.20) borrowed from the University of Zurich (UZH). The settings used in the collection of data (Table 2.3) were chosen based upon those from Zekollari *et al.* (2013) who carried out ice thickness estimates using a MALA Ground Explorer GPR at Morteratsch glacier in the Alps. The glacier was of a similar size and ice thickness was also believed to be similar which made these settings suitable. A wavelength velocity of 0.167 m/ns is considered the standard for glacier ice (Binder *et al*., 2009; Baojuan *et al*., 2015). *The initial plan of waypoints was designed to give a good, even coverage across the glacier tongue whilst also focusing on areas where overdeepenings were thought to exist from interpretation of previous GPR work carried out by VAW in 2015 and used in Feiger et al. (2018) (Figure 2.9 & Figure 2.10). In total, 12 transects were collected (3 longitudinal, 7 lateral and 2 diagonal) totalling approximately 3.3 km (Figure 2.21).*

Table 2.3: MALA Settings for February fieldwork, taken from Zekollari et al. (2013)

GPR parameters	
Antenna	25 MHz RTA
Antenna Separation	6.2 metres
Time Window	1412.2ns (121.06m, 2024 smp)
Wavelength Velocity	0.167 m/ns
Acquisition Mode	Time triggering – interval 1 second
Sampling frequency	1411.02 MHz
Max time window	Long
Autostacks	OFF
Stacks	32

Figure 2.20: MALA GPR device with 25 MHz Antenna coil - Findelengletscher February 2017.

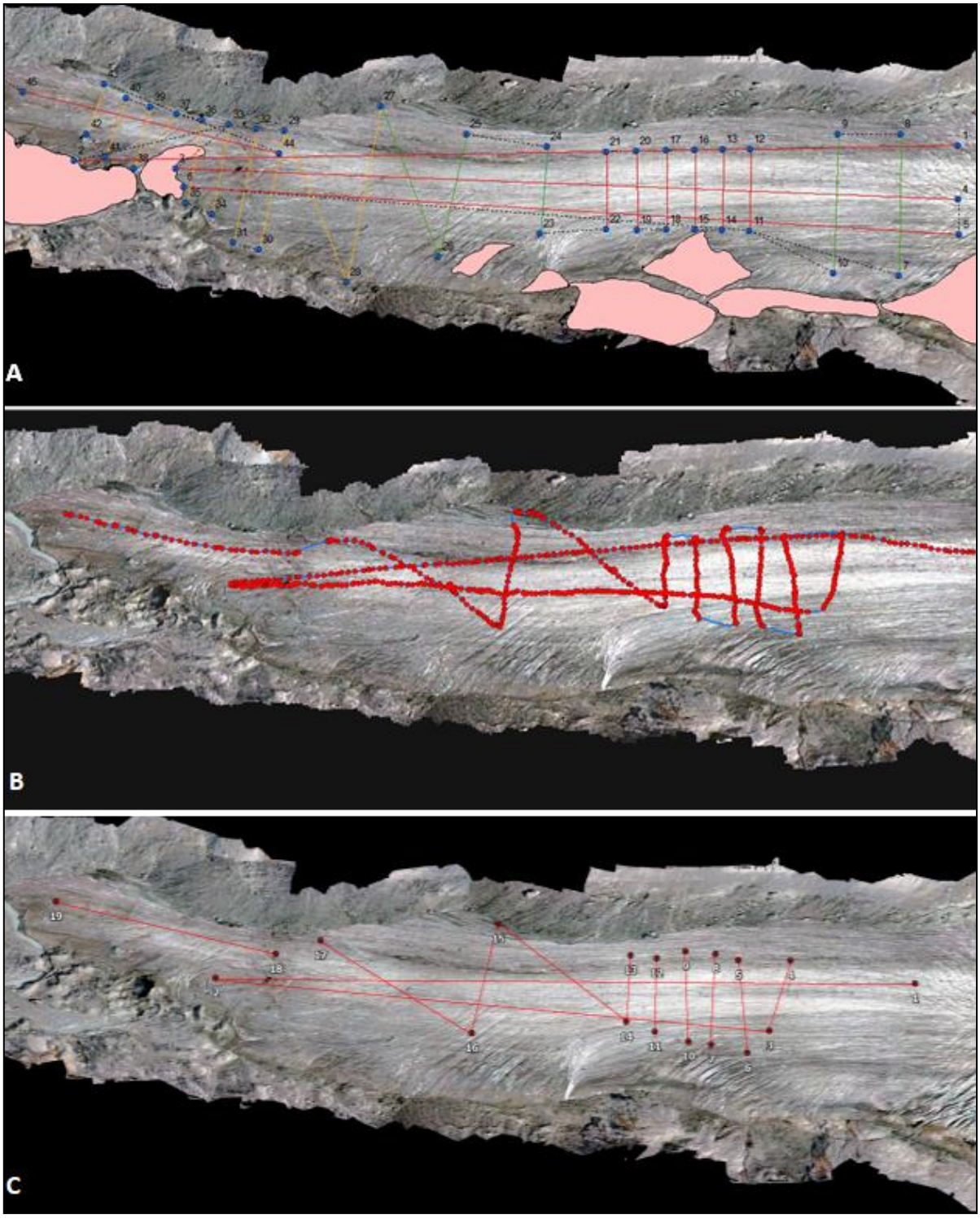

Figure 2.21: A) proposed transects to be measured on February GPR fieldwork. Note the red shaded areas were considered unsafe due to crevasses or steep terrain. Priorities were given to transects red being high, amber medium and green low. B) actual transects measured (red dots) and the route taken (blue line). C) Start and end points of each transect.

2.3.2.3 Fieldwork July 2017

For the GPR work carried out in July, a PulseEKKO GPR (Figure 2.22) was used from the Laboratory of Hydraulics, Hydrology and Glaciology (VAW), ETH Zurich. This device differed from the MALA in that it could more easily be carried parallel to the valley sides and therefore a considerably stronger and clearer bedrock reflector was expected (Langhammer, 2017). The settings used for the PulseEKKO device can be seen in Table 2.4. A 50MHz antenna was considered the most suitable for glacial fieldwork due to a good balance between depth and resolution. According to Moorman & Michel, (1998) a vertical resolution of ~1 m was estimated through computer modelling when using a 50MHz antenna. A Tx-Rx (transmitter-receiver) separation of 1 metre was deemed appropriate, with each held by an individual. A 1 m string was used and kept taut to ensure antenna separation was consistent which can be seen in Figure 2.22

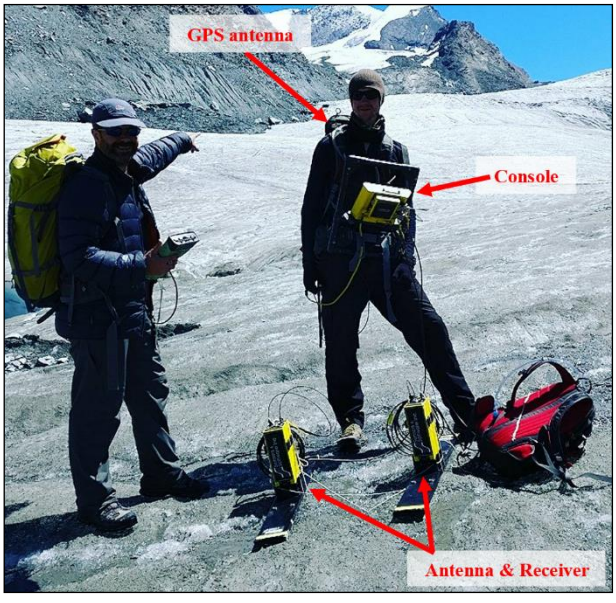

Figure 2.22: Pulse Ekko GPR set up at Findelengletscher.

Table 2.4: PulseEKKO Settings for July fieldwork.

GPR parameters		**Survey parameters**	
Frequency	50 MHz	Survey type	Reflection
Time Window	660 ns	Start offset	0 m
Step Size	0.25 m	GPR trigger	Time interval
Sampling interval	0.4 ns	Antenna separation	1 metre
Stacks	DynaQ	Antenna polarization	Broadside
Transmitter	pE PRO Auto	Antenna orientation	Perpendicular
Velocity	0.167 m/ns	GPS	Interval
Voltage (V)	1000 V		

In the July fieldwork a total of 13 transects were recorded, 12 of which were suitable for analysis (nine Lateral and four longitudinal) covering a total of 3.91 km (Figure 2.23, Blue lines). Transects were linked with DGPS (Differential Global Positioning System) coordinates during collection using a Leica CS15 GNSS DGPS system carried on the back of the researcher. XYZ coordinates were linked automatically to each trace recorded. True to Langhammer's (2017) research, and to maximise the potential for more coherent traces, antenna and receiver were lined up parallel to the direction of the valley sides (glacier flow) in the recording of all transects. Again, as with the February fieldwork, in order to mitigate the risk of injury, crevassed and steep areas were avoided (Figure 2.23). Unfortunately, lack of ground-based data in more high-risk areas is fairly common in glacial data collection (Gergan *et al*., 1999, Fischer, 2009, Linsbauer *et al*., 2012). From both GPR fieldwork a broad coverage of the glacier has been recorded. An assessment of the glacier bed and sub/en-glacial features can now be inferred, with results reported in Chapter 3.

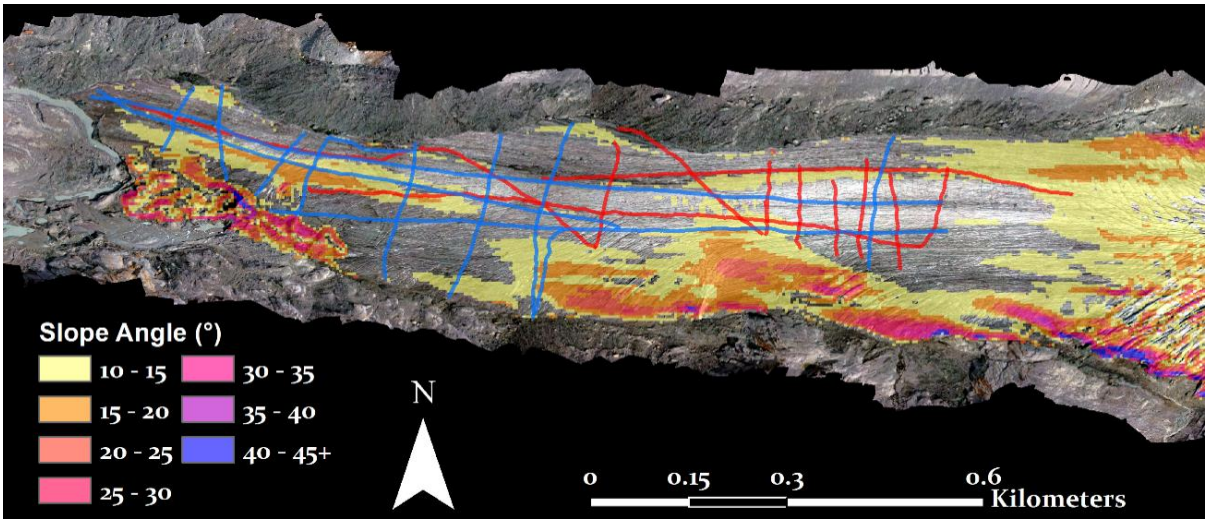

Figure 2.23:. Red and blue lines represent GPR transects from February and July respectively. Location on steep slope angles across Findelengletscher are indicated by shaded areas.

2.3.3 Post processing & interpretation

The raw data collected required post-processing so that it could be more easily interpreted. This involved the removal of background noise, so that any features captured could be more easily identified. This in turn helps with the interpretation of traces collected.

2.3.3.1 ReflexW

In order to process the data collected using both the MALA and Pulse Ekko equipment, ReflexW software was used (Sandmeier 2007). This software allowed the data to be displayed in a 2D graph format. It is considered that the simplification of the image by removal of noise is a very important factor for optimising the interpretation (Fan *et al*, 2019). In order to improve the visibility of the glacier bed and other englacial or subglacial media, various editing steps were required. A workflow of these steps can be seen in Figure 2.24.

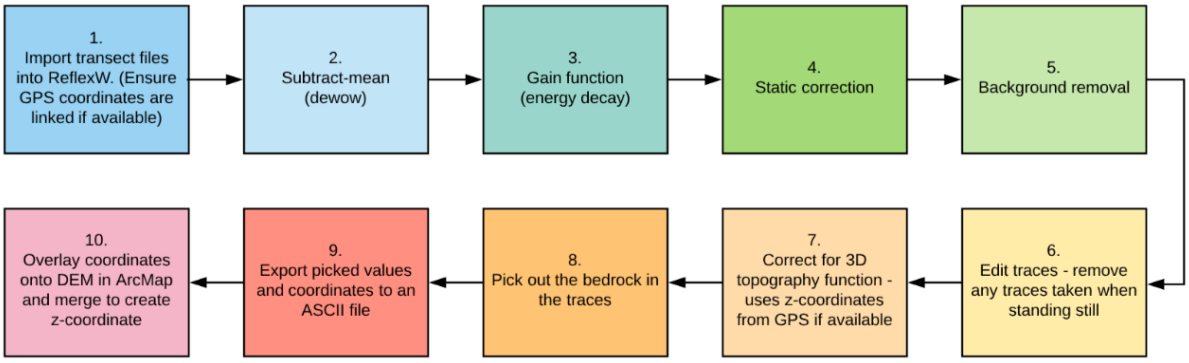

Figure 2.24: Flow diagram of the processing steps taken for GPR traces in ReflexW.

Once the traces were successfully imported into the ReflexW software, the first filter required is the 'subtract mean (de wow)' which removes the initial DC (direct current) bias from the signal by applying an average to each trace thereby correcting for signal saturation (Irvine Fynn, 2006; Szymczyk & Szymczyk, 2013). 'Dewowing' or 'wow' elimination is considered a very important step (Jol, 2008) and is generally used in the processing of traces in GPR applications including those of a glaciological nature (Jol *et al*., 2004; Irvine-Fynn *et al*., 2006; Degenhardt Jr, 2009; Bælum & Benn, 2011). A time window filter of 20 ns was applied as this seemed to offer the clearest results. Following on from this, a gain function (energy decay) was applied in order to improve the visibility of the low-amplitude reflections (Schwamborn *et al.,* 2008).

Next, in order to gain a more accurate estimate of the depth of reflectors, a static correction, or calibration of the 'zero time' (Gerber *et al*., 2009) was applied to the traces (Figure 2.25). The purpose of this is to change the start time of the trace to when the first waves are picked up by the receiver (Heilig *et al.,* 2010).

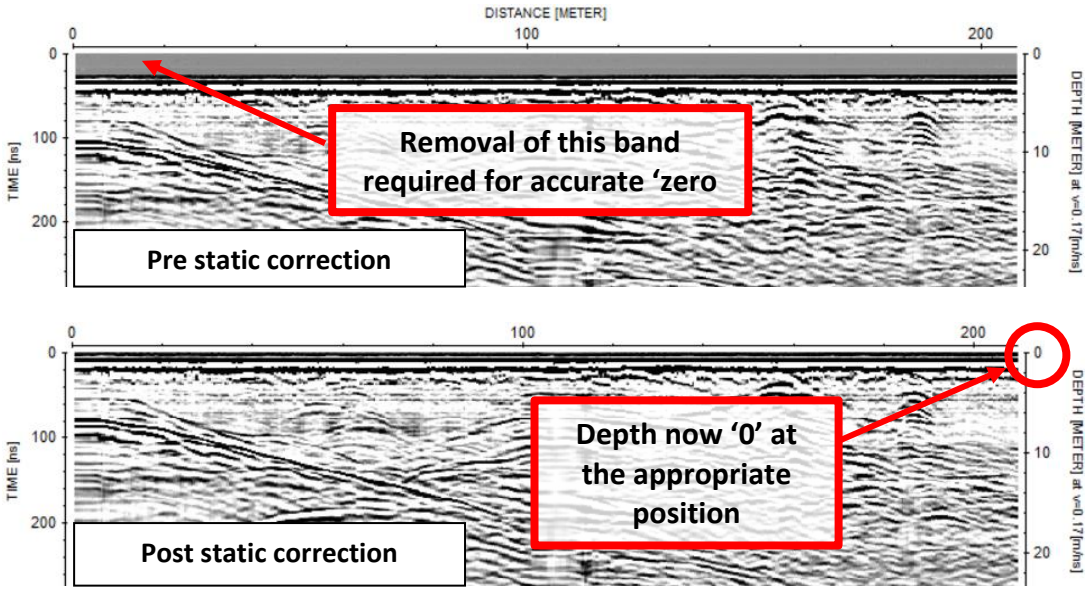

Figure 2.25: Two traces showing the before and after effect of static correction whereby the zero time is calibrated.

The next processing step carried out was a background removal to remove any excess noise by subtracting the average from the overall signal noise (Kim *et al.,* 2007). Excess noise tends to consist of external reflective signal scattering often presenting itself as a horizontal ringing effect.

The editing of traces was the next step taken. This consisted of removing duplicate traces caused by standing still whilst the acquisition mode was set to 'time interval' causing a duplication of traces which presents itself in ReflexW as a stretched band as can be seen in Figure 2.26.

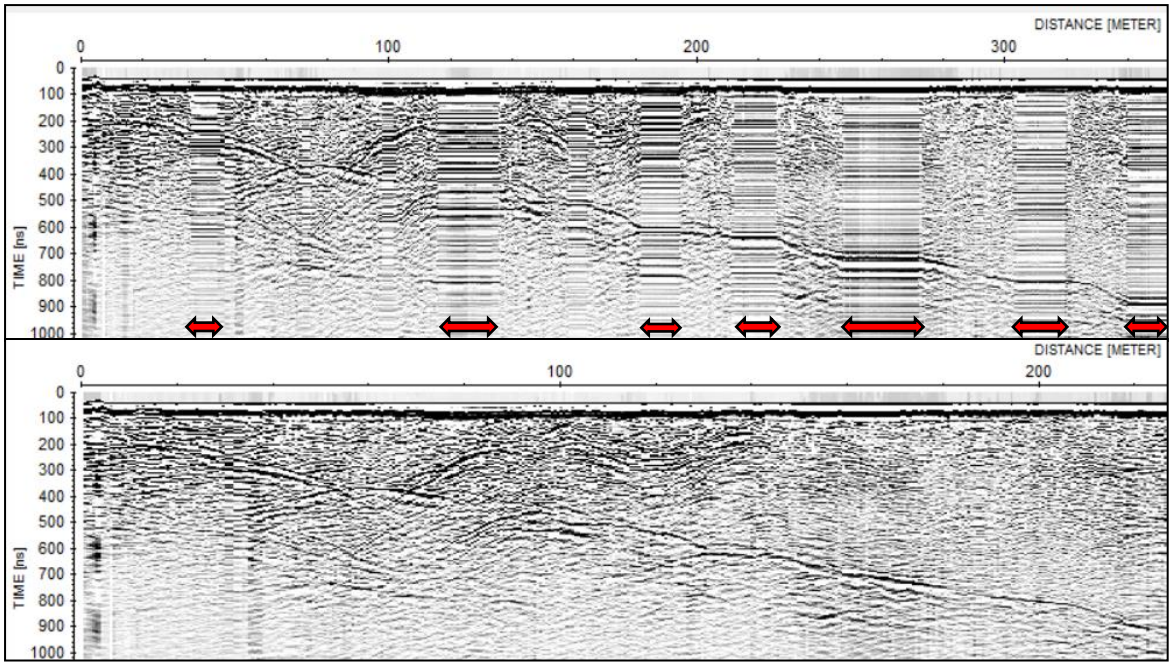

Figure 2.26: Before (above) and after (below) editing traces of GPR data through ReflexW (red arrows indicate time periods where traces were being recorded whilst stationary).

In order to see how the bedrock reflector compares to the ice surface, a 3D topography correction can be carried out. This applies the GPS z-coordinate to each trace to show the changing altitude of the ground at which the trace has been recorded (Figure 2.27).

In general, from estimates of the accuracy of GPS coordinates of traces during GPR work, a higher accuracy is often obtained for xy coordinates than z (Dobiński *et al*., 2017). It was considered that a more accurate method for estimating the z-coordinate of the GPS trace data could be obtained than what was recorded during the July fieldwork and as a method for estimating February altitudes. The xy-coordinates were overlain on the digital elevation model created from the UAV structure from motion data (explained in detail later in this chapter – Section 2.4.4). A z-coordinate measurement for each point was taken from this layer. The depth of the bed reflector (or ice thickness) was then subtracted from this new DEM z-coordinate for each trace to give an approximation of the bedrock (Grab *et al*., 2021).

For the 6th July fieldwork, the DEM from the following day (7/7/17) was used. For the 7th February GPR data, the closest available GPS was used (5/7/17). The Garmin GPS used in the February fieldwork offered a horizontal accuracy of ~3 m (Oderwald & Boucher, 2003). However, the vertical error of the coordinate data could be reduced by using this method.

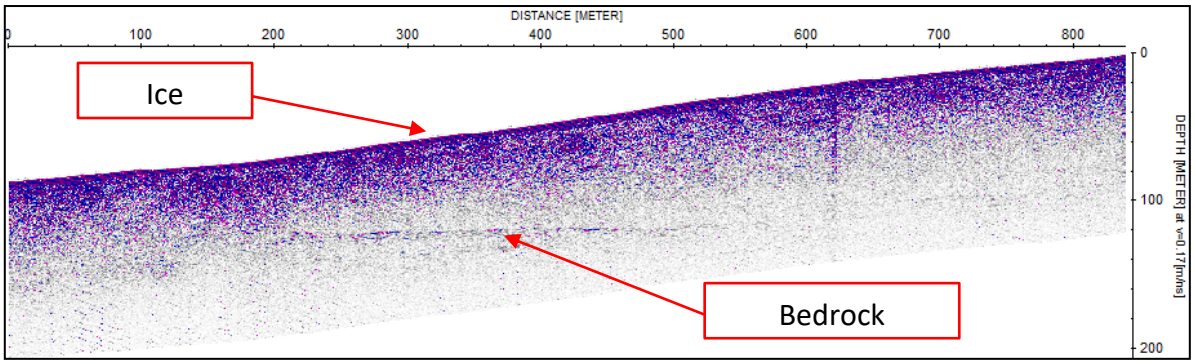

Figure 2.27: A longitudinal transect (transect 15, July 2017) with an applied 3D topography correction. The surface slope of the glacier can be seen clearly - moving up glacier from left to right.

2.3.3.2 Bed Identification

Picking is the process by which a marker is placed at an appropriate depth to indicate a significant change in the polarity of the trace. The estimated location of the bedrock was traced using this method. This measurement was then saved alongside xy coordinates from the GPS measurements. It is not always clear where the bedrock might be, due to many potential reasons such as the bedrock being too deep or the trace being reflected by an object above the bedrock instead or scattered by too much water in the ice (Saintenoy *et al.*, 2013; Marcer *et al.*, 2017) or water supraglacially (Figure 2.19). In this case the trace was left blank. Figure 2.28 shows how much of the bed could be clearly seen for the July fieldwork. Of the 3.91 km measured, a bedrock estimate was recorded for 2.83 km, or 72.38% of the transects measured.

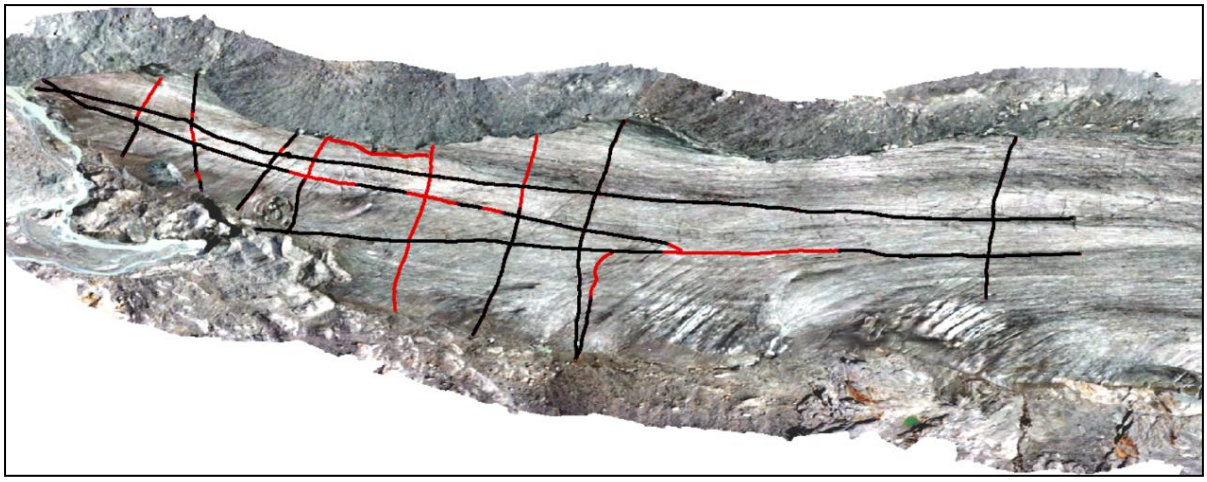

Figure 2.28: Image showing July 2017 Findelengletscher transects and picked bed. (Black shows sections that have been successfully picked. Red shows lack of clear bed reflector.)

2.3.3.3 Polarity interpretation

It is possible to draw conclusions about the nature of the material reflected back by the trace based on its polarity (Pattyn *et al*., 2009; Bælum & Benn, 2011). For example, there is a strong reflection subglacially from the ice-bedrock interface which shows a clear positive-negative-positive (or black-white-black in the imagery) polarity (Figure 2.29). Therefore, it can be assumed that other objects within the ice that reflect in a similar way have a higher dielectric constant (or ability to store electrical energy) than the ice around it (Moorman & Michel 1998). Geological based materials tend to have a higher dielectric constant than ice. This change will be displayed on the trace by a thick-banded 'positive-negative-positive trace' (substrate material). However, if a considerable increase in the velocity of the wave occurs at an interface, such as a void-space within the ice where the radar waves would dramatically increase, a reflection will be created in the trace with a reversed polarity or a 'negative-positive-negative' trace (air from a void in the ice). By close examination of the trace, it should

be possible to estimate, or at the very least narrow down, what the cause of the reflector is (Bælum & Benn, 2011; Conyers 2015).

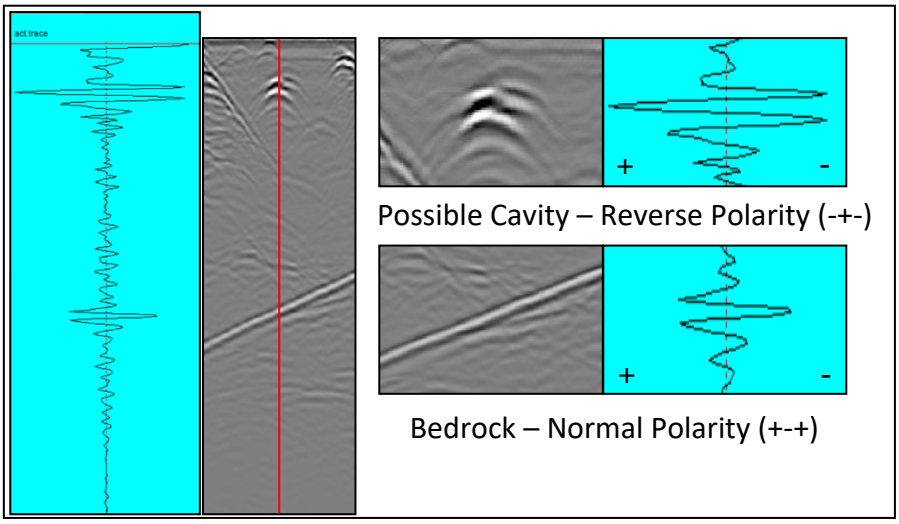

Figure 2.29: A comparison of two reflectors along the same trace, the lower reflector is assumed to be the bedrock and displays a normal polarity whist the upper reflector shows a reversed polarity which could suggest an air cavity, perhaps a relic from a closed crevasse (example taken from data collected by author at Griesgletscher 30/6/17).

2.3.3.4 Hyperbola fitting – velocity analysis

Identification of the shape and size of hyperbolae can help to estimate in what medium the reflector occurs in. Hyperbolae have a natural crescent shape, but the curvature of this shape is affected by the velocity of the radar wave. The radar wave moves at a slower speed through denser materials. For example, the velocity through ice is widely considered to be 0.167 m/ns (Binder *et al*., 2009; Baojuan *et al*., 2015), whilst through air and water the velocity is considered to be 0.33 and 0.032 m/ns. respectively (Murray *et al*., 2007; Bradford *et al*., 2009). Therefore, the hyperbola arc changes shape based on the material surrounding it. As can be seen from Figure 2.30, software can be fitted to the arc to give an estimation of what

velocity it was travelling at, and therefore the state of the material (Dou *et al*., 2017). In these cases, air filled voids were located.

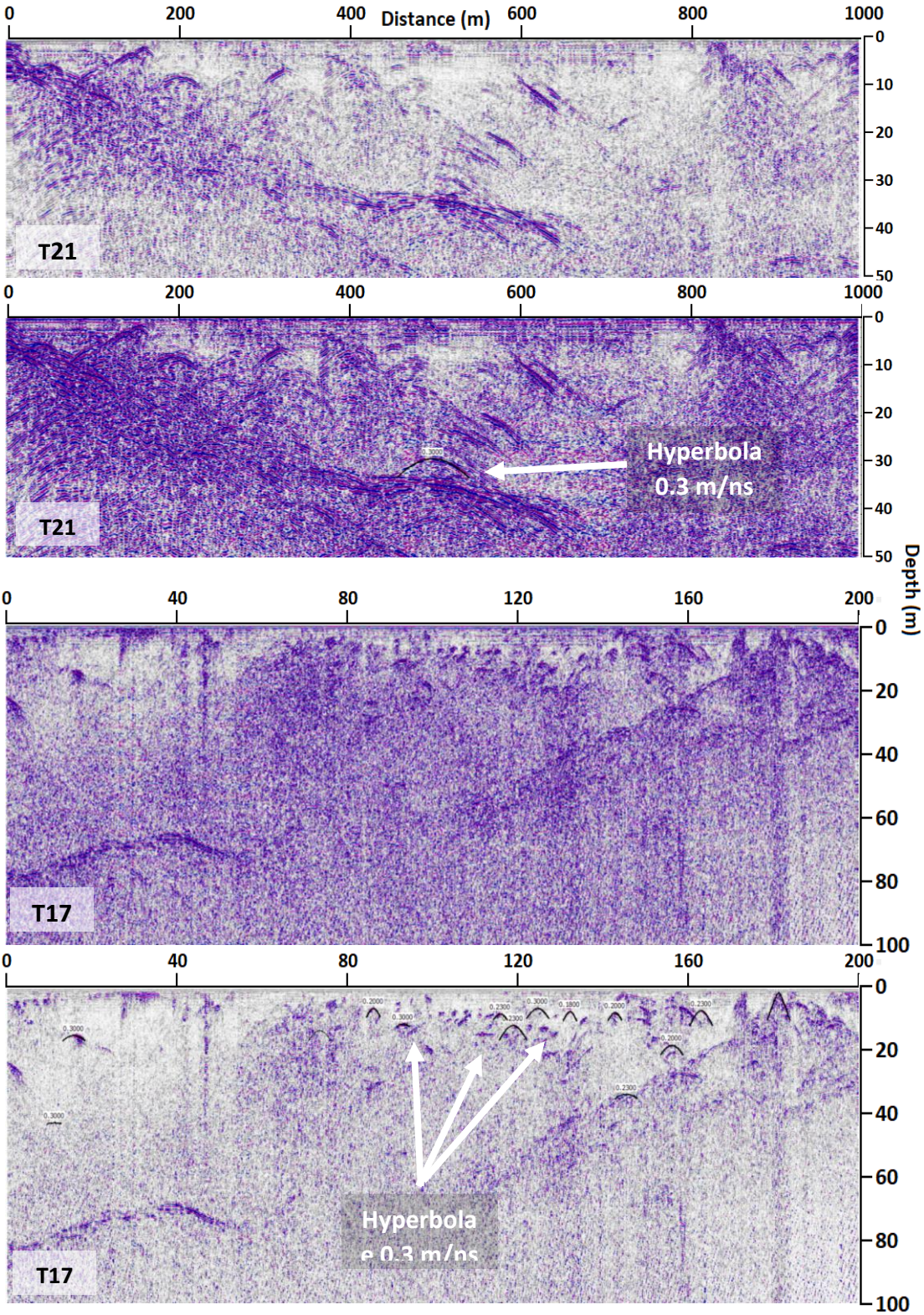

Figure 2.30: *Hyperbola fitting for transects 17 and 21. Considered to be air filled voids*

2.3.3.5 Cross validation

In order to ensure that the GPR traces are as accurate as possible a cross-validation of traces was carried out, also known as a 'depth estimate quality assessment' (Saintenoy *et al*., 2013). It was hoped that by comparing and interpreting data traces from where two transects crossed, a better and more reliable estimate of the bed could be obtained. Furthermore, the error between 'crossover' points could be ascertained and used as a good indicator of internal error. Crossover points were looked at in detail and a table of differences between picked bedrock estimations was created, (Table 2.5)).

Table 2.5: Differences between individual transect depths at cross-sectional points for Findelengletscher during February GPR fieldwork.

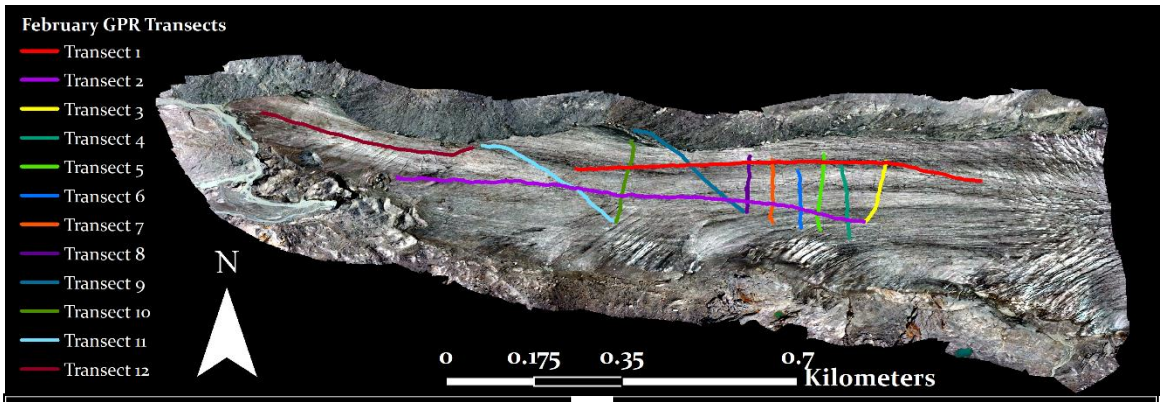

Transects	First Depth	Second Depth	Dif.	Transects	First Depth	Second Depth	Dif.
1 & 3	71.59	70.29	1.35 m	2 & 10	58.05	61.32	3.27 m
1 & 5	71.59	72.9	1.31 m	2 & 9	77.52	74.74	2.78 m
1 & 4	71.59	76.99	5.4 m	2 & 8	76.69	88	11.31 m
1 & 7	77.12	84.38	7.26 m	2 & 7	75.27	78.17	2.9 m
1 & 8	77.6	82	4.4 m	2 & 6	70.12	72.32	2.2 m
1 & 9	75.68	75.68	0 m	2 & 5	68.59	73.67	5.08 m
1 & 10	67.74	64.34	3.4 m	2 & 4	67.75	72.61	4.86 m
2 & 11	49.47	72.96	23.4 m	2 & 3	68.29	80.12	11.83 m

The crossover points of the February and July GPR work respectively were evaluated on their own initially (Table 2.5, & Table 2.6), then compared to each other (Table 2.7) to gain a better

idea of how the internal error compared over two separate visits to the field using different sensing equipment. As can be seen from the box plots in (Figure 2.31) the error across both individual fieldwork as well as a comparison of the results of both give similar difference levels (~5 m). By combining all 67 of these transect intersections, an overall internal error in bedrock estimates was calculated at 4.8 ± 1.27 m. This is in keeping with similar results obtained by Ai *et al.* (2014) who noted a root mean standard error of ~4.6 m with some outliers above 15 m. It can be concluded that the bed is now known to an accuracy of within several metres.

Table 2.6: Differences between individual transect depths at cross-sectional points for Findelengletscher during July GPR fieldwork.

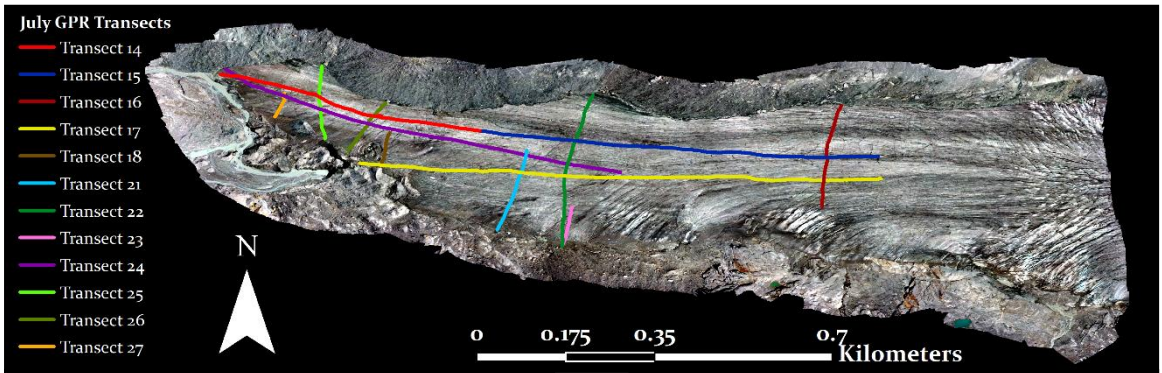

Transects	First Depth	Second Depth	Dif.	Transects	First Depth	Second Depth	Dif.
14 & 24	14.52	14.08	0.44 m	24 & 21	42.54	42.79	0.25 m
24 & 27	25.72	26.62	0.9 m	17 & 21	37.95	39.37	1.42 m
14 & 25	42.16	40.82	1.34 m	15 & 22	59.7	49.79	9.91 m
24 & 25*	36.29	38.97	2.68 m	24 & 22	50.43	52.45	2.02 m
14 & 26**	44.26	32.2	12.06 m	17 & 22	50.39	49.46	0.93 m
24 & 26***	48.21	43.27	4.94 m	15 & 16	94.32	85.75	8.57 m
18 & 17	12.58	35.86	23.28 m	17 & 16	75.16	78.2	3.04 m
Not quite overlapping *40 cm, **60 cm, ***4 m							

Table 2.7: Bedrock estimations at intersections of GPR transects between February and July fieldwork.

Transects	July Bedrock	Feb Bedrock	Dif.	Transects	July Bedrock	Feb Bedrock	Dif.	Transects	July Bedrock	Feb Bedrock	Dif.
15 & 1	2605.13	2609.76	**4.63**	17 & 4	2650.82	2650.86	**0.04**	22 & 2	2610.99	2614.31	**3.32**
15 & 10	2615.62	2612.59	**3.03**	17 & 5	2651.08	2651.34	**0.26**	22 & 11	2610.91	2614.31	**3.4**
15 & 9	2618.15	2615.03	**3.12**	17 & 2	2648.87	2653.17	**4.3**	24 & 2	2612.62	2613.27	**0.65**
15 & 8	2623.74	2623.33	**0.41**	17 & 6	2648.55	2650.39	**1.84**	24 & 11	2613.23	2595.85	**17.38**
15 & 7	2629.58	2631.47	**1.89**	17 & 7	2642.31	2641.61	**0.7**	24 & 10	2615.11	2615.05	**0.06**
15 & 6	2632.12	2637.7	**5.58**	17 & 8	2627.21	2630.63	**3.42**	25 & 12	2588.79	2589.07	**0.28**
15 & 5	2632.74	2642.85	**10.1**	17 & 9	2622.65	2632.84	**10.2**	26 & 12	2606.06	2588.01	**18.05**
15 & 4	2633.61	2641.28	**7.67**	17 & 10	2615.34	2615.96	**0.62**	12 & 14	2594.15	2595.39	**1.24**
15 & 3	2637.11	2652.4	**15.3**	17 & 11	2610.5	2607	**3.5**	12 & 14	2590.06	2587.47	**2.59**
15 & 11	2593.36	2589.85	**3.51**	18 & 2	2615.23	2618.82	**3.59**	12 & 14	2589.61	2588.01	**1.6**
16 & 1	2644.99	2653.08	**8.09**	21 & 2	2611.34	2613.4	**2.06**	12 & 14	2586.4	2585.2	**1.2**
16 & 2	2651.3	2658.91	**7.61**	22 & 1	2616.05	2609.76	**6.29**	27 & 12	2591.89	2591.45	**0.44**
17 & 3	2651.56	2652.42	**0.86**								

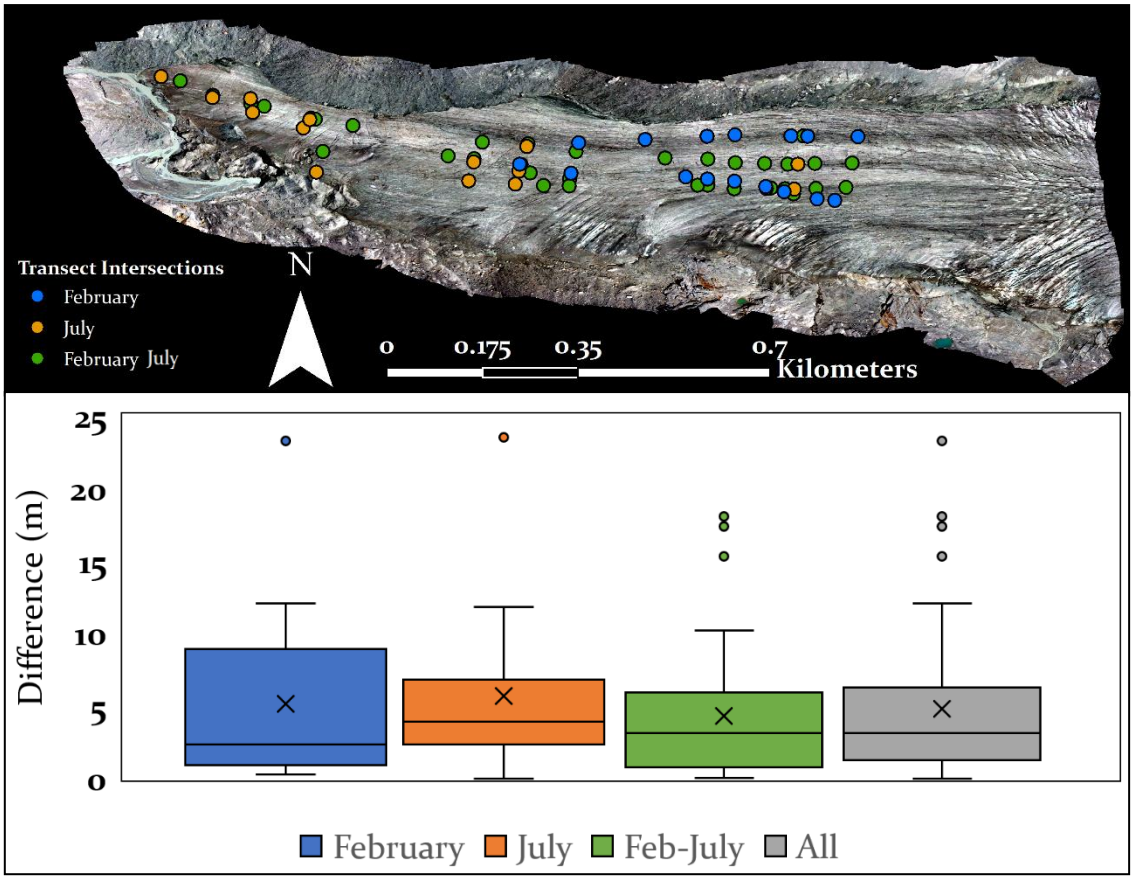

Figure 2.31: Above: Location of all GPR transect intersections. Below: Box plot of cross comparison GPR points between different fieldwork. From all points an error level of 4.8 ± 1.27 m was calculated.

2.3.4 GPR uncertainties

Whilst GPR is more accurate than other methods in estimating the depth and topography of subglacial bedrock, there are various sources of error involved in both the collection and the processing of this method (Saintenoy *et al*., 2013) which will be discussed in the following sub-sections.

2.3.4.1 GPR coordinate error

The geospatial location of the recorded transects are important in applying the GPR results to 3D models in the processing of data. The GPS device connected to the GPR contains a certain degree of uncertainty. During the February 2017 fieldwork, the GPS system associated with the MALA suffered connectivity issues on site due to the wear and tear on the wires and connection port and no GPS data was recorded. A backup Garmin eTrex 10 Handheld GPS was carried during the data collection with a horizontal accuracy of approximately 3 m (Oderwald & Boucher, 2003). With data collected in the summer 2017 fieldwork campaign, the GPS used in conjunction with the Pulse EKKO GPR was a Leica GNSS GS10. A decimetre horizontal accuracy was observed in keeping with Dobiński *et al.* (2017).

2.3.4.2 Transmitter & receiver location error

With both the MALA and PulseEKKO GPR, the distance between the transmitter and receiver varied slightly due to the difficulties in keeping a constant and equal spacing between these on difficult terrain. As mentioned in Section 2.3.2.1, using the MALA GPR in February fieldwork required three people on skis to operate. Dragging the antenna coil behind and trying to stay on a heading was difficult and lead to a slight flexing in the 6.2 m distance between transmitter and receiver. With the Pulse EKKO, again, a minimum of three people was required to operate the device; one checking the readings and navigating whilst the other

two kept the transmitter and antenna 1 m apart using measured string that was kept taught between the two. In some cases, due to the rough terrain (such as crossing small proglacial streams) the distance could not be kept constant. This effect may have a small error effect on the depth measurements of any reflectors.

2.3.4.3 Assumed wave velocity

In order to calculate the depth of any reflectors, an estimated constant wave velocity through the ice had to be assumed. Universally the velocity for glacial ice is between 0.167 and 0.17 m/ns (Binder *et al.*, 2009, Moore *et al.*, 2011, Martín-Espanol *et al.*, 2013). As Findelengletscher is a temperate glacier, higher levels of sub and englacial water are likely to be present, therefore 0.167 m/ns was preferred as it is closer to the velocity of water. However, this estimate does not take into consideration the different densities and therefore travel time, of snow (0.22 m/ns (Bælum & Benn 2011)), firn (0.19 m/ns (Pettersson *et al*., 2003)) and glacier ice (Saintenoy *et al*., 2013). Whilst this affect would be negated in the July measurements of Griesgletscher and Findelengletscher due to very little snow or firn being present at the time of data collection, the February data would certainly have been affected by a layer of snow and firn of ~1 m. Indeed, Saintenoy *et al.* (2013) considered that this effect carries with it a relative error of 0.3%, whilst (Lundberg *et al*., 2000) found that for 2 m of hard packed snow an error of 0.4 m of depth was found. Whilst it is important to mention this error, it is unlikely to have affected the readings in a significant way (Bælum & Benn 2011). Of course, no snow was present during the July fieldwork. However, in Winter 2016 up until the commencement of fieldwork 102.7 cm of precipitation had fallen in the area (Meteoblue, 2018). By comparing transect cross-over points (Table 2.7), there was no evidence that this bias was occurring with February bed estimates found to be deeper than July in the majority of cases.

2.3.4.4 Interpreting features – post processing

Once the data has been processed to offer as clear an image of reflectors at the bed as possible, the image needs to be 'picked'. This process consists of manually selecting points where a reflector, assumed to be that of the bedrock, meets the subglacial ice as indicated by a change in noise from the signal. It is possible that the bedrock or any features at or near to the bed, can be mistaken for the actual bed due to the overall clarity of the data. This is likely due to reflections from valley sides, englacial reflectors such as large sediment, or high levels of englacial water which can diffuse the signal of reflected electromagnetic waves. Unclear or misleading reflections can lead to inaccurate interpretations of the bedrock. As discussed in Section 2.3.3.5 Cross validation, for transects that intersect, comparisons of the depths of crossover points were made in order to more accurately predict the bed. Differences between crossover points acts as a good indicator of internal error.

2.3.4.5 Interpreting features – hydrological flow

Once a bed mask has been created it is possible to calculate how water travels beneath a glacier using the following formula (2) taken from Shreve, (1972) which can be applied calculate the 3D hydraulic potential surfaces of the bed (Φ) where ice overlays it.

$$\Phi = \rho_w g h_b + F \rho_i g H \quad (2)$$

Where ρw and ρi is the density of water and ice respectively (1000 and 917 kg m-3), g is acceleration due to gravity, hb is the elevation of the glacier bed and H is ice thickness (calculated by the DEM minus hb). F is the ratio of non-local, water pressure subglacially, or the floatation criterion, which for this study is assumed to be 1. By combining this formula to hydrological calculations of flow direction and accumulation we can form a view of where the main subglacial conduits are located.

2.3.5 Summary of GPR

In Summary, two successful visits to the field have garnered 27 transects covering the lower 1.5 km of the terminus of Findelengletcher. Significant areas of bedrock were located and within a 4.8 m ± 1.27 m error range which is suitable for showing deviations within the bedrock topography believed to be an order of magnitude higher. This data has set the foundations for the following chapter where the GPR data will be discussed in more detail and a bed model produced along with discussion over other reflectors found englacially and subglacially and their significance.

2.4 UAVs

2.4.1 The potential for UAVs in glacial environments

UAVs have been a viable method in the collection of glacial data for decades (Mulac *et al*., 2004; Egan *et al*., 2005). Initially these vehicles took the form of balloons or kites, and these are still used in modern day studies (van Wynsberghe & Turak, 2016; Jacob *et al*., 2018). In recent years UAVs in the form of fixed wing or multi-rotor, battery powered aircraft have become more prevalent in the scientific community, largely due to advances in battery power (Nex & Remondino, 2019) and improved portability (Schreiber, 2016).

The growth in popularity of UAVs as a method of data collection is due to several factors. Firstly, the closer proximity of the camera to glacial features means that higher resolution imagery can be obtained (centimetre as opposed to metre scale) compared to satellite data (Martin *et al*., 2018). An advantage that this type of data collection has over direct individual point measurements, is that access to otherwise hard to reach areas affected by such factors such as steep topography or crevasses, is negated (Rossi *et al*., 2017; Puppala, 2019).

UAV data fills the gap between high-resolution, individual directly obtained measurements and large-scale, low resolution satellite data. The growing computing power and complexity in structure from motion (SfM) software and their respective algorithms has enabled their widespread use in scientific research (Bash *et al*., 2018) and suggests the role of UAVs will continue to grow in the future (Gaffey & Bhardwaj, 2020).

2.4.2 UAV Equipment Selection

In deciding which type of UAV was most suitable for use in this study, numerous factors were considered. Firstly, it was important to consider which type of UAV was best suited to the needs of the study. Table 2.8 shows a comparison of the different types of UAV for this study, with the most suitable choice for various factors underlined.

Table 2.8: *Comparison of types of UAV.*

	Fixed Wing	**Multi-Rotor**	**Balloon**
Flight Time	Medium	Low	<u>High</u>
Landing difficulty	<u>Medium</u>	Low	Low
Cost	High	<u>Low</u>	Medium
Weather resistance	Medium	Low	<u>High</u>
Wind resistance	<u>Medium</u>	<u>Medium</u>	Low
Flight accuracy	Medium	<u>High</u>	Low
Portability	<u>High</u>	<u>High</u>	Medium

From Table 2.8, it can be seen that a multi-rotor UAV was the best choice for this study. Due to the costs of multiple visits to the field site and the remote locations of the field site, the cost and portability of the UAV were considered to be the overriding factors when deciding upon which type and model of UAV to use. Multi-rotor UAVs are more suitable to the work required in glacial environments than fixed-wing UAVs due to their ability to take off vertically which allows for deployment from relatively inaccessible areas (Hackney and Clayton 2015). It is also likely that topographic data sets recorded from quadcopters are of a higher quality

than their fixed-winged equivalent due to higher levels of control and better quality gimbles for image acquisition (James & Robson, 2014). Flights were carried out using a DJI Phantom four multi-rotor quadcopter as shown in Figure 2.32 (specifications shown in Table 2.9) with four intelligent batteries as well as an Apple iPad interface with the remote controller.

Figure 2.32: *DJI Phantom 4*

Table 2.9*: Specifications for the DJI Phantom 4*

Aircraft	Weight (inc. camera & battery)	1380 g
	Diagonal Size (Excluding Propellers)	350 mm
	Max Wind Speed Resistance	10 m/s
	Max Flight Time	Approx. 28 minutes
	Operating Temperature Range	32° to 104°F (0° to 40°C)
	Satellite Positioning Systems	GPS/GLONASS
	Automatic Flight Planning	No
Battery	Capacity	5350 mAh
	Voltage	15.2 V
	Battery Type	LiPo 4S
	Energy	81.3 Wh
	Max Charging Power	100 W
Camera	Sensor	Effective pixels:12.4 M
	Lens	20 mm (35 mm format equivalent) f/2.8 focus at ∞
	Field of Vision	94°
	ISO Range	100-1600 (photo)
	Electronic Shutter Speed	8 - 1/8000 s
	Image Size	4000×3000
	Photo	JPEG, DNG (RAW)
	Supported SD Cards	Micro SD

2.4.3 Field collection of UAV images

Across the two field seasons, nine orthomosaics were produced from a total of 38 separate flights (Table 2.10). Three field campaigns were performed in late August 2016, Early July 2017, and Early September 2017. All flights were carried out using the DJI Phantom 4.

Table 2.10: UAV Flight Statistics at Findelengletscher.

Model Name	Date	Location	Flights	Flight Times	GCPs	Tie-Points	Images
F1	22/08/16	Findelen	4	13:46 – 16:28	9	8	765
F2	27/08/16	Findelen	4	09:11 – 13:31	9	8	731
F3	31/08/16*	Findelen	5	11:28 – 13:52 (09:58 – 10:10)	8	8	721
F4	03/09/16	Findelen	4	09:31 – 11:43	9	9	757
F5	06/09/16	Findelen	4	09:37 – 11:52	9	9	699
F6	05/07/17	Findelen	4	10:26 – 13:20	20	0	681
F7	07/07/17	Findelen	4	13:03 – 14:58	20	0	736
F8	03/09/17	Findelen	4	13:40 – 16:09	19	0	790
F9	07/09/17	Findelen	5	10:10 – 12:23	19	0	789

**Flights concluded on 1/9/16*

Flights were initially recorded using a 'waypoint flying' method for autonomy, whereby the UAV automatically traces a flight route within the DJI application by flying the route and recording markers at specific coordinates and altitude. However, this method dramatically reduced flight time and therefore the area that could be covered. This was discontinued in lieu of manual flying after the first two complete sets of flights.

Image acquisition was recorded every 5 seconds using the automated feature within the DJI application and flight speeds were kept at a constant 2.5 m/s where possible following the methodology of Tonkin *et al*. (2014) and Tonkin & Midgley, (2016) to keep image blur low. This translated to an image being recorded every 12.5 m.

Image overlap is an important factor to consider when producing a 3D model with high accuracies (Fonstad *et al*., 2013). If overlap is too high the processing time is significantly

increased, whilst low overlap can increase inaccurate points in the 3D model (Fonstad *et al*., 2013). It is important to select an appropriate number of images to produce an accurate 3D model without greatly impacting on processing time. Generating the 3D model is a RAM intensive process, an approximation of just how much memory is required to process a model is outlined in Table 2.11 (Agisoft PhotoScan, 2018a). Agisoft PhotoScan, (2018b) recommends an average lateral and side overlap of at least 80% and 60% respectively for aerial imagery. Overlap between photos was varied due to the lack of automation, however all fell within acceptable levels (Figure 2.33). Figure 2.34 shows an example of the lateral overlap of two images stitched together, at 90%. Notably however there is a data gap in model F1 where the gap between the flight lines occurring in separate flights was underestimated which will be discussed in more detail in Section 2.4.4.4 Processing issues.

Table 2.11: *Memory consumption required in the creation of Agisoft SfM models. Figures are based on 12-megapixel images. Taken from (Agisoft 2018).*

Photos	100	200	500	1000	2000	5000	10000
Lowest quality	25 MB	50 MB	125 MB	250 MB	500 MB	1.25 GB	2.5 GB
Low quality	100 MB	200 MB	500 MB	1 GB	2 GB	5 GB	10 GB
Medium quality	400 MB	800 MB	2 GB	4 GB	8 GB	20 GB	40 GB
High quality	1.6 GB	3.2 GB	8 GB	16 GB	32 GB	80 GB	160 GB
Ultra-high quality	6.4 GB	12.8 GB	32 GB	64 GB	128 GB	320 GB	640 GB

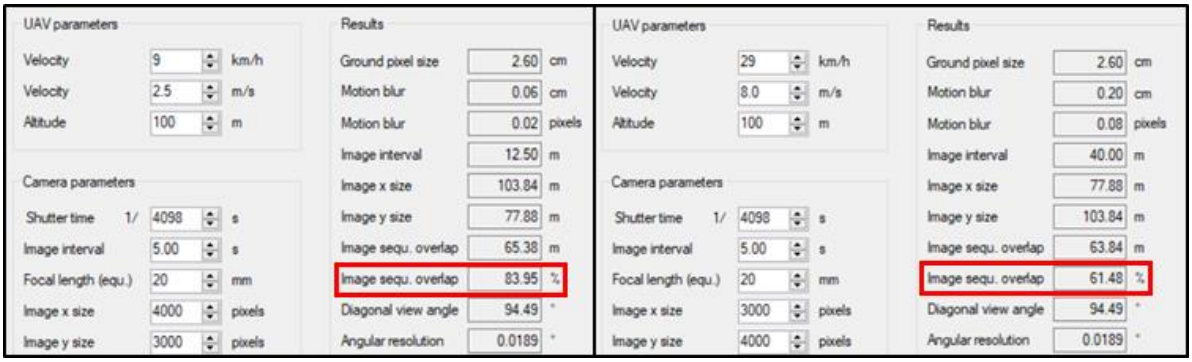

Figure 2.33: *Left: Image lateral overlap Right: Image side overlap as calculated by UAVphoto (2014) UAV and camera parameters were input according to flight parameters. Side overlap was replicated by flipping the x and y size and altering the velocity to '8' and image interval to '5' to simulate the approximate 40 m gap between lateral flight paths of the UAV.*

Figure 2.34: *Typical lateral overlap between two images (red and yellow outline). (Image from Flight 2, 27/8/16).*

Due to the time taken to process and write imagery onto the SD card within the UAV in 'raw' format (> five seconds), photographs were recorded in 'jpeg' format so that images could be captured every five seconds (Cruzan *et al.*, 2016) and a suitable lateral overlap could be obtained. Due to the size of the data (approximately 3-4x that of JPEG (Morgan *et al.*, 2017)) storage of this data in RAW format would have been more expensive. Furthermore, in order

to use images in Agisoft they must first be converted to a JPEG format (Prieto & Ramos, 2015), therefore recording in RAW format is only necessary for the purposes of altering properties such as contrast or brightness before post-processing (Marziali & Dionisio, 2017). Indeed Jiroušek *et al.* (2014) found the differences in models from RAW and JPEG formats to be negligible.

Focal length is a determination of how much of a scene will be recorded, and its magnification with a shorter focal length resulting in a broader image with smaller magnifications The focal length of the Phantom 4 was fixed at 20 mm and an aperture of f/2.8.

ISO values are representative of an automated lightening of an image. This is sometimes necessary to make a dark scene clearer, with better contrast. However, too high an ISO level can create noise which reduces the clarity of the image. All images were shot with an ISO level of 100 (lowest possible for the camera used). Shutter speed works in a similar way in controlling light levels. A slow shutter speed allows more light in, creating a brighter image. However, any movement from the camera or target can cause motion blur to occur (Zhang *et al*., 2020). As the UAV is moving at a constant speed, it stands to reason that the shorter the shutter speed, the less motion blur occurs. A far away object will have less motion blur than a close one due to the relative distance travelled being much shorter in relation to the camera aspect. By this logic, the higher the altitude of the UAV, the less motion blur will occur due to shutter speed. By using the automatic camera setting with fixed aperture and ISO levels, the shutter speed varied based on the light levels of the scene. Shutter speeds varied between 1/382 and 1/4098 with a mode of 1/4098, faster speeds than that of Immerzeel *et al.* (2014).

2.4.3.1 Ground Control Points

Ground control points (GCPs) are a necessity to improving the accuracy of the DEM. By pinning the model at certain points to true, highly accurate coordinates using dGPS (differential global positioning system), a better estimation of the real-world location of the study area can be obtained. In order that these GCPs can be accurately measured, they need to be bright and contrast well with the surrounding background colours. Fluorescent orange and purple canvas was chosen for the construction of these GCPs. From the first fieldwork (2016) GCPs were 1 m^2 with a purple 30 cm^2 square in the centre with another 10 cm^2 square cut out in the centre of this (see Figure 2.35 - left). This design was chosen so that the centre of the GCP could be seen from long distances. Canvas was chosen as the material for the GCPs as it is flexible, lightweight, reusable and can withstand extreme weather conditions, however it was necessary to weigh the canvas down with rocks to keep it secure against winds. For GCPs placed directly on ice, a combination of pegs and rocks was used.

In the 2016 field season nine GCPs were used. A Magellan ProMark 3 dGPS was used to derive GCP locations. For the 2017 season, more GCPs would be able to be recorded thanks to the availability of a faster, more portable, and more accurate dGPS device – the Leica GPS1200 series, borrowed from VAW. Previous GCPs were cut into quarters and a duct-tape cross applied. Based on analysis of the 2016 image dataset it was concluded that the GCP centre-point estimation error would not be exacerbated by shrinking the GCP size. This would also not impact on the weight to be carried to the field site. The two differing GCPs used can be seen in Figure 2.35**.**

Figure 2.35: *Different GCPs shapes and sizes used between 2016 (left) and 2017 (right).*

2.4.3.2 UAV data collection issues

In-flight altitude measurements were stated relative to the take-off location coordinates. Therefore, flights were carried out at similar altitudes to that of the glacier, in this way altitude above the ice could remain constant and reliable. However, as the UAV moved up glacier, the altitude relative to the underlying glacier shrank, therefore it was necessary to steadily increase altitude as the flight path continued. An estimated average altitude of 100m above the glacier was recorded; the higher the altitude, the lower the spatial resolution would be (Anurogo *et al*., 2017), so it was important to get the balance of a high resolution with limited motion blur whilst still capturing a good-sized area. All images were recorded in full nadir (Turner *et al*., 2015; Wigmore & Mark, 2016), i.e., with the camera lens facing straight down. In this way, it was hoped that the steep slopes of the crevasses could be better represented by the models as images would be shot straight down into them.

As can be seen in Table 2.10, the set of flights that make up each orthomosaic took on average, just over 2 hours and 30 minutes to complete. Within this time, shadows created by the angle of the sun and topography had moved somewhat. Every effort was made to keep

flights as close together as possible. The availability of when flights could be conducted was constrained by weather conditions, however, where possible flights were carried out when the sun was as close to its zenith as possible in order that any shadows on the resultant images would be kept to a minimum. This was due to evidence from previous studies that shadows can affect the accuracy of feature tracking (Luckman *et al*., 2007; Yang *et al*., 2020). This is backed up by comparing two DEMs of the same area of bedrock and looking at estimated differences in elevation (Figure 2.36).

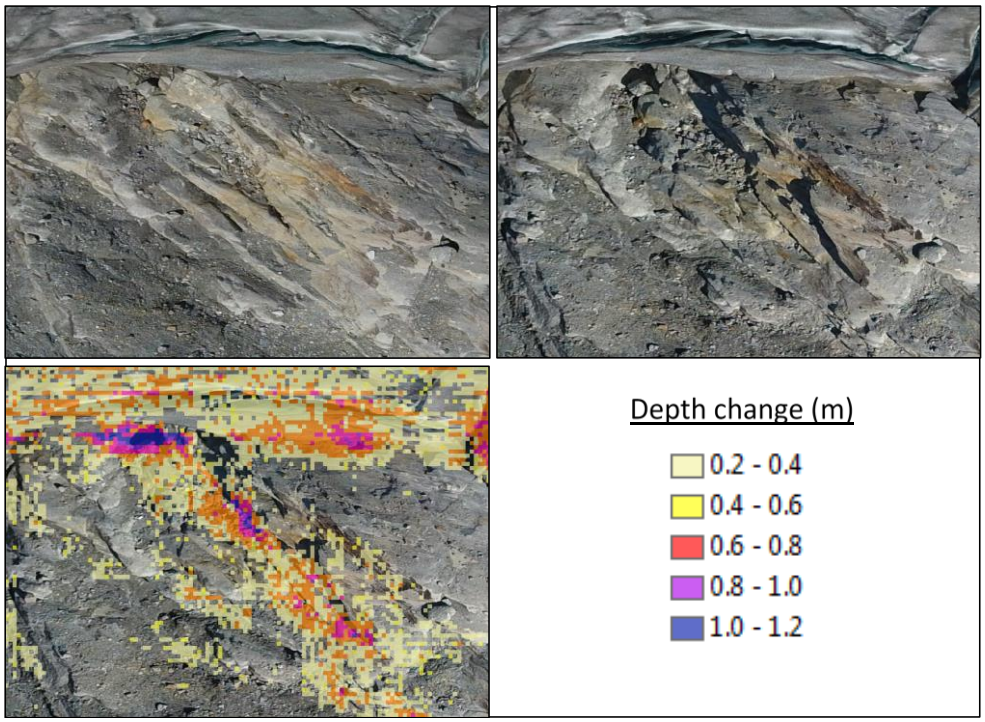

Figure 2.36: *Shadow effect on DEM estimates. Top left: flight 030917. Top right: flight 070917. Bottom left: Flight 030917 with DEM loss overlay.*

For health and safety reasons, flights were only conducted when wind speed was less than 10 m/s (DJI, 2016). This was measured using an anemometer pointed in the direction of the prevailing wind for five minutes prior to each flight. To protect the electrics within the UAV,

no flights were initiated during periods of precipitation (Gainullin *et al*., 2018). In the case of the set of flights carried out on the 31st August 2016 (Table 2.10), a flight was aborted midway through due to sudden rainfall, with the conclusion of the flight plan carried out the following morning when conditions were clear. Low cloud cover was also a condition in which no flights could be carried out due to reduced visibility both in the images recorded and the line of sight between the pilot and the UAV. During fieldwork, low cloud cover occasionally grounded flights for a short time or led to an entire day where it was not possible to fly as can be seen in Figure 2.37. High cloud cover on the other hand, represented ideal conditions due to the reduction in shadowing effects on the images ensuring more reliable SfM results (Luckman *et al*., 2007) as well as making the UAV easier to keep sight of against a grey backdrop than a blue, clear sky. However, sunlight increases contrast which may help with the image alignments and, later, feature tracking software.

Figure 2.37: *Left: Low lying cloud conditions on 30/08/17 looking south across Griesgletscher. Right: Low fog at Findelengletscher looking east up valley 6/9/16.*

Due to the limited battery life of the UAV (approx. 20 minutes) and low speeds necessary for reduced motion blur (Tonkin & Midgley, 2016), four flights were required to cover the field site thoroughly. At the time of fieldwork, UAV law and regulations require that the pilot

always be within 'line-of-sight' of the UAV at all times and fly no higher than 150 m from the ground (FOCA, 2018). Therefore, it was required that flights were conducted from at least four different take off points as can be seen in Figure 2.38 so that the area of interest could be covered without losing sight of the UAV. Figure 2.38 shows an example of the individual flights that make up one of the orthomosaic images. In total, models suitably covered an area of approximately 1300 x 300 m.

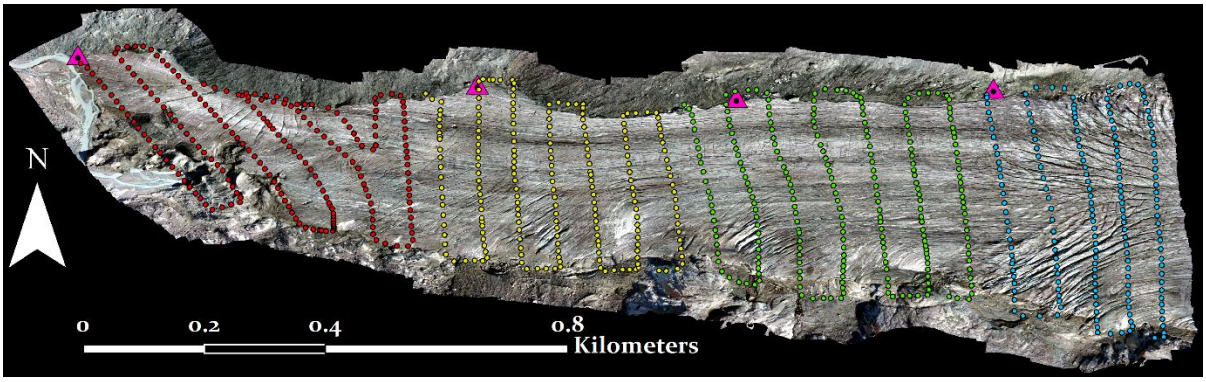

Figure 2.38: *Four individual flights that make up an orthomosaic (shown beneath). Individual dots represent the location of images captured, and pink triangles represent take off/landing points. (6/9/17).*

2.4.4 Processing imagery

Structure from motion (SfM) is a processing method by which a three-dimensional representation of a scene can be inferred by how differences in camera location affects the two-dimensional images recorded from multiple viewpoints (Westoby *et al*., 2012) (Figure 2.39).

In order to create three-dimensional imagery from multiple two-dimensional images, algorithms are used to detect the same feature points on multiple images and track the movement of these points across these images. In the case of glacial scene reconstruction,

the shape of a corner of an object such a clast would be used. Now advances in software such as Agisoft PhotoScan enables a more simplistic workflow approach (Ryan *et al*., 2015) and this, more user-friendly software, combined with modern advances in UAV technology such as image quality, internal GPS tagging of imagery and user-friendly operating with a low price tag, make the entire SfM process more accessible and more accurate.

Agisoft PhotoScan Pro (www.agisoft.com) software was therefore used in this study. The optimised workflow for the processing of images taken can be seen in Figure 2.40. This process can be loosely divided into a few key stages.

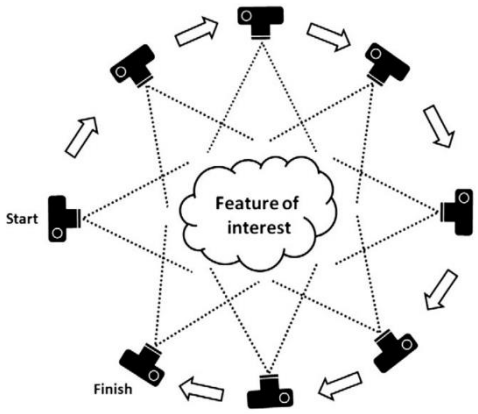

Figure 2.39: *Creation of 3D structure using multiple viewpoints from a moving camera (figure taken from Westoby et al., 2012).*

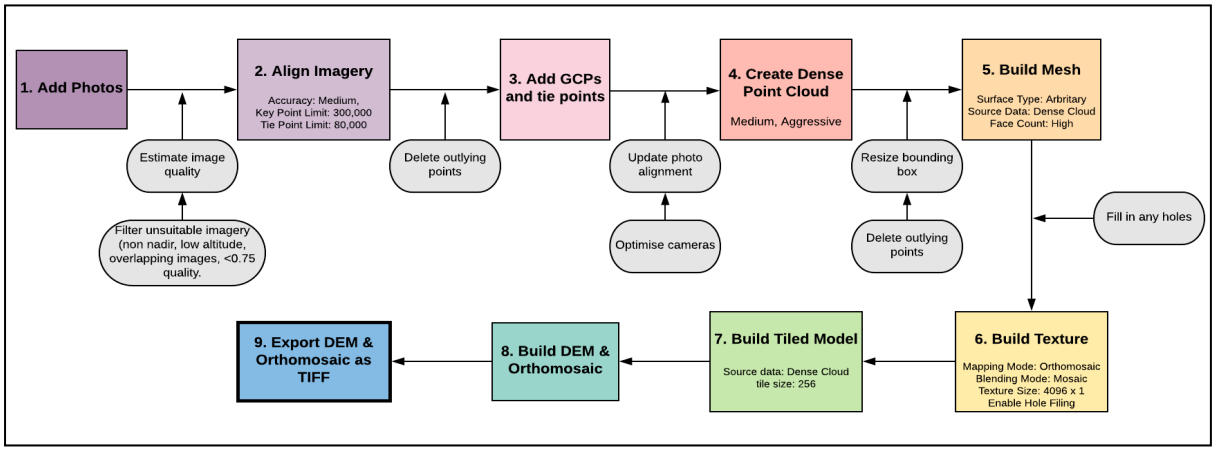

Figure 2.40: *Agisoft PhotoScan work-flow diagram.*

2.4.4.1 Image alignment

Images from a day's flights were uploaded into the software. Agisoft has the facility to estimate the quality of each image based on the sharpness of contrast within the image. A number between 0 and 1 is assigned to the image to denote image quality (see Table 2.12) 1 being the highest. Where there was still sufficient image overlap, images below 0.75 were discarded where image overlap levels were not impacted beyond recommended levels (lateral - 80%, side - 60%). Furthermore, the images were checked for non-nadir images, and these were discarded also. Due to the high levels or RAM required for processing the amount of data, a 'Medium' accuracy was selected. This was the highest quality possible based on the processing speed of the available computer (see Table 2.11). The process of 'chunking' the data has been suggested as a method for enabling higher quality models through more efficient processing (Ward, 2019), however these presented alignment and accuracy issues due to the low amount of GCPs at any one 'chunk'. Therefore, for overall accuracy it was considered best to process the entire field-site in one go.

Once this has been processed, the image locations are displayed on a 3D plane with a sparse point-cloud representing the points where the same feature points have been recognised on different images. At this stage it is possible to delete any of these points that are clearly out of place, this can most clearly be seen by points that do not conform to the z-value of similar surrounding points. These outliers were removed. Next, the GCP coordinates were added and manually aligned with the imagery. Tie-points were then added to the orthomosaics where GCPs coverage was low. Tie-points act in a similar way to GCPs in that they create a point where the model is tied together however, without the added accuracy of dGPS coordinates. The creation of tie-points was limited to clear edges of objects such as clasts, debris or

supraglacial channels and were spread across the model in order to reduce any distortion far from GCPs.

After all the images for a single GCP were aligned, the model was updated using the 'update orthomosaic' tool which shifts the entire model to fit around the more accurate DGPS derived GCP coordinates. The model was continually updated until all GCPs had been aligned. Finally, the 'optimise camera' tool is used in order to realign the cameras based on the edited sparse point-cloud.

Table 2.12: *Image recording and quality results.*

Model	Image Quality (0-1)	Av. Image Quality	f.	ISO
F1	0.780 – 0.903	0.865	2.8	100
F2	0.778 – 0.909	0.873	2.8	100
F3	0.787 – 0.966	0.880	2.8	100
F4	0.809 – 0.909	0.858	2.8	100
F5	0.773 – 0.913	0.883	2.8	100
F6	0.777 – 0.870	0.829	2.8	100
F7	0.750 – 0.884	0.846	2.8	100
F8	0.800 – 0.881	0.861	2.8	100
F9	0.759 – 0.867	0.809	2.8	100

2.4.4.2 Dense point-cloud

Once the cameras have been correctly aligned, the dense point-cloud can be created. The quality to which this can be done is again based on the amount of RAM available; this is the most memory intensive part of the process. A 'Medium' quality was chosen for all models due to the availability of processing power (see Table 2.11). This setting processes the original photos whilst each step down in quality downsizes the image size by a factor of four (Agisoft, 2018). In total there are five levels of quality: Ultra High, High, Medium, Low and Lowest. The depth-cloud first calculates the depth maps for each image by computing the distance between every pixel within an image and the camera location, it does this for every image

taken. According to Hueff (2015), the quality level of the dense point-cloud showed no visible improvement to the DEM. However, from a comparison of DEMs specifically at areas where there is a high relief such as crevassing, the quality selected has a clear effect on the resolution, and therefore accuracy of the model, as can be seen in Figure 2.41. Agisoft PhotoScan Pro has different in-built filtering algorithms for estimating this based on the type of scene being depicted. The best results for landscapes such as the Findelengletscher field-site were obtained by using an 'Aggressive' depth filtering.

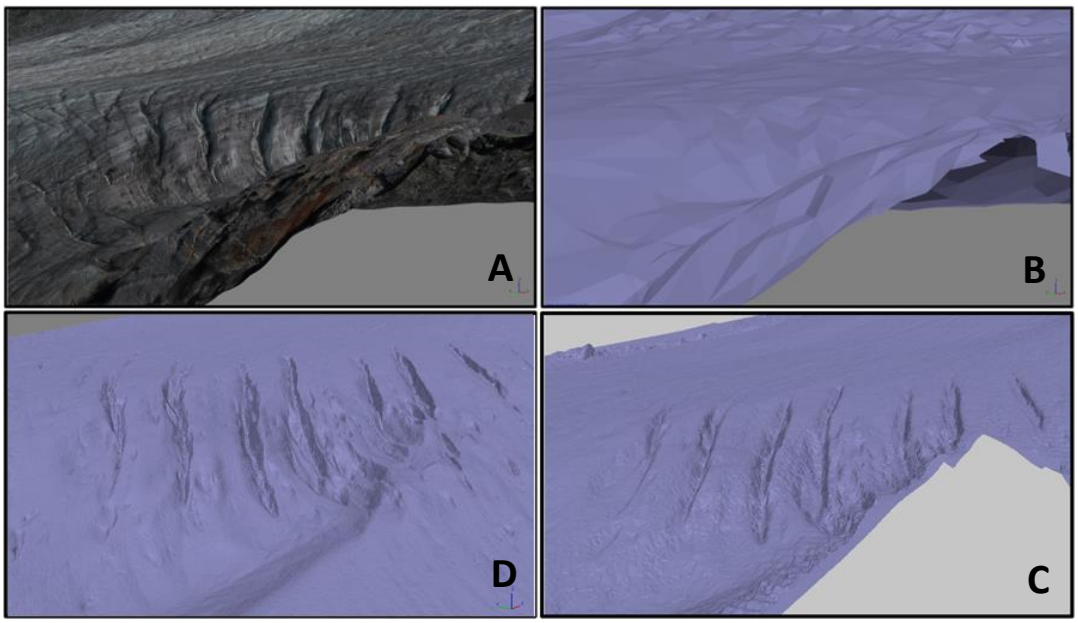

Figure 2.41: *Difference in DEM resolution between 'Low', 'Medium' and 'High' processing options in Agisoft PhotoScan (**A**: 3D image overlay of the DEM. **B**: Crevasses at 'low' quality. **C**: Crevasses at 'medium' quality. **D**: Crevasses at 'high' quality).*

2.4.4.3 Generating a mesh

From the dense point-cloud points, the Agisoft PhotoScan software creates a polygonal mesh that is representative of the surface topography of the field site. A surface type setting of 'Arbitrary' produced more accurate results and was more memory intensive (Agisoft, 2018).

Once this mesh has been created a texture can be applied to the DEM for the purpose of building the orthomosaic. This is done by the steps 'Build Texture' and 'Build Tiled Model'.

After this processing has been completed for each model, they can be exported in the form of a digital elevation model (DEM) and an orthomosaic, the former of which contains just the xyz coordinate mesh, the latter contains the combined pixels from all of the stitched images across the entire field site. The overall resolution could be adjusted at this stage, however in general the orthomosaic was found to be ~4 cm with a DEM resolution of four times this (~16 cm). The resolutions varied across the different models recorded due to differences in quality, amount and height of images recorded as well as area covered and overlap, these differences can be seen in Table 2.13.

Table 2.13: *Agisoft PhotoScan Model Statistics.*

Model No.	Control Point Error (m)	Pixel error	Point Cloud	GCPs	Tie-points	DEM resolution (cm)	Ortho. resolution (cm)
F1	0.43	0.44	37,265,090	9	8	16.0	4.00
F2	0.41	0.56	36,325,458	8	8	16.2	4.05
F3	0.36	0.55	34,640,860	8	8	16.6	4.14
F4	0.45	0.60	38,562,553	9	9	16.3	4.09
F5	0.39	0.56	36,862,913	9	9	16.4	4.11
F6	0.06	0.32	31,769,806	20	0	15.9	3.97
F7	0.22	0.34	35,140,461	20	0	15.1	3.77
F8	0.18	0.31	40,190,304	19	0	14.0	3.50
F9	0.02	0.34	48,256,844	19	0	12.3	3.07

2.4.4.4 Processing issues

In the processing of the images a few issues were noted. Firstly, the initial model that was recorded (F1) contained an area where an insufficient overlap between images was apparent. This caused unsuitable levels of error in both the DEM and orthomosaic differences at this area (Figure 2.42). The lack of data for this area created a gap in the mesh which was closed

and smoothed using software available in Agisoft PhotoScan. Regardless, the area in question was therefore not considered in any of the future calculations of glacier change.

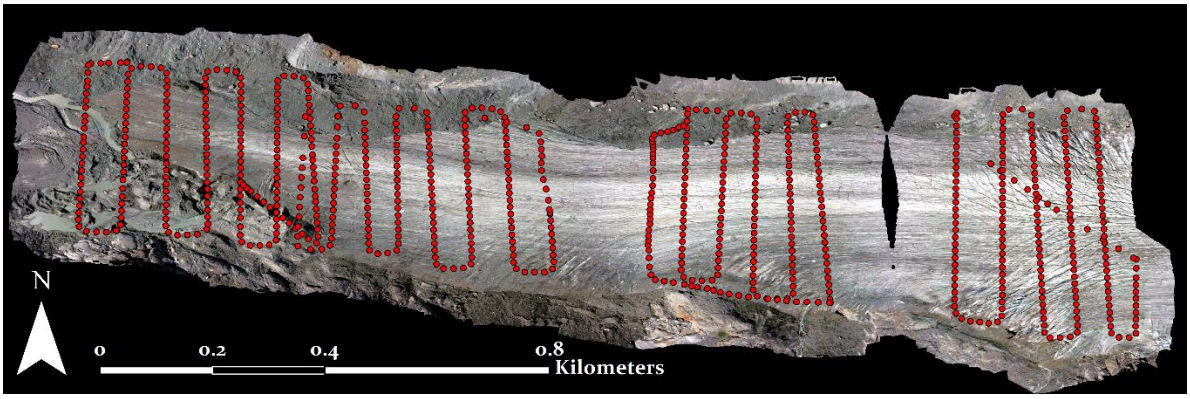

Figure 2.42: *Area in F1 where an unsuitable level of image overlap is recorded.*

The coordinate system recorded by the dGPS software for F7 were recorded in Swiss CH 1903 rather than WGS 84 coordinate system. This initially led to an unacceptable reprojection error when corrected (+1 m). Thankfully, many of the GCPs recorded were the same as the previous model from 2 days earlier and on stable (not in flux) ground. Therefore, the model was re-processed using only these GCPs aided by using the glacier surface GCPs as tie-points only and a more accurate model was produced.

2.4.5 Summary of UAV work carried out

In summary, three separate field seasons (one in 2016 and two in 2017) made up of 38 flights have garnered nine successful 'snapshots' of Findelengletscher with orthomosaic resolutions of ~4cm and DEM resolutions of ~16cm (see Table 2.10), the reason for the difference in resolution between orthomosaic and DEM is due to the downscale factor which was 4x due to the RAM specification of the processor. By comparing the differences between these images over time, a representation of the glacier flow dynamics can be ascertained. How these results are created will be discussed in the following section (Section 2.5) and the findings from these comparisons will be examined in Chapters 4 and 5.

2.5 COSI-CORR

In order to analyse the flow dynamics of the glacier between measurement periods it was necessary to analyse the change in pixels values between models. In other words, features on the glacier can be identified in two sets of imagery and a directional value as well as a velocity value (created by dividing the distance by the number of days between the images) assigned to this time period. This was done using the software tool COSI-Corr (Co-registration of Optically Sensed Images and Correlation). Predominantly this tool has been used to analyse very coarse data such as that from satellite imagery (Jawak *et al*., 2018; Wang *et al*., 2021; Das, 2021), however this method has been used successfully in processing much higher resolution data from UAV derived imagery (Kraaijenbrink *et al.*, 2016). The process by which COSI-Corr can derive glacier velocity in the form of vector fields and a displacement map is shown in Figure 2.43.

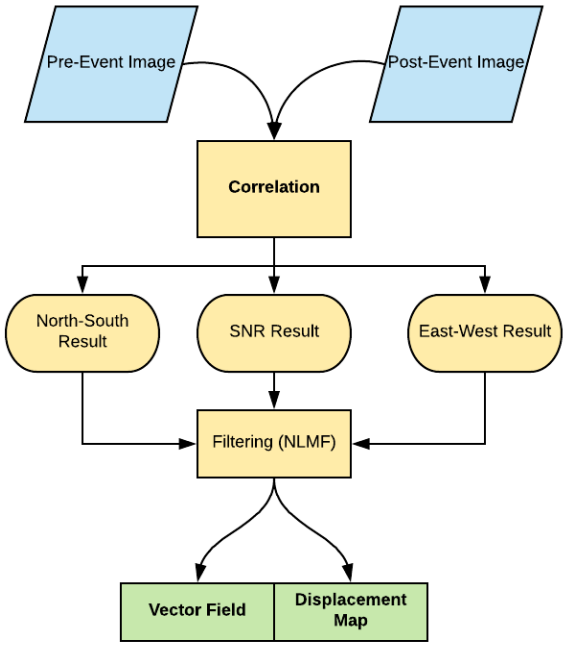

Figure 2.43: *Workflow process for calculating glacier velocities using COSI-Corr software. (Modified from Jawak et al., 2018).*

Once the orthomosaics (created by Agisoft PhotoScan Pro) have been exported in the form of a TIFF, they are all then fitted to the same resolution size (4x4 cm) for comparison purposes using the ArcMap tool 'Resample'. The data resolution is then further coarsened by a factor of four using the 'Aggregation' tool to reduce noise. The final resolution of the images used is therefore 16 cm, however it is important to note that COSI-Corr operates at subpixel levels (Leprince *et al*., 2007a) so results are not constrained to factors of 16 cm.

A pre- and post-event image are selected for frequency correlation. This step consists of two parts. Firstly, the approximate displacement between the images needs to be estimated and an appropriate window size needs to be selected. This should be anywhere from two times (Ayoub *et al*., 2009) to five times (Leprince *et al*., 2007a; Kraaijenbrink *et al.*, 2016) the expected displacement. However, the window size should not be less than half the displacement (Heid & Kääb, 2012). The larger the initial window size, the more that the noise can be reduced, however this is a trade-off, as too large a window size can lead to data being missed. According to Kraaijenbrink *et al.* (2016), by reducing the final window size, some of this data can still be recorded. However, from testing this appeared negligible. The right balance of these settings is vital to the generation of legible results with as little noise as possible.

The data area that can be measured using COSI-Corr over long periods of time (such as from late summer to early summer the following year), will be reduced due to the increase in noise which makes surface patterns harder to detect. The more time that has elapsed, the more noise there is likely to be between two time periods. Patterns can still be recorded by increasing the window sampling size, this however reduces the area where results can be

seen. The larger the window size, the more precise the correlation. However, the smaller window sizes are responsive to localised movement (Baird *et al*., 2019). For this reason, the window size is the most crucial factor to determine in the COSI-Corr process (Baird *et al*., 2019). Ayoub *et al.* (2009) suggest a window size approximately 5x that of the feature displacement, so it stands to reason that larger window sizes are needed to capture larger levels of glacier movement.

From trial-and-error testing, the best results were found with a window size of 64 pixels by 64 pixels for time periods of two to five days. However longer time periods introduced significantly more noise. The time difference of 58 days between models F7 & F8 (7th July- 3rd September) and 302 days between F5 & F6 (6th September to 5th July) caused significantly more noise to be present. This was due to the landscape changing more considerably and the overall displacement being higher. It was therefore necessary to increase the window size to 512 pixels by 128 pixels for both these time periods. Due to the size of the window, the area that could be measured was also considerably reduced. A robustness iteration of four and a mask threshold of 0.9 was used as this gave good results and was prevalent in the literature (Ayoub *et al*., 2009; Scheidt & Lancaster 2013; Stumpf *et al*., 2014).

To further de-noise the dataset a non-local means filter (NLMF) algorithm can be applied. This has been shown to reduce gaussian noise without compromising the fine details already found (Ayoub *et al*., 2009). The NLMF works by comparing surrounding values in a 5x5 grid around each pixel. A filtered value is calculated as an average of all the values within this grid and weighted by how similar they are to the pixel at the centre of its grid. A signal-to-noise (SNR) filter is also applied to the data. The H value (degree of denoising) was set at 2 and the

search area dimension was set to a size of 21 x 21 in line with recommendations by Ayoub *et al.* (2009).

In order to define the East/West and North/South direction of displacement as one vector the following formula (3) is applied to the data where b^1 and b^2 are the different band values.

$$\sqrt{b^1 + b^2} \tag{3}$$

by dividing this by the number of days between the pre-event image and the post-event image (t) an average displacement per day can be attained. This can be used to standardise the data as time windows varied from 2 to 302 days. The data can then be exported as an ERDAS IMAGINE file for display in ArcMap for both directional and velocity values.

$$\sqrt{\frac{b^1 + b^2}{t}} \tag{4}$$

2.6 CREATING A BASELINE MODEL

The behaviour of ice flow velocities of glaciers has long since been simplified for modelling purposes (Le Meur *et al*., 2004). The main constraint to ice flow is friction from the bed, which causes velocities at the margins to slow relative to the centre (Figure 2.44). Looking at a cross-section of a glacier (Figure 2.45), ice velocities increase the further away it is from the ice-bed interface. Depth plays a role in velocity as the thicker the glacier the more internal deformation occurs (Glen, (1955)) and the faster the glacier moves in the centre where ice is thickest.

Basal sliding also contributes to glacier flow and at a glacier with a smooth U-shaped bed, there would be more meltwater towards the central and deepest point of the glacier which would reduce the friction with the bed and therefore increase basal sliding rates at these locations as discussed in Section 1.3.3. As mentioned previously (Section 1.3.2), sliding and not internal deformation is the process behind the majority of ice flow velocity (Willis *et al*., 2003). Therefore, easily the most significant effect on glacier flow velocities is the water storage (and therefore reduced friction at the bed) within the glacier (Iken & Bindschadler, 1986; Benn *et al*. 2017). Bartholomaus *et al.* (2008) show a strong diurnal correlation between ice speed and water storage with a lag of around 6 hours for the valley glacier of Kennicott Alaska (Figure 2.46).

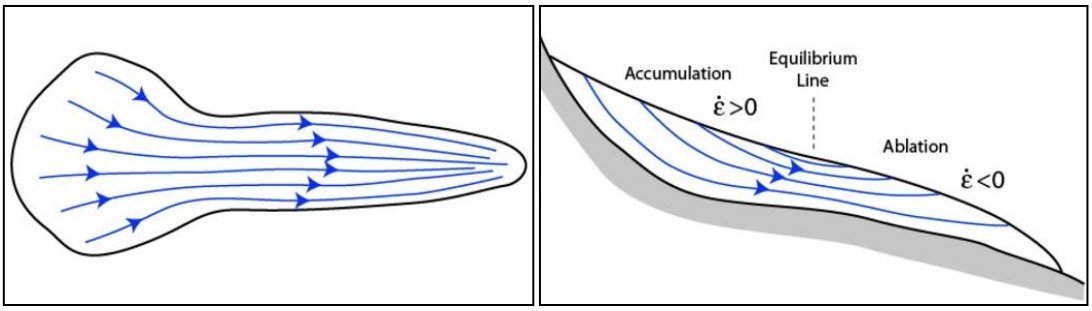

Figure 2.44: *Birdseye view (left) and side view (right) of typical glacier flow patterns (taken from Hudleston, (2015)).*

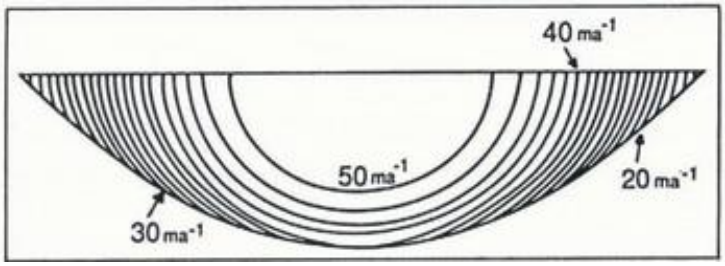

Figure 2.45*: A velocity solution for a parabolic cross-section using the adjusted sliding law as proposed by Harbor (1992). The maximum ice depth in this case was 310 m and the surface width 1240 m, the approximate dimensions of the Athabasca Glacier, Canada.*

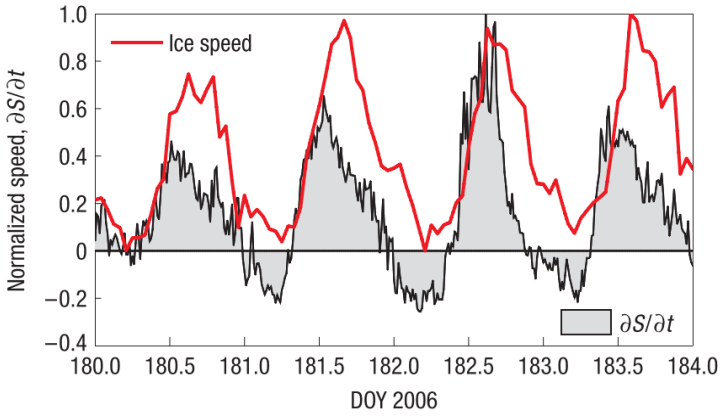

Figure 2.46: *Correlation of diurnal ice speed and water storage (taken from Bartholomaus et al., 2008).*

2.6.1 Creating Baseline Velocities

Subtracting data from a baseline to obtain residual data as a means to understand where disparities in the data are present is a technique used in previous work (Copland *et al*., 2003; Bingham *et al*., 2006; Scherler and Strecker, 2012) and are used here to guide us to areas of interest where velocities can be compared to GPR and mass loss data to infer what might be occurring at a local resolution. The baseline can be used as an 'average' when set against other results to highlight any changes that could be considered important.

To create a baseline of how ice flow at Findelengletscher moves, two sets of orthomosaic pairs a year apart were used. Feature tracking using COSI-Corr was undertaken for an Orthomosaic pair made up of UAV flights from 3rd and 6th of September 2016 and another made up of flights from 3rd and 7th September 2017. The resultant velocity map from both these time periods were averaged together and then smoothed using a radial base function. A focal statistic filter was then used to further smooth the velocity findings from this time period. It was important when creating the interpolation, that the data was smoothed enough so that velocity differences arising from topographic features would still register, whilst

smaller scale changes were completely smoothed so that residuals would still be picked up upon comparison of the interpolation to other velocity outputs.

Figure 2.47 shows a 2D model of baseline and interpolated (smoothed) velocities along the central flow line. The resulting smoothed ice flow velocity map along with the velocities between the two orthomosaic pairs can be seen in Figure 2.48. The two periods used for the baseline occur exactly one year apart and by averaging these velocities a more reliable estimate of conditions at the end of the melt season can be obtained. The velocity findings over the wintertime period (6th September – 5th July) were not chosen as a baseline due to there being much higher signal noise over this time leading to less clear data trends and a smaller area that could be sampled using COSI-Corr. The velocity of the two orthomosaic pairs does vary somewhat with 2016 velocities visibly higher than 2017, likely due to average temperatures being 1.76°C warmer (6.06°C vs 4.29°C) and average discharge being 2.83 m^3 s (5.67 m^3/s vs 2.84 m^3/s) higher in 2016 (Meteoblue, 2018).

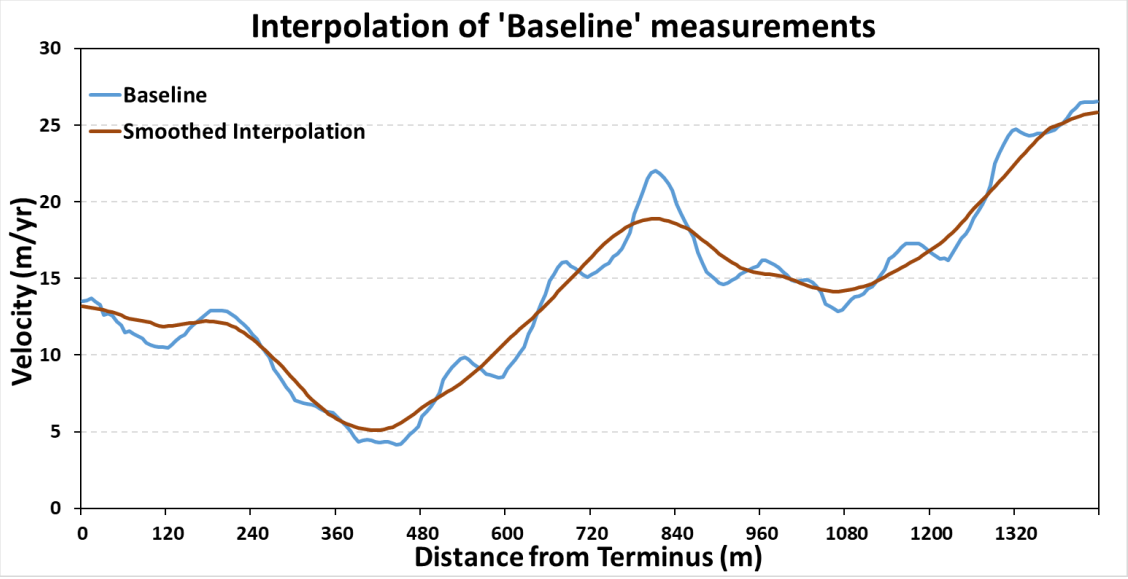

Figure 2.47: *Smoothing of baseline velocities.*

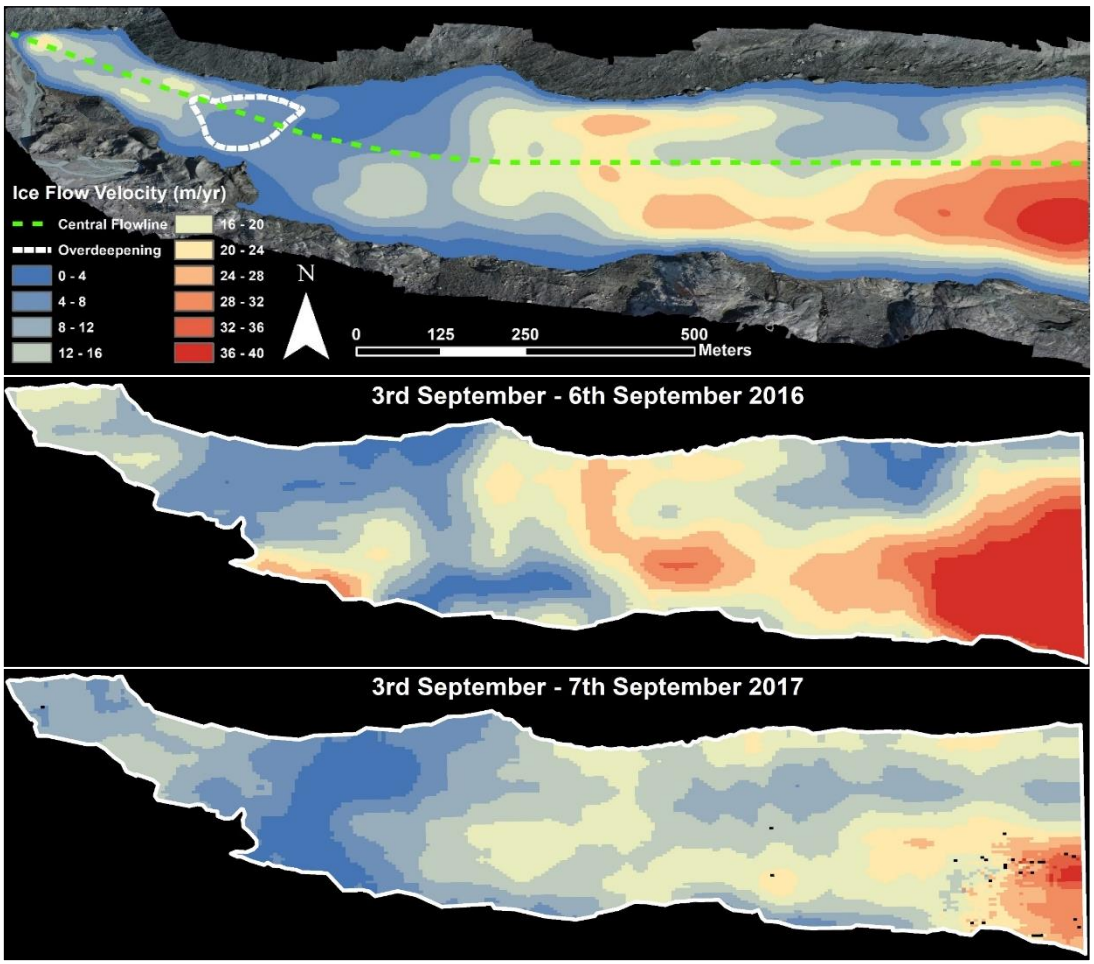

Figure 2.48: *Interpolated/smoothed baseline of glacier velocities (top) made from averaging velocities of two late melt season periods a year apart (middle and bottom).*

2.7 SUMMARY OF METHODOLOGY

This chapter has discussed the various methods by which data has been gathered and processed. Firstly, the identification of a suitable field site for study where overdeepenings were present and an in-depth look at that site, its history and features.

GPR data has been collected in both February and July 2017 to establish the bedrock topography, and more specifically the location of overdeepenings beneath the ice as well as

features within the ice. 27 transects spanning the bottom 1.5 km of Findelengletscher have been collected and these will be further examined and interpreted in Chapter 3.

UAV flights have been carried out over the course of 3 separate fieldwork to obtain high-resolution orthomosaics and DEMs of the Findelengletscher terminus over nine time periods from 2016 and 2017. This data has enabled the examination of ice flow velocities and ice loss across the field site both spatially and temporally which will be covered in Chapter 4 and 5 respectively.

The combination of a topographic model of the bedrock along with a DEM of the ice surface can help our understanding of how glaciological processes have shaped the bed.

3. BASAL TOPOGRAPHY AND PROCESSES AT FINDELENGLETSCHER

3.1 CHAPTER OVERVIEW

This chapter will develop the results of the GPR work outlined in Chapter 2 to (a) produce a digital model of the ice-bed interface that is necessary to support the interpretation of ice flow patterns at Findelengletscher (see Chapter 4 & 5) and (b) investigate ice-bed form and process. The latter will be achieved through analysis and interpretation of bed morphological characteristics (including ice-surface to ice-bed gradient ratio), predicted pathways of subglacial water flow, and basal and internal GPR reflector characteristics. The reflector patterns obtained through fieldwork, and their characteristics, permit insight into bed properties, drainage system characteristics, and ice structure that influence glacier flow, hydrology, and sediment transport processes. When combined with an accurate map of the topography of the ice surface, an improved knowledge of the glaciological processes that shape the bedrock can be obtained (Magnússon *et al*., 2017).

In brief, this chapter will show how GPR techniques can be utilised to analyse the bedrock topography and glacial features as well as the hydrological flow pathways occurring beneath the glacier. A simple diagram showing the multifaceted inter-reliability of these factors can be seen in Figure 3.1. The more these three factors agree with each other the stronger the case that estimated glacial conditions are correct. For example, the GPR traces are used to

create the bed model, which is used to create estimated hydrological flow pathways, this in turn can be used to support GPR data when looking more closely at specific features within or beneath the ice such as subglacial/englacial channels.

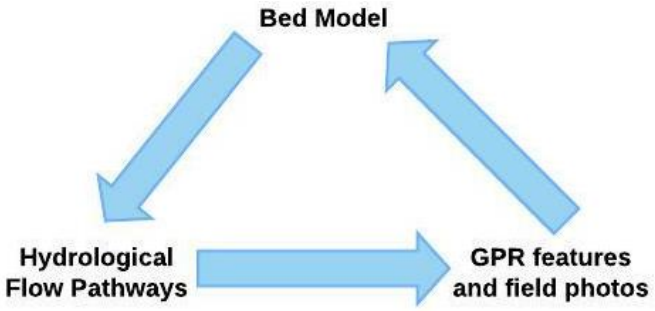

Figure 3.1*: Multi-faceted approach undertaken in this chapter to understand glacial conditions at Findelengletscher.*

3.1.1 Importance of understanding basal topography

Techniques such as dye tracing, the use of boreholes and basal sediment discharge enables inference of hydrological, erosional, and depositional conditions beneath glaciers (Gordon *et al*., 1998; Swift *et al*., 2021) however a lot of work on the subject remains theoretical (Hubbard *et al*., 1998; Carlson *et al*., 2007; Beaud *et al*., 2018) and observations from real glacier beds are needed to validate them. These boundary conditions have an influence on the local direction and velocity of ice flow, the rate of basal sliding and basal water pressures (Kamb, 1987; Rignot *et al*., 2011; Gong *et al*., 2017). Inversely the conditions which are more easily measurable such as surface elevation, ice flow velocities and bedrock topography are used in models to infer boundary conditions such as basal friction, sliding and water pressures (Joughin *et al*., 2010; Lee *et al*., 2015; Gong *et al*., 2017). Placing reasonable constraints on ice-bed morphology permits temporal and spatial patterns of ice flow and the processes

responsible to be better understood. For example, by comparing the gradient of the ice-bed interface to that of the ice-air interface we can determine whether conditions are favourable for changes in subglacial drainage that lead to sediment deposition or subglacial water ponding (see Section 1.4.4).

Study of basal topography also permits conclusions to be drawn regarding the processes and patterns of glacial erosion (Hall & Glasser, 2003; Pedersen *et al*. 2014; Patton *et al*. 2015) and this too has wide relevance. For example, many countries worldwide are seeking to identify sites for long-term storage of radioactive waste in geological (i.e., underground) repositories, for which the depth and pattern of bedrock erosion under future glacial conditions is a first-order concern (Shilts, 1984; Werder, 2016; Claesson Liljedahl *et al*., 2016). Understanding of basal topography and the effects of sediment evacuation rates is also important for hydroelectric companies that need to manage the infill of reservoirs by sediment influx and the potential for damage to turbines as a result of this (Winkler, 2014; Felix *et al*., 2016). Furthermore, the potential for new lakes left by retreating glaciers is also of importance to hydropower companies and their planning of future projects (Linsbauer *et al*., 2012; Haeberli *et al*., 2016; Farinotti *et al*., 2019). Indeed, Farinotti *et al. (*2019) suggest that in Switzerland, three quarters of the storage area potential for hydropower could become ice-free by 2050. Another example of the need to understand the location and nature of bedrock topography and erosion is to help predict and mitigate flood risk to downstream settlements from new lakes that form within glacially eroded bedrock basins as mountain glaciers undergo retreat (Frey et al. 2010; Haeberli et al. 2016). The risk of glacial lake outburst floods (GLOF) is significant in mountainous environments where glaciers are receding and down-wasting (Harrison *et al*. 2018) which is the trend for most of the Alps, Himalayas and Andes (Linsbauer

et al. 2016). Cathala *et al*. (2021) suggests that overdeepenings specifically can provoke catastrophic GLOF hazards.

As mentioned in Section 1.4.2.2, basal topography affects drainage characteristics (Rippin *et al*., 2003). For example, adverse slopes cause significant lateral diversions of meltwater (Sharp, 2006) within the drainage system which may divert subglacial meltwater into englacial channels (Hooke et al. 1989; Clason *et al*.,2015). In a secondary way basal topography can cause localised surface crevassing (McGrath, 2012) which can directly affect how and where initially supraglacial meltwater travels, either supraglacially, englacially or subglacially. The localised crevassing funnels surface meltwater quickly to the bed in concentrated areas (Röthlisberger, 1972; Hooke, 1991), discussed previously in Section 1.2.1.1. Rippin *et al*. (2003) suggests that the effects of bed topography on drainage patterns increases where decreasing water pressure occurs. Therefore, at periods of decreasing melt the bed topography plays a more significant role in the shaping of drainage patterns and routing.

3.1.2 Structure of chapter

Section 3.2 presents the results of the GPR fieldwork from both the February and July surveys and the bed models that were derived from these. Several possible models were produced. The models are compared to the results of a previous survey by Feiger *et al.* (2018) to (a) check model validity and (b) establish any areas of bed change that may be revealing of basal processes. Section 3.3 will take a closer look to determine the nature of specific reflectors within and beneath the ice that may provide clues about the nature of meltwater movement within the system. Section 3.4 will focus on the interpretation of the findings from the previous two sections, as well as calculating subglacial drainage pathways based on the bedrock topography. Section 3.5 examines ice loss both seasonally and annually across the

glacier terminus and compares this with the bedrock morphology of Findelengletscher and inferred drainage pathways. Finally, Section 3.6 will provide a summary of the key findings from this chapter.

3.2 BED TOPOGAPHY MODELS

The inherent inaccessibility of glacier beds (Brædstrup *et al*., 2016; Zhan, 2019; Steinemann *et al*., 2020) means GPR methods are commonly used to define the depth to bedrock and discern basal and internal ice characteristics (Garambois *et al*., 2016; Grab *et al*., 2021). Bedrock reflectors picked from a network of intersecting GPR transects can be amalgamated to produce a net of empirically known bed points that, using interpolation, can be used to produce a complete bed model (Langhammer *et al*., 2019). The following (sections 3.2.1 to 3.2.3) detail the results of the two GPR surveys at Findelengletscher in February and July 2017 (see Section 2.3.2) and compare the finished models with previous work (Fieger *et al*., 2018; Grab *et al*., 2021).

3.2.1 Model creation

3.2.1.1 Overview

In order to create a DEM of bedrock topography it is important to first locate the boundaries of the glacier. Here, the ice thickness is regarded as '0' and this forms an outline to the model. Ice thickness estimates from GPR transects in tandem with GPS recordings of these traces subtracted from ice surface DEMs (Lamsters *et al*., 2020, Grab *et al*., 2021) are input into the model so that all three dimensions can be mapped as point data. All points (including subglacial bedrock and boundary markers) are fitted to a smoothing spline (Egli *et al*., 2021) using a radial base function (RBF) which appeared to offer the most accurate representation

of the bed. RBF is an exact interpolation technique whereby the surface must pass through measured sample points, it predicts the values of the space between sample points in order to create a suitable estimate of topography for areas of the glacier not surveyed directly with GPR (i.e., crevassed or overly steep, dangerous areas). The more transects available (and therefore the more data points) the more accurate and higher resolution the data will be due to more resolved detail being captured.

Because bedrock erosion is relatively slow, meaning actual bed elevation change between February and July 2017 is likely to be insignificant relative to the uncertainties in estimating the exact depth of bedrock, estimates of the glacier bed from different time periods can be combined to provide a larger sample of transects and therefore a more accurate estimate of the glacier bed model. Nonetheless, erosion or redistribution of sediment (rather than bedrock), especially by subglacial fluvial processes, will have some effect. Zechmann *et al.* (2021) found sediment redistribution levels at Taku Glacier, Alaska to be 2.8 ± 0.9 m a^{-1} and 2.9 ± 0.9 m a^{-1} in 2003 and 2015 respectively. Therefore, it is necessary to carefully interpret areas of change for possible insight into subglacial processes such as seasonally changing englacial conduits (Church *et al*., 2020).

3.2.1.2 Glacier outline delineation

It is often difficult to locate the boundaries of a glacier (Shulka *et al*., 2010), especially when large amounts of sediment and debris can obscure the underlying ice and therefore the specific spectral signature, which leads to errors in automated digitisation (Bolch *et al*., 2010; Burns & Nolin, 2014). Findelengletscher was no exception in this regard, with sediment covering overlying ice to the true north lateral of the glacier as well as to the south of the terminus (Figure 3.2). The outline as estimated by Swisstopo (2018) is shown in Figure 3.2 and

varies considerably from what can be seen and manually or automatically digitised from remote sensing imagery. The estimated extent of the ice is important as depth is considered to be greater the wider the glacier with the thickest ice close to the centreline. For example, many glacier models use glacier extent as a criterion for estimating the bed topography (Farinotti *et al*., 2009a; Paul & Linsbauer, 2012; Maanya *et al*., 2016). As GPR depth measurements give only a one-dimensional transect of the glacier, finding the true border of the glacier is important as this can be assumed as having an ice depth of '0' and data can be smoothed from this point to GPR traced ice depths. From carrying out ground truthing of the field site, the Swisstopo (2018) boundaries are considered to be most accurate. These debris covered areas were delineated by field inspection, analysing the UAV imagery, and using contour maps to see where significant changes in topography are as these tended to guide the location of the extent of the northern lateral border. Where GPR traces exist that suggest that ice thickness tends towards '0' at non-debris covered margins, the glacier will be considered to end at these margins. In this way it is hoped that the most accurate estimate of the current glacier boundaries will be presented. Given the width of the glacier including debris covered ice, the central flowline for Findelengletscher is likely further north than it would appear from the just the debris free area.

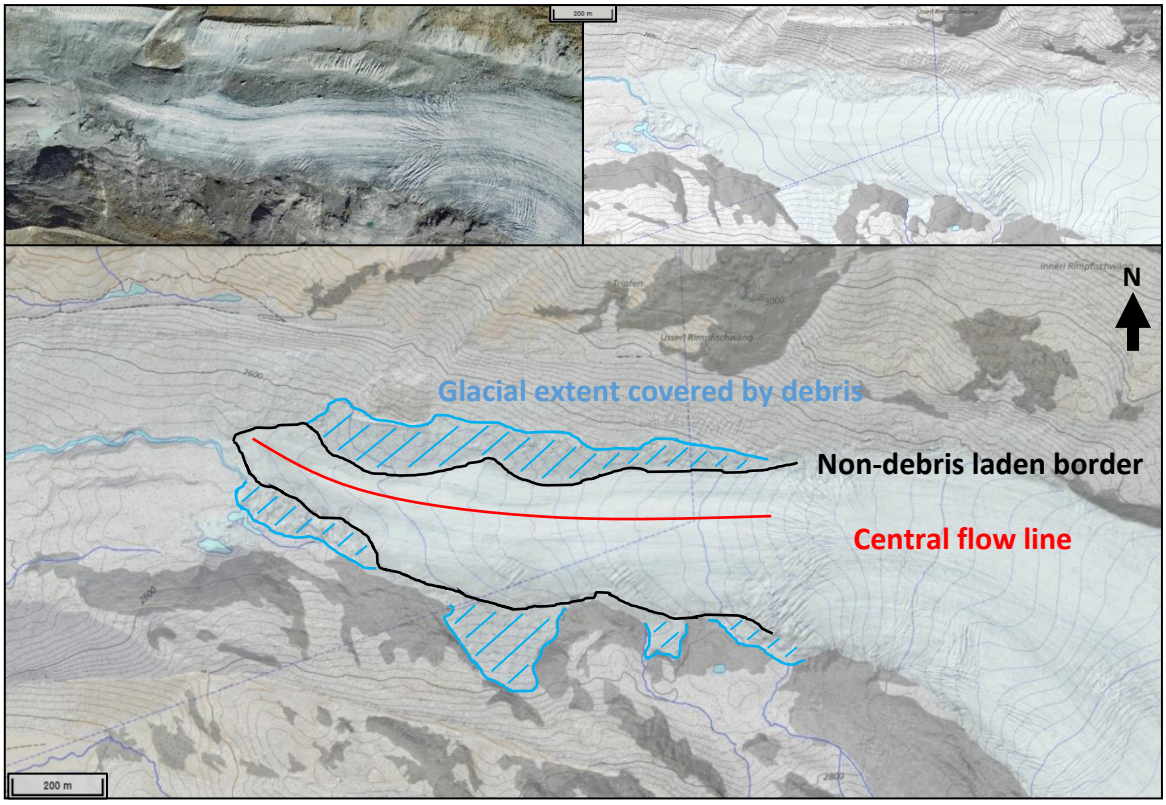

Figure 3.2: *Differences in estimating glacier boundaries for Findelengletscher. Top Left: satellite image (Google Maps, 2018). Top Right: Map SwissTLM (Swisstopo, 2018). Bottom: both overlaid and annotated to show difference in boundaries, black line represents visible boundary, blue areas represent sediment laden dead ice. Red line represents the estimated central flow line.*

Feiger *et al.* (2018) appears to have taken the debris-free ice to be the full extent of the glacier and therefore discrepancies at the margins of the Fieger *et al.* (2018) model relative to the models produced for this work are anticipated. Figure 3.3 shows the bedrock estimate of Feiger *et al.* (2018) with 10 m contours lining up with the non-debris covered glacier outline, particularly noticeable by the steep increase in ice depth on the true north margin of the glacier. It should be noted that this estimate covered the entire glacier rather than just the terminus and had a resolution of ~25 m. Based on data from Swisstopo (2018) and ground-truthed field site observations, the glacial margins are outlined based on Figure 3.4.

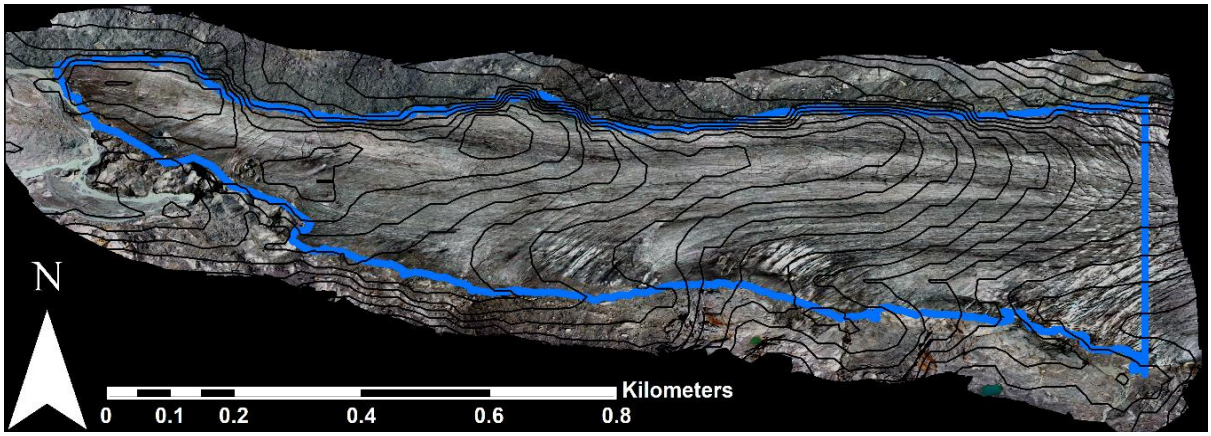

Figure 3.3: *Feiger et al. (2018) bedrock topography estimate, 10 m contours overlaid on UAV derived image of Findelengletscher (5th July 2017), non-debris covered glacier outline shown in blue.*

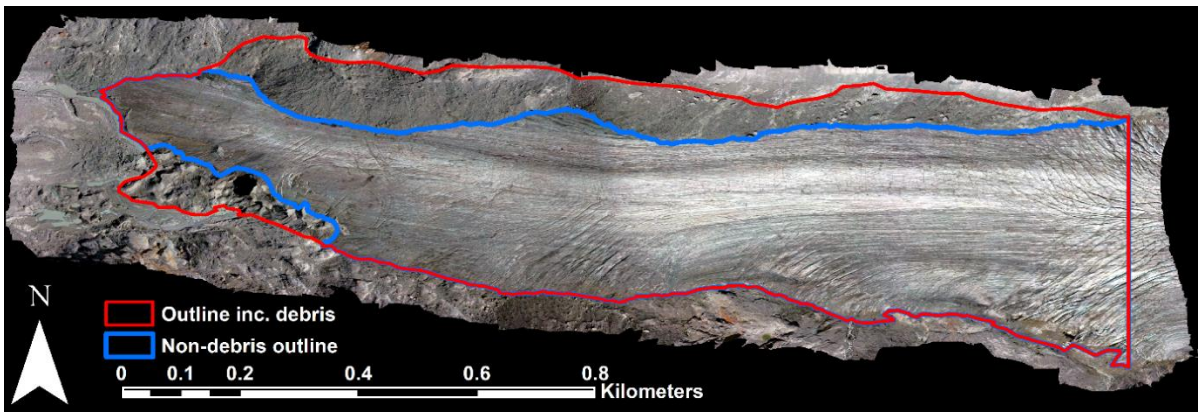

Figure 3.4: *Outline of the terminus of Findelengletscher for clear ice and overlying debris-covered ice overlain on orthomosaic image taken on 27th August 2016.*

3.2.2 Results (Models A to D)

During the July 2017 fieldwork 12 suitable transects were recorded (see Section 2.3.2.3). As expected from these transects, ice depths are shallower at the margins of the glacier with greatest depths towards the centre (Figure 3.5). However, towards the southwest of the glacier, depth gradients are much shallower. Figure 3.5 serves to give an overview of the bedrock depth observed from the GPR analysis before a bedrock mask was fitted

encompassing all bed observations. However, many other features were observed from the traces not related to bed depth. These will be discussed in more detail later in Section 3.3.

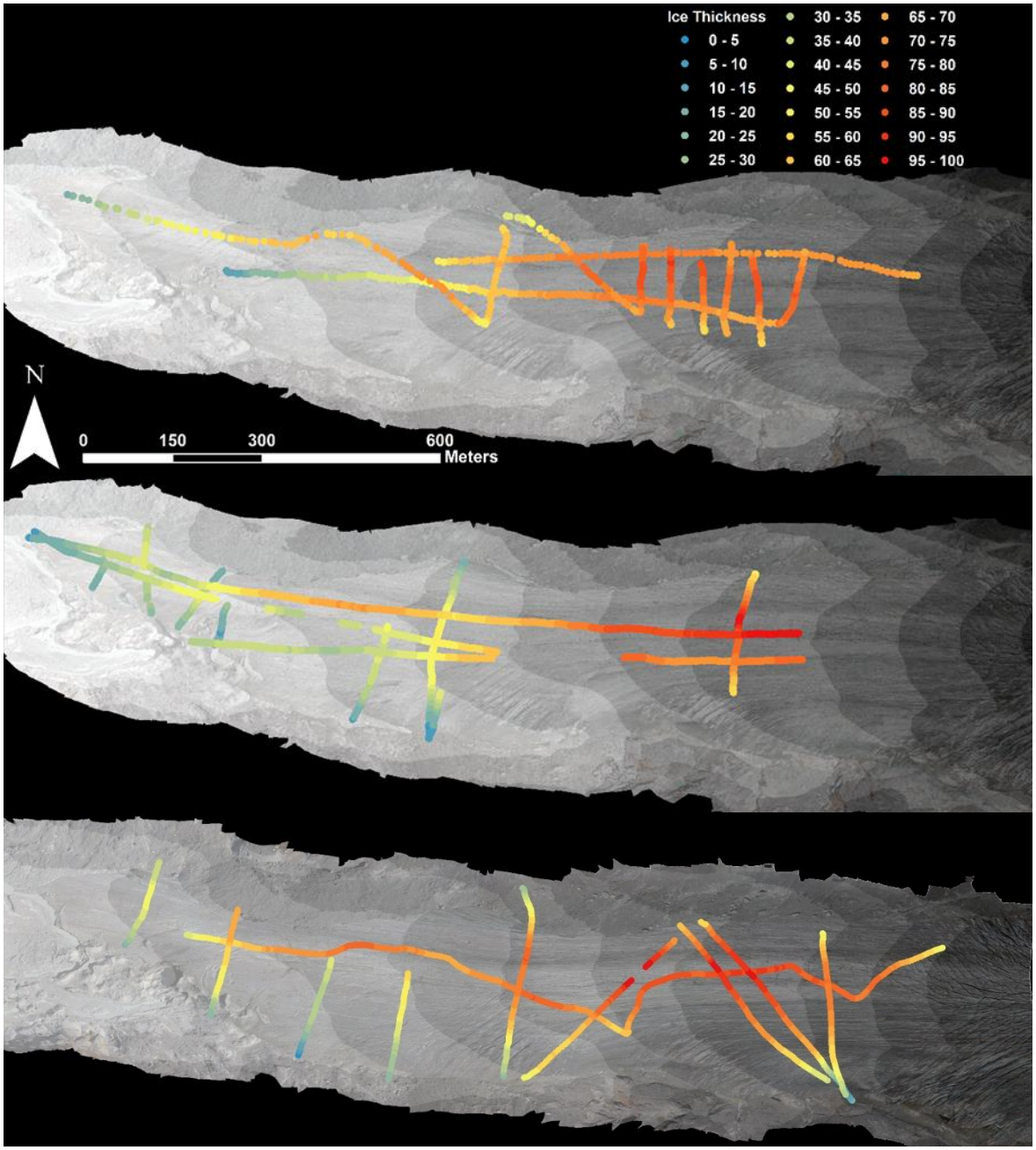

Figure 3.5: *Map of the February 2017 (top), July 2017 (middle) and VAW April 2015 (bottom) GPR transects showing ice thickness where a clear bed reflector could be obtained (altitude of DEM minus altitude of bedrock). DEM of the ice surface in greyscale at 20 m intervals from 5th July 2017.*

Four models were created based on the depth of bed traces from various combinations of the February, July and VAW (2015) field data (Table 3.14, Figure 3.6). These four models varied slightly in their approximation of the bed. Importantly however, when used later in this chapter (Section 3.4.3.1) to show hydrological flow paths there was a strong agreement between them. The bed masks were further smoothed using a focal statistics filter. Figure 3.7 shows this model overlaid with contours every 2 m. The resolution of the bed models is 16 cm, the same as the DEM of the ice surface as mentioned in Section 2.4.4.3.

An overdeepening at the terminus is suggested by the bed models. This is in keeping with previous works which also suggested an overdeepening in this area (Iken & Bindschadler, 1986; Haeberli *et al.,* 2013). The central flow line, likely to correlate with the deepest longitudinal bed, flows along the north edge of the glacier's clear ice but near the centre (as is more typical) of the glacier when the debris rich dead ice is considered (as mentioned in Section 3.2.1.2.

Table 3.1: *Descriptions of the various bed models generated*

Model Name	Description
Bed Model A	Radial Base Function of February and July transects approximating the bed between clear reflectors.
Bed Model B	Radial Base Function of February and July transects combined using only clear bed reflectors.
Bed Model C	Radial Base Function of February, July, and April 2015 (VAW) transects using only the points where transects cross with a similar bed depth (<5 m).

Bed Model D	Radial Base Function of February, July, and April 2015 (VAW) transects combined using only clear bed reflectors.
Feiger *et al*. (2018)	Bed calculated from GPR data from surveys conducted April 2015, interpolated by the ice thickness estimation model (ITEM) (Farinotti et al. 2009a) and smoothed by the minimum-curvature method (Briggs, 1974). The DEM was from Swisstopo (2016).
Grab *et al*. (2021)	DEM acquired through the 2019 release of swissALTI3D (Swisstopo, 2019). Ice thickness obtained through GlaThiDa (GlaThiDa consortium, 2019). Results from a glacier thickness algorithm (GlaTE) and ice thickness and volume estimation method observation-based (ITVEO) were averaged to provide a bed estimate with resolution of 10 m.

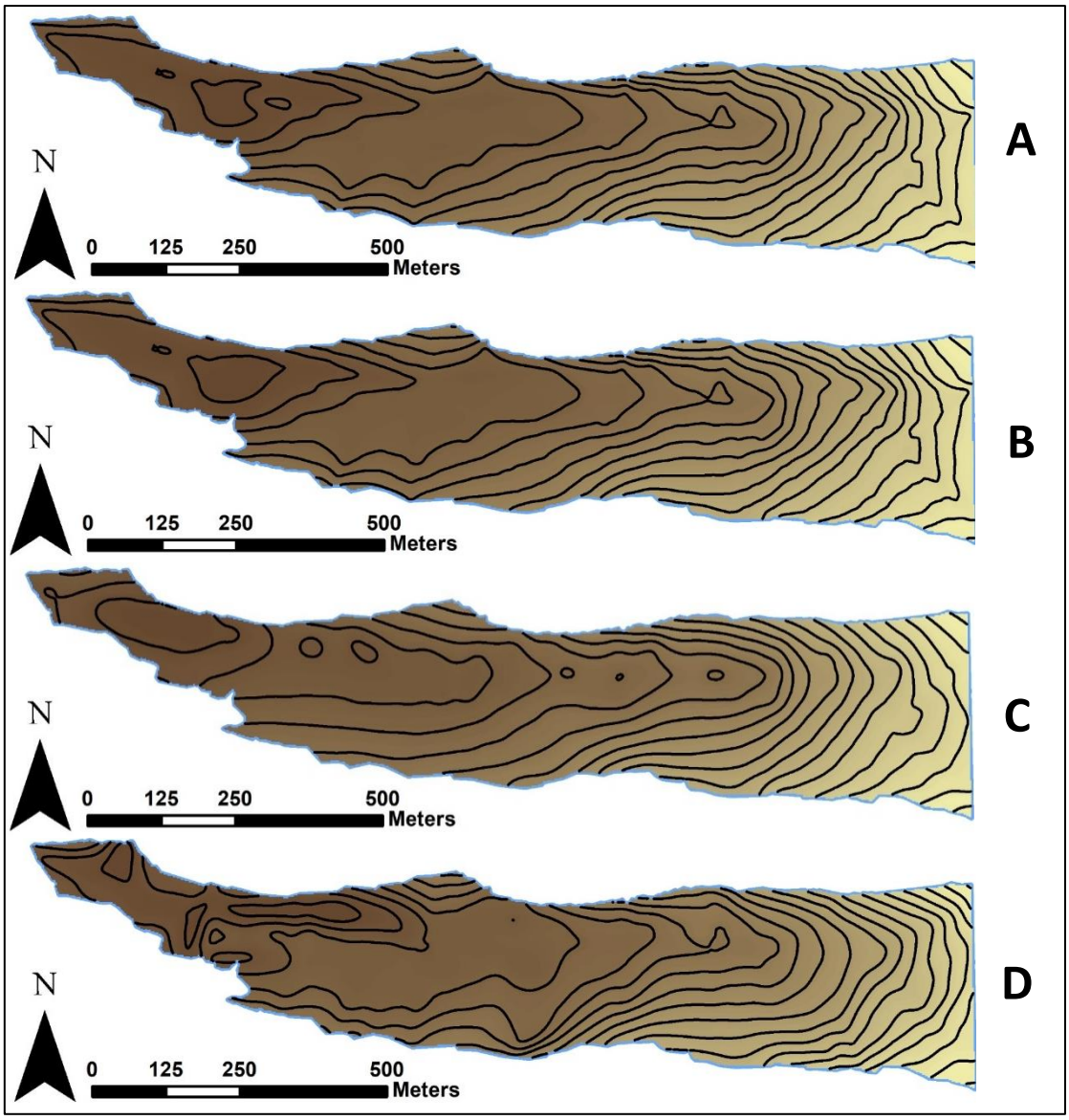

Figure 3.6: *Four bed models of Findelengletscher, created via Radial Base Function with contours every 10 m. (See Table 3.14 for a description of how each was derived)*

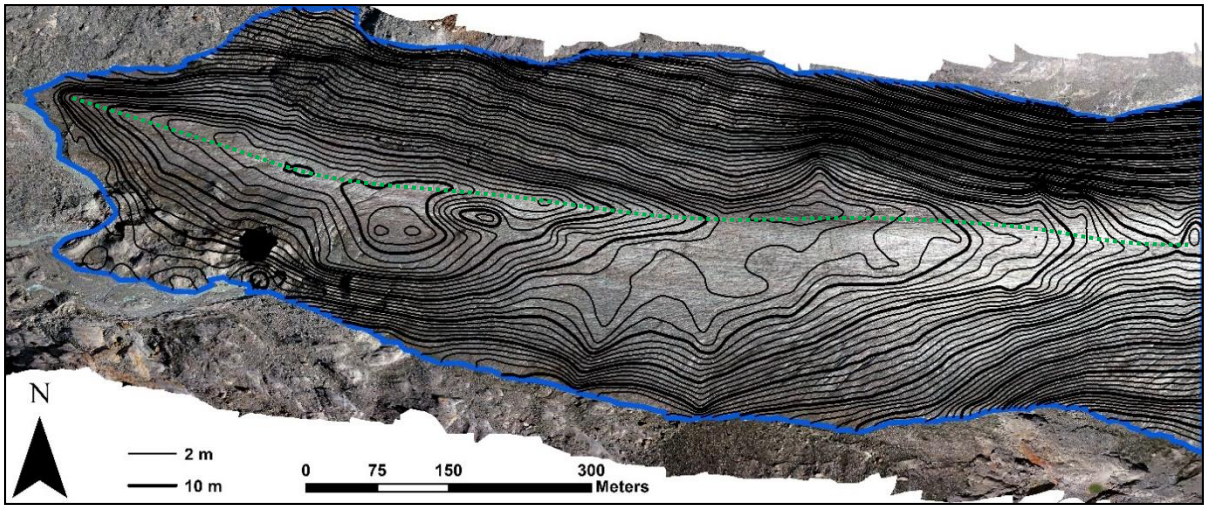

Figure 3.7: *A Radial Base Function calculation of the bed topography (Bed Model A) of Findelengletscher. An estimated flow line based on maximum longitudinal depth is depicted by a green dashed line.*

3.2.3 Model intercomparison results

A comparison of the four models created from smoothing the transects can be made to show variations in results. The models of Feiger *et al.* (2018) and Grab *et al.* (2021) will also be compared to show which areas are in agreement and which areas differ. Figure 3.6 shows the differences between the four models (see Table 3.1). The difference between Bed Model A and B are small, with only a modest area close to the overdeepening changing, as can be seen in Figure 3.8. A protrusion of ~12 m is present in Bed Model A, but not B. It is likely here, that a strong englacial reflector has been mistaken for part of the bed topography, this is likely to happen more in this model when effectively guessing between different reflectors as to which is the bed when the trace is not clear. It is believed that fewer, more certain reflectors led to better results, although this mentioned artifact was the only clear difference between Bed Models A and B after the masks were smoothed. Bed Model C shows a series of 'bullet hole' shapes (Figure 3.6, Figure 3.8), likely owing to the sparsity of reflectors when only using

intersecting points from a combination of three surveys (see Table 3.1). Bed Model D shows a similar 'lumpy' appearance to the bed at the terminus, likely due to variations in depth between surveys within a small area. The combination of three different GPR surveys using two different DEMs across more than two years led to some contradicting depth estimates and ultimately Bed Model B was preferred. In subtracting Bed Model D from Bed Model B, it can be seen that a considerable slope of ~25 m is present at the location of the collapsed cauldron, close to the main portal. This is seen in Figure 3.8 where blue (bed estimate of D at a higher altitude than B) and red (bed estimate of B at a higher altitude than D) areas appear very close to each other. The fact that this occurs at a cauldron feature is useful for two reasons. Firstly, the bed could be seen at the collapse, and it was evident that such a slope did not exist. Secondly it would suggest that this cauldron feature was the cause of the erroneous bed estimate at from the VAW (2015) data as the inclusion of this is the only difference between Bed Models B and D.

The Bed Models (A-D) were compared to that of Feiger *et al.* (2018) and Grab *et al.* (2021) which can be seen in Figure 3.9. The location of the overdeepening does vary between this study's findings and previous published work. From contour analysis method for identifying overdeepenings found in Patton et al. (2015), where a contour has 90% the length of the preceding contour, an overdeepening's boundaries could be more concisely predicted. Much of Patton's methodology could not be applied to this specific site due to the overdeepening exclusion parameters of this study being ice-sheet scale rather than valley glacier. However, the contour analysis and elongation with respect to ice flow direction could be applied.

Figure 3.10 shows 1 m contours of each overdeepening with the outer extent defined by the contour analysis method of Patton et al. (2015) with all overdeepenings showing an

elongation in line with glacier flow. This way an example of the difference overdeepening estimation between models can be seen. The important point to note here is that whilst there is a small discrepancy as to pinpointing the exact location of the overdeepening, all three models do find an overdeepening to be present, and within an area of ~200 m. When deciding upon a model to base findings on going forwards, it was considered that Bed Model B offered the most suitable results due to its similarity with that of previously published work and smoother, undulating topographies expected of an "ideal glacier" (Nye, 1951) rather than the sharp relief noticeable in Bed Masks A, C and D. It should be noted at this stage that there is a high level of error (~5 m) from the GPR surveys when compared to the size of the overdeepening. However, the Grab *et al.* (2021) and Feiger *et al.* (2018) models do not accurately appraise the northern lateral extent of the glacier leading to errors too. GPR data from the terminus of Findelengletscher for Grab *et al.*, (2021) consisted of two transects (Figure 3.9) and were not considered to be high resolution enough to accurately capture the outline of shape of the overdeepening. Feiger et al., (2018) data consisted of more GPR transects, however as mentioned, the glacier extents were not accurately estimated. Furthermore, the transect that crosses the cauldron near the portal suggested bed altitudes of 2524 m whilst the altitude at the main egress portal, a short distance away was 2611 m. It seemed highly unlikely that an adverse slope of 87m is present between these two locations. This is the same transect that caused the very lumpy area alluded to in Figure 3.6D. The overdeepening present in Feiger *et al*., (2018) is also present in Bed Model D, however as they both use the same bed data here and this immediate area is not covered clearly from transects in February and July surveys, this similarity is to be expected.

It is believed therefore, that the three overdeepenings highlighted in Figure 3.10 are not separate overdeepenings, rather the same overdeepening that has not been clearly defined,

in the case of Grab *et al*., (2021) due to limited GPR transects and Feiger *et al*., due to inaccuracies in the interpretation of the data. Bed Model B that has been arrived at by interpretation of a high density of GPR transects is believed to be the most accurate of the three and will be used to guide interpretations in this body of work.

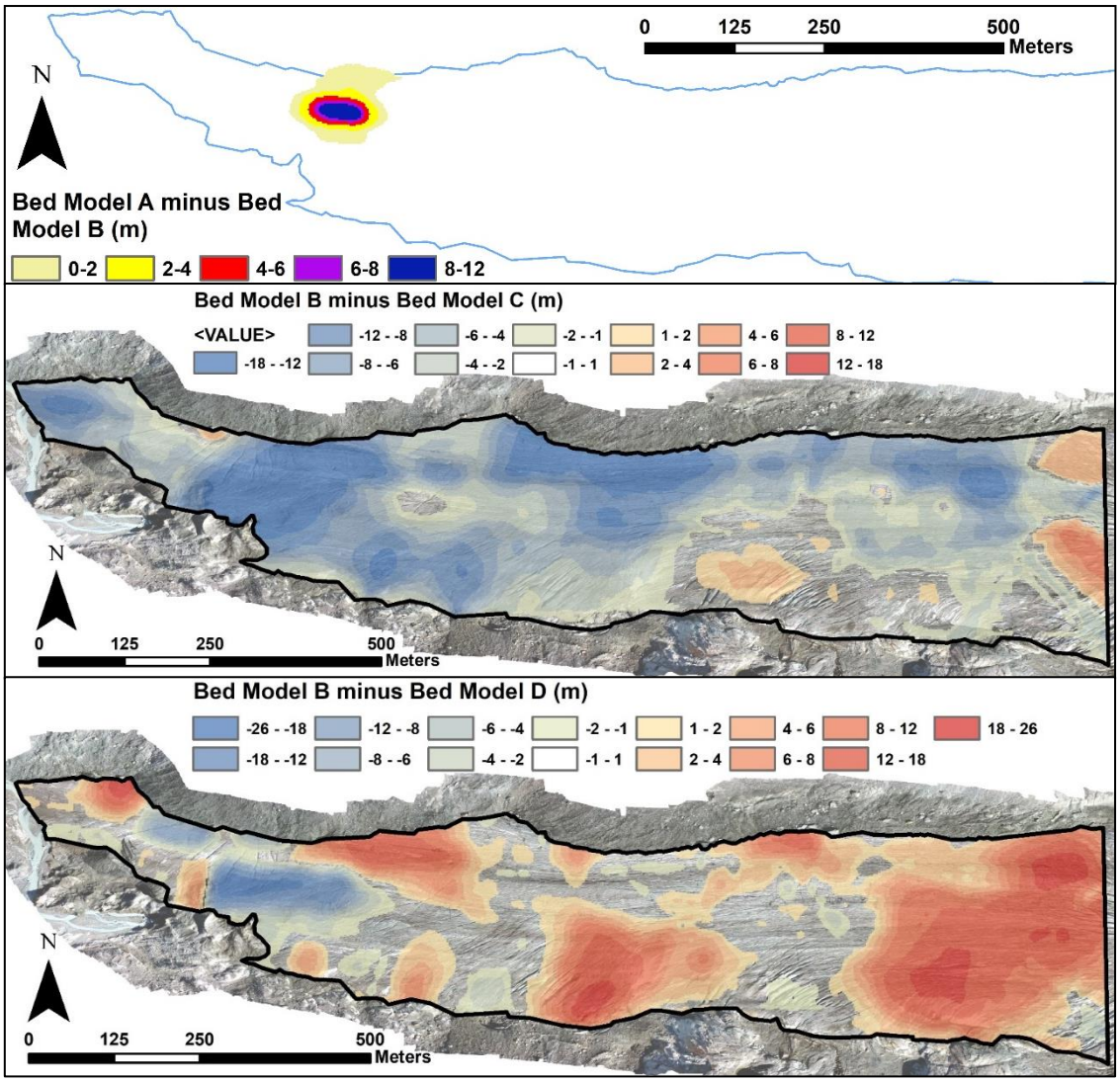

Figure 3.8: *Comparisons of differences between Bed Model B and A, C and D.*

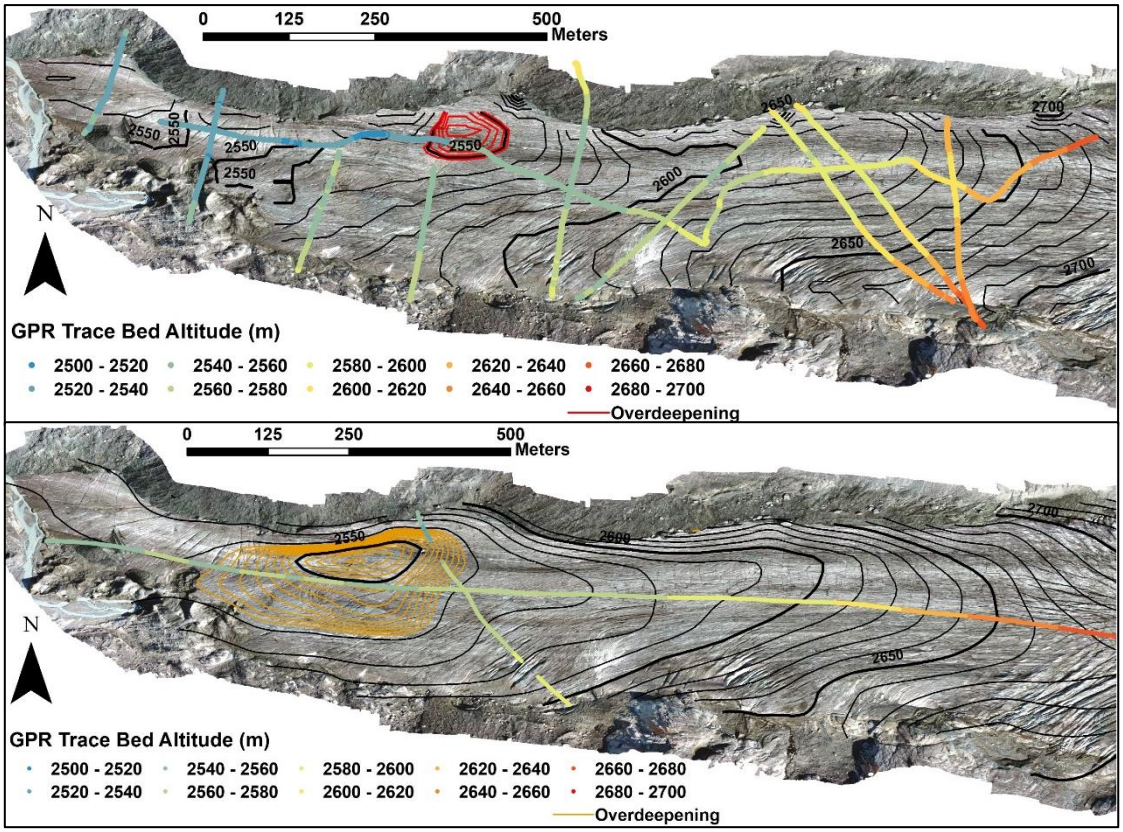

Figure 3.9: *10 m contour maps of the bed of Findelengletscher from Feiger et al. (2018) (above) and Grab et al. (2021) (below). GPR transects used in these calculations are coloured based on the altitude of bed estimates. Overdeepenings from these estimations are shown in red and orange respectively to match that of Figure 3.10.*

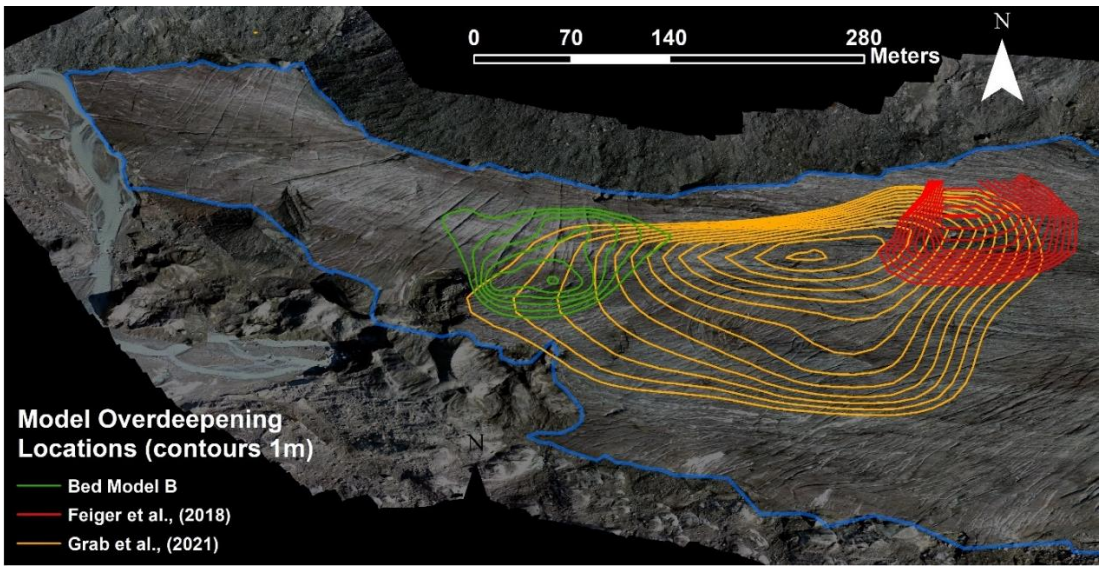

Figure 3.10: *The location of three bed model overdeepenings and estimates as to where the overdeepening is situated. Contours are every 1 metre.*

3.3 INTERNAL ICE STRUCTURE AND FEATURES DISCOVERED

3.3.1 Overview

A model for the bed topography beneath Findelengletscher has now been obtained. However, bed reflectors were not the only features of note in the trace data and a deeper examination of these and what clues they might give as to the inner workings of the hydrological system within the glacier will be covered in this section.

Touching on the interpretive GPR methods covered in Section 2.3.3.3 and 2.3.3.4, once a reflection from a known surface is identified, the polarity of this trace can be used for the identification of other reflectors by determining the dielectric constant relative to ice (Moorman & Michel 1998). This therefore can show the type of the reflector present as discussed in Section 2.3.3.3, which in the case of the terminus of glaciers is usually either air, water, or debris. Using this method, it was possible to identify various obstacles or variances englacially that could be of note. For example, hyperbola fit to a curve of 0.3 m/ns can represent a void within the ice (Murray *et al.,* 2007), (see Section 2.3.3.4) perhaps created by the closing of a crevasse. This combined with a reverse in polarity of the signal, suggesting a change in density of the strata from high (ice) to low (air) gives a strong indication that a void is present.

3.3.2 Results

The results of the GPR trace analysis are divided into categories based on their characteristics and spatial location both within the glacier, and in relation to other features. These generally fell into one of four categories: voids, subglacial channels, basal sediment, and the development of cauldrons.

3.3.2.1 Basal Ice and sediment at Findelengletscher

Above the basal layer where debris/bedrock is in contact with the bottom of the glacier, debris-rich planes are often present that extend englacially from the bed at an observed angle of 20-85° (Boulton, 1970). These englacial bands often contain basal sediment transported towards the surface at this angle. Due to the dielectric difference between this debris and the ice itself, GPR can register the angle and extent of this basal ice.

Evidence of basal ice overlaying subglacial sediment can be observed from both the February and the July 2017 GPR surveys (transects 12 & 14 respectively). Notably, both transects agree as to the depth and extent of this feature as can be seen in Figure 3.11**.** Englacial features carrying basal ice and sediment are encouraged by adverse slopes from overdeepenings (Cook & Swift, 2012). Swift *et al.* (2006) propose that, due to the high longitudinal stresses produced by the varied slope angles of overdeepenings and their inefficiency towards subglacial drainage, englacially thrusted basal sediments can occur. This is supported by Evans (2008) who suggest that the spatial relationship between the adverse slope of an overdeepening and the debris rich supraglacial ice indicates a relationship and possible operation of supercooling. Figure 3.12 shows the area where the observed basal ice band is likely to appear at the surface (indicated by the red circle) if it carries on its trajectory from where the GPR trace failed to pick it up. This image was taken in early July 2017; by September evidence of the deposited sediment was clearer (see Figure 3.13b), although slightly further up the glacier than indicated by the red circle. This is due to the surface melt. The emerging sediment deposits are at a different angle to the controlled moraine to the south which may indicate a gap in time. Looking forward to the melt season of 2019, this area is now a moraine where basal ice sediment has been deposited. The chronology of conditions at the terminus shows an agreement with the illustration from Cook & Swift (2012) in Figure 3.13a. Stranded

ice down-glacier of this debris band is ‘dead’ essentially separated from the stress gradients of the rest of the glacier.

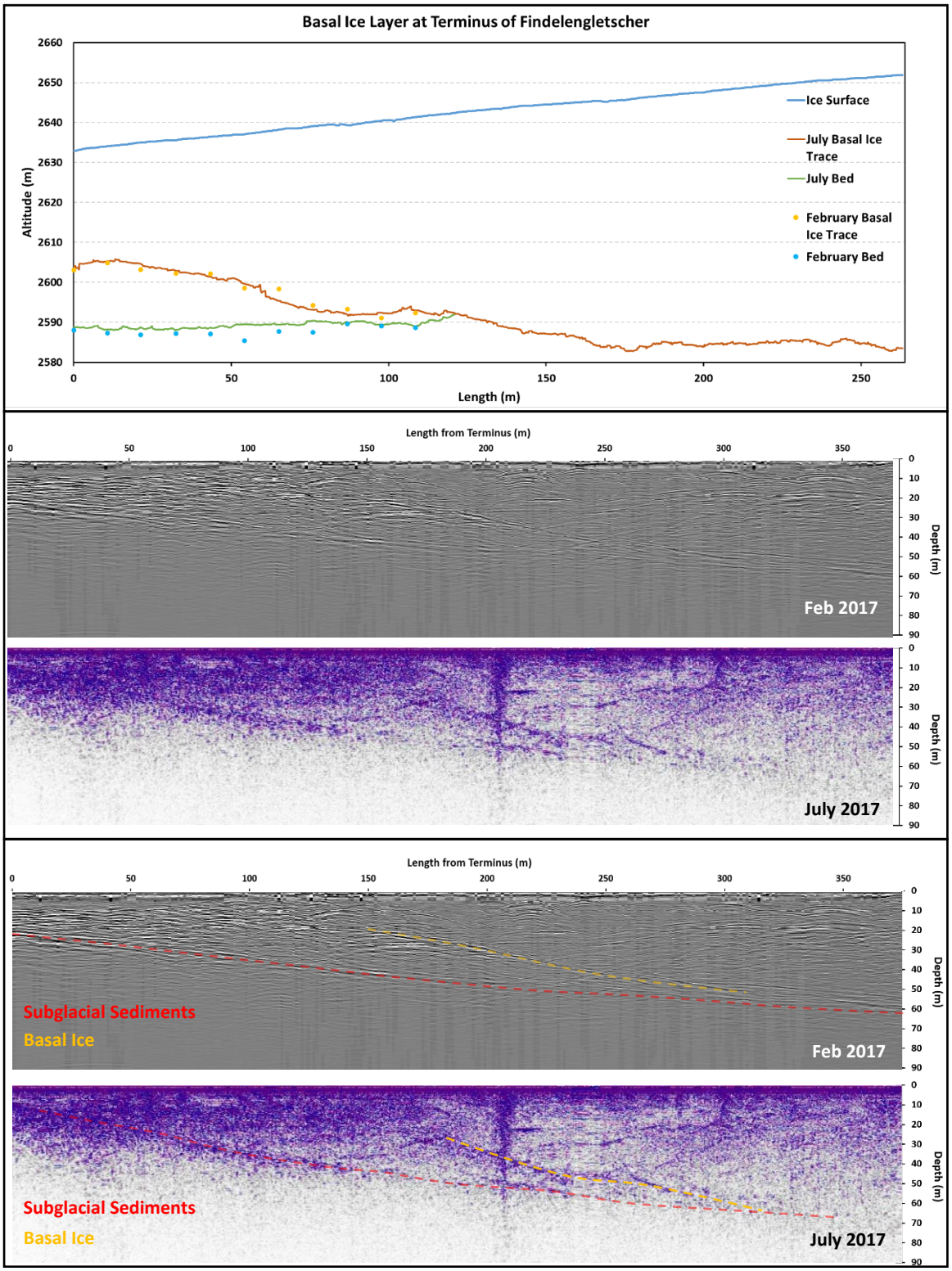

Figure 3.11*: (Top) Comparing the picked traces from the July and February GPR transects. (Middle) Unannotated view of the GPR traces with grey being February and purple being July. (Bottom) Annotation of the basal ice feature as seen using ReflexW.*

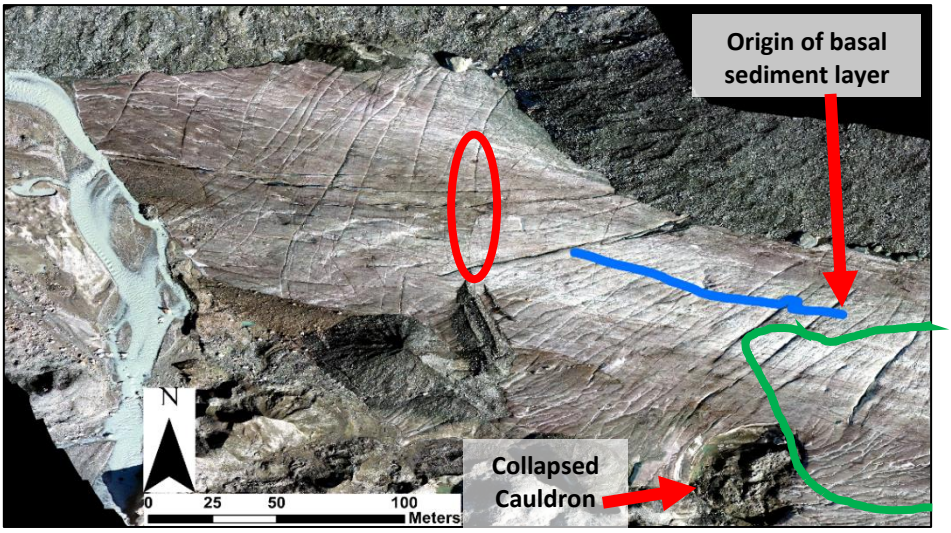

Figure 3.12: *Image of where the basal ice is expected to reach the surface if its angle up through the ice remains constant (red circle) and where the trace denoting basal ice in the transects from both February and July 2017 was recorded, with the origin point of this basal ice layer at the very edge of the image (blue line). Green light denotes the extent of the overdeepening in Figure 3.10.*

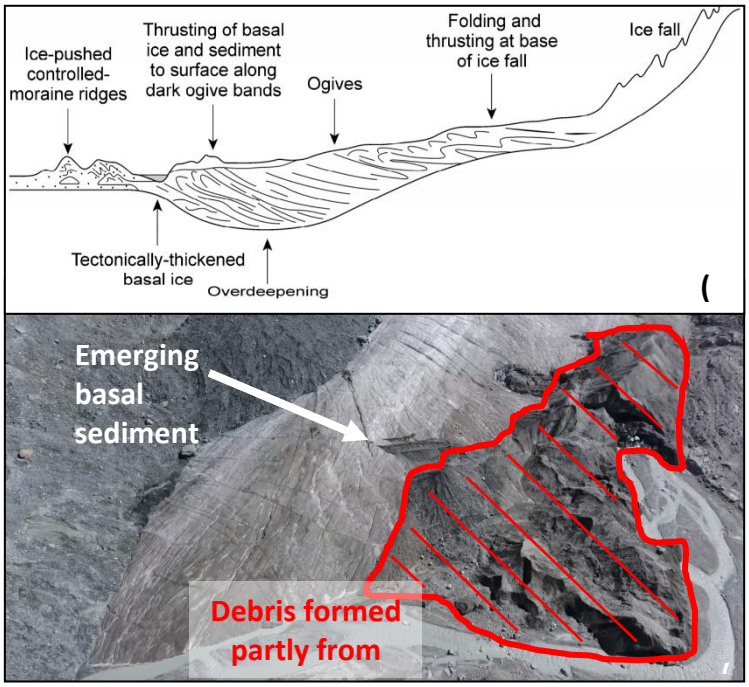

Figure 3.13: *(A) Illustration showing the formation of sediment-rich englacial thrusting and hummocky controlled-moraines at Kviárjökull, Iceland taken from Cook & Swift, 2012. (B) aerial image of Findelengletscher terminus showing debris-rich basal ice being deposited on the right side looking up glacier (image taken 7/9/17).*

3.3.2.2 Cauldrons

Across the summer melt season of 2017, two distinct cauldron features at the terminus of Findelengletscher were seen to evolve. By comparing GPR transects taken early in the season and overlaying them on late season orthomosaics various features can be recognised with hindsight. Going forward, this may help to identify and predict the development of these cauldron features before they occur. Transect 20 from 6th July fieldwork shows features believed to be sub-surface crevasses which have yet to display on the surface. However, these features can be clearly seen at the head of a developing cauldron (see Figure 3.14) in 7th September aerial imagery. This gives us a clear location of the boundaries of the cauldron forming. We can then infer back to the transect that anything occurring within the bounds of these two crevasse features is related to the development of this feature. In this case, in Figure 3.15 the near-surface crevasse features are believed to be water or sediment filled due to their small size and polarity, possibly fed from supraglacial sources. The strong reflector below these near-surface crevasse features is believed to be a large air-filled void due to its reversed polarity. Figure 3.15 shows a longitudinal transect that cuts through the location of the developing cauldron from February (Transect 2). A strong reflector is present at a similar depth as the reflector in Transect 20 highlighted in Figure 3.14 with the same polarity. This gap is likely caused by the melting and steady collapse of ice around a subglacial channel which runs through both cauldrons (highlighted further in 3.4.1). The volume of sediment and water at this location obscures a clear bed reflector beneath.

Cauldrons appear to present themselves along the line of the estimated subglacial flow path Figure 3.16. Here the collapsed cauldron (‘2016’) is apparent, the cauldrons that began developing in 2017 are labelled as such. The 2018 shows the location where significant collapse has occurred also.

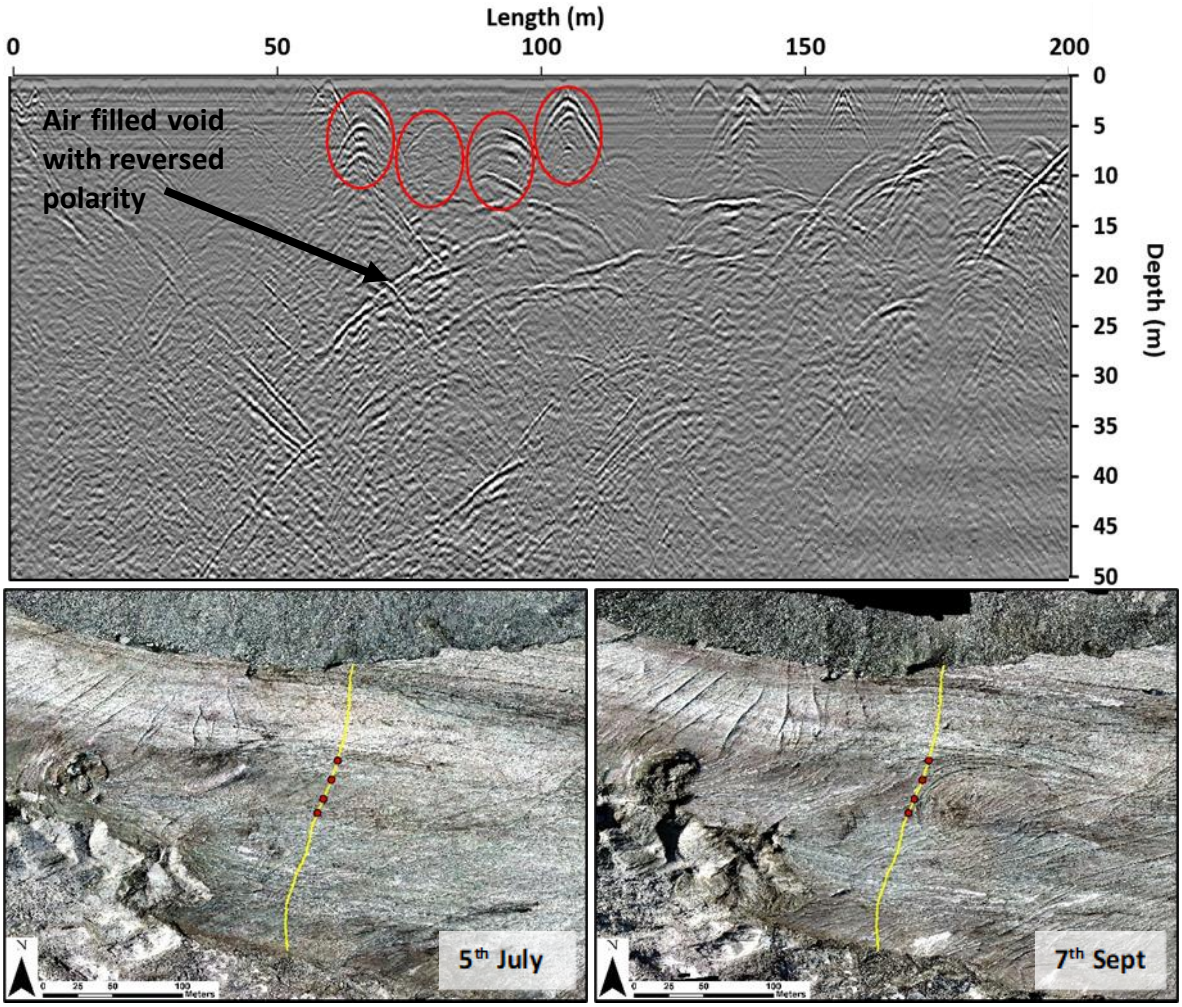

Figure 3.14*: Above) Transect 20 (taken on 6th July 2017) showing various near surface crevasse features highlighted in red. Below) location of the transect and features on the glacier for two different time periods over the course of the melt season.*

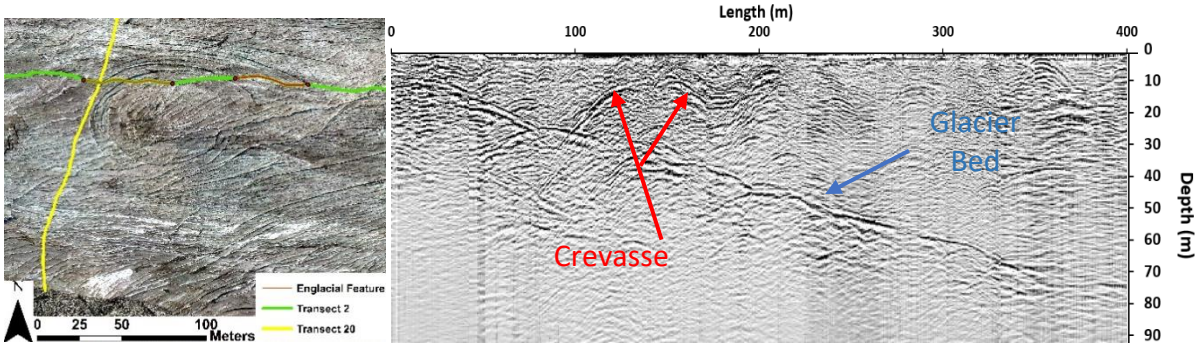

Figure 3.15*: Left: Transect 2 & 20 transects overlain over a cauldron feature from an orthomosaic dated 7th September 2017. Right: ReflexW GPR for Transect 2 taken in February showing crevasse features of the cauldron prior to surface crevassing occurring.*

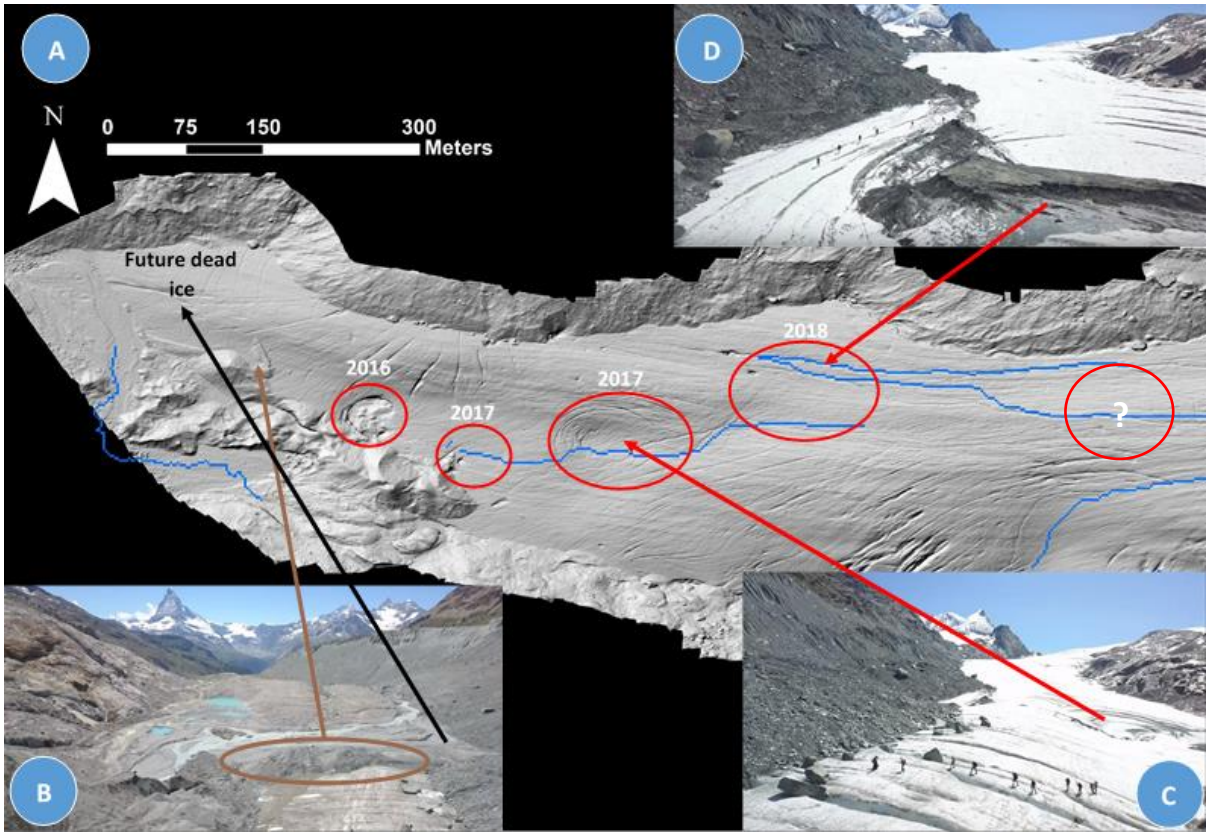

Figure 3.16: *A) Hillshade of 7th September 2017 DEM annotated showing estimated subglacial flow path (see Chapter 3.4.1) and cauldron locations. The date refers to when crevasses were first noted to form rather than the collapse. B) Image from summer 2019 showing sediment moraine. C & D) Field images showing collapse of cauldrons. N.B. Images B-D taken from https://www.youtube.com/watch?v=KqYxjEGoc78*

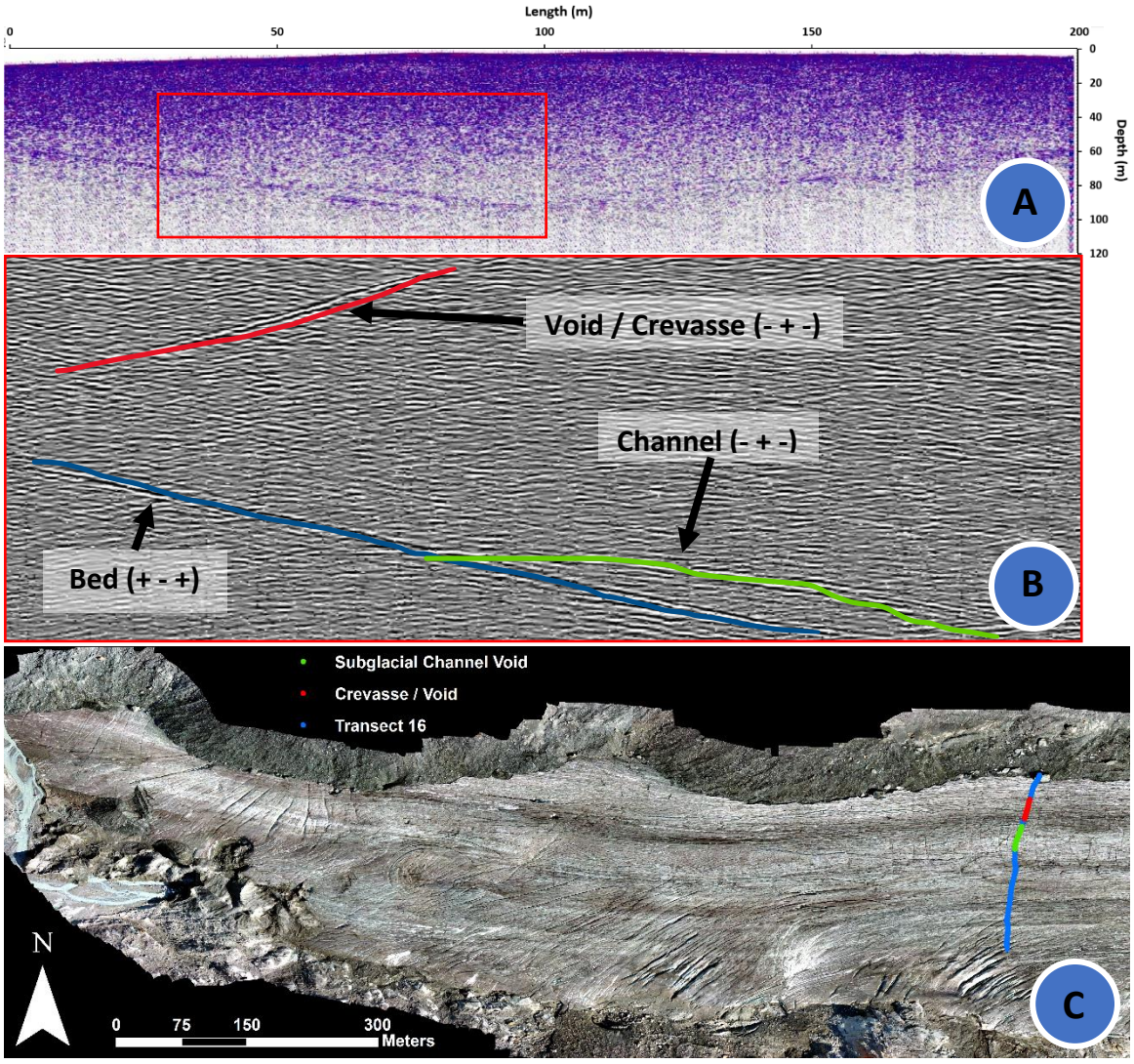

Figure 3.17*: GPR trace of Transect 16 highlighting features related to the development of a cauldron. GPR survey dated 6th July 2017.*

3.3.2.3 Air and water-filled voids

Various voids were identified from the GPR traces recorded. Air-filled voids were more easily identifiable due to the reversal in polarity clearly suggesting a less dense material than ice, which can only realistically be air. A good example of this can be seen in Transect 15 which shows a clear air-filled void (Figure 3.18). Numerous other voids were seen in transects 20 (Figure 3.15), 2 (Figure 3.16) and 16 (Figure 3.18). Air filled voids were considered to not be

connected, it being more likely based on their depth and location that they are relic surface crevassing from a short way up glacier that have subsequently been closed via ice creep. Also of note in Transect 15 are the two reflectors, a less clear one beneath a clear reflector, both with '+ - +' polarities. There are numerous interpretations of this:

1) The top reflector could be an englacial water channel or water filled void flowing above the bedrock, the trace appearing weaker below due to the scattering of the trace weakening the signal to the bed.
2) A basal sediment layer forming between the basal ice and bedrock
3) An englacial thrust containing a sediment layer and perhaps some meltwater.

It is believed that this feature is either (1) an englacial water channel flowing above the bedrock, the trace appearing weaker below due to the scattering of the trace weakening the signal to the bed or (2) the entire area between the two features is where the transect cuts across the main subglacial melt channel. In support of (1); for water to flow in as efficient way as possible to the terminus, the water travels across the top of an overdeepened section as seen in Figure 3.18d. However, to support (2) the location of this feature lines up well with where the predicted flow path of subglacial meltwater occurs (Figure 3.18c). Based on the other evidence from the field site such as the collapsing cauldron string and the seasonal mass loss data which will be discussed later in this chapter, this feature is most likely to another basal sediment layer similar to that identified further down glacier in section 3.3.2.1.

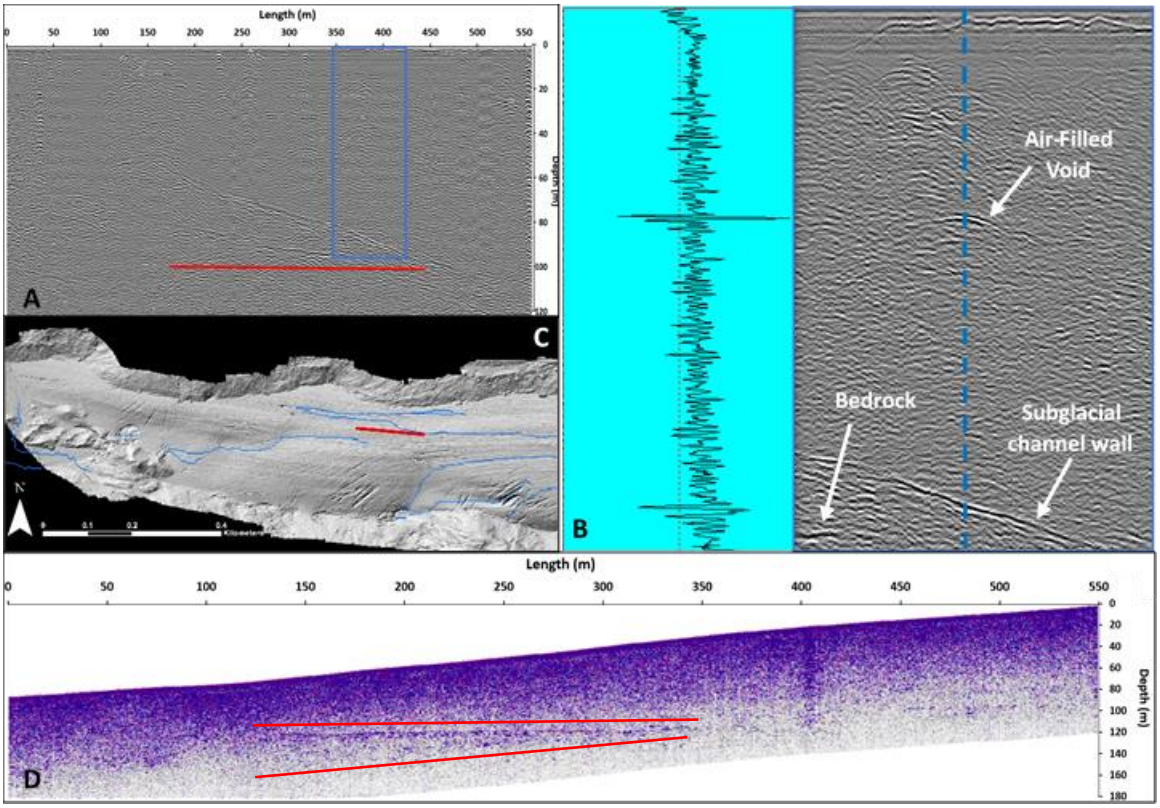

Figure 3.18*: (A) Transect 15 showing the extent two reflectors one on top of the other, running longitudinally (red line). (B) An annotated close up of the trace highlighted by the blue rectangle with wiggle-window to show the polarity of the trace. (C) A hillshade DEM with the extent of the feature in red and estimated subglacial flow paths (blue). (D) A topographically corrected view of the trace left to right being east to west with the two reflectors outlined by the two red lines.*

3.4 BED MORPHOLOGY SIGNIFICANCE

3.4.1 Overview

The aim of this section is to establish process-form characteristics and relationships within the terminus region that assist in our understanding of the evolution of overdeepenings and their significance towards erosion and the water flow regime. Initially results pertaining to the overdeepening will be discussed, followed by the potential for supercooling to be

occurring here. Following on from this, analysis of the subglacial flow routing will be examined along with insights from reflector analysis.

3.4.2 Bed morphology of Findelengletscher

3.4.2.1 Overdeepenings

From the bed model created, and models of Feiger et al. (2018) and Grab et al. (2021), an overdeepening is seen to be present near to the terminus (Section 3.2.2 - Figure 3.10). Various sources of secondary evidence lend themselves to support the primary GPR results for this overdeepening. As previously mentioned in Section 2.2.1.2, previous studies also hypothesise the presence of an overdeepening (Iken & Bindschadler, 1986; Haeberli et al., 2013, Feiger et al., 2018; Grab et al., 2021). As discussed in Section 3.3.2, the presence of a debris-rich basal ice layer both englacially (from GPR traces) and observational, from on-site observations supraglacially (emerging debris – Figure 3.13), support evidence of an overdeepened basin (Moore et al., 2011). Furthermore, evidence of basal sediment consistent with supercooled basal ice is present in the area mentioned in chapter 3.3.2.1 as shown in Figure 3.11, 3.14 & 3.19. As supercooling is understood to occur when the bed slope is 1.2-1.7 times that of the ice surface slope, this strongly reinforces the presence of an adverse slope from an overdeepening.

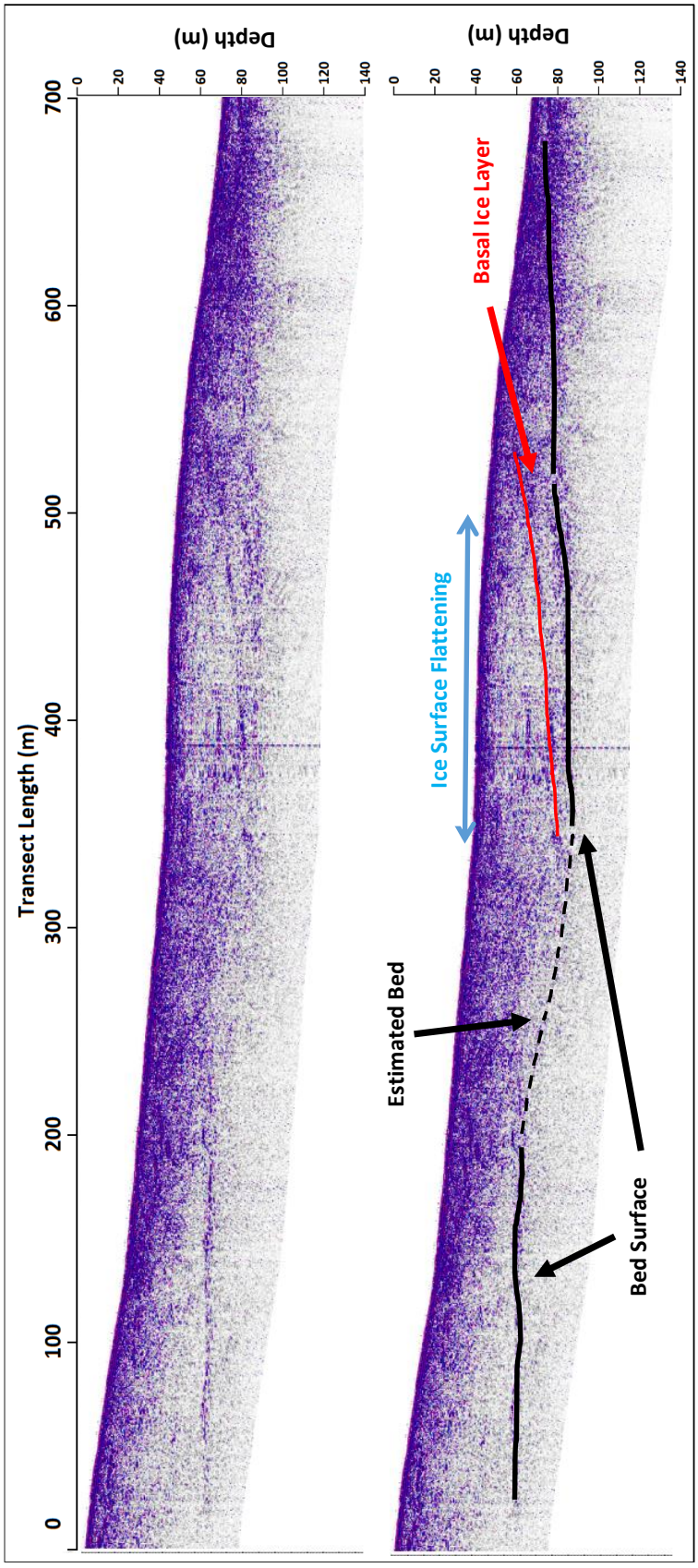

Figure 3.19 – *A longitudinal transect (transect 24) showing the presence of adverse slope of an overdeepening along with a basal debris layer Recorded 5th September 2017.*

3.4.2.2 Analysis of Supercooling and ponding levels along the flow line

According to the estimated hydrological flow line in Figure 3.20, conditions were at a suitable condition for supercooling across all bed models created at three locations (indicated by the red arrows A-C). These three points where the bed slope has exceeded the slope of the ice surface by 1.2 to 1.7x will be examined in order. Firstly, **A**) occurs right next to the portal and eskers. It is possible that the upslope of an esker has been considered here, as opposed to the ice surface slope. **B**) occurs at or around the location of Transect 21, which shows a reflector that has been discussed in Section 3.3.2.2 as either a channelised subglacial conduit with englacial crevasses above brought on by strain from weight of the above ice as the channel melts, or an englacial conduit, filled with meltwater and/or debris due to rerouting around or over the overdeepening as suggested by Church *et al.* (2019). It is also possible based on the location of this reflector that this reflector could be caused by supercooled debris being entrained into the ice. **C**) represents another potential area of supercooling and again a transect at this position may offer some explanation as to whether there may be supercooling occurring here. Longitudinal Transect 15 (Figure 3.18) shows two reflectors moving apart from each other with distance travelled downstream. As with **B**), this could be another englacial conduit or an entrained debris band caused by supercooling. As the polarity is not reversed it is safe to assume that the material captured here is denser than ice.

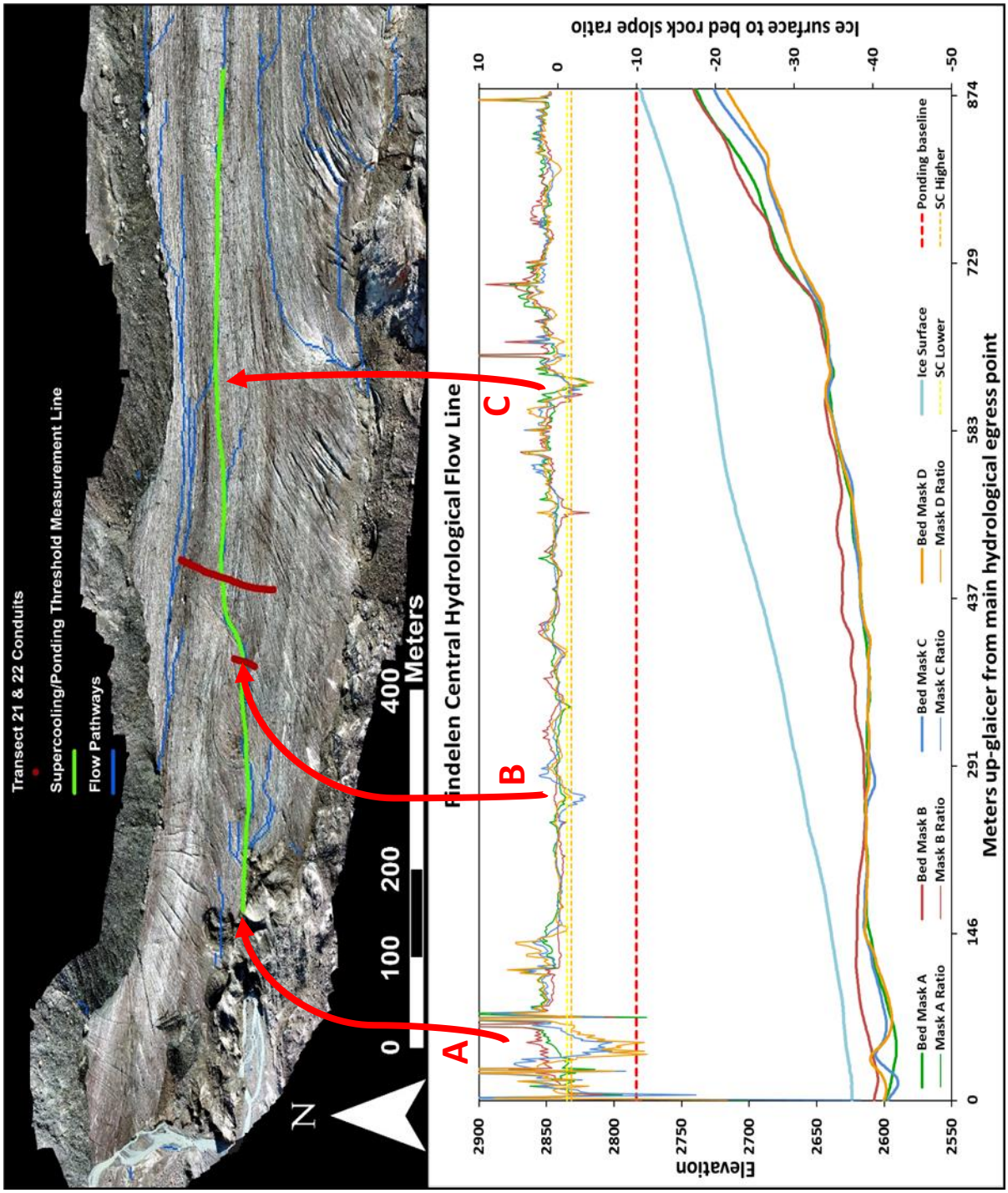

Figure 3.20*: Top) Bed Model B flow pathways and location of the estimated central flow line. Bottom) Supercooling and ponding thresholds when calculating slope angles along the main hydrological flow line. Slope angle is measured based on the altitude of points along this line 2 m apart.*

3.4.3 Subglacial water flow: routing and system morphology

The morphology of conduits alters through the year (as previously mentioned in Section 1.2.2) based on the variance of discharge at the glacier (Church *et al*., 2020). Changes in the volume of meltwater travelling through these channels cause expansion and contraction of these conduits. Indeed, conduits can disappear entirely in the winter due to lack of meltwater. Discharge data are available at Findelengletscher from a gauging station approximately 1 km downstream. Discharge levels were steadily increasing at the time of the GPR survey, having an average daily discharge of 504 m^3/s (Figure 3.21). However not close to peak discharge which occurred on the 3rd August for 2017 with an average daily discharge of over 1034 m^3/s. It can be assumed therefore that the hydrological system is at its most efficient and channelised at or shortly after peak discharge.

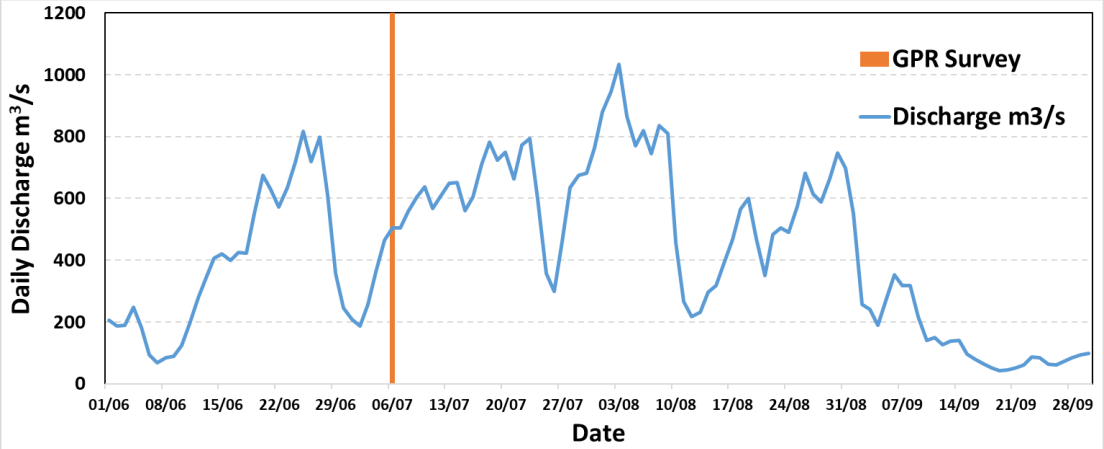

Figure 3.21*: Average Daily Discharge rates (m3/s) for Findelengletscher Summer 2017. Orange line indicates when the GPR survey was carried out over that summer.*

3.4.3.1 Calculation of flow routing implied by the various bed models

Flow routing beneath a glacier based on its topography can be calculated using Shreve hydraulic potential (Shreve, 1972) (see Section 2.3.4.5). The ice surface used is the DEM

created from the 7th July UAV survey. This was used in conjunction with the bed depth traces from the GPR surveys on the 5th February and 6th July 2017 from the four models discussed in Section 3.2.2 to produce the ice thickness which was required measurement for this equation.

As can be seen from Figure 3.22, there is a broad agreement across the four bed models created as to the predicted hydrological flow paths beneath the glacier. Working backwards from the main meltwater portal to the south of the terminus, the estimated location of the subglacial channel can be predicted. Using GPR surveys these subglacial channels can be mapped (Egli *et al*., 2021a) which is what will be looked at in the following section. It should be noted that the Shreve hydraulic potential calculation doesn't consider the flow routing of water supraglacially from surface runoff and entering the glacier from crevasses and moulins. The majority of the ice surface slope slopes towards the south so it is likely that there is an increased input of melt to the southern section of the glacier.

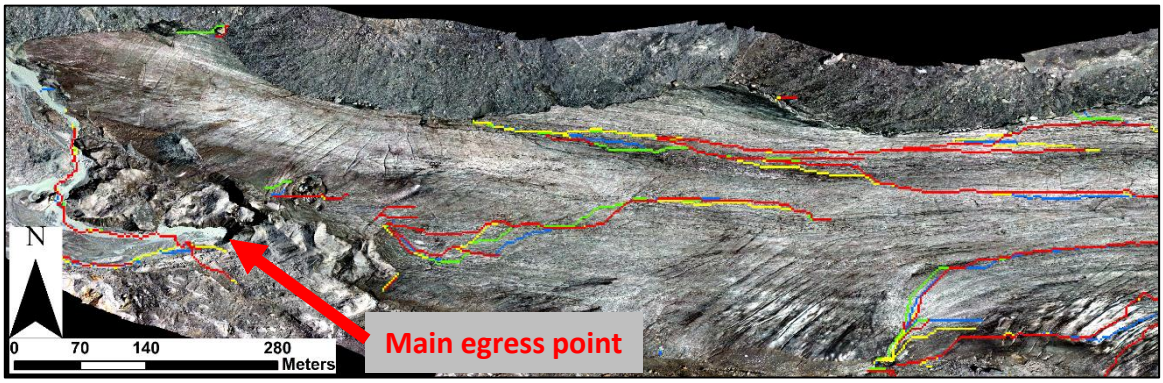

Figure 3.22*: Subglacial flow pathways for four bed models outlined in Table 3.1 (Chapter 3.2.2.1). Green – Bed Model A, Red – Bed Model B, Blue – Bed Model C, Yellow – Bed Model D.*

3.4.3.2 Additional evidence for flow routing and morphology

By comparing the hydrological flow path of previous work comparisons can be made as to the validity of the findings and the reliability of the methods. The flow path from the data of Feiger *et al.* (2018) can be seen in comparison with bed models generated in this study (Figure 3.22). Despite the coarse resolution, a main hydrological channel crosses the glacier from north to south at a very similar location to those estimated by bed models (Figure 3.22) before exiting the glacier where the egress point can be seen from the orthomosaic image (Figure 3.23). It should be noted that the method for calculating flow routes (see Section 2.3.4.5) tends to push flow routes out laterally to the edges of the glacier where the thickness of ice is '0'. It was observed on site that the degree to which this actually occurs is considerably less than suggested, particularly regarding Figure 3.23. On site there was evidence that supported the hydrological flow routing, as evidence of a lateral flow path was present in a location depicted by the Shreve hydraulic potential calculation (Figure 3.24)

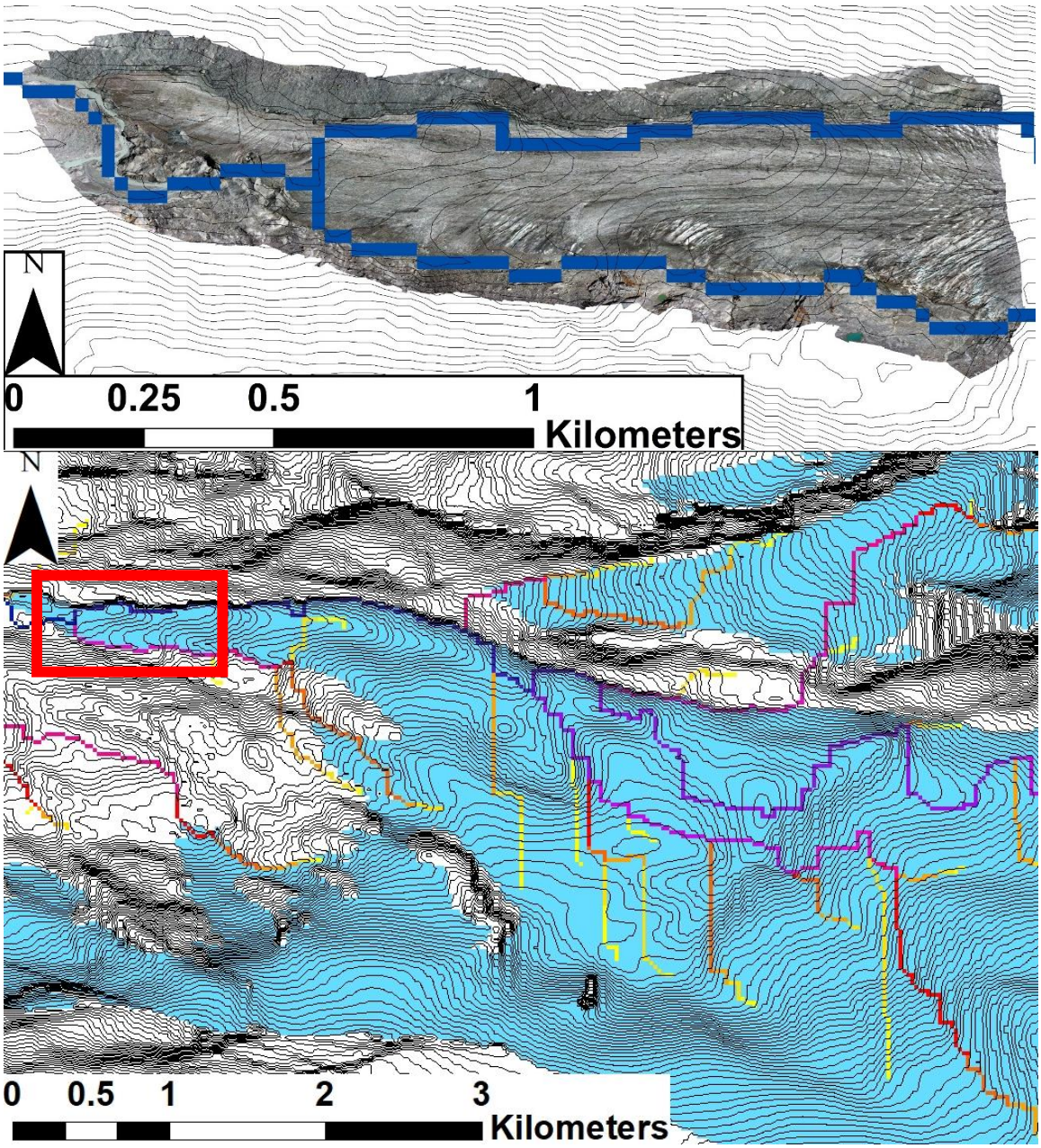

Figure 3.23: *Glacial flow path derived by equation (1) using Feiger et al. 2018 data for Findelengletscher (Below). Close up of flow paths at snout (red rectangle) overlaid with orthomosaic from 5th July 2017. (Above).*

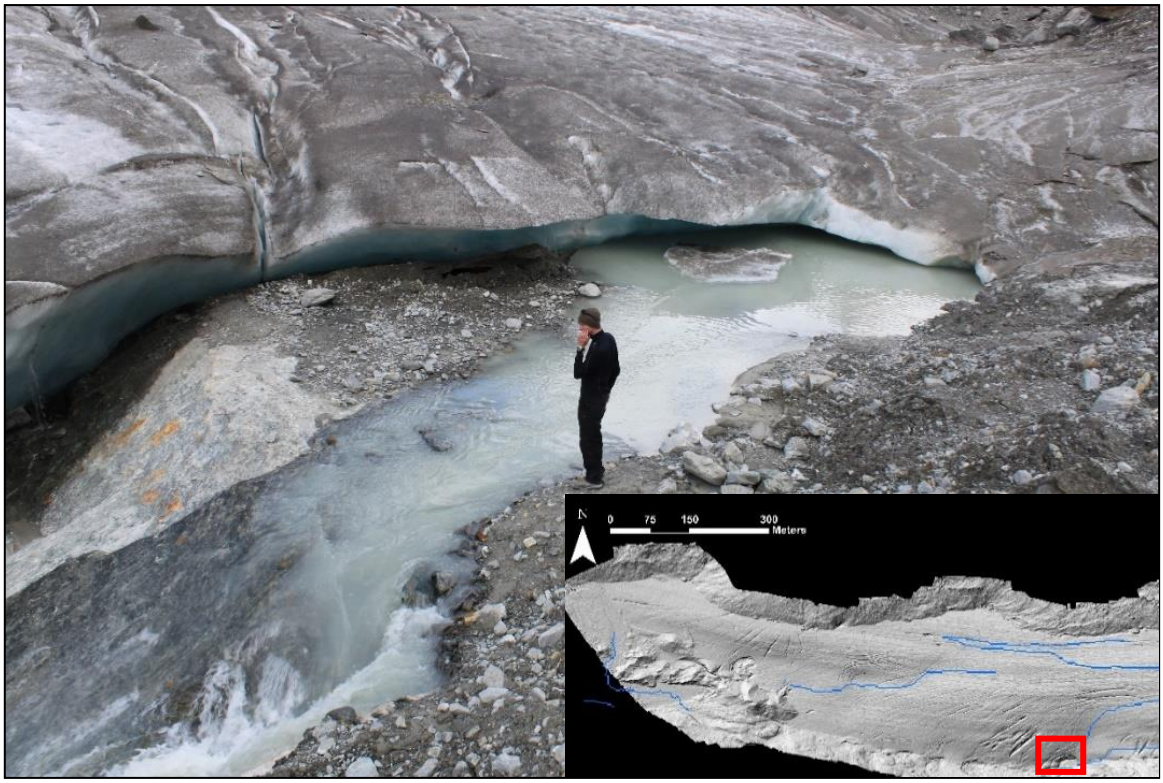

Figure 3.24*: Field photo showing the emergence of a lateral hydrological flow path from beneath the glacier. The water continues to flow down hill back into the depths of the glacier off-camera to the left (July 2017).*

The calculated flow routes were compared back to the GPR transects to see whether there was any suggestion of a subglacial channel to add further confidence to these findings.

An overview on a map of where Transects 21 and 22 are located is shown in Figure 3.25. Transect 21 (Figure 3.26) shows a cross-glacier trace displaying a strong bed reflection. Notably, a hyperbola above the bedrock at a velocity of 0.3 m/ns can be seen. This velocity is consistent with the density of air (Bradford *et al*., 2009). Furthermore, the polarity of the trace is 'negative-positive-negative' suggesting an increase in wave-velocity at the interface and therefore a void just above the bedrock which is a channel. The depth difference between this channel and the bed is approximately 6 m which suggests that by this stage in the melt

season (6th July) the drainage system is likely to have become channelised, at least in this location. Concentric features in the ice above this are representative of crevasse features likely caused by stresses from channel melting.

Transect 22 (Figure 3.27) shows a cross-glacier trace 60 m up glacier from Transect 21. A feature that suggests a subglacial channel at the deepest point of the bed is present, with a maximum thickness of 12 m. However, the trace is weak due to overlying crevasses nearer to the surface, thought to be the beginnings of a cauldron (Figure 3.16 - D). It should be noted however that the width of this feature (over 100 m) does seem overly large, especially considering the size of the main egress portal is much narrower than this. It is quite possible that instead of the roof of a subglacial channel, the trace could be an englacial conduit or sediment filled crevasse.

Both these traces line up with the estimated flow paths discussed in Chapter 3.4.1 which can be seen in Figure 3.25 which adds support to the analysis of the GPR. Transect 16 also shows another potential subglacial channel that lines up well with the estimated flow path (Figure 3.17). From these estimations and supporting GPR trace features we can be confident that a main subglacial flow path has been identified.

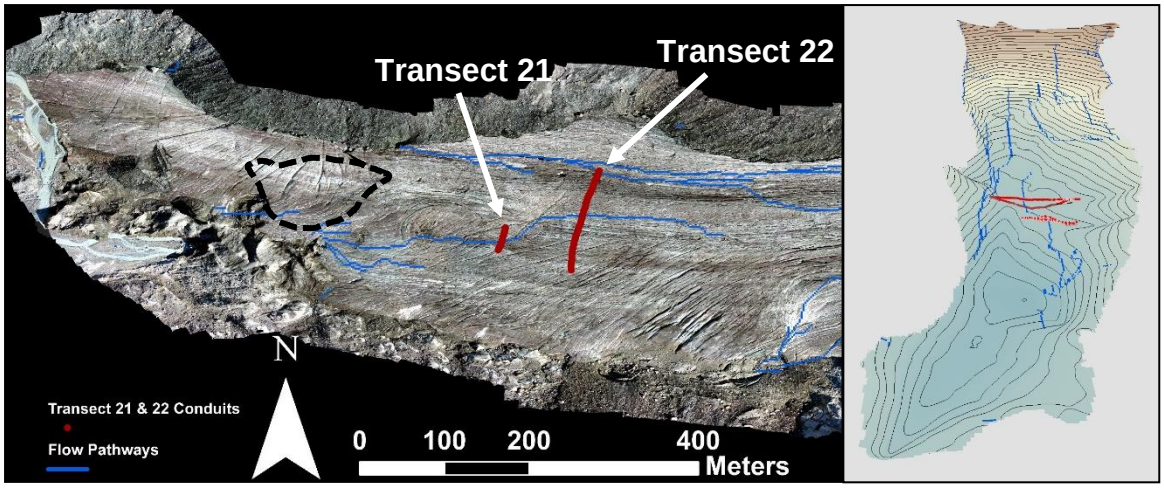

Figure 3.25*: Left) Flow paths (blue), overdeepening (black) and transect 21 & 22 transposed onto an orthomosaic image of Findelengletscher (7th September 2017). Right) 3D image of same data on the bed model with contours every 5 m looking East up valley from above snout of Findelengletscher.*

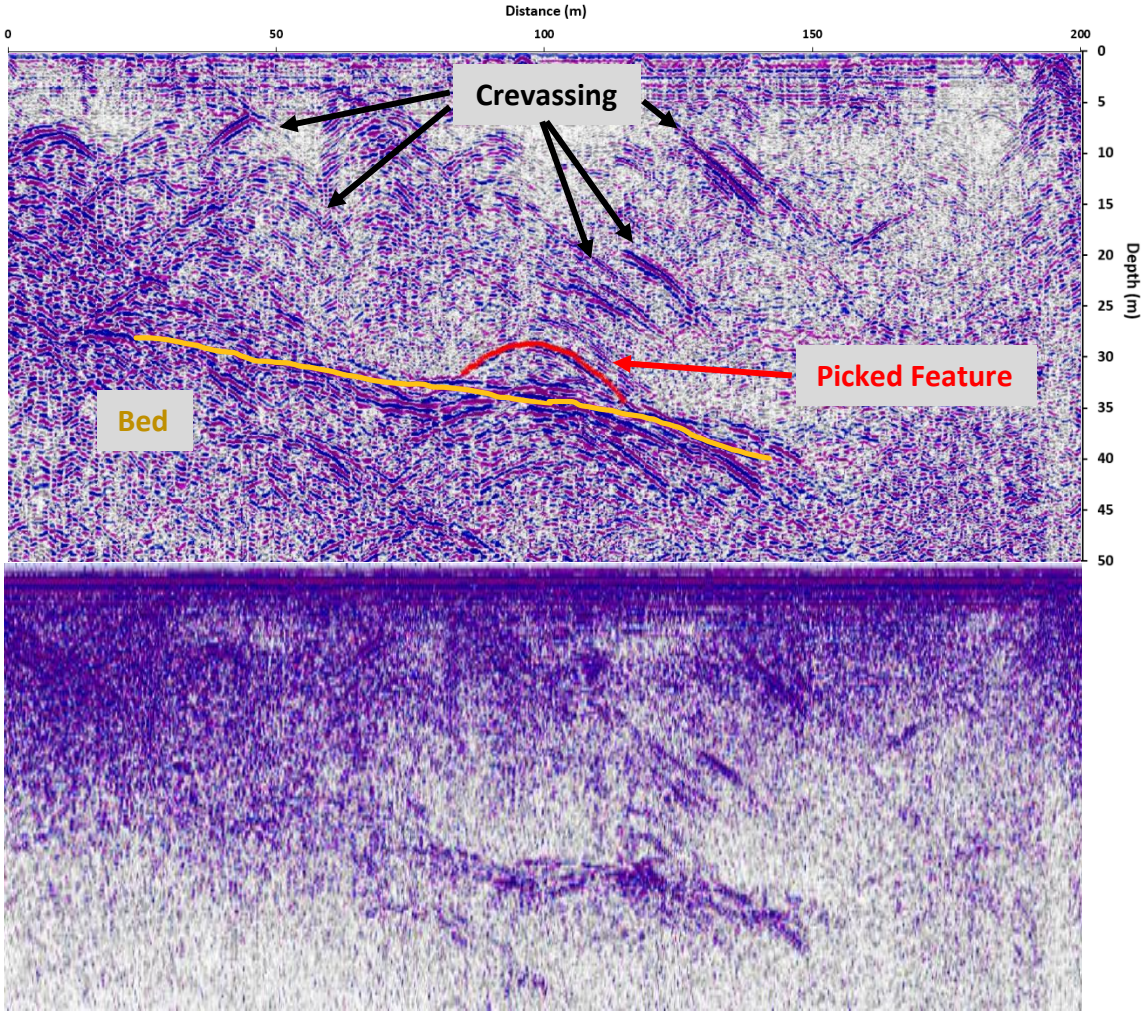

Figure 3.26*: Hyperbola located above bedrock at transect 21 taken 6th July 2017.*

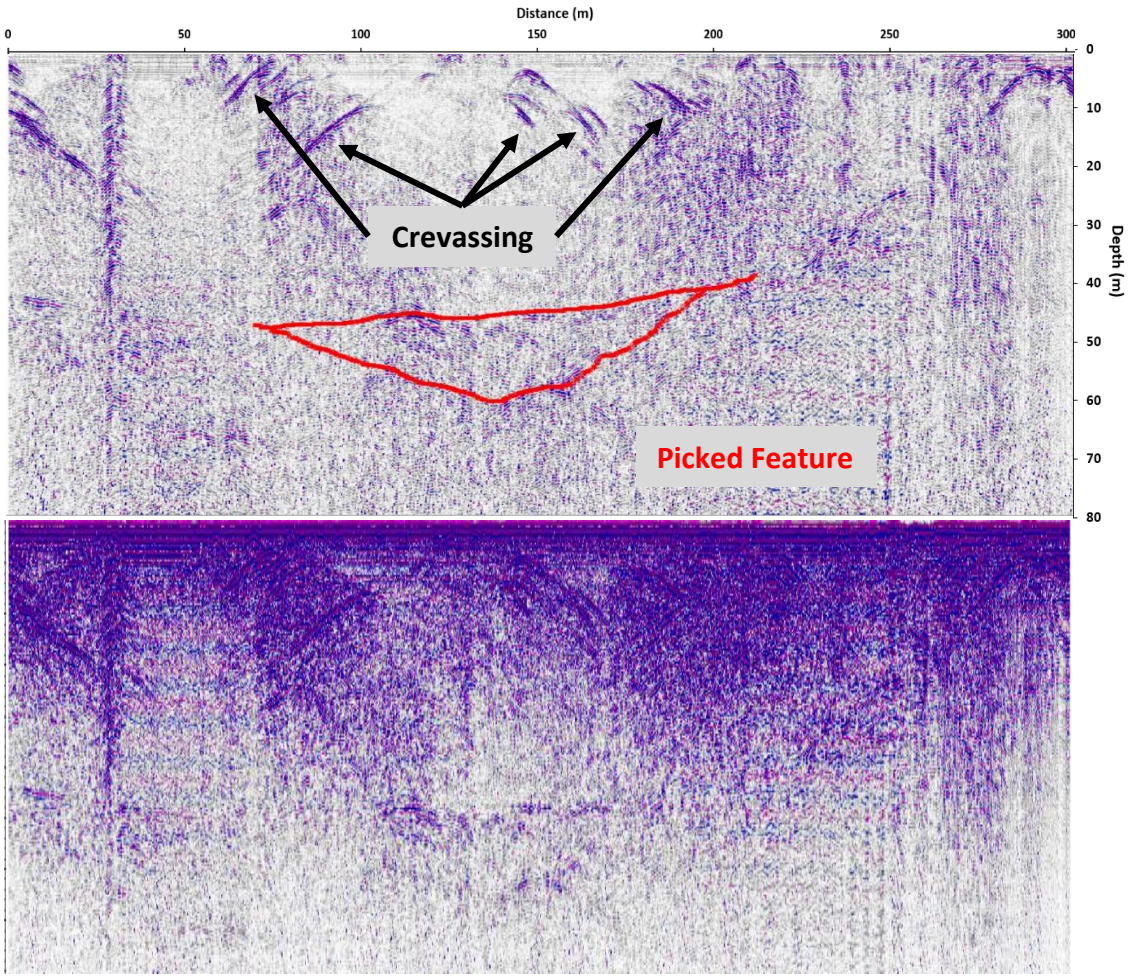

Figure 3.27*: Possible subglacial channel at Transect 22, taken 6th July 2017.*

3.5 ELEVATION CHANGE

Obtaining elevation change data has been calculated by differencing the DEMs created from the UAV data. The Z coordinate (or changes in ice thickness) is of equal importance as the XY coordinates when reaching an understanding of the process at work within and beneath the glacier. Figure 3.28 & Figure 3.29 show both the annual (September 2016 to September 2017) and summer (7th July – 3rd September 2017) elevation change of the Findelengletscher terminus. A general pattern of ice loss across the glacier terminus is present as expected from a glacier in retreat, with between 9 -12 m of ice thickness loss across most of the area covered.

In terms of surface area, a total area of 0.038 km^2 has been lost by the glacier at the study site (bottom 1.5 km of Findelengletscher) between September 2016 and 2017. A further 0.087 km^2 has been lost between September 2017 and 2019. Looking just at the length of terminus retreat from 2016 to 2019, 180 m has been lost (Figure 3.30). As also shown in Figure 2.13 in Section 2.2.2, this general pattern indicates that Findelengletscher is, and continues to be, in a consistent state of retreat since the late 1980's. Localised patterns of ice loss at Findelengletscher provide important clues as to what may be occuring within and beneath the glacier. For example, we can see from Figure 3.28 and 3.29 but certainly clearer in the latter annual comparisons, that annual and seasnonal ice loss respectively, is pronounced at the cauldron features, showing us that they start to form initially by the loss of ice mass from their centre. With an annual loss of 15 m (approximately half of that occuring between July and September), roughly twice as much as that of the surrounding glacier, a depression begins to form with surface crevasses developing due to internal stresses in the ice from the opening up of, and erosion caused by developed channelised drainage pathways. As discussed in Section 3.3.2.1, these crevasses form internally before they appear at the surface but present themselves by internal crevasses that can be picked up by GPR and localised elevation change shown through DEM comparisons. The formation and subsequent collapse of these cauldron features cause an accelerated glacier retreat (Kellerer-Pirklbauer & Kulmer, 2019; Elgi *et al.* 2021a). Figure 3.30 shows how the glacier's rapid retreat along the subglacial pathway has led to an isolation of ice beyond these cauldron collapses which will end up being dead ice, detached from the rest of the glacier. Another spatial pattern of note from both Figure 3.28 & 3.29 is the increase in ice loss around areas where predicted subglacier flow pathways are present. The southern lateral margin for example, shows a high level of negative elevation change where subglacial meltwater flow pathways are estimated to flow from the centre line

of the glacier down to the margins and it is likely that, similar to the caudron features near the egress portal, these channels are causing an increase in localised melt. Figure 3.24 shows where this subglacial channel exits the glacier at the margin before rentering the system subglacially. The location of the meltwater channel in this figure serves to support the estimations of flow pathways from bedrock masks created by GPR surveys (Figure 3.22). The size of the meltwater stream is likely to produce significant localised ice loss.

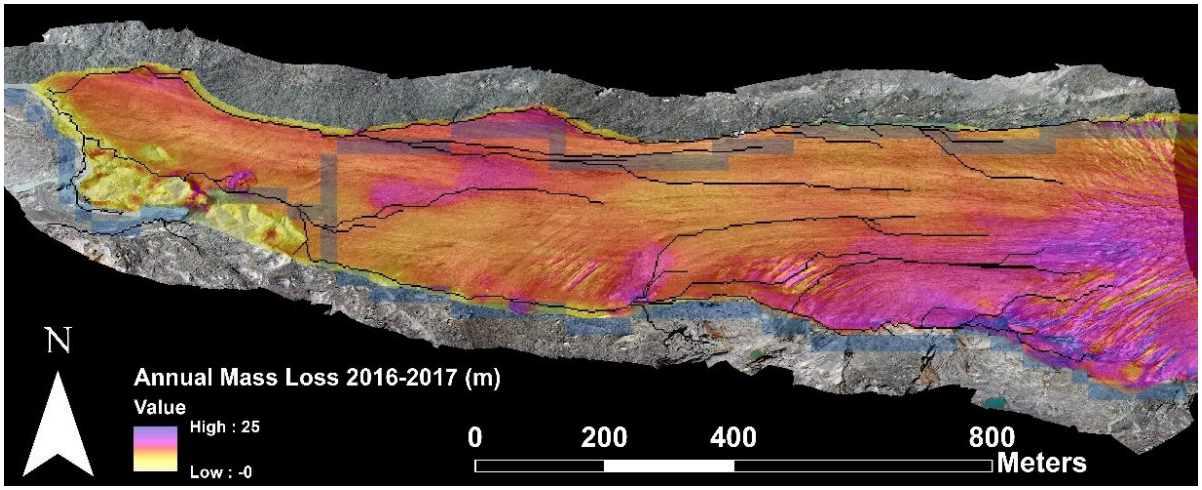

Figure 3.28*: Subglacial flow pathways (blue coarse data from Feiger et al. (2018), black data from bedrock mask created by this study) compared to annual elevation change.*

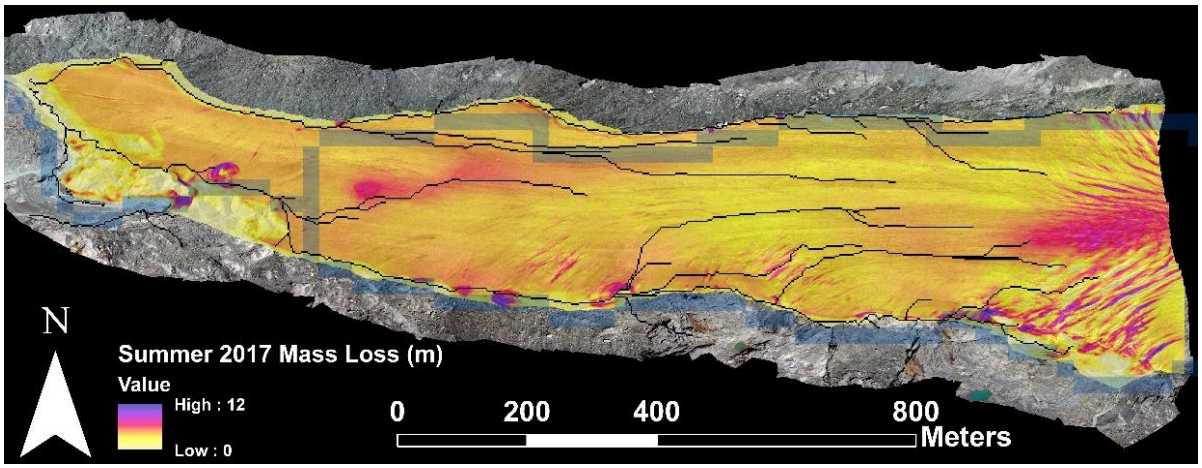

Figure 3.29*: Subglacial flow pathways (blue coarse data from Feiger et al. (2018), black data from bedrock mask created by this study) compared to summer elevation change.*

Figure 3.30*: Retreat of Findelengletscher 2016-19. Outlines of 2016 and 2017 extents overlain over Planet imagery (2020) from late summer 2019. World Imagery - Source: Esri, Maxar, GeoEye, Earthstar Geographics, CNES/Airbus DS, USDA, USGS, AeroGRID, IGN, and the GIS User Community.*

3.6 SUMMARY

Transect data from GPR work as well as onsite evidence of supercooling and surface thrusts and various second-hand sources (Iken & Bindschadler, (1986); Haeberli *et al. (*2013); Feiger *et al. (*2018)) all point towards an overdeepening being present at the terminus. Glacial hydrology looks to skirt to the south of this overdeepening towards the main egress point as this is the flattest, most efficient path it can take. From the bed model created by recording and combining bed reflectors from three different GPR fieldwork, flow paths have been generated that support that this is the approximate route of the meltwater. This is backed up by reflectors of subglacial channel features in the GPR, tell-tale features such as cauldrons forming along the predicted flow line and mass loss data across seasonal and annual timescales providing evidence towards the development of a changing seasonal drainage system from a distributed to a more channelised system.

Now that an understanding of the subglacial landscape has been ascertained, the next step will be to examine the spatial dynamics of Findelengletscher and how this compares to a typical flow field for a glacier with a smooth 'normal' bed. This will be answered in the following chapter.

4. SPATIAL VARIATION IN FLOW VELOCITY AT FINDELENGLETSCHER

4.1 INTRODUCTION

This chapter investigates the spatial variability of glacial velocities at Findelengletscher. Understanding where and why glacier velocity patterns are different when the bed is complicated by undulations is the primary aim of this chapter. How variability in the glacier bed associated with the presence of overdeepenings affects flow patterns at Findelengletscher is the second aim set out to be answered in this thesis (see section 1.5) and will be the focus of this chapter. The methods (SfM and feature tracking) used to obtain spatial velocity patterns presented in the chapter are described in Chapter 2.

For the study, the glacier terminus area was divided into sub-areas to aid the analysis and interpretation of the results. Velocity data will then be presented and compared for summer and winter periods across all AOIs (Areas of Interest) with a special focus on the overdeepened area (Section 4.2). To aid interpretation of the velocity data, a 'model' of glacier surface flow pattern was created by smoothing the observed glacier velocities using a spatial filter with a wavelength greater than the wavelength of features of interest in the subglacial topography (Section 4.3). The results are interpreted using knowledge of the bed topography established by GPR and other methods (see Chapter 3).

4.1.1 Rationale

There are several key reasons as to why investigating spatial flow patterns are important using these specific multifaceted methods. Spatial patterns can provide clues as to the topography of the underlying bed (Gudmundsson, 2003). As the bed is known from the GPR surveys carried out, variations in flow velocity can be compared to the topography beneath it, and a more complete picture of the inner processes (such as the hydrological regime) of the glacier can be formed. Subglacial water pressures vary spatially (Mair *et al*., 2001) and these have an effect on surface velocities (Iken & Truffer, 1997). As discussed in Section 1.3, surface velocities are not uniform, for example, 'sticky spots' can occur, where localised areas of ice move slower than neighbouring ice (Alley 1993; Stokes *et al*., 2007). Obtrusions in the bed provide form-drag (Kyrke-Smith *et al*. 2018). In these instances, ice must deform to overcome large obstacles at the bed. Generally, the more that the ice is seen to deform around these obtrusions, the higher the resistance the bed is providing to the localised ice flow. Subglacial basins or overdeepenings are likely to be associated with low basal drag due to the absence of obstacles and the storage of water and sediments at the bed. These features typically exhibit high basal water pressure and materials with low skin friction (the resistance to sliding along an interface; Minchew & Joughin, 2020). This will lead to plug-flow (Mair *et al*. 2003), in other words, where flow is predominantly caused due to sliding and there is very little deformation. Conversely, the deformation of ice around obstacles leaves an imprint on the ice structure that, if the obtrusion is large enough, should be visible using short-term high resolution image comparisons.

Using SfM from UAV surveys combined with the bed topography known from GPR surveys to better understand flow patterns has not often been looked at before (Lamsters *et al*., 2020)

and will give a more complete view on the overall processes of the glacier linking surface flow rates to an understanding of bed topography. The high resolution of the data allows for small changes to be identified across short timescales in a way that satellite imagery simply currently cannot (Dugdale, 2007).

4.1.2 Structure of Chapter Four

Section 4.2 will describe how the direction and velocity of ice flow at Findelengletscher differs from what is expected of an 'ideal' (Nye 1951) temperate valley glacier and why. Section 4.3 will take a closer look at mass loss patterns across the glacier and compare this to the ice flow findings from Section 4.2. Finally, Section 4.4 will sum up the key findings from this chapter. Figure 4.1 shows the workflow diagram of this chapter, how it builds on works from previous chapters and helps shape Chapter 5 which is concerned with the temporal relationships in the data.

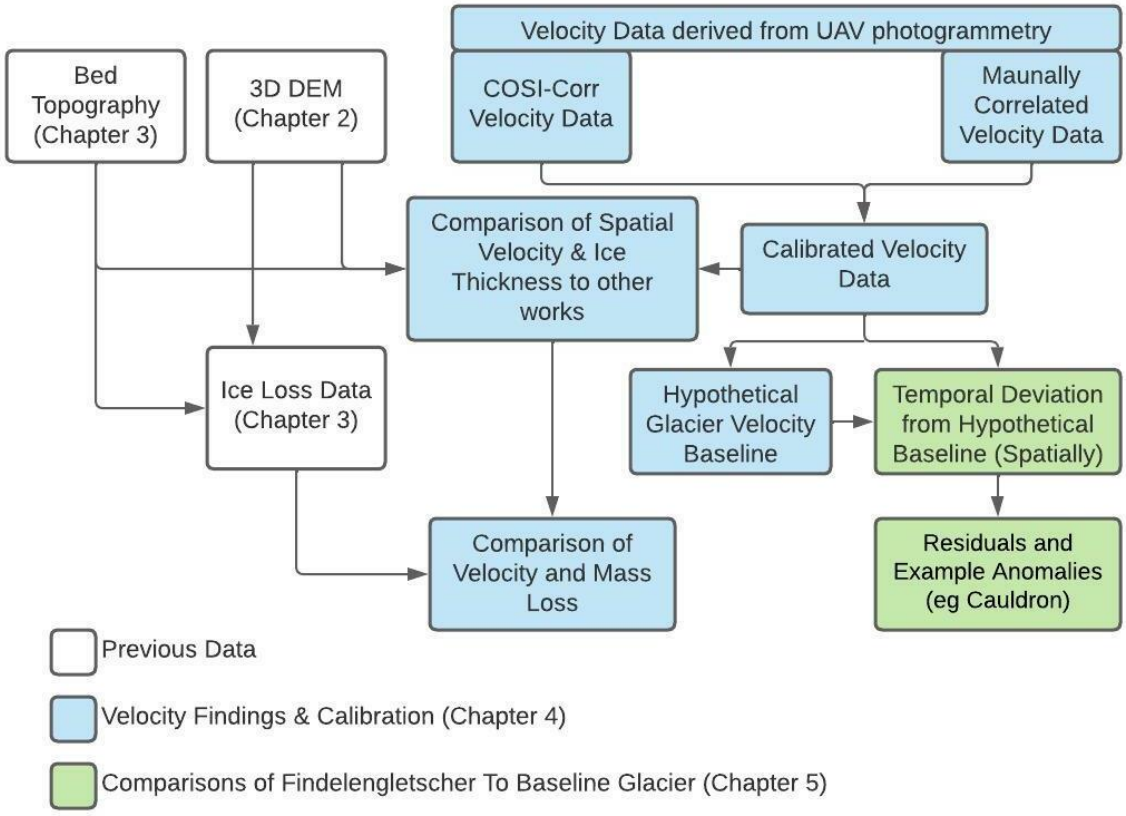

Figure 4.1*: Workflow diagram of data available and what will be achieved in Chapter 4 (and 5).*

4.2 ICE FLOW BEHAVIOUR AT FINDELENGLETSCHER

By comparing the behaviour of ice flow velocities and directions at Findelengletscher – a glacier with steep undulating topography to that of what is expected at a uniform glacier – we can begin to understand how different these patterns are when the bed topography is not so simple and show how much of an effect the bed topography is having on the dynamics of the ice.

4.2.1 Areas of Interest (AOIs)

To better visualise the flow patterns of Findelengletscher, the field site was divided up into eight 'areas of interest' (Figure 4.2). Short descriptions of the AOIs are presented in

Table **4.1**. AOI's borders were decided by dividing the field site with uniform, straight lines to avoid 'cherry-picking' of specific results whilst also being broadly divided into distinct areas; either by features within its borders (e.g., cauldrons, portals, thrusts etc.), the general topography (flatter vs steeper ice surface) or observed dynamics (velocity and ice loss). For example, the decision for section 4 & 5 and 6 & 7 to be split roughly down the centre line is that the ice surface of the northern side of the glacier was flatter (when viewed cross-sectionally) and velocities were higher than that of the southern side.

The decision was taken for these areas to cover the entirety of the glacier i.e., stretch all the way to the border rather than have a distance buffer from the extent of the glacier, to maximise the amount of data recorded. It should be noted however that the inclusion of areas so close to the edges of the glacier may cause data to be more platykurtically distributed.

Table 4.1: *Descriptions of the separate AOIs for ice flow velocity and direction analysis at the field site.*

Identifier	Explanation
AOI 1	The terminus of the glacier where material is seen to be being deposited.
AOI 2	The area where the overdeepening is located (based on the Bed Model created in Chapter 3) as well as the main portal where meltwater exits the glacier.
AOI 3	The area where the subglacial flow path crosses the glacier from North to South. This area also captures the ringed cauldron features where ice loss was noticeably high as well as the lowest points of where Grab *et al.* (2021) and Feiger *et al.* (2018) predicted the overdeepening to be (Figure 3.10).
AOI 4	A highly crevassed area on the south of the central flow line with a high ice loss and steep slope down to its lateral boundary.
AOI 5	An area along the central flow line prior to the overdeepening where the ice surface slope is steeper than the areas immediately up and downslope.
AOI 6	Similar to area 4 - a highly crevassed area on the south of the central flow line with high ice loss - but further up glacier.
AOI 7	Similar to area 5 - an area along the central flow line – but further up glacier where the ice surface is noticeably flatter and higher observed ice velocities
AOI 8	An area of high velocity and ice loss just after the heavy crevassing of the ice fall that makes up the upper most extent of the field site.

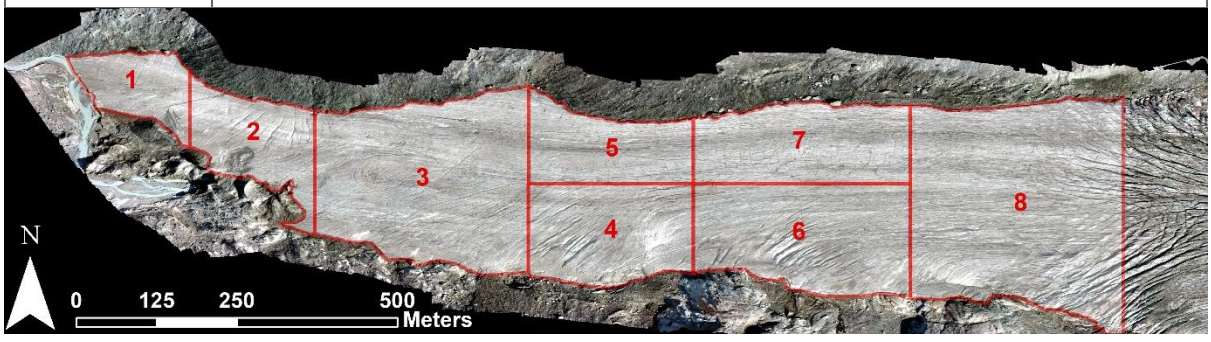

Figure 4.2*: Individual areas of interest at Findelengletscher.*

4.2.2 Feature Tracking

To calculate flow velocity at Findelengletscher, comparisons of per-pixel patterns in orthomosaics from different time periods are made using COSI-Corr (as discussed in Section 2.4.6). By recording the distance and direction these pixels have moved and dividing that distance by the number of days between orthomosaics, an average daily velocity can be obtained which will then be multiplied by 365 to standardise measurements to yearly levels. When comparing summer to winter velocities, this will standardise the data as time-periods between each set of UAV flights differ. Ranges of ortho-pairs using this COSI-Corr vary from a few days (Leprince *et al*., 2007b; Jawak *et al*., 2018) to upwards of a year (Tiwari *et al*., 2014; Das, 2021) which shows how robust COSI-Corr can be (Heid & Kääb, 2012).

4.2.2.1 Velocity Data for 2016 and 2017

Large scale patterns of velocity are best viewed over the winter period in order to remove the seasonal impact of hydrology. Whilst a considerable amount of noise is present – predominantly in the southern section of the glacier likely due to the higher levels of crevassing here – a general pattern of velocities slowing as they approach the terminus can be seen (Figure 4.3). The reason for this, as outlined in Section 2.6, is due to the driving stress from internal deformation due to ice thickness. Therefore, as the ice thins towards the margins and terminus, the ice thickness is reduced and so is the amount of internal deformation and therefore ice flow velocities. Similarities can be seen between Figure 4.3, specifically the winter ice velocities, and Figure 4.4 (ice thickness) to support this point.

Velocities over longer periods of time (e.g., F5-F6 – winter; F7-F8 – summer 2017) average out to produce a consistent velocity that slows as it approaches the terminus (Figure 4.3) as is the case with most temperate valley glaciers (Copland *et al*. 2009). From the distribution of

ice thickness at the glacier terminus (Figure 4.4), calculated by subtracting the Bed Model from the closest DEM (see Section 3.2.1), it can be assumed that due to reduced internal deformation, the velocity will tend to decrease as it reaches the terminus. However, ice thickness is not uniform in this regard and prior to the overdeepening an area where ice thickness is lower is present (marked on Figure 4.4 as A). Therefore, based solely on internal deformation alone, velocity would be expected to decrease in this area. However, there are more factors at play here which will be discussed in Section 4.2.2.5 where a closer look at the overdeepening will be taken. There is quite a high degree of 'speckle' in Figure 4.3 which, as discussed in Section 2.5, is due to the longer time period and increased noise and reduced window size because of this.

Taking first the data from Summer 2016 where comparisons between 5 orthomosaics were recorded between the dates of 22nd August and 6th September (15 days) and average velocities obtained, it can be seen in Figure 4.5, that velocities are significantly reduced over the overdeepening highlighted in the previous chapter (Section 3.2). This will be discussed in further detail in (Section 4.2.2.5). Interestingly, velocities where a main subglacial flow path is expected, and future cauldron developments have been observed (Section 3.3.2 - Figure 3.17), are low relative to the rest of the measured area at between 22-29 m yr^{-1} as shown in Figure 4.5. This figure shows that the area prior to the overdeepening where the main flow path is located has a lower velocity than the overdeepened areas next to it.

By comparing Figure 4.4 and Figure 4.5, it can be seen that higher velocities occur in the two areas with the highest ice thickness, whilst the area in-between these has a much lower velocity (approximately half). This suggests that a relationship between ice thickness and velocity exists. The ice is shown to be moving fastest in the region of the heavily crevassed

area to the very East of the study area (furthest up-glacier) at 55-128 m yr^{-1}. Following the central flow line up-glacier and comparing the bedrock and ice surface slope angle ratio, areas where the supercooling threshold is being met can be identified. Figure 4.6 shows this occurring at several points within the overdeepening.

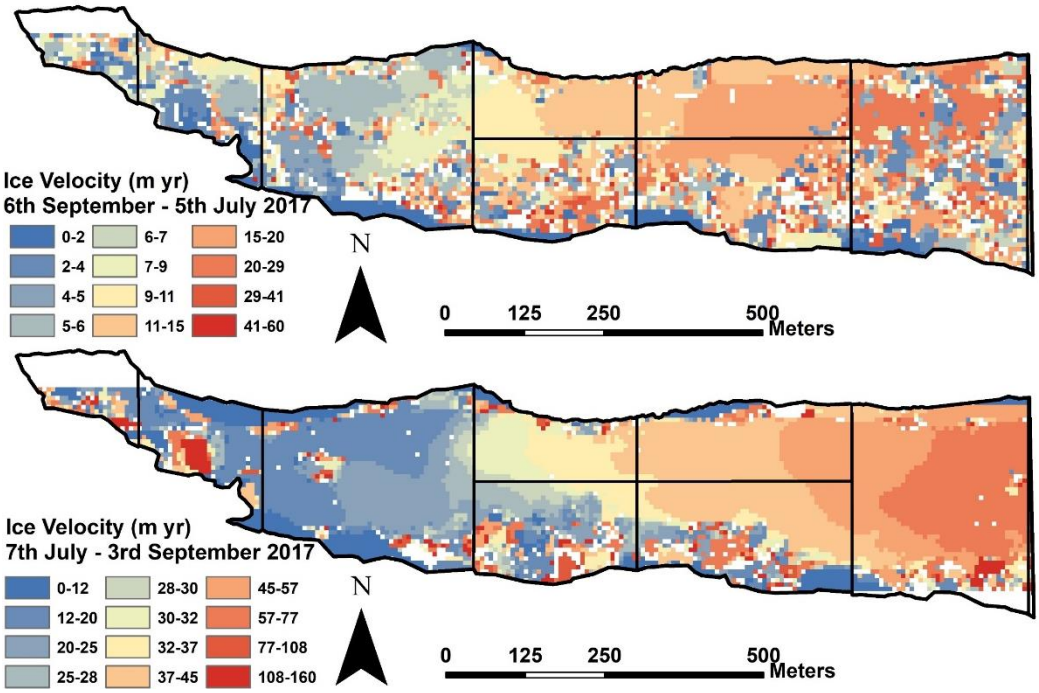

Figure 4.3*: Winter and Summer ice flow velocities at Findelengletscher. AOI grid is overlain for reference.*

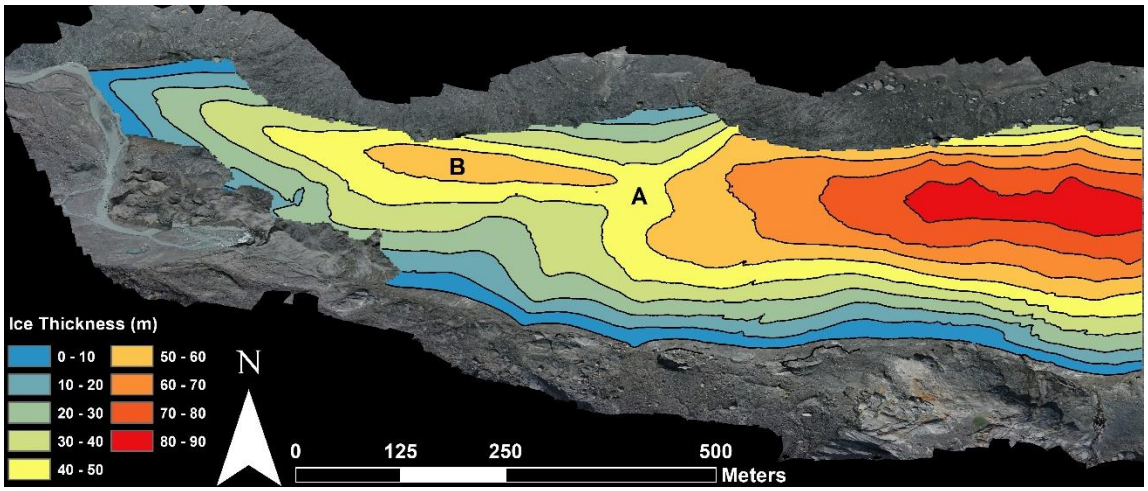

Figure 4.4*: Ice thickness of Findelengletscher terminus (areas of dead ice have been excluded). A denotes a shallower area just prior to the overdeepening and B shows the location of the overdeepening (from GPR surveys conducted 7/2/17 & 6/7/17 – Section 2.3.2. DEM from 5/7/17 UAV flights – Section 2.4.3).*

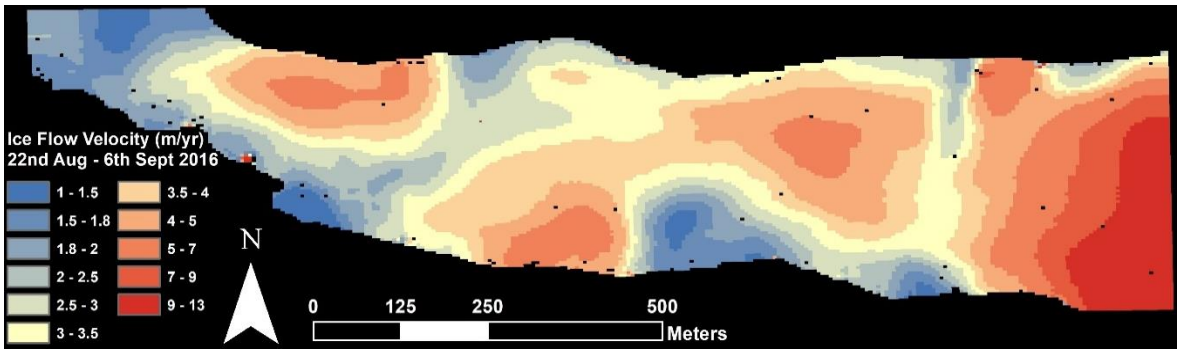

Figure 4.5*: Average velocity rates between 27th August and 6th September 2016.*

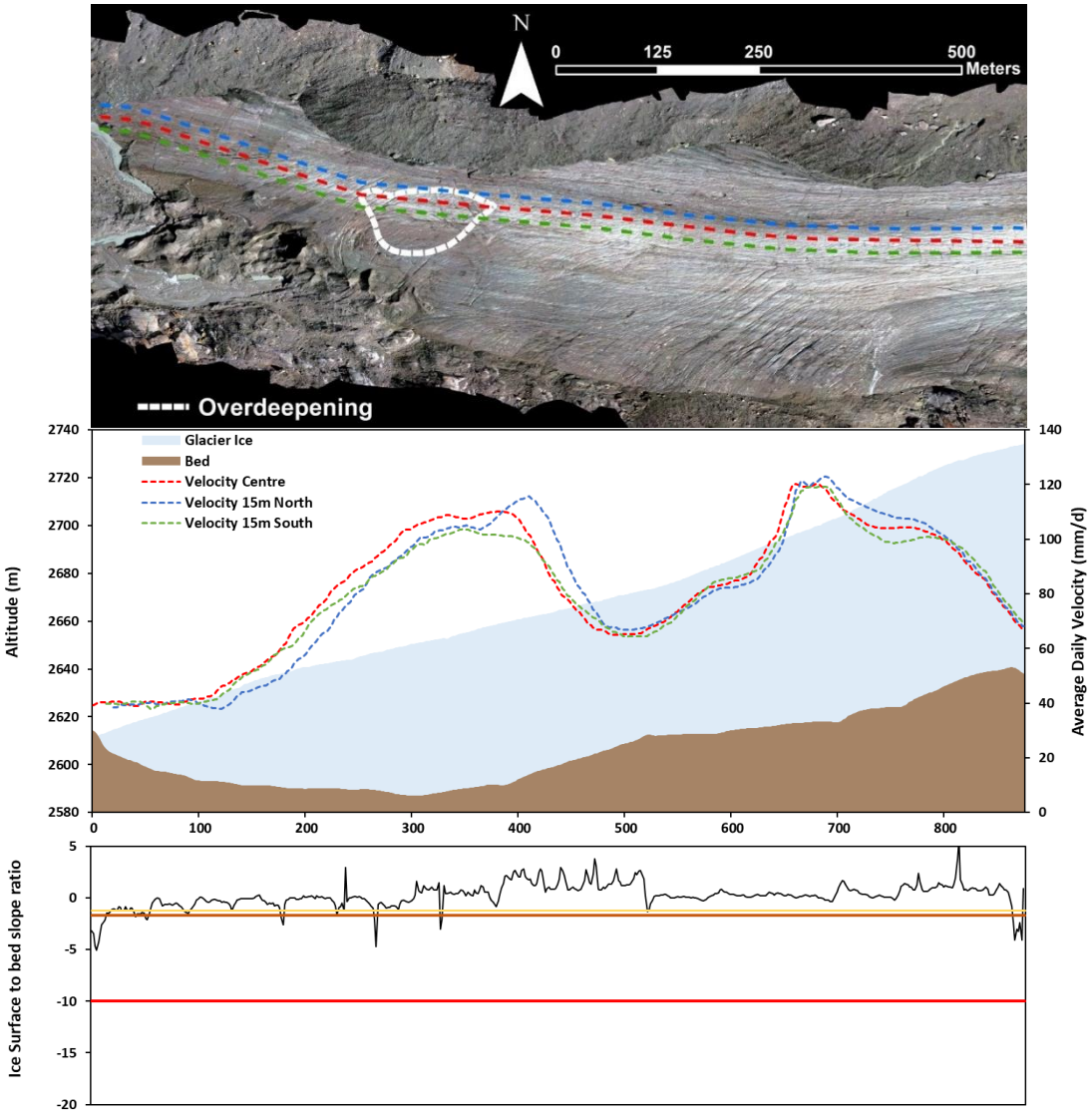

Figure 4.6: *Top) Central and 15 m north and south flow line of Findelengletscher terminus. Middle) Velocities along and 15 m either side of the central flow line of Findelengletscher between August 27th – September 6th, 2016. Bottom) Supercooling/ponding ratio smoothed over a 6 m area.*

4.2.2.2 Validation Dataset – Manual Feature Tracking

Manual estimates of velocity can be obtained by direct comparison of overlain orthomosaics however these observations are considerably sparser, time consuming and subject to human error (Kraaijenbrink *et al*., 2016). By comparing COSI-Corr estimates to that of manually plotted comparisons, the former can be validated. Table 4.2 shows manually estimated velocity rates per year over winter and summer time periods. As mentioned in Section 4.2.2.1 Velocity Data for 2016 and 2017, the sampling area is reduced here due to the increased noise from these longer time periods. Mean velocities and standard deviations in the eight AOIs were calculated and found to roughly match the same velocities and standard deviations obtained through the COSI-Corr process (Figure 4.7). Figure 4.8 shows the locations of these manual estimates which were concentrated on features such as horizontal crevasses and supraglacial debris. By comparing the manual and COSI-Corr derived values, using a paired t test, a two-tailed P value of 0.017 was found which is considered to be statistically significant in their similarity.

Table 4.2: *Estimates of average ice flow velocity per year via manual and COSI-Corr feature tracking for both winter (6/9/16 – 5/7/17) and summer (7/7/17 – 3/9/17) within the areas denoted in Figure 4.5.*

Area	COSI-Corr Summer Velocities m/yr	Manual Summer Velocities m/yr	COSI-Corr Winter Velocities m/yr	Manual Winter Velocities m/yr
1	29.96	20.25	7.00	8.57
2	34.79	17.08	6.5	7.19
3	21.54	14.27	8.26	6.75

4	35.91	19.71	13.34	7.63
5	34.82	23.00	11.61	13.65
6	38.59	27.60	13.70	12.63
7	43.70	19.75	15.05	19.74
8	54.53	23.50	13.86	23.50

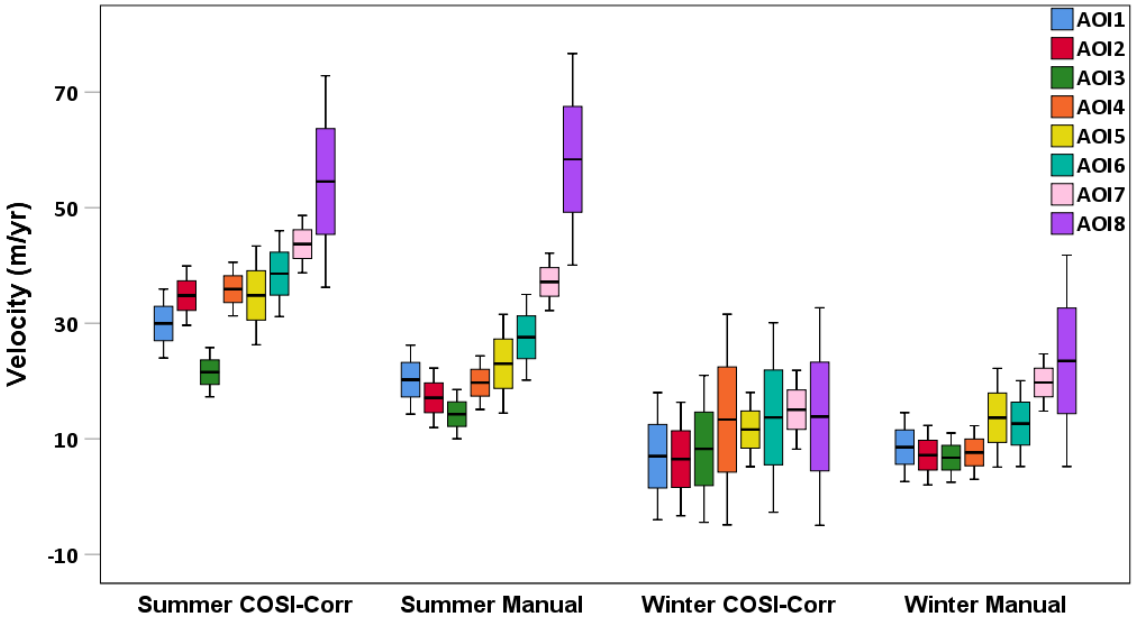

Figure 4.7*: Box plots of means and standard deviations for all AOIs from both Winter and Summer periods for both manual and COSI-Corr derived velocity.*

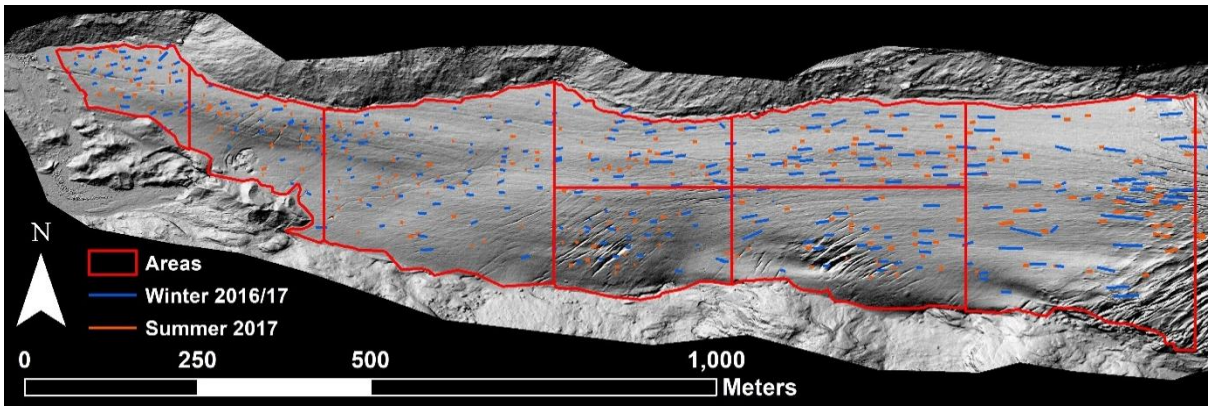

Figure 4.8*: Manual estimation locations and areas for Table 4.2.*

4.2.2.3 Feature tracking changes across Findelengletscher

Results of spatial velocity data for Summer (5th July – 7th September 2017) and winter (6th September 2016 – 5th July 2017) are shown in Figure 4.9. The first thing to note is that as expected, winter velocities are significantly lower than that of summer, on average 3.45 times lower (Figure 4.7). Summer velocities are seen to be low in AOI1, with predominant directions ranging from WNW to NNE. Velocities in AOI2, when compared to AOI1 are much lower which would explain the transverse crevasses in this area appearing due to longitudinal stress. Velocities in the winter at these two areas show similar findings. With the main flow pathway cutting SW across the overdeepening and the water exiting the glacier though a portal to the south of this area (46°00'32.9"N, 7°49'42.9"E).

Comparing velocities from AOI4 & 5 show that the glacier moves on average 41% faster in AOI5, the north of the glacier than the south. This would suggest that the central flow line is located slightly north of the AOI4-5 border (running through AOI5) as per the GPR findings and where higher velocities are expected. Moving further up glacier, AOI6 and 7 show a similar set of findings with glacial velocities averaging 82% faster at AOI7 than AOI6. Both AOI4 & 6 are heavily crevassed areas to the south of the glacier that have high slope angles down towards the medial extents. AOI5 & 7 on the other hand are flat and situated over the deepest parts of the glacier when looking transversely and therefore will exhibit higher velocities from internal deformation alone.

AOI8 was highlighted due to the high velocities present here, 54.53 m yr on average across the summer melt season – comfortably the area with the highest velocity. This location also experienced substantially higher annual ice loss than any other AOI within the field site (25 m), (see Figure 3.28).

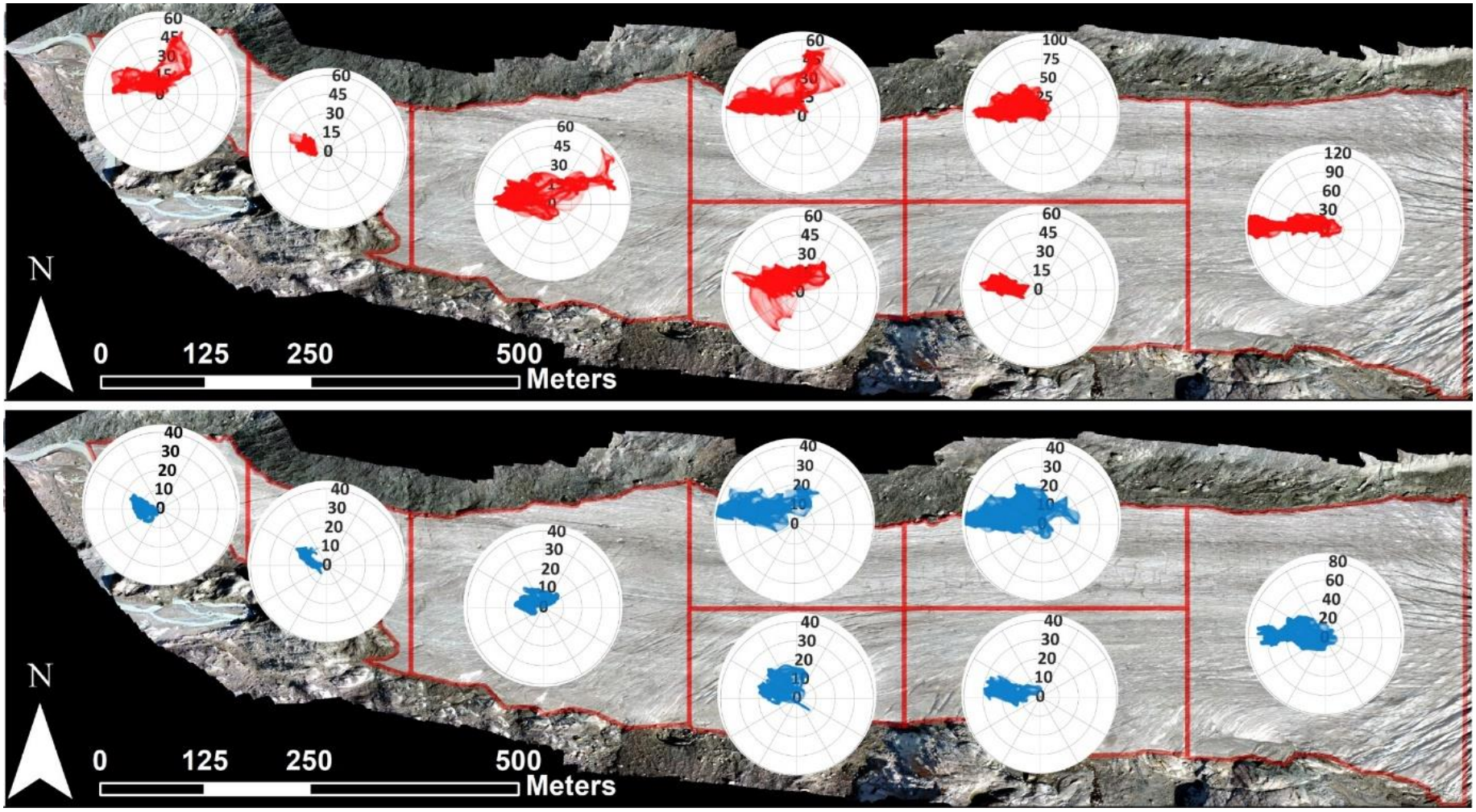

Figure 4.9*: Individual areas of interest at Findelengletscher (depicted in Figure 9) showing velocities and direction over the summer 2017 (red) and winter 2016/17 (blue) seasons.*

4.2.2.4 Flow directional variability

As expected, when taken as a whole, flow direction is generally down glacier. However, Figure 4.9 shows that there are some levels of divergence from this downhill (westerly) movement. For example, in the summer, AOI3 shows some easterly movement as well as the predominant westerly trend. AOI1, 4 and 5 also show a good deal of directional variability in the summer. All show a general trend of moving downslope however there is movement towards the lateral areas of the glacier too.

Winter periods show more uniform downhill directional movements more than summer. There is more movement in general across the glacier in the summer, so it is expected that there is more variability also. Directional movement is more uniform in the up-glacier areas of the study site (AOI5, 7, and 8) in both summer and winter, however the down-glacier areas exhibit less predictable behaviour. More consistent and uniform directional measurements can be seen in AOI6, 7 and 8. These areas are the furthest from the terminus and therefore less affected by variations in meltwater availability.

As already mentioned, manual comparisons of the glacier flow directions were also recorded for the longer time periods between F5 and F6 (6th Sept 2016 – 5th July 2017) and F7 and F8 (7th July 2017 – 3rd September 2017) due to the increased noise in the COSI-Corr results (Figure 4.8) and Table 4.1. It can be seen from Figure 4.8 that the variance in direction is a lot higher down-glacier than up-glacier from manual estimates. When comparing these findings to COSI-Corr data of AOIs, the same trend can be seen (Figure 4.9).

Directional differences appear to change very little when comparing the same AOIs from Summer and Winter except for AOI3 (discussed above) and AOI1; due perhaps to low ice thicknesses and melt

4.2.2.5 Velocity changes across the Overdeepening

The overdeepening identified in the previous chapter can be explored in further detail to see whether bedrock morphology and the associated processes this causes can influence ice flow velocity and direction. Alley *et al*. (2003a) state that overdeepenings are important components of the glacial environment and through enabling suitable conditions for supercooling and other processes of a hydrological and sedimentary nature, exercise "first-order controls" (Alley *et al*., 2003 p.140) on how a glacier behaves.

Noticeably, from Figure 4.10 velocities are slightly higher along the central flow line when compared to flow lines 15 m either side which is to be expected. However, an area of high velocity immediately up-valley of the overdeepening and 15 m to the north of the central flow line can be seen, with velocities of 4 m yr^{-1} more than the centre line, present in this area. This is likely to be due to this area being on the lee side of a moulin and as such has a greater supply of meltwater increasing the lubricative effect on the bed in this area. However, it is also possible that this small area of increased velocity is due to uncertainties in velocity from the method used to acquire velocity.

These examples show the potential for small changes in surface velocity across a glacier to provide support for subglacial features below. The availability of higher resolution data at glaciers currently, particularly UAV derived data and in the future from ever-improving satellite imagery could drive the potential for these observations to be incorporated into ice thickness observations in order to estimate bed topography (Gantayat *et al*., 2014).

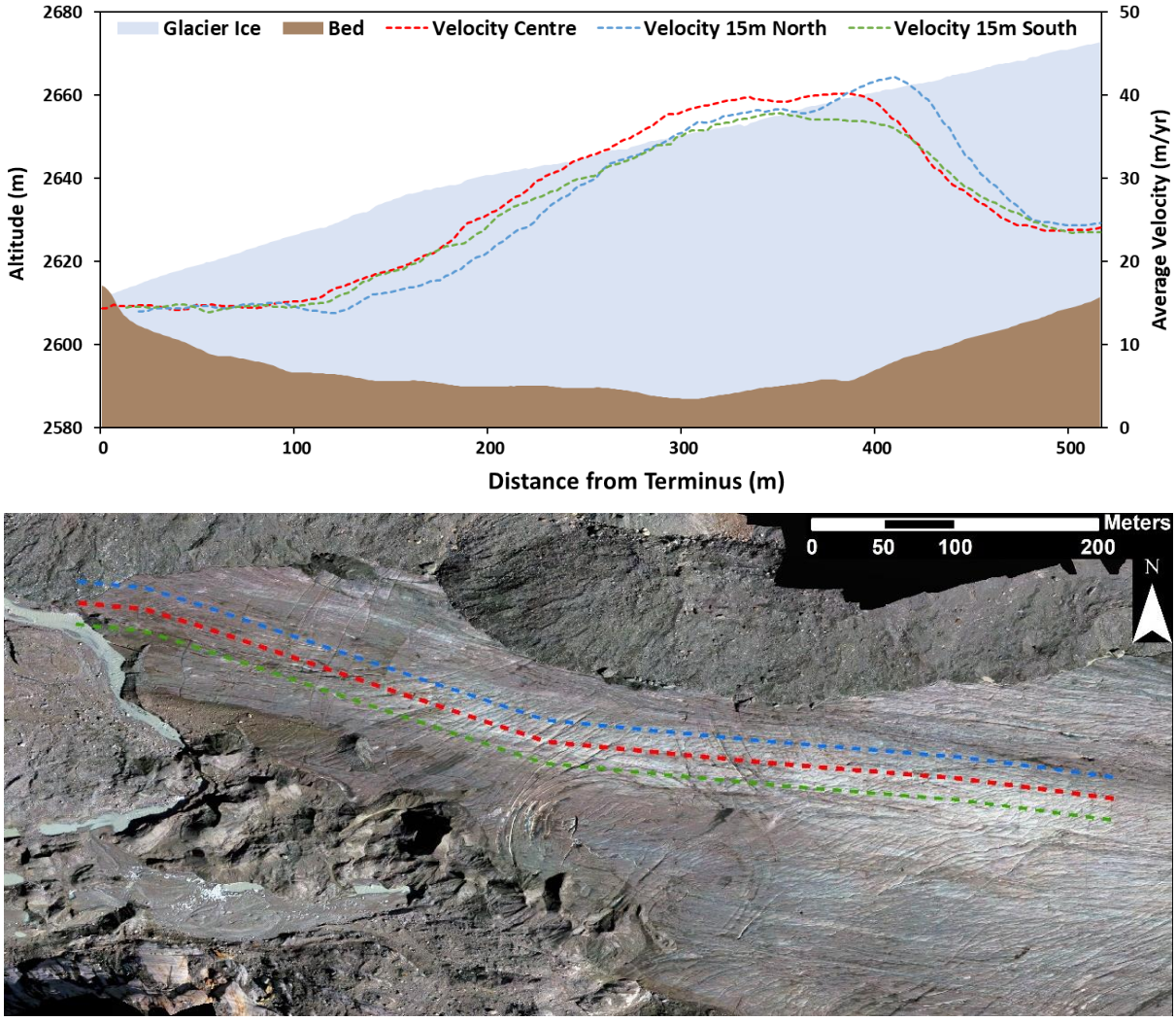

Figure 4.10*: Surface velocities from August 27th – 6th September 2016 along the central flowline through the overdeepening at the terminus of Findelengletscher.*

4.3 SUMMARY

In conclusion, the key findings from this chapter are as follows:

Longitudinal velocities across the overdeepening range from ~20 - ~40 m yr and were shown to mirror the pattern of those found in other valley glacier overdeepening studies (Hooke *et al*., 1989; Alley *et al*., 2003), underpinning the reliability of using small scale velocity fluctuations as a method for predicting the locations of overdeepenings remotely. The

velocity findings also contradict findings where ponding is present at the overdeepening, suggesting that ponding is not occurring beneath this glacier.

The ice flow velocity has been plotted on a spatial level and comparisons made. In keeping with studies (Copland *et al*., 2009; Truffer *et al*., 2009) average velocities were found to decrease when approaching the terminus. Directional flow was also found to be much less uniform closer to the terminus. Manual and automated (COSI-Corr) feature tracking agreed on both these aspects.

The presence of supercooling at the adverse slope of the overdeepening may reduce ice flow velocities due to the refreezing of basal meltwater along with removal of basal sediment increasing friction. However, there was no conclusive evidence that this was what was occurring despite reduced ice flow velocities being recorded here (and the presence of basal sediment entrained in ice noted in Section 3.3.2.2).

The following chapter will focus on the temporal differences in glacier flow velocities, looking at how glacier velocities change over time seasonally and comparing these results to the interpolation of baseline velocities developed in this chapter.

5. TEMPORAL PATTERNS OF FLOW VELOCITY AT FINDELENGLETSHER

5.1 INTRODUCTION

This chapter is concerned with the dynamics of flow (i.e., velocity patterns over time) at Findelengletscher and how these might be influenced by subglacial topography and its implications for the subglacial hydrology of the glacier (See Chapter 1). Velocity measurements were obtained at Findelengletscher during two late-Summer periods (2016 and 2017) and one spring period (2017, enabling comparison of annual, late-summer, winter, spring, and spring-summer velocities during the 2016-17 balance year. Interpretation of these patterns has been aided by comparisons with the temporal flow pattern that would be anticipated in the ablation region of a typical temperate Alpine glacier that does not have a significant overdeepened area at the bed (e.g., Haut Glacier d'Arolla; cf., Mair *et al*. 2001). As per chapter 4, the velocity data have been obtained using SfM and feature tracking methods (Chapter 2), and interpretation is further aided by knowledge of bed topography and hydrology (e.g., by application of GPR; see Chapter 3). The chapter utilises the subareas of the glacier surface used in Chapter 4 as 'areas of interest' (AOIs) to assist the analysis and interpretation.

5.1.1 Structure of the chapter

Section 5.1 will discuss the aims of this chapter and the importance of investigating ice flow behaviours temporally. Section 5.2 will look at the role of climatic conditions on glacier dynamics before comparing velocity between the baseline model and Winter, Spring and Summer periods. Section 5.3 will take a closer look at temporal changes to the glacier at specific Areas of Interest. Following on from this, a comparison of the flow velocities and ice loss at the glacier will be the focus of Section 5.4. Finally, Section 5.5 will investigate ice loss from a temporal perspective. Finally, the major findings of the chapter will be summed up in Section 5.6.

5.1.2 Importance of understanding temporal flow patterns

Understanding how glacier dynamics behave and change on a temporal scale is important when exploring the seasonality inherent with subglacial hydrological transport of sediment due to the ever-changing hydrological conditions within and beneath a glacier as outlined in Chapter 1 (Section 1.2).

Overdeepenings are suspected of inhibiting the growth of channelised systems (Cook & Swift, 2012) which would mean around this area there would be a speed-up of glacier velocity for longer durations as the system would remain inefficient at expelling meltwater around this overdeepening and not form channelised, efficient hydrological flow routes.

If this prolonged period of higher velocity due to reduced drainage efficiency is present over substantial enough areas to affect large parts of the glacier, including for example the riegels between overdeepenings, it would signify that glaciers with overdeepened beds are more sensitive to a warming climate, and would provide an increased rate of discharge due to

higher velocities. In ocean terminating glaciers this would result in more discharge into the ocean and a more rapid sea level rise.

5.2 EXPECTED GLACIER REACTION TO CLIMATIC CONDITIONS

Whilst all glaciers behave differently, the consensus is that a trend across mountain glaciers exists whereby – relative to winter and annual velocities – glaciers show a speed up in the spring when melt meets a distributed system and a slowdown in the autumn when melt enters a channelised system that grows during late spring and early summer. Sundal *et al.* (2011) shows this broad pattern (Figure 1.7) when comparing summer velocities as a percentage compared to winter. Here, a) is the traditional model where melt is high, and a spring event is followed by channel evolution and therefore summer slowdown and b) where melt water was not as high, and the channel system did not evolve as widely or efficiently. By comparing these two patterns to the findings at Findelengletscher, a pattern as to the development of the hydrological system can be seen.

It is expected that when comparing Findelengletscher to that of its interpolated baseline, average velocities would be slower in the winter, slightly faster in summer and much faster in spring. Orthomosaic pair dates for these dates are shown in Table 5.1. The spring period is represented by an orthomosaic pair 2 days apart, therefore it is important to consider temperatures and other climatic conditions at this time and decide whether this is representative of 'Spring' as a whole. Average 24-hour temperatures were 10.85°C across the two-day measurement period compared to 8.12°C during June and July (Swisstopo, 2018) suggesting that velocities may be slightly over reported. However, during the two days no precipitation was recorded compared to 173.7 mm in June and July (Swisstopo, 2018), this

lack of precipitation could reduce the amount of sliding from reduced friction caused by the precipitation. Ultimately though it is considered the conditions recorded were largely representative of Spring.

Table 5.1: *Model orthomosaic pairs and their time spans.*

Model	Orthomosaic 1	Orthomosaic 2	Time Period (Days)
F2-F3	27th August 2016	31st August 2016	4
F3-F4	31st August 2016	3rd September 2016	3
F4-F5	3rd September 2016	6th September 2016	3
Winter (F5-F6)	6th September 2016	5th July 2017	302
Spring (F6-F7)	5th July 2017	7th July 2017	2
Summer (F7-F8)	7th July 2017	3rd September 2017	58
F8-F9	3rd September 2017	7th September 2017	4

The interpolated baseline velocities from two sets of orthomosaic pairs from the late summer melt seasons of 2016 and 2017 were averaged and the results smoothed to create a baseline model (discussed in Section 4.3). The subtraction of three of these models (Winter, Spring and Summer) from the baseline will show residual data which will be used to analyse seasonal patterns at Findelengletscher.

5.2.1 Climatic Influences on Dynamics

As can be seen in Figure 5.1, in both the 2016 and 2017 melt-season, the discharge shows a strong association with atmospheric temperature. A small lag (due to meltwater transport times) in the discharge's response to temperature change indicates that the temperature (and therefore levels of melting) directly affects the discharge of the glacier. For example, where temperatures are high, discharge rates are also greater and vice versa. This is especially clear from a number of instances in Figure 5.1, namely mid-July 2016 and late June, mid-August and early September 2017, where both temperature and discharge rapidly decrease. Instances where increased temperature has brought about a noticeable increase in discharge

are mid-June and late-August 2016, and mid to late-June and early August 2017. 2017 showed discharge to be higher than in 2016, due to temperatures also being warmer, this despite an receiving less precipitation across this time period (MeteoBlue, 2017) suggest that the melt from increased temperatures is the dominant factor in discharge rates.

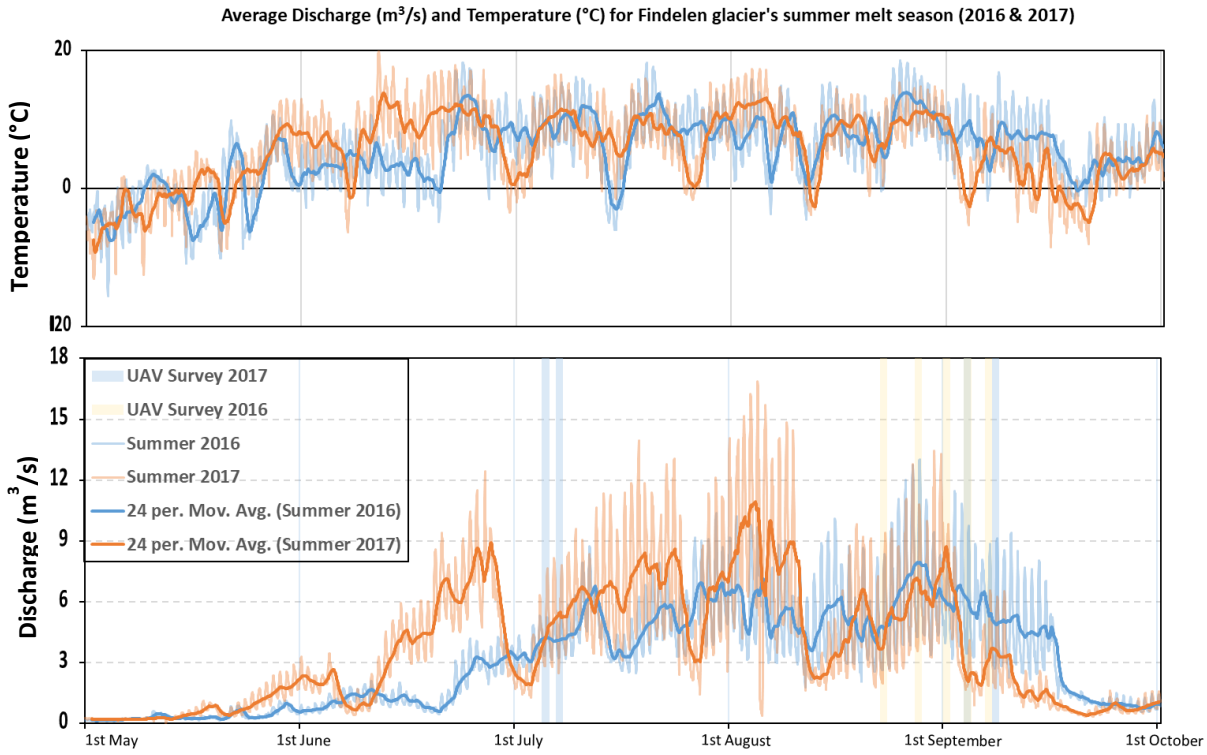

Figure 5.1: *Temperature (°C) (above) and discharge (m^3 s) (below) of Findelengletscher over the summer melt seasons of 2016 and 2017.*

By calculating the averaged velocity data across the entire study area for the Winter, Spring and Summer orthomosaic pairs as well as the baseline velocities (calculated by averaging flights from 3rd-6th September 2016, and 3rd-7th September 2017) can be obtained. By comparing them to average atmospheric temperatures during the time periods between these orthomosaic pairs (Figure 5.2 & Figure 5.3), it can be seen that a similar trend exists whereby temperature and ice flow velocities are positively correlated.

From the dataset it is also possible to compare velocities from mid-melt season to that of the late-melt season within a single year (Figure 5.4). The average temperatures (and discharge) in July 2017 were substantially higher than in September 2016 and 2017 when measurements were carried out (Figure 5.5). It was expected that average glacier velocities would be higher in July due to a less developed hydrological system being in place beneath the glacier as discussed in Section 1.2.2, where a less efficient transport system causes more water to stay within the system for longer, lubricating the bed, decreasing friction, and increasing sliding. During the 5^{th} – 7^{th} July time-period, much warmer temperatures (Figure 5.3) and drainage volumes (Figure 5.2) were recorded which led to increased meltwater providing more favourable conditions for sliding (Herman *et al*., 2011). So, it could just be a case of more meltwater inputs being available at this time than to do with the drainage system.

By cross-referencing ice flow velocity with average temperatures present at the time of the four coupled UAV flights, it can be seen that there is a strong link between these two variables and that therefore temperature is a considerable driver behind ice flow velocity and is responsible for significant changes to the glacier's flow speed (Figure 5.3).

Looking in more detail at the regression analysis of velocity vs both discharge and temperature, for each of the AOIs, we can see that positive correlations exist in all areas. The weakest areas of correlation were AOI 4 and AOI 5 for velocity vs temperature (R^2=0.52 and 0.66 respectively), suggesting that these areas were not as affected by temperature as the rest, however these areas displayed the higher positive correlations between velocity and discharge. The strongest relationships between temperature and velocity were found to be at AOI 1 and AOI 8 with R^2=0.83 and 0.84 respectively, the terminus and the area immediately down glacier of the ice fall respectively. Expectedly a strong correlation of between discharge

and temperature was found to exist, which would likely have been stronger but for the lag time between temperature and discharge which in some cases appeared longer than the sampling period (Spring – 2 days and Baseline – 3-4 days) which can be seen in Figure 5.2. It should be noted that the number of data points, due to the limited time periods between UAV flights, meant for a limited regression analysis. The overdeepening present in AOI 2 did not appear to affect the relationship of the velocity in this area to discharge or temperature (R^2=0.70 and 0.73 respectively) compared to other AOIs. However, it can be seen in Figure 5.3 that velocities did increase in this area into the summer where most AOI velocities decreased.

Figure 5.4 shows the average velocity of the glacier across the field site over the period of study. The velocity peaked during the Spring measurement and dropped to its lowest velocities during winter. During periods where high velocities were recorded, the spread of velocities were high, whilst during periods of relatively low flow standard deviations were small. This is considered to be due to the errors at the margins where velocities were near zero being included in the data. It is possible due to the window sizes and manual estimations of the glacier boundary, that some velocities are included that are not part of the flowing glacier. When velocities are higher the difference between these low velocity errors and the high velocity results are more noticeable. Temperatures during the beginning of September 2016 were on average 1.83°C higher than at the same time in 2017 (Figure 5.1), and this is a possible reason why velocities were faster in 2016, especially considering the glaciers strong correlation between velocity and temperature (Figure 5.3). Further exacerbating this difference in velocity could be the lack of precipitation at this time in 2017 (Figure 5.4).

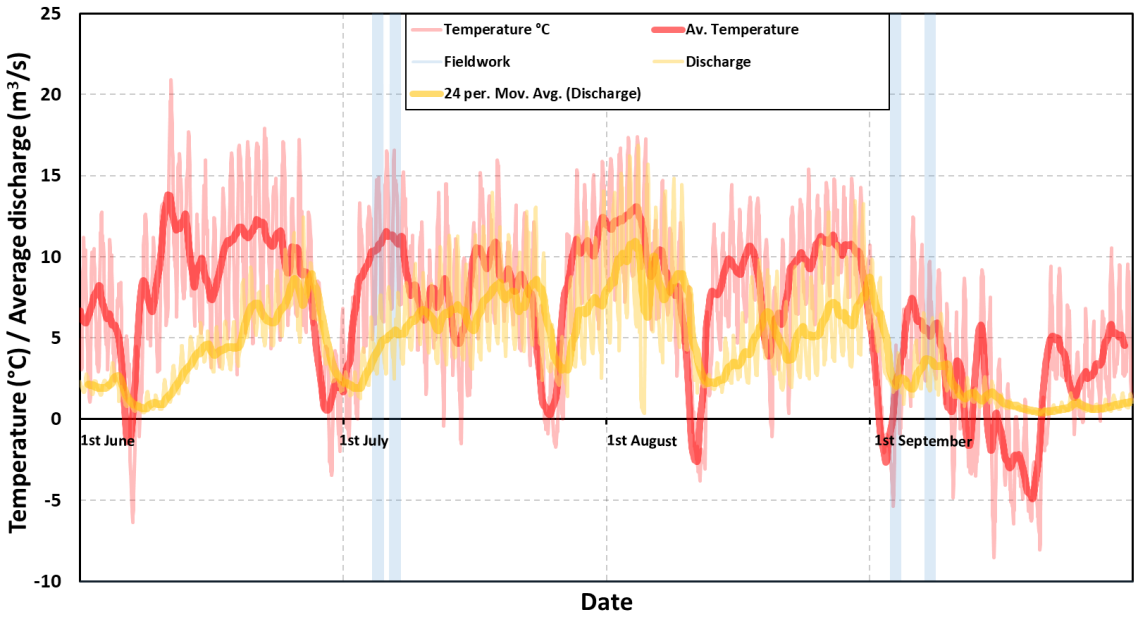

Figure 5.2: *Hourly temperatures and discharge at Findelengletscher over the 2017 melt season. Dates of UAV surveys are visible in light blue.*

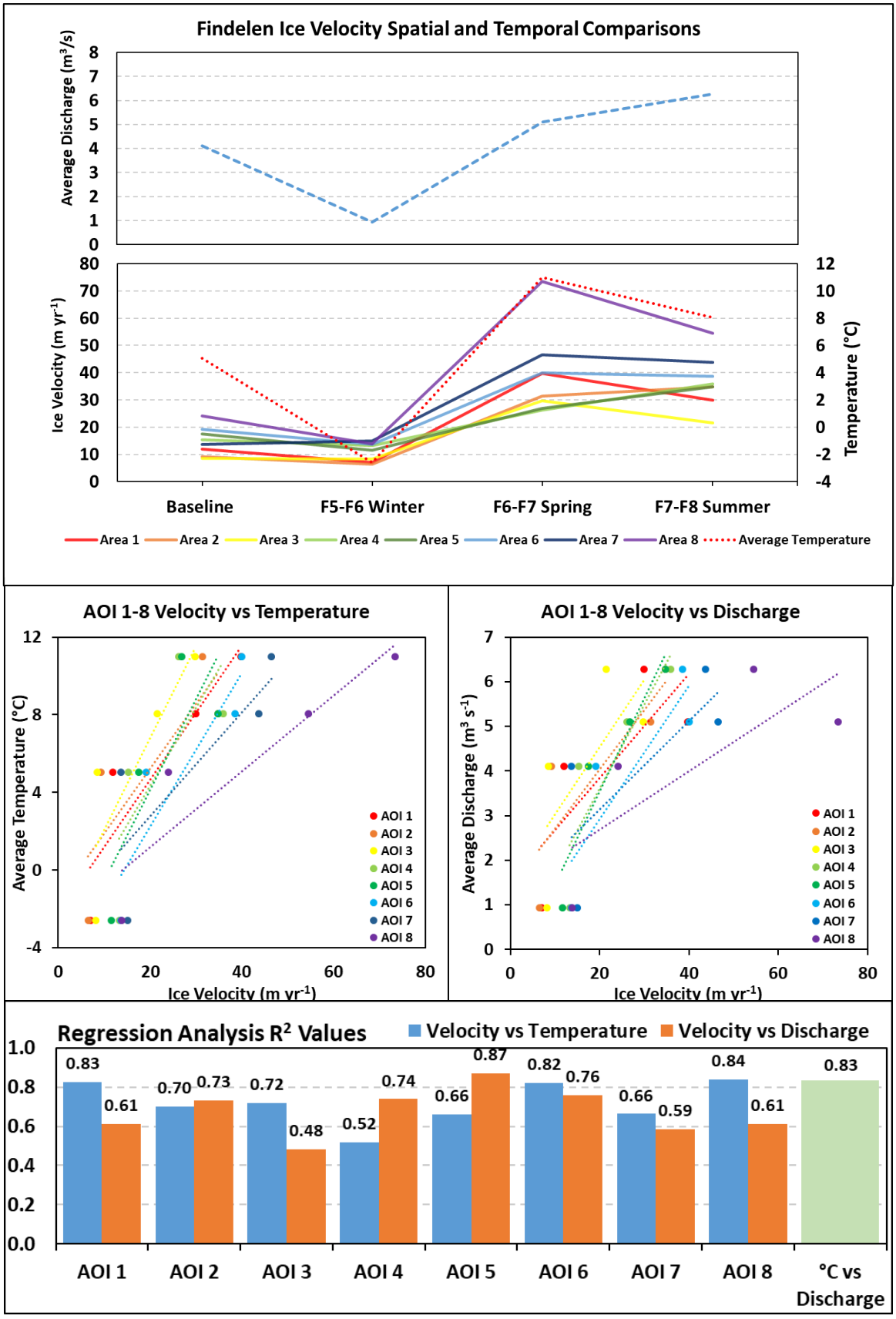

Figure 5.3: *Graph of ice flow velocities per area and average temperatures from time periods that data was collected.*

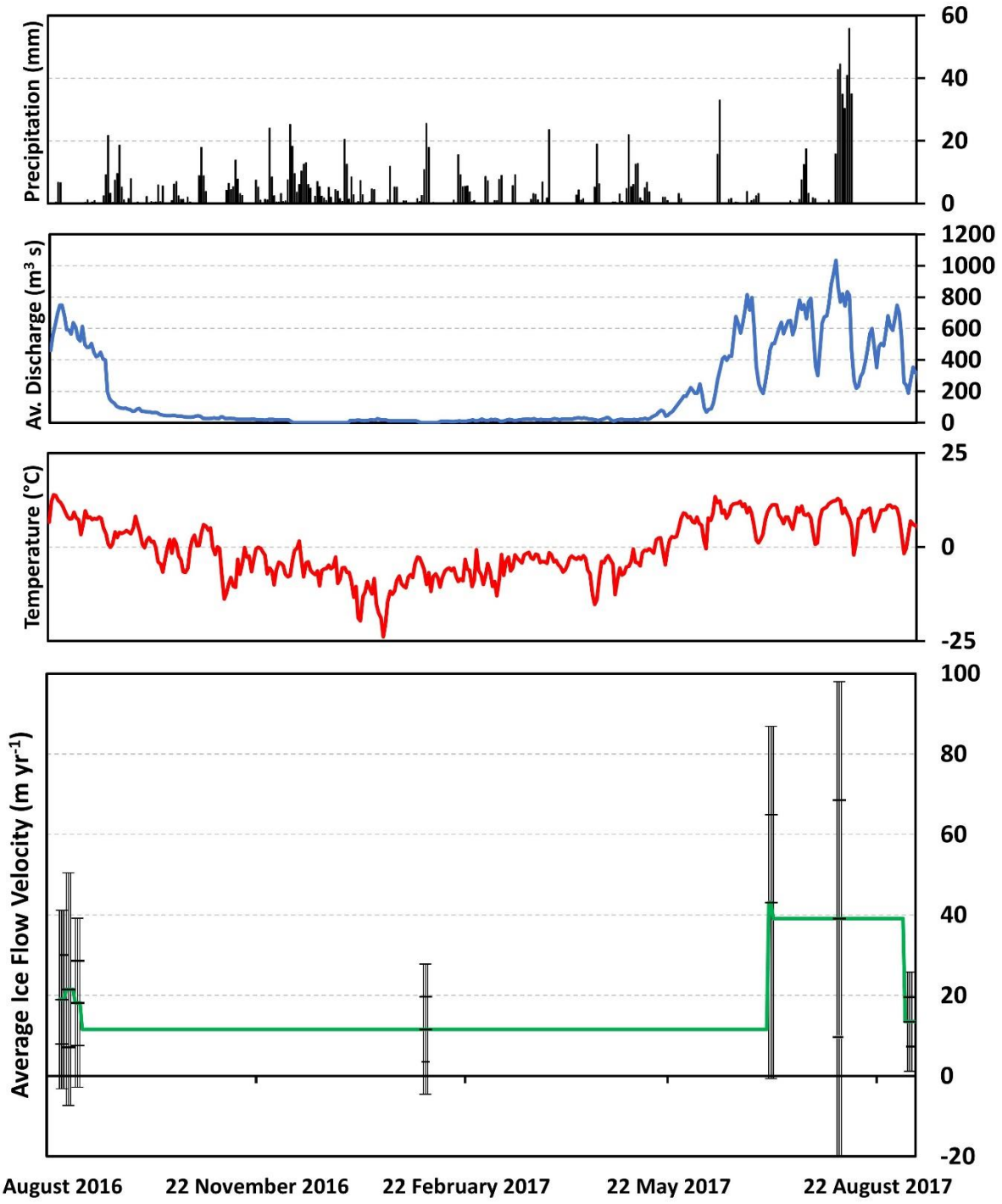

Figure 5.4: *Atmospheric conditions (precipitation, discharge and temperature) and mean velocities (black error bars show 1 and 2 standard deviations, green line represents averaged velocity between orthomosaics) at Findelengletscher over the study period.*

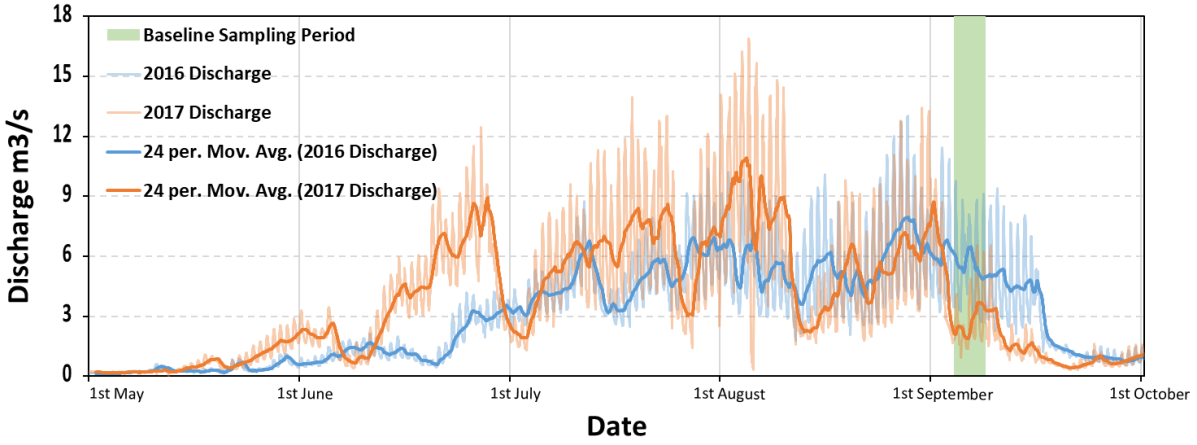

Figure 5.5*: Average Discharge (m^3/s) for summer melt seasons of Findelengletscher (2016 & 2017).*

5.2.2 Comparing Findelengletscher Data to Baseline Expectations

The following section will look at the residual findings for the three seasonal orthomosaic pairs (Table 5.1). Seasonal comparisons between the three time periods will be made.

Firstly, as previous discussed (Section 4.2.2.1) broad glacial velocities from Findelengletcher agree with what would be expected. A tendency towards higher velocities at the central flow line where ice thickness is greatest, which can be seen when comparing velocity percentage change patterns in Figure 5.6 with ice thickness levels in Figure 4.4, where velocity acceleration relative to the baseline approximately mirrors areas of high ice thickness. and decreasing ice flow velocities as the glacier approaches the terminus (Ai *et al*., 2019) (Figure 5.6, 5.7 & 5.8). It is when we look at the glacier more closely that we get findings that would be unexpected from a glacier with a uniform bed and profile. Smaller scale features show more individual characteristics that are influenced by the nuances in the bed-ice interface such as variances in localised mass loss over hydrological flow paths (Figure 3.28; Figure 3.29) Furthermore, supercooling, and velocity variability caused by an overdeepened bed have

made the terminus of this glacier into a complex system (Figure 4.6). Ultimately the morphology of the bedrock is responsible for setting into motion many different feedbacks that show up more clearly over shorter time periods and affect small areas.

The interpolation of glacier velocities shows some interesting patterns (Figure 2.48). Firstly, an area of higher velocity in the final 250 m is noted just down-glacier of the overdeepening. Secondly, velocities at the location just up-glacier of the overdeepening (AOI3) are low compared to that of the overdeepened area which may be indicative of a more distributed system of englacial routing at the overdeepening (Church *et al*., 2019). The baseline model shows higher velocities at AOI5 than AOI7, which would make sense considering the former has a steeper ice slope than the latter.

Importantly the levels of discharge during the time periods between orthomosaic pairs was low relative to the rest of the summer as can be seen in Figure 5.5. Therefore, velocities of the baseline will reflect autumn levels of ice flow whereby temperatures are still warm enough for surface melt and the drainage system is efficient enough to transport this melt efficiently, but in comparison to mid-summer velocities will be noticeably lower. If the subglacial hydrology is more distributed, it is expected that higher velocities would be present towards the end of the melt season.

5.2.2.1 Winter Velocity 2016/17

Looking at the Winter residuals, created by subtracting the Winter orthomosaic pair from the interpolated velocity model, it can be seen that in general velocities are much slower, particularly just up-glacier of the overdeepening and at the far eastern extent of the field site, just down-glacier from the ice fall (Figure 5.6).

A more uniform rate of ice flow is expected in the winter months (Amundson & Burton, 2018) due to the lack of meltwater and the increased basal sliding that this facilitates. Added to this, diurnal fluctuations are found to be virtually non-existent during the winter months (Nienow *et al*., 2005) due to the lack of supraglacial melt, and this leads to slow, steadier ice flow velocities. Looking at the percentage change to average ice flow velocity between the interpolated data and the winter period shows that a 10-200% increase in velocities over AOI7 and northern parts of AOI3 (Figure 5.6).

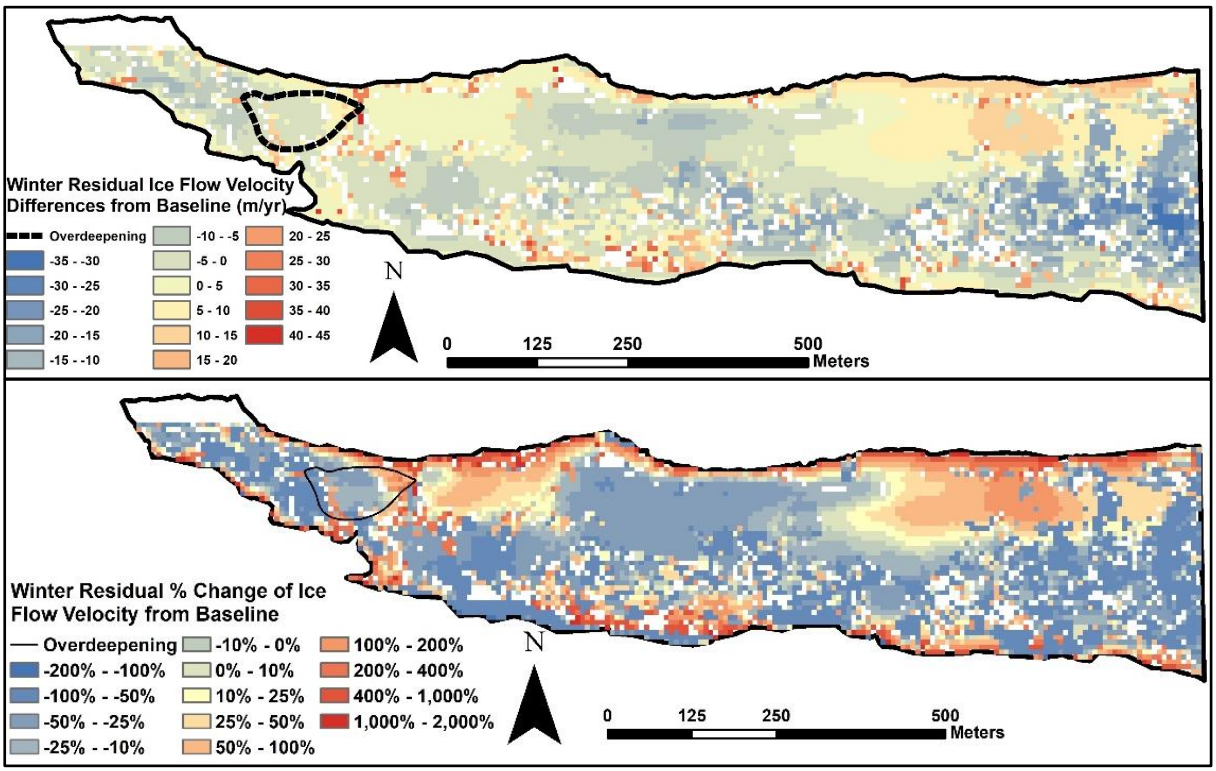

Figure 5.6: *Residual data from Winter (6th September – 5th July).*

5.2.2.2 Spring Velocity 2017

In this section we will look at how flow velocities change during the beginning of the melt season at points of interest on the ice surface such as above adverse slopes, overdeepenings, crevassed areas and areas displaying high levels of surface melt). The velocity patterns in Figure 5.7 show several circular features are present in the centre of the glacier. These align

with the area around the collapsed cauldron feature to the north of the portal, the two early-stage cauldron features highlighted in (Figure 3.17), as well as two other features further up valley along the central flow line and two other circular features at the south of the glacier along the lateral extent. Looking at the percentage change to average ice flow velocity shows fairly uniform increases of between 40-80% across much of the glacier for Spring (

Figure **5.7**). However, the centre of the glacier exhibits four distinct areas where percentage change between the interpolated data and spring was negative (velocities were slower in Spring than during the intervals used for the interpolation at the end of the melt season). AOI2 where the overdeepening is located shows only low levels increase in velocity at the adverse slope of the glacier (10-30%), whilst immediately up-glacier of the overdeepening, velocities were higher (60-80%).

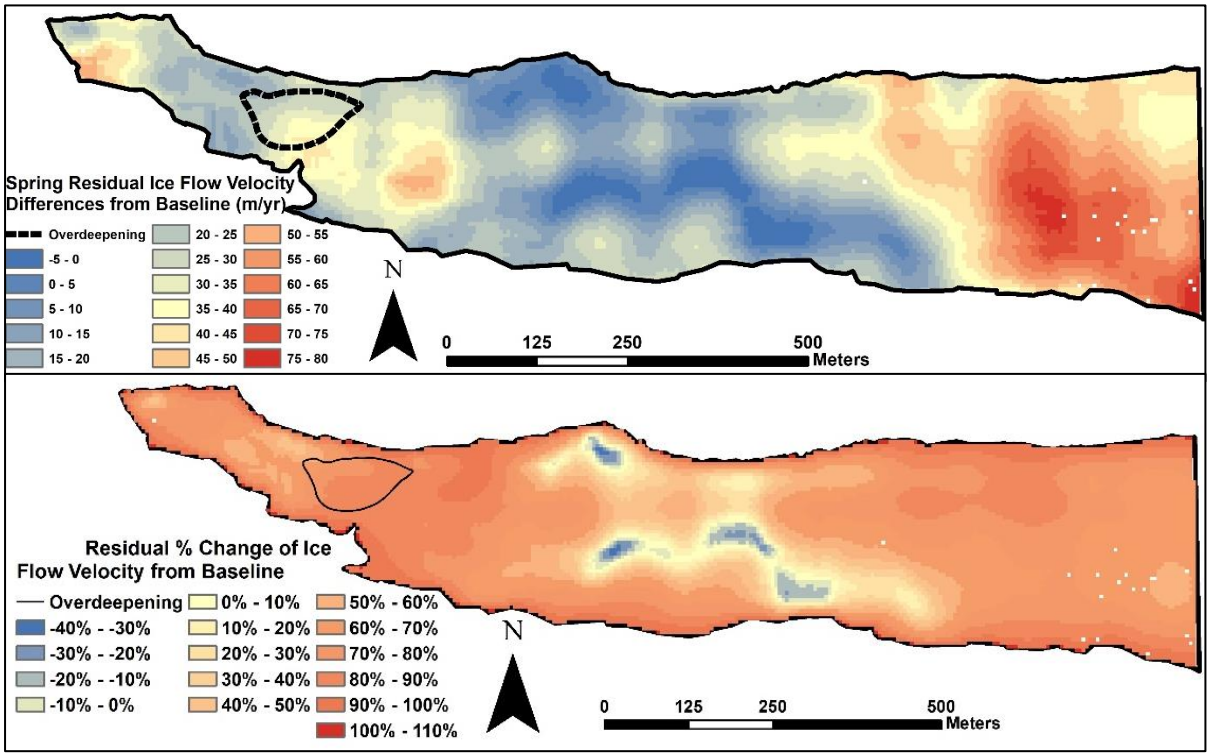

Figure 5.7: *Residual data from Spring (5th July – 7th July).*

5.2.2.3 Summer Velocity 2017

The summer velocities show some distinct patterns in glacier flow with average flow velocities lower than that of Spring but with one area with a noticeable exception, that being the collapsed cauldron feature to the north of the portal (Figure 5.8). This feature collapsed at some stage in this summer period and has led to estimations of glacier flow being very high in this area. The average velocities of 140-150 m yr^{-1} here are inaccurate due to the complete collapse of the feature. An error in the comparison of the orthomosaic pairs has led to velocity levels being miscalculated at this location.

Another area of interest here is located 200 m East of the cauldron collapse near the main water egress portal (see Figure 3.17 circles labelled '2017'), again in the area where mass loss was found to be significantly higher than the surrounding ice. As discussed in the previous section (5.2.1.2) this area is where a significant subglacial flow channel is situated. The difference in the residual data across the summer time-period suggests that velocities are between 40-70 m yr^{-1} higher at this location, a slight increase when compared to residual velocities at the same location in spring (35-55 m yr^{-1}). The percentage change to average ice flow velocity shows velocity increases across summer of 200-400% faster over the course of the summer for most of the glacier (Figure 5.8). An increase in velocities at AOI7 and northern parts of AOI3 of 400-700% was seen. The presence of a cauldron feature can be made out from heightened velocity change percentages ~100 m east of the overdeepening.

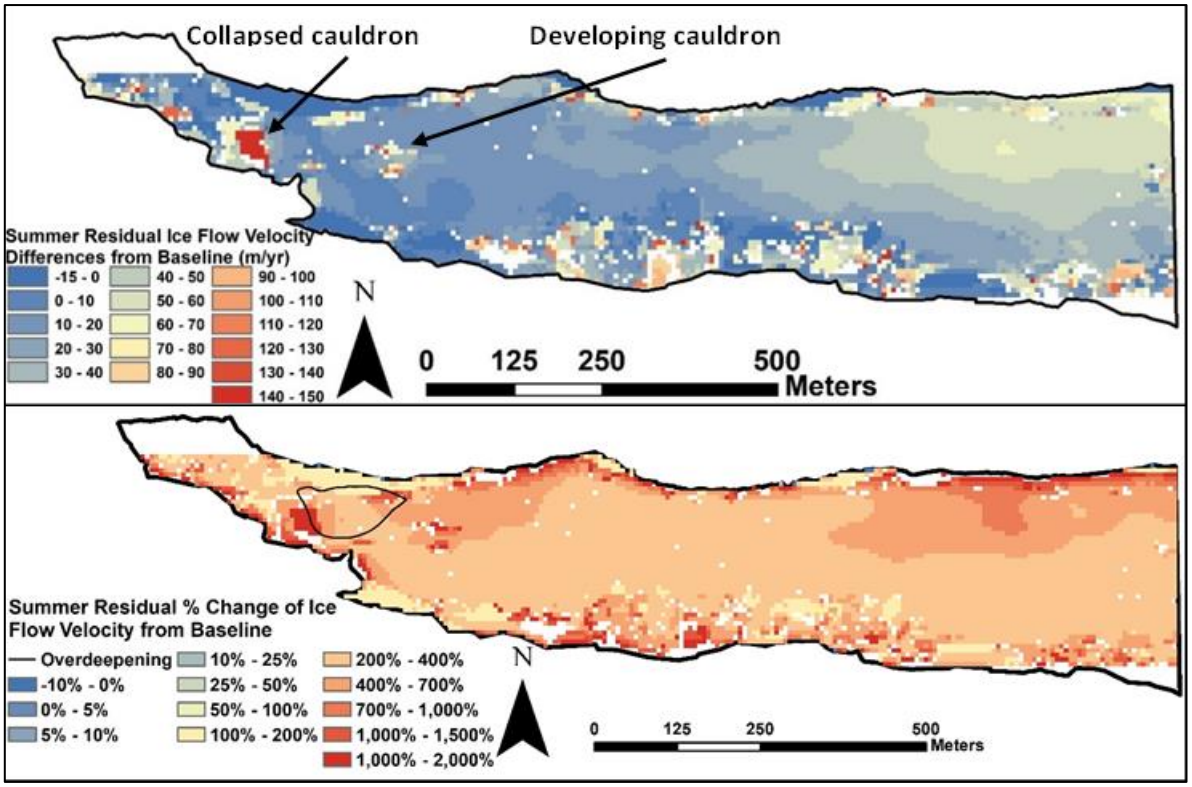

Figure 5.8: *Residual data from summer melt season, both velocity difference (m/yr) and percentage change from the baseline (7th July – 3rd September).*

5.3 TEMPORAL VELOCITIES AT AREAS OF INTEREST

In this section, the temporal variability of the areas of interest will be focused on. Results will be presented by looking at each AOI individually starting at the terminus and moving up-glacier (see Figure 5.9 for a map of the AOIs).

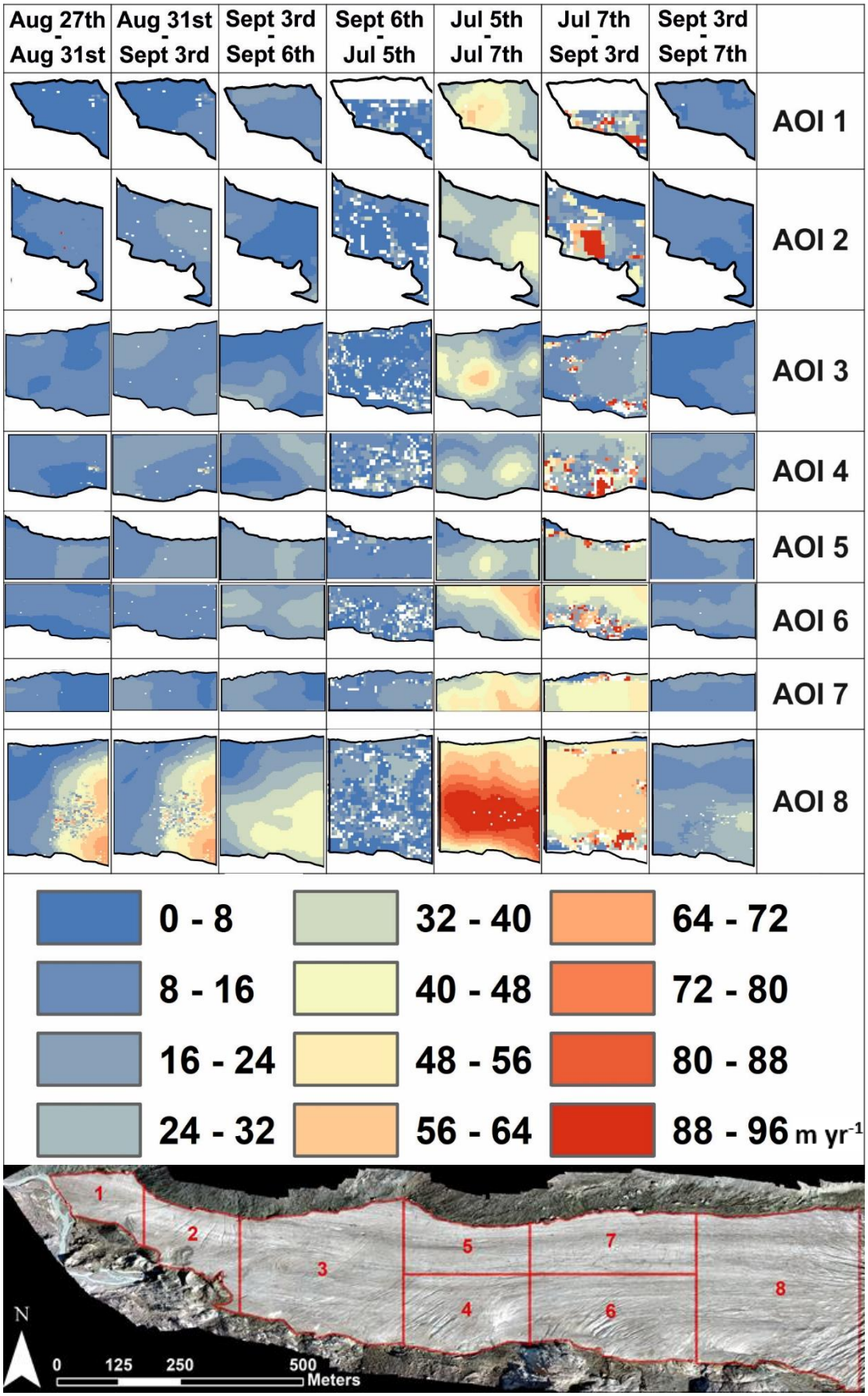

Figure 5.9: *Individual AOI and orthomosaic pairs grid.*

5.3.1 Areas of Interest 1-3

Temporal variations at the terminus of Findelengletscher show steady velocities over the end of the summer 2016 (F2-F3, F3-F4 and F4-F5) of 9-14 m yr^{-1} (Figure 5.10). As expected, velocities are found to dip during the winter (F5-F6) and peak during the Spring before getting slower as the summer comes to an end. Standard deviation (SD) of Winter, Spring and Summer are high when compared to the other orthomosaic pairs due to the longer time-period between orthomosaics.

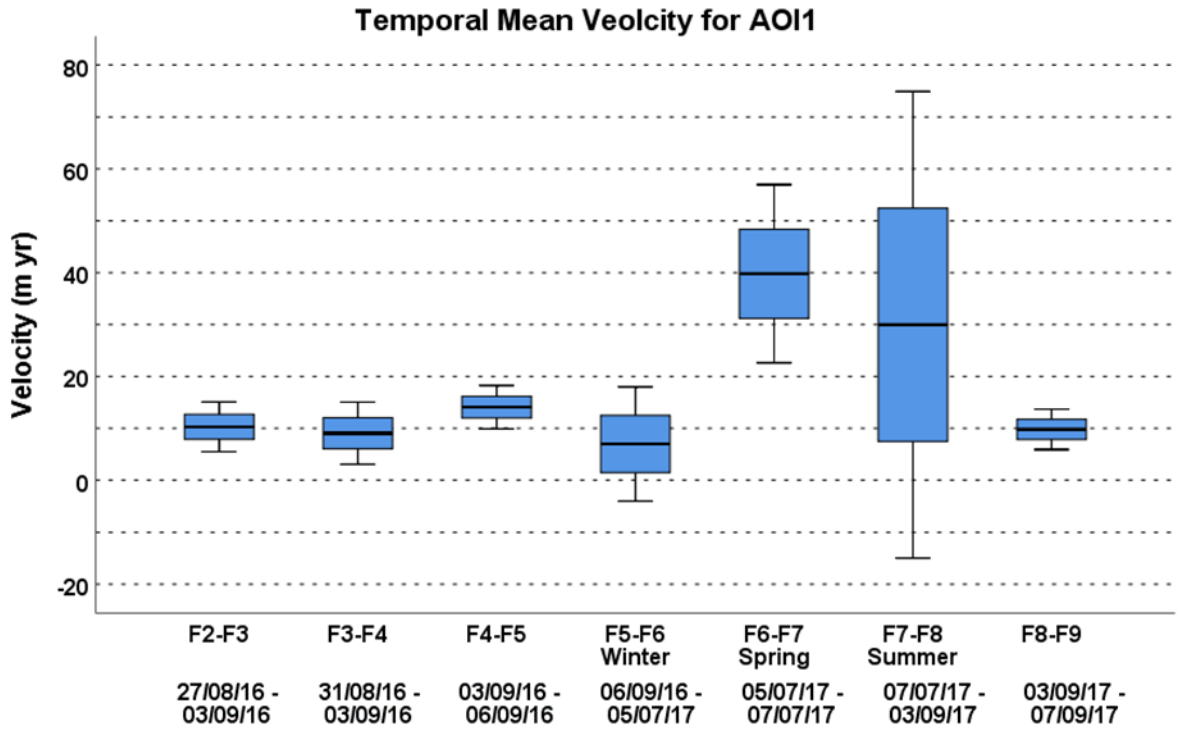

Figure 5.10: *Boxplots of AOI1 temporally from Orthomosaic pairs stretching from 27th August 2016 – 7th September 2017.*

AOI2 shows relatively consistent velocities with small standard deviations (Figure 5.11). The notable exception to this is during the Summer (F7-F8) where the velocity range varies considerably with a SD of 41.36 m. This is likely due to the collapse of a cauldron feature

during this period and the error this has been produced through a lack of pixel recognition between the orthomosaic pair. As expected, there is a general trend of velocity reduction at the end of summer 2016 and continuing through winter followed by higher spring velocities. Velocities were found to remain high for longer than surrounding areas over the summer period before slowing down toward the end of the summer.

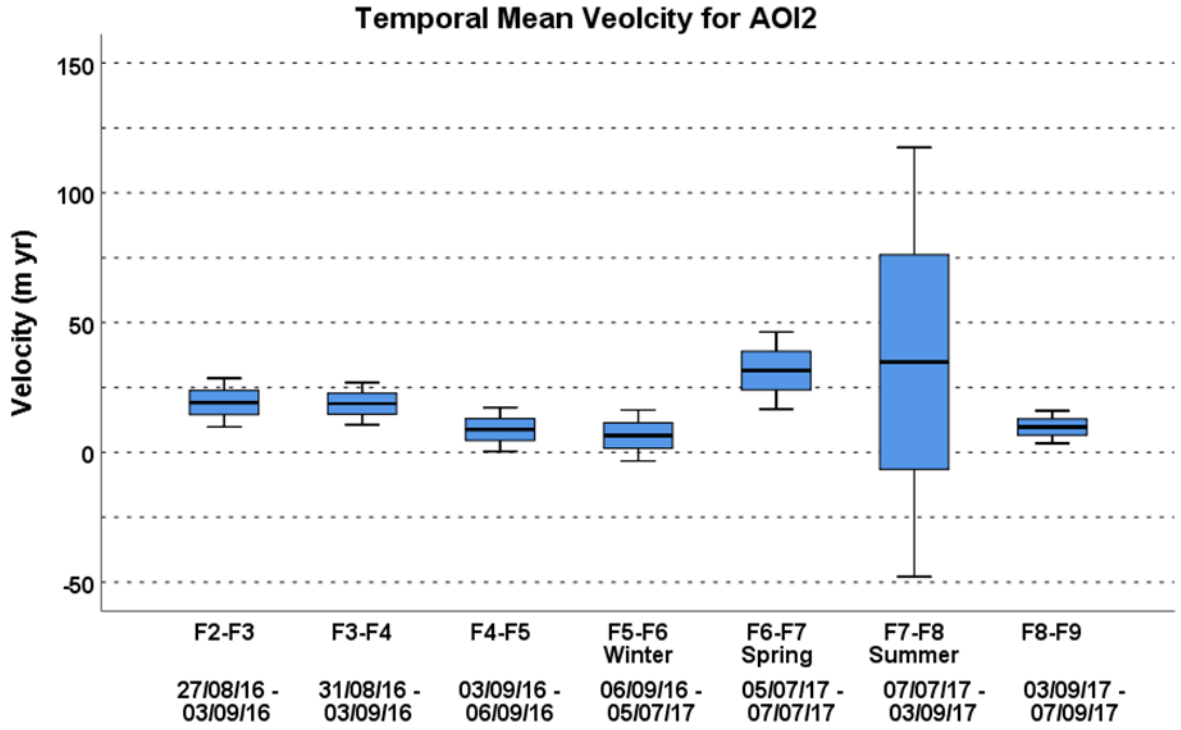

Figure 5.11: *Boxplots of AOI2 temporally from Orthomosaic pairs stretching from 27th August 2016 – 7th September 2017.*

The temporal velocities at AOI3 also follow the general trend of decreasing at the end of the summer and into the winter from 20m yr^{-1} (Figure 5.12) down to 10m yr^{-1}. Spring saw the average velocities peak, rising to 30m yr^{-1}, before declining into the summer and autumn. Comparison between the three AOIs (1, 2 and 3) shows that AOI3 has the largest SD of velocities across all time periods with the exception summer (F7-F8) velocities at AOI2, which as mentioned is a notable anomaly.

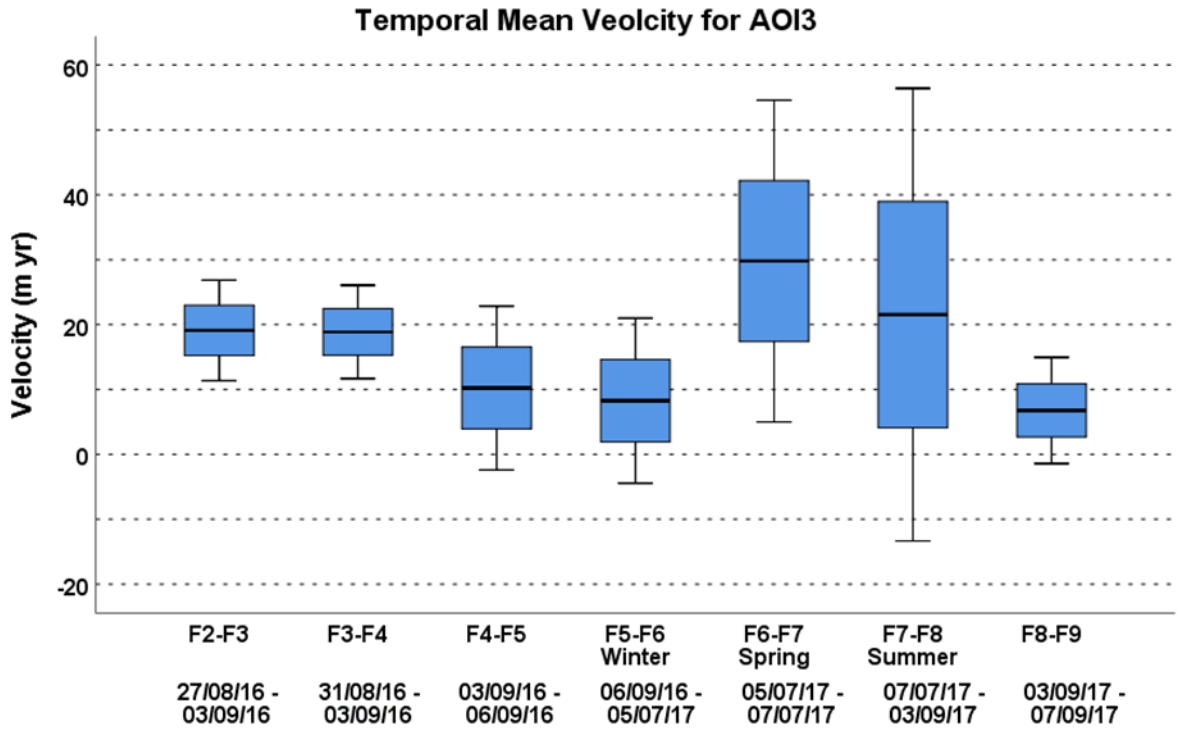

Figure 5.12: *Boxplots of AOI3 temporally from Orthomosaic pairs stretching from 27th August 2016 – 7th September 2017.*

Figure 5.13 looks in detail at AOI1 – AOI3 with a focus on the overdeepening discussed in Chapter 3. It can be seen here that the elevated area of velocity seen in most of these time periods (with the exception of 3rd – 6th September 2016) fits well with the overdeepening suggesting that velocities remain high into the late summer here both in 2016 and 2017. The area up glacier from the overdeepening where the channelised subglacial flow channel is understood to be (see Figure 3.25) and indeed seen to be after the glacier had retreated (Figure 3.30), demonstrates approximately 50% lower velocities than at the overdeepened area.

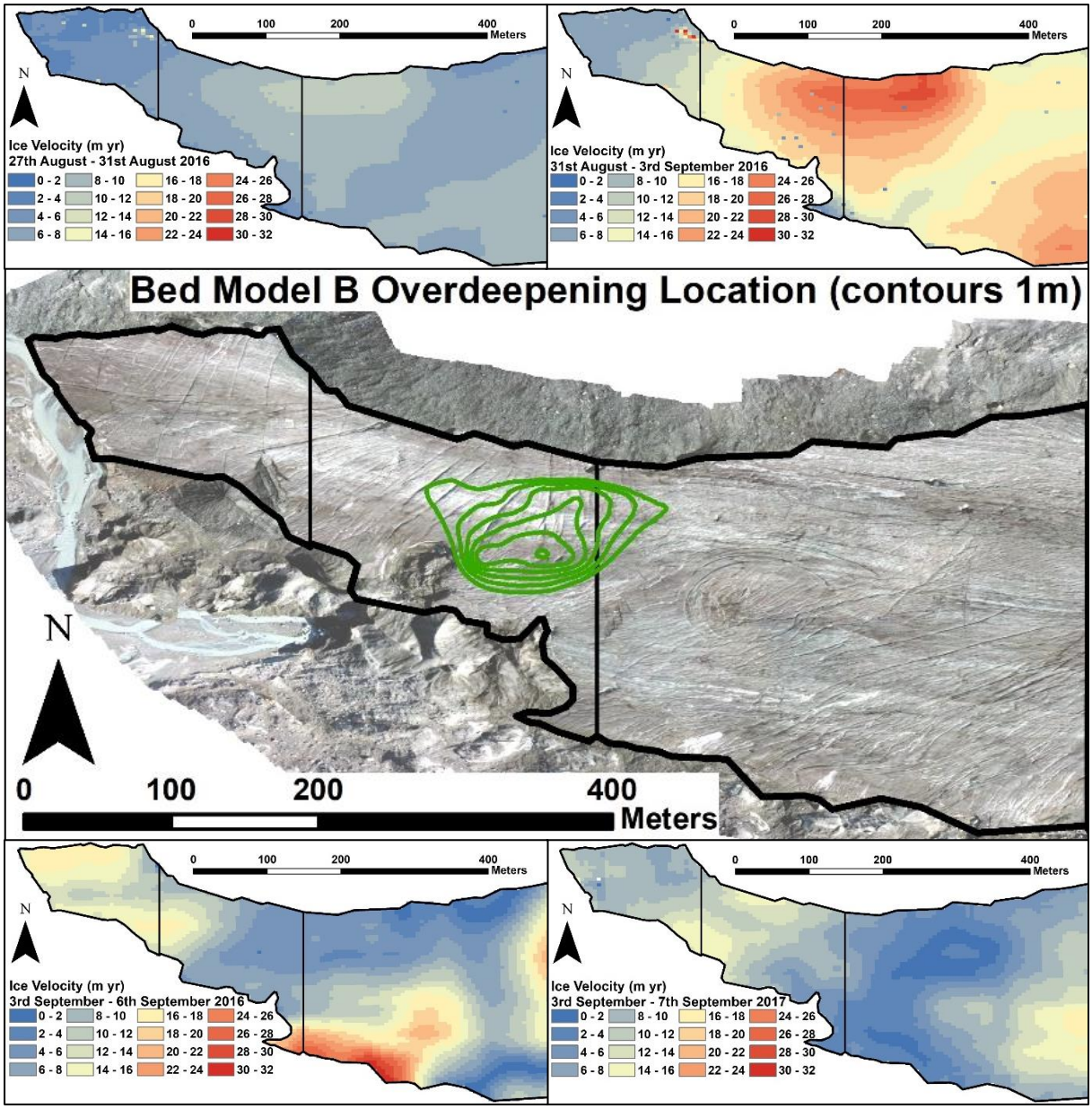

Figure 5.13: *Surface velocity at Findelengletscher overdeepening in late summer 2016 and 2017.*

5.3.2 Areas of Interest 4-7

The temporal mean velocities for AOIs 4-7 will now be described. These areas make up the mid-section of the field site. AOI 4 shows the pattern of steadily decreasing velocities through late summer and winter from 18.3 m yr^{-1} to 13.3 m yr^{-1}, before nearly doubling in speed in

spring to 26.2 m yr^{-1} (Figure 5.14). Whilst more terminal areas would decrease in velocity during the summer, AOI4 shows peak average velocities of 35.9 m yr^{-1} with a large spread of values before ultimately decreasing back to late summer velocities akin to the previous year.

Mean velocities across the year follow a very similar pattern for AOI5 to AOI4 with the velocity peak of 34.8 m yr^{-1} coming later in the melt season than spring (Figure 5.15). Between them, AOI4 and 5 cover the entire lateral extent of the glacier up-glacier from the overdeepening so it is not surprising to see them act similarly to one another. The surprising point here is that they continue to have higher velocities than the terminus regions late into the melt season, peaking later in the melt season.

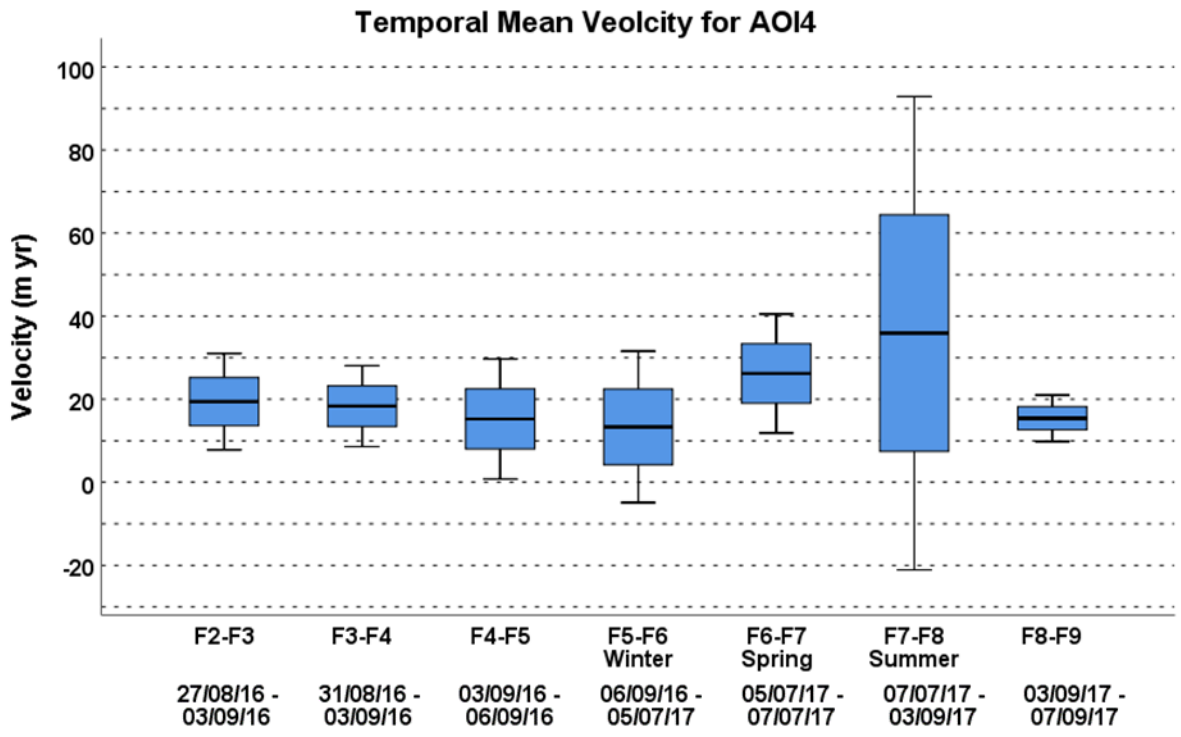

Figure 5.14: *Boxplots of AOI4 temporally from Orthomosaic pairs stretching from 27th August 2016 – 7th September 2017.*

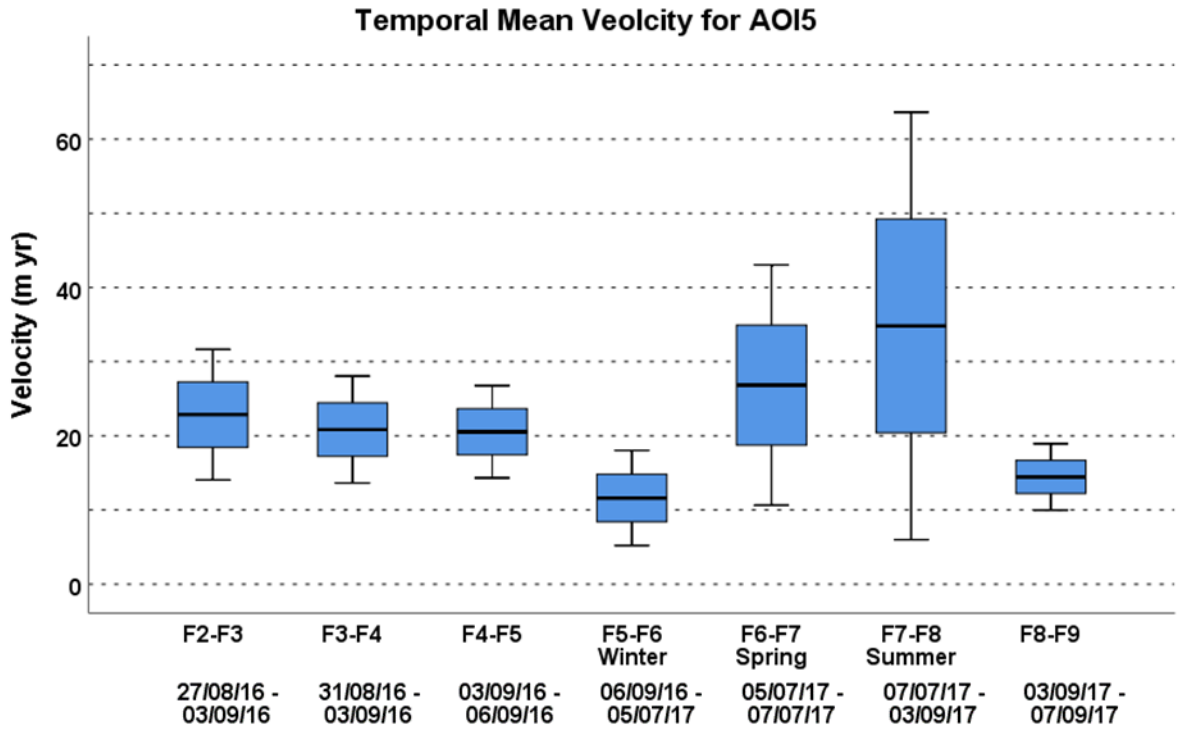

Figure 5.15: *Boxplots of AOI5 temporally from Orthomosaic pairs stretching from 27th August 2016 – 7th September 2017.*

Looking slightly further up-glacier at AOI 6 and 7, it can be seen that these two AOIs have similar average velocities during the 2016 summer and the pattern of velocity decline into winter is evident for both areas (Figure 5.16 & Figure 5.17). However, AOI6 displays a jump in velocity between 3rd and 6th September 2016 (F4-F5) where velocities are almost 10 m yr^{-1} higher than at AOI5 (Figure 5.18). Manual comparisons of the orthomosaics garnered no clear reason for this rise in velocities and, due to its steep relief, no GPR data is available here, so it is unclear why this increase in velocity occurs. Both areas peak in spring, but velocities are higher in AOI7 than AOI6 by 6 m yr^{-1} which continues into the summer where velocities remain 5 m yr^{-1} higher. Spring and summer velocities at both these areas are much higher than AOI 4 and 5 but similar to the terminus regions velocity peaks are found during spring rather than Summer.

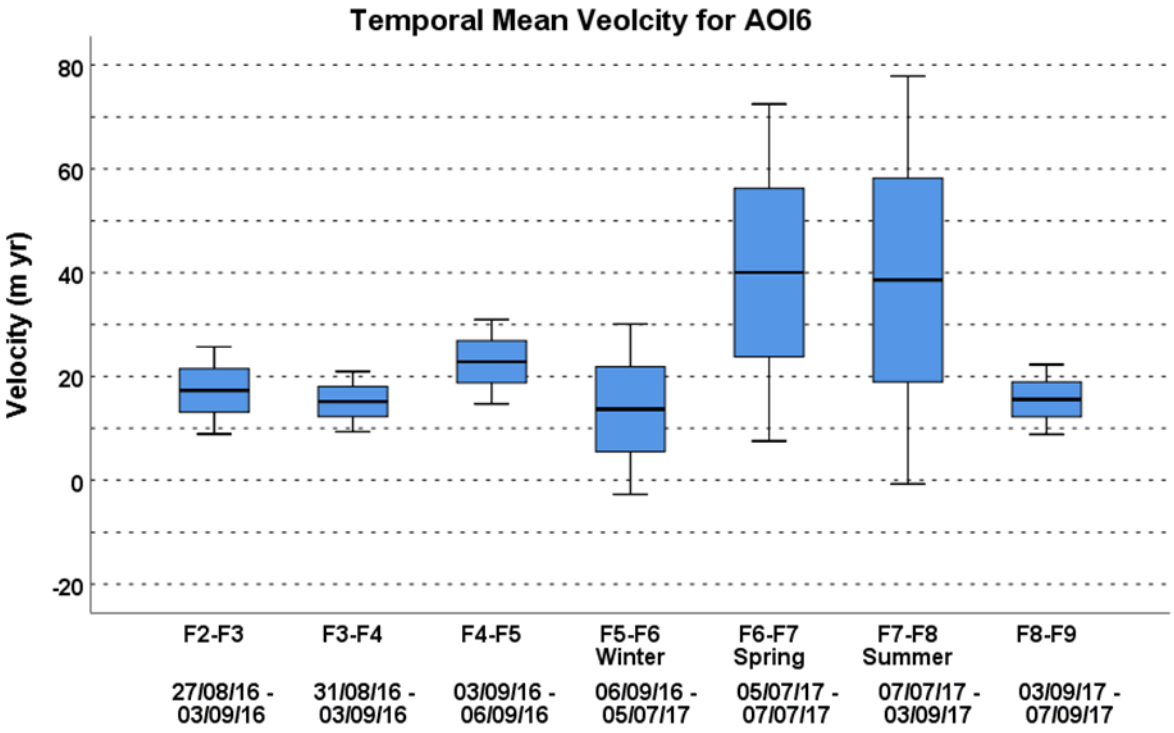

Figure 5.16: *Boxplots of AOI6 temporally from Orthomosaic pairs stretching from 27th August 2016 – 7th September 2017.*

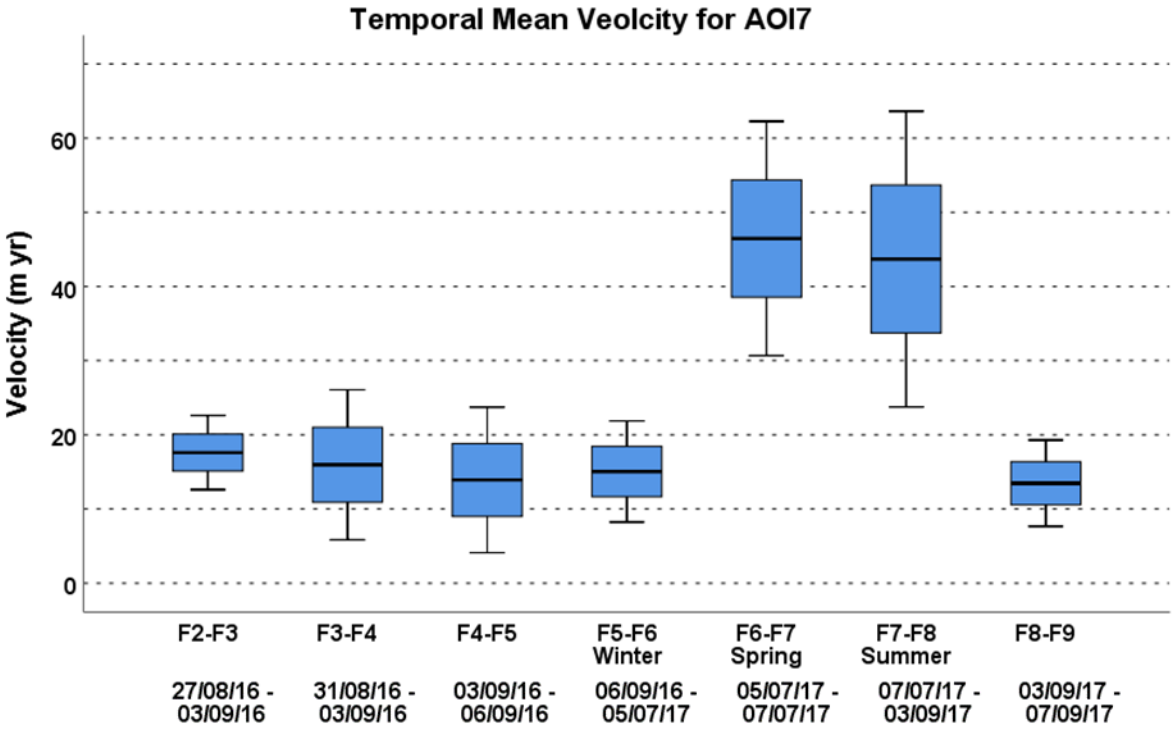

Figure 5.17: *Boxplots of AOI7 temporally from Orthomosaic pairs stretching from 27th August 2016 – 7th September 2017.*

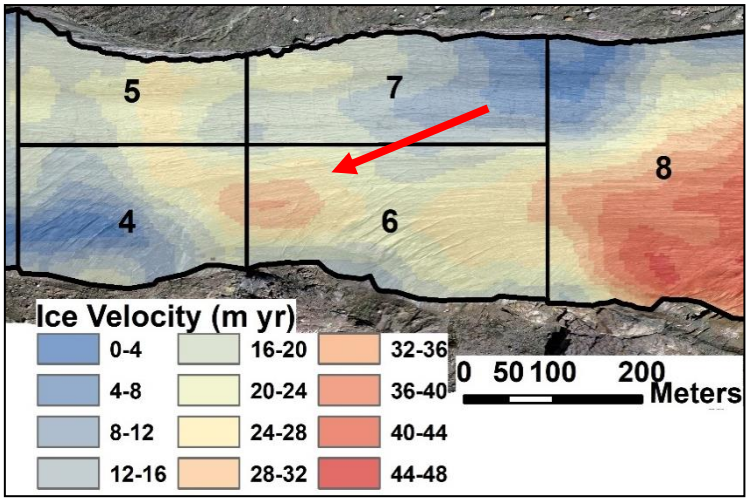

Figure 5.18: *Location of velocity increase at AOI6 (3rd – 6th September 2016).*

5.3.3 Area of Interest 8

AOI8 shows considerably higher average velocities than all other AOIs (Figure 5.19). A high spread of velocity values across the time period are evident, in the same way that was found at AOI3, this is likely due to both the larger size of this area and therefore bigger differences in conditions such as ice thickness, ice slope, and bed topography as well as the complexities of the area such as high localised ice loss (see Section 3.5).

The temporal profile of AOI8 shows the expected decrease in velocities towards winter where they averaged 13.86 m yr^{-1} and peak velocities during the spring (73.49 m yr^{-1}). This gives a much larger range than any of the other areas.

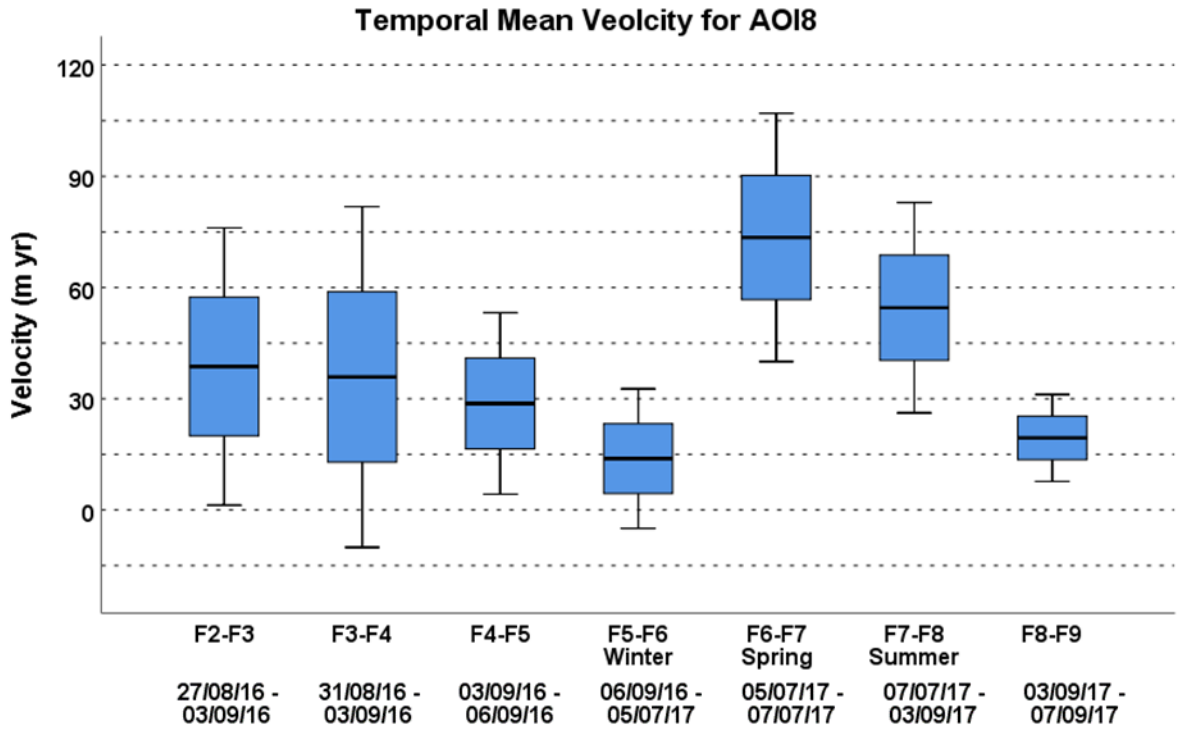

Figure 5.19: *Boxplots of AOI8 temporally from Orthomosaic pairs stretching from 27th August 2016 – 7th September 2017.*

5.4 ICE LOSS OVER TIME AT FINDELENGLETSCHER

The temporal changes in ice thickness loss at the glacier can also reveal clues as to the inner workings of the glacier, most importantly the bed topography and potential hydrology system. Mass loss both annually and over the summer melt season have been looked at already (Section 3.5). However, by comparing and contrasting the ice loss across seasonal timescales, we can gain an idea of the temporal patterns at work here and how they may help inform us of what is occurring hydrologically.

Broadly, as expected there is a strong agreement between ice loss and temperature (Figure 5.20). Looking at the spatial patterns of mass loss over Winter, Spring and summer however

gives a much more complicated picture. All of these periods produce very different patterns of ice loss across the glacier (Figure 5.21).

The winter period produced the least ice loss, likely with melt occurring at either end of the time window between orthomosaics, e.g., September 2016 and June 2017 and very little occurring in the winter months. Most of the melt occurred in the south of the glacier at higher altitudes and the northern edges closer to the terminus.

Melt across all three periods does show areas of similarities. For example, a cauldron type feature that developed over the year shows consistently high melt in this specific area across all seasons. Figure 5.22 shows a field image of this location; note the circular crevasse typical of cauldron development. Evidence that this feature is a result of subglacial flow routing as mentioned in Section 5.2.2.2 can be seen from the field image Figure 3.24.

The Spring ice loss image (Figure 5.21) shows a more uniform ice melt across the bottom ~800 m of the terminus, notably more loss was evident from the cauldron feature adjacent to the portal before its collapse. The area constituting AOI 6 and 7 showed very little melt during this period.

Specific areas where much higher mass loss is occurring than the surrounding glacier can be seen in Figure 5.21. For example, the cauldrons located in the centre of AOI3 which are melting at a rate of ~50 m yr over during the summer orthomosaic period. Crevasse widening can be seen in this image (Figure 5.21) as well as the development of two moulins to the north of the developing cauldrons previously mentioned. An area of high ice loss is noted just down-glacier of the ice fall in AOI8. The ice loss imagery very clearly picks up the collapse of the cauldron next to the main egress portal.

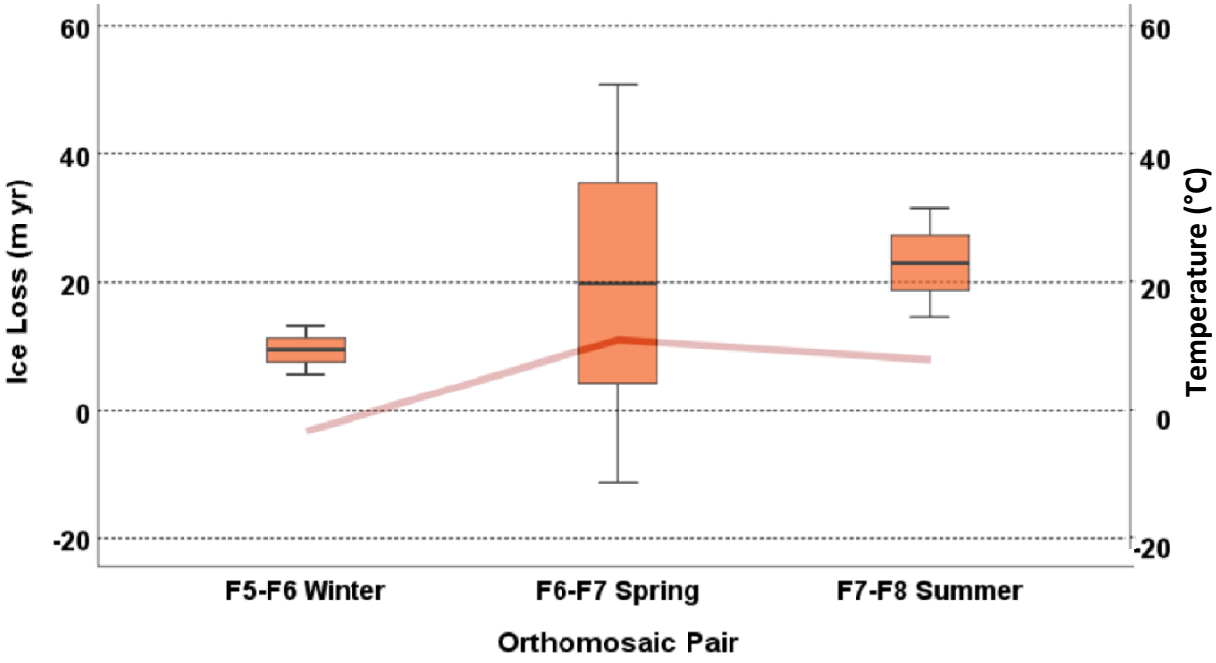

Figure 5.20: *Box and whisker plots showing ice loss to two standard deviations at Findelengletscher. The red line represents average 24 hr temperatures between orthomosaic pair images.*

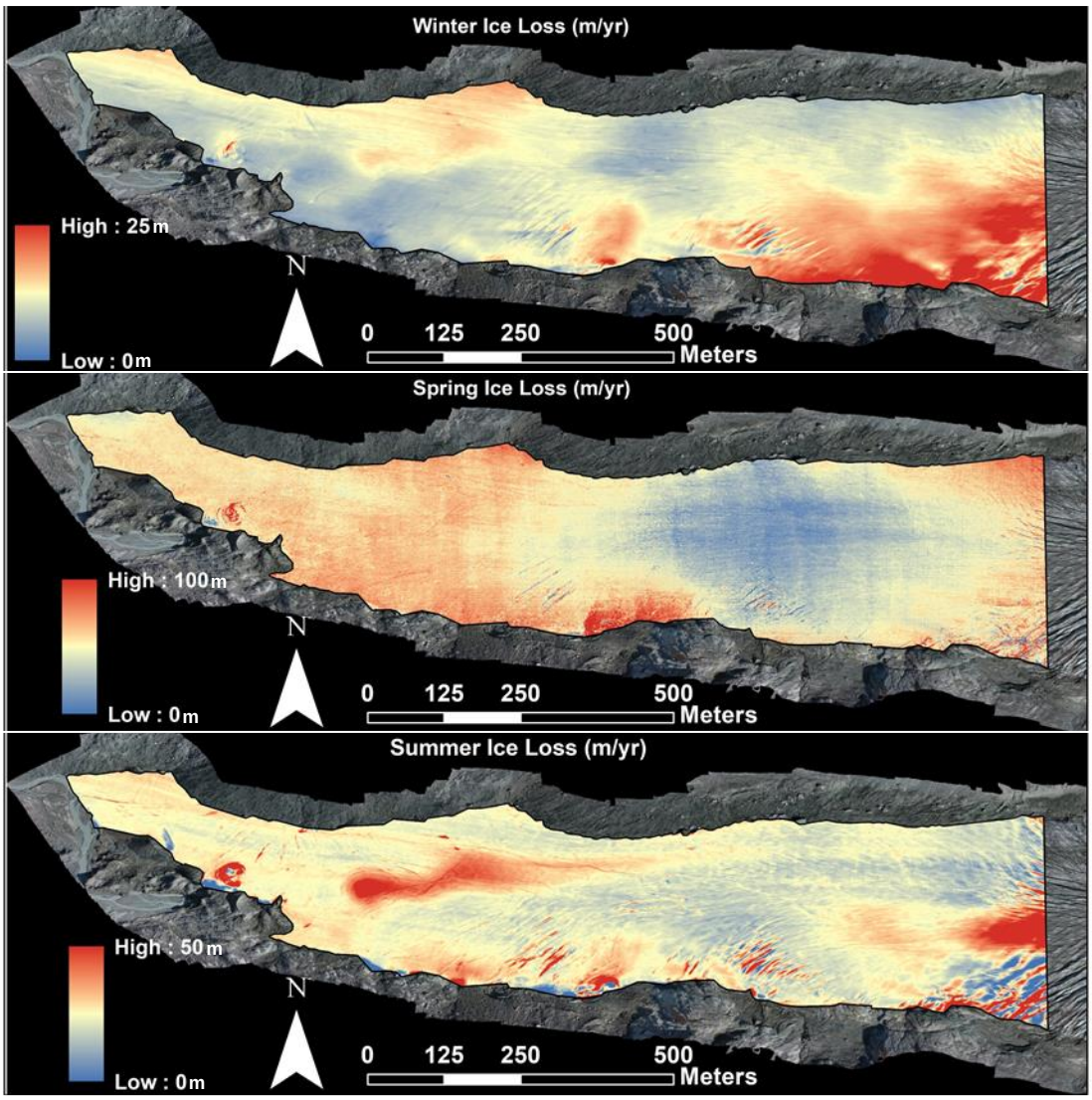

Figure 5.21: *Temporal Ice loss at Findelengletscher for Winter (6th September to 5th July), Spring (5th-7th July) and Summer (7th July – 7th September). Values represent the rate of ice loss per year if values persisted at these rates.*

Figure 5.22: *Southern lateral cauldron development (highlighted in red) in AOI4, looking North-East.*

5.5 SUMMARY

Findelengletscher does broadly show the same velocity patterns as a normal glacier, in that fastest flow is during spring and slowest flow is during winter. However, small scale features cause the glacier to act differently in very localised areas.

The interpolated velocity map of Findelengletscher was successfully used to highlight areas where residual velocities were present across Winter, Spring and Summer. It was found that the glacier behaves in a similar way than expected from a glacier with no undulations. Where velocities are slowest in the winter, peak in the Spring and steadily decline across the summer due to either the increased efficiency of the hydrological regime through the melt season, lower temperatures (and therefore less meltwater) or a combination of the two. The limitation of the sample size for spring is noted here, being only 2 days with higher-than-average spring temperatures during that time and therefore likely more melt, although discharge was still quite low during this period (Figure 5.2). Smaller scale features in the ice

such as crevassing or englacial voids are where clues as to what effect the topography has on the hydrology and velocity can be found.

The presence of circular velocity features, seen in Spring (Figure 5.7) correlated with where cauldron features had been beginning to form and ice loss was locally high. The positioning of these features in a chain up glacier is understood to be an indicator of a subglacial channel which melts ice at the ice-bed interface causing these circular supraglacial-basins. Two subglacial channels were mapped in this way. Ice loss was found to vary considerably from one season to another with the relationship between topography and hydrology playing a role in this.

The overdeepening located in AOI2 was found to maintain relatively higher velocities into the late melt season, even with the Spring measurement period occurring during higher-than-average temperatures which may have exaggerated the extent of early melt season velocities, making late summer velocity slow-down appear more considerable than actually was the case.

6. DISCUSSION

6.1 INTRODUCTION

In this chapter, the key findings from chapters 3, 4 and 5 will be discussed in further detail. Firstly, the velocity results from Findelengletscher will be discussed along with the residuals data from chapter 5 (Section 6.2). Hydrological patterns, including the temporal evolution and spatial routing of the drainage system will then be covered (Section 6.3), followed by discussion on overdeepenings and their effect on seasonal drainage (Section 6.4) Patterns of ice loss will then be discussed (Section 6.5) before finally analysing the presence and development of cauldrons at Findelengletscher (Section 6.6)

6.2 VELOCITY PATTERNS

As discussed in chapters 4 and 5, velocity patterns at Findelengletscher varied considerably both spatially and temporally. There is considerable interplay between multiple factors such as atmospheric conditions (precipitation, temperature), topography and basal sediment, stresses on the glacier (internal deformation, longitudinal stresses etc.), melt in its various forms (snow, supraglacial and subglacial) and the fluctuating state of the hydrology within and beneath the glacier. Simply said, there are a lot of different factors that influence the overall velocity of the glacier and distinguishing one factor as a cause is somewhat simplistic. The truth is more that a combination of factors act together to provide specific conditions for how a glacier flows.

6.2.1 General velocity patterns in temperate valley glaciers

There is a strong relationship between velocity and melt (Iken, 1974). Meltwater at the base of the glacier increases water pressures, reduces friction, and increases sliding rates (Stevens *et al*., 2021). There is agreement between times of high water inputs and increased velocity (Iken, 1974). Because the amount of meltwater available is entirely due to atmospheric conditions (Wójcik-Długoborska & Bialik (2021), there will exist at all glaciers a pattern of variation to that meltwater. On both a diurnal and seasonal level, due to variable temperatures, meltwater availability and therefore velocity will fluctuate on these timescales (Jansson, 1996; Purdie *et al*., 2008; Bartholomaus *et al*., 2008; Stevens *et al*., 2021). Indeed Purdie *et al.* (2008) found variations of 0.87 m d^{-1} and 0.64 m d^{-1} in summer and winter respectively, a variation of ~26% at Fox Glacier, New Zealand. This is a good comparison glacier to Findelengletscher due to it also being a temperate valley glacier with a negative mass balance. Seasonally, average summer ice flow velocities will be higher than in winter due to the enhanced sliding by migration of surface meltwater to the bed (Zhang *et al*., 2021). The typical pattern of velocity at valley glaciers from a temporal perspective is a peak in velocities in the early melt season where high concentrations of meltwater are travelling through the glacier in inefficient systems (Cook & Swift, 2012). Across the remainder of the melt season, despite discharge rates staying constant, the glacier becomes more efficient at processing meltwater and water pressures and basal sliding rates and therefore surface velocities would be reduced (Figure 6.1) and decreased significantly further during the winter season (Hooke *et al*., 1989; Willis, 1995; Hubbard *et al*., 1998). Variations between peak velocities at early melt season and late melt season at two valley glaciers were found to be ~19% at Worthington Glacier, Alaska (Pfeffer & Welch, 1996) and ~20% (Hooke *et al*., 1989) at Storglaciären, Sweden.

Spatially, ice velocities in the ablation zone at Findelengletscher show a clear decrease in line with proximity to the terminus, much the same as the findings of Zhang *et al*. (2021). Furthermore, looking at a cross-section, (see Figure 6.2) the glacier will be at its maximum velocity at or near the centre with velocities steadily decreasing towards both lateral margins (Harbor, 1992; Kraaijenbrink *et al*., 2016; Robson *et al*., 2018; Zhang *et al*., 2021) due to the effects of lateral drag (Nye, 1965). Internal deformation from high ice thickness would also help increase surface velocities, however this is less pronounced at the terminus of valley glaciers due to thinner ice.

All glaciers, not just valley glaciers, have been seen to follow the intra-annual trend of high velocities in the early melt season followed by steady decline towards the end of the summer. When compared to the work of Willis *et al.* (2003) we can see that seasonally, the surface velocity of Haut d'Arolla follows the same broad pattern as Findelengletscher of having the highest velocities in the early melt season and lowest in the summer. (Figure 1.7). Both being valley glaciers of a similar size with very similar climatic conditions, the fact that these temporal velocity patterns are similar supports validity of these results. Davison *et al.* (2013) also found the same pattern at the Greenland Ice Sheet (GIS) (shown in Figure 6.3). This similarity suggests that the same hydrological processes occur regardless of scale and that findings at Findelengletscher can be scaled up (Chandler *et al*., 2013; Nienow *et al*., 2017).

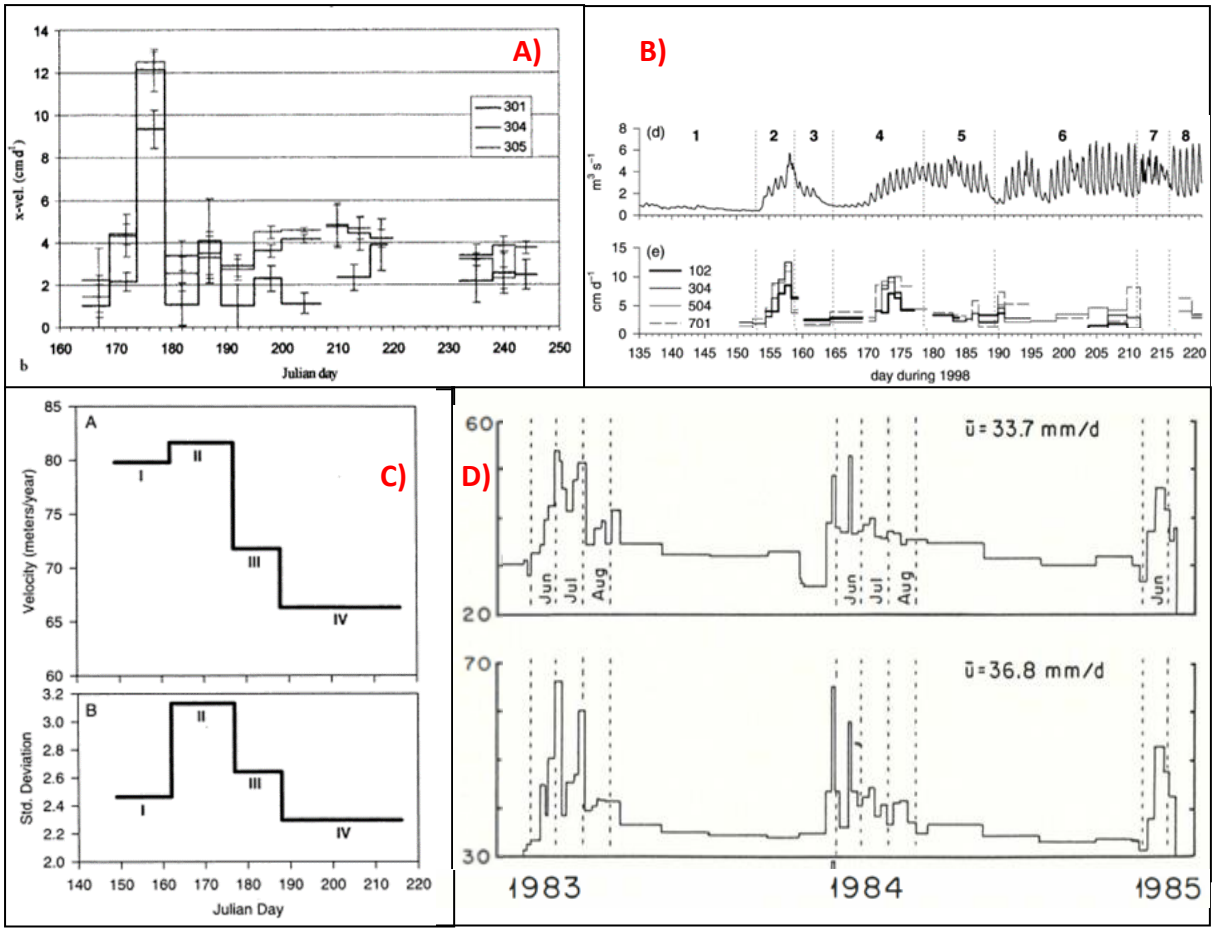

Figure 6.1: *Longitudinal velocities of A & B: Haut d'Arolla, Switzerland across the 1994 and 1998 melt seasons (Mair et al., 2001; Swift et al., 2005), C: Worthington Glacier, Alaska 1994 (Pfeffer & Welch, 1996 p45), D: Storglaciaren, Sweden 1982-85 (Hooke et al., 1989).*

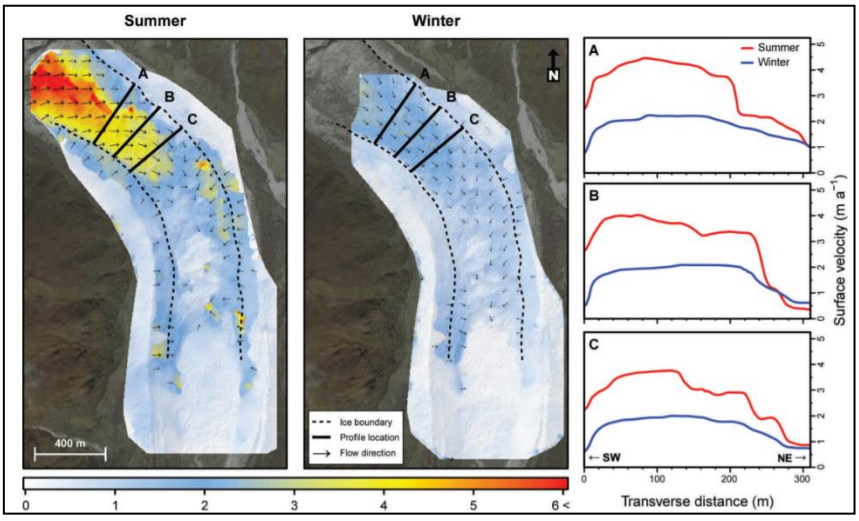

Figure 6.2: *Temporal and spatial patterns of ice flow velocity of Lirung Glacier, Nepal in 2013 Summer and 2013-14 Winter. (Kraaijenbrink et al., 2016).*

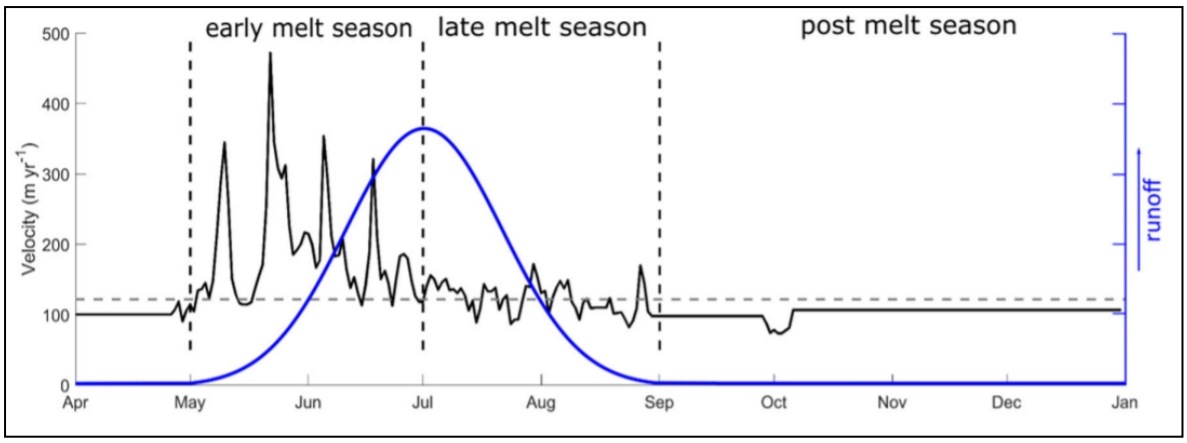

Figure 6.3: *Velocity and runoff rates at Greenland Ice Sheet (Davison et al., 2019).*

6.2.2 Velocity patterns at Findelengletscher

The broad velocity patterns observed at Findelengletscher show a similar temporal story to those of other glaciers (Hooke *et al*., 1989; Mair *et al*., 2001; Swift *et al*., 2005) in that velocities peaked during the early melt season, with a slight decrease in velocities towards the back end of the melt season and then remained low across the winter period (see Figure 5.3). Variations between early melt season and late melt season velocity at Findelengletscher were found to be ~10%, which is consistent with those found by Iken & Truffer (1997) (despite their measurements of early melt season being May-June and this work being July) in Figure 6.4, and not dissimilar to values of ~20% found in the literature for the temperate valley glaciers of Storglaciären, Sweden and Worthington Glacier, Alaska (Hooke *et al*., 1989; Pfeffer & Welch, 1996).

Velocities slow as the ice reaches the terminus (Copland *et al*. 2009). This is due to the thinning of ice and therefore less movement from internal deformation along with higher levels of friction relative to the glacier's size from the natural tapering of the glacier snout. Such a reduction in glacier velocity is in keeping with the findings of Iken & Truffer (1997) who

took regular velocity measurements at the terminus of Findelengletscher between 1979-1994 at 3 locations and found slower velocity speeds as the glacier approached the terminus both year on year as the glacier retreated and due to the location of the measurement points near the terminus (Figure 6.4). Comparing the findings of Iken & Truffer (1997) with velocities from 2016 and 2017 at measuring points still covered by ice it can be seen that velocity rates follow the trend of decreasing, likely due to the retreating and thinning of the glacier, whereby the measurement points, in this case B and D, get closer to the terminus every year (Figure 6.4). Figure 4.4 shows the thickness of the ice at the Findelengletscher terminus. As rates of internal deformation increases with ice thickness (Glen, 1955), if sliding is disregarded, the thicker areas of ice should flow at greater velocity than the shallower areas at the periphery of the glacier.

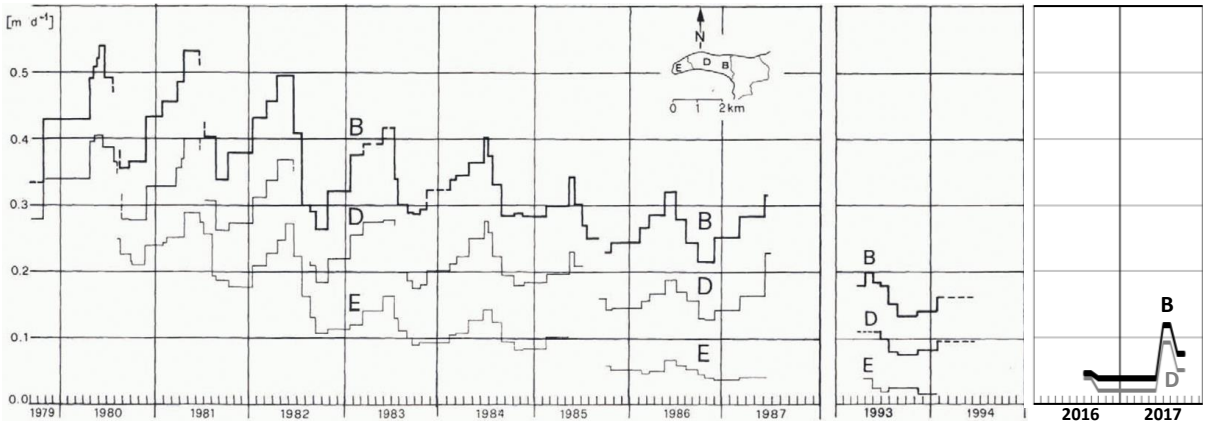

Figure 6.4: *Velocity measurements of three poles placed along the centre line of Findelengletscher 1979-1994 (taken from Iken & Truffer, (1997)).*

Spatially there were some broad agreements when comparing the results of Findelengletscher to other temperate, land terminating valley glaciers. For example, velocities were seen to increase with distance travelled from the terminus (See Figure 4.3). The high resolution of imagery achieved by the UAV flights enabled smaller scale movements

over short time periods to be assessed also and these were more telling of local conditions than the overall pattern across a larger area. The field site was split into AOIs to accommodate this, with small areas of variable velocities noted, particularly around areas that displayed ice loss such as at the developed and developing cauldron features.

6.2.2.1 Areas of Interest 1-3

There is considered to be a lot more happening within AOI3 than AOI1 and 2. For example, the glacier is much wider in AOI3, and this will lead to larger variations in depth laterally which will cause bigger variations in velocity across this area which can be seen in the results (Figure 5.10, 5.11, 5.12 & 5.14). Added to this, there is a lot more atypical activity in this area. For example, noticeable ice loss variance and developing crevasses e.g., across the main hydrological flow channel. The cauldron collapse in AOI2 during the summer period of 2017 (F7-F8) also gives potentially misleading velocity data and led to the largest standard deviation of velocities across all time periods and AOIs. The collapse of this feature has created considerable noise that makes analysing the true velocity of this narrow area difficult. There is a general trend of velocity reduction at the end of summer 2016 and continuing through winter followed by higher spring velocities due to higher levels of meltwater (from snowmelt etc.) and an inefficient drainage system. Looking around the outside of the cauldron feature, it does appear that velocities remain high in this area during summer 2017 with some areas showing 24-32 m yr^{-1}, very similar to those in Figure 5.13 where velocities at the overdeepening were found to be higher than the area where a main subglacial conduit from the channelised system is considered to be located (Figure 3.25; 3.28).

6.2.2.2 Areas of Interest 4-7

The seasonal velocities for AOI4 and AOI5 peak in the Summer rather than the Spring. A reason for this might be due to the steeper surface slope in these areas, especially compared to AOI 3, 6 and 7 which are much less steep in the direction of glacier flow by comparison. Dow *et al.* (2015) suggest that steeper ice slopes cause subglacial channels to grow significantly faster than at flatter areas therefore it is believed that as velocities reduced due to a reduction in meltwater, the steeper slope in this area was able to stay efficient for longer, with continued subglacial channels and the increased basal sliding that comes with that.

Cook and Swift, (2012) and Swift et al., (2021) suggest that at overdeepened valley glaciers, the basal water pressures and therefore sliding velocities are likely to remain high later into the melt season due to a slower switching of flow to englacial conduits than at non overdeepened beds. It is possible that this is what can be seen at AOI4 and AOI5 where peak velocity is occurring later than the rest of the field site, although from the GPR bed models this would be occurring ~300 m up-glacier of the overdeepening. It could also be considered that AOI4 and AOI5 are higher up and therefore there would be a lag here with regard to hydrologic influence.

AOI6 and AOI7 velocities both peak in Spring, with AOI7 displaying a greater velocity by 6 m yr^{-1} during spring and remain higher into the summer period. Velocities are much higher in both these areas when compared to AOI4 and AOI5 and Summer slow down rates are low which could suggest that a channelised drainage system develops earlier up glacier.

6.2.2.3 Area of Interest 8

AOI8 displays the highest velocities of all of the areas. These high velocity levels at this area are down to a heavily crevassed ice fall a short distance up-glacier that divert supraglacial

melt into the internal workings of the glacier and cause less friction at the bed and therefore more localised basal sliding in this area. Increased internal deformation from ice thickness is considered to play a part too albeit a smaller one, as this area displays a high ice thickness compared to the rest of the terminus region (Figure 4.4). The ice fall immediately up glacier of this area explains why velocities are generally high. The glacier moving down a steeper slope above this area on the lee-side of the ice fall will add compressional stresses to the ice ahead of it, causing it to flow faster.

6.2.2.4 Comparisons between Areas of Interest

Having assessed the temporal behaviour of each AOI individually, a look at how these areas compare to each other will be useful in considering patterns across the entire study area. Figure 6.5 shows the temporal profiles of each AOI and how they compare to one another. AOI8 has the highest average velocity range, going from 13.86 m yr^{-1} in the winter to 73.49 m yr^{-1} in the spring. The higher the differences between velocities across the 8 areas, the more longitudinal stresses will be acting on the glacier in these regions. For example, at a glacier with uniform velocity travelling over a smooth bed, there would be no longitudinal stresses, whereas at a bumpy bed velocity would change longitudinally as the glacier flowed over adverse slopes. This would cause more compressional and decompressional stress as the ice is effectively compacted and stretched. The lowest average range (9.5 m yr^{-1}) across all areas can be seen during the winter (F5-F6). This would indicate that longitudinal stress is also lowest during the winter months. In comparison the highest range of velocities is found in spring (47.29 m yr^{-1}). The general trend is for the glacier to slow as it reaches the terminus (Ai *et al*., 2019) and therefore it is reasonable to conclude that this causes compressional stresses within the glacier, certainly at the terminus and these stresses are highest during the melt

season due to the magnitude of the velocity range and the diurnal differences in melt (Stevens *et al., (*2021).

The highest spread of velocities (standard deviation) in each AOI was during the summer (F7-F8). This is likely due to the size of the time window between orthomosaics leading to increased noise between the orthomosaic pair. Spring (F6-F7) would be expected to have the biggest range of velocities due to higher velocities in general occurring here, however due to the short sampling window (2 days) there would likely not be enough time for velocities to differ considerably.

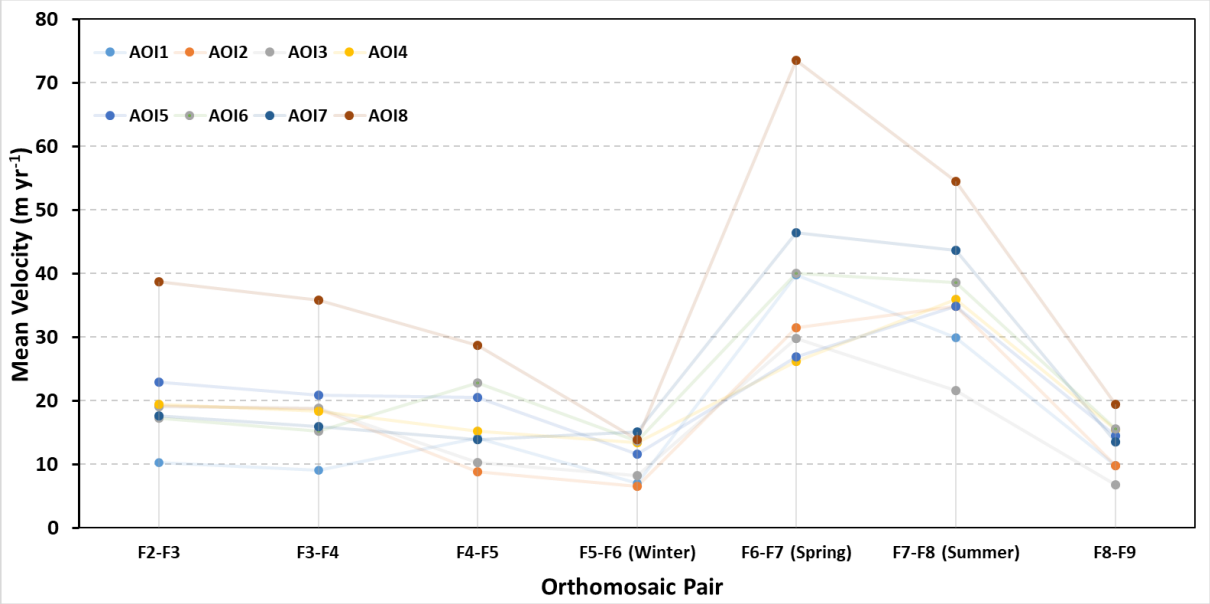

Figure 6.5: *Line graph of Mean Velocities temporally (orthomosaic pairs) and spatially (AOIs).*

6.2.2.5 Velocity observations for 2016 and 2017

Data from Summer 2016 where comparisons between 5 orthomosaics were recorded between the dates of 22nd August and 6th September (15 days) and average velocities obtained. The area prior to the overdeepening where the main flow path is located (AOI3)

has a lower velocity than the overdeepened area next to it (Figure 4.5). Usually, it is expected that the more subglacial water available, the faster velocities will be due to the lubricative effects on the bed interface (Joughin *et al*., 2008; Schellenberger *et al*., 2015; How *et al*., 2017). The fact that this isn't occurring here suggests that melt in this section is being efficiently routed by a channelised system given the lateness of the melt season that these velocities were measured.

As presented in Chapter 4, velocities are found to be on average 3.45 times lower during the winter (Figure 4.7; 4.9). This slowdown in velocity is likely due to low levels of meltwater within the glacier and therefore more friction at the bed at AOIs 1 & 2. This would cause a reduction in sliding at these areas. Indeed, future aerial imagery of the field site from Summer 2019 (see Figure 3.30) show that this area effectively becomes cut off from the main glacier body and becomes 'dead ice' as the glacier retreats up glacier leaving behind a section of ice located in AOI1 & 2. However, this reduction in velocity could simply be due to the slowdown in ice flow towards the glacier margin as ice thins and becomes compressional up the adverse slope of the overdeepening, particularly given the similar pattern observed in winter.

Velocities at AOI8 are notable as they are very high when compared to the rest of the ablation area studied with average velocities of 54.53 m y^{-1}. The location of this AOI, shortly after a riegel where crevassing is prevalent and on a steeper downward slope morphology would lend itself towards high velocities. Supra glacial meltwater can enter the interior of the glacier through localised crevasses directly before AOI8 and increase sliding rates due to less friction at the bed, increasing velocities. The high meltwater influx here from supraglacial to en/subglacial transport due to the heavy crevassing could explain why mass loss is so high in this area with high melting of the glacier through meltwater conductivity.

As outlined in Section 4.2.2.4, flow direction is generally down glacier. Figure 4.9 shows that there are some levels of divergence from this down glacier movement particularly at AOI3. In the summer some easterly movement is detected. This is thought to be attributed to the opening of cracks around the cauldron area. This happens in a circular fashion as the ice in the centre collapses from beneath and stress causes cracks to widen believed to be due to subglacial melt (see Section 3.3.2.4). However, the crevasses that open are more pronounced up and down stream rather than transversely.

AOI14 and AOI5 show considerably directional variability in the summer with movement towards the lateral areas of the glacier too. Winter periods show more uniform downhill directional movements more than summer. This is likely due to a more stable environment with regard to temperature and meltwater. The colder temperatures and scarcity of meltwater decrease the amount of movement due to sliding.

Directional movement is more uniform in the up-glacier areas of the study site (AOI5, 7, and 8) in both summer and winter, however the down-glacier areas exhibit less predictable behaviour. This is attributed to a more unstable and ever-changing environment across the melt season as well as fluctuations in temperature and meltwater that are at their most changeable at the terminus (Harper, 1993) but could also be, in part, due to errors within the velocity data. Ice loss is also a factor in increasing the noise and masking glacier flow directions. It explains why directional findings are more uniform in the winter when less loss is occurring. The loss of ice can expose lines of sediment from closed crevasses which are not vertical within the ice. As the above ice melts, it can give the impression of ice moving in the direction that the new sediment is appearing as shown in Figure 6.6. This, along with small

scale melting and widening of crevasses towards the glacier upslope explains why some directional data in Figure 4.9 appears to be moving upslope.

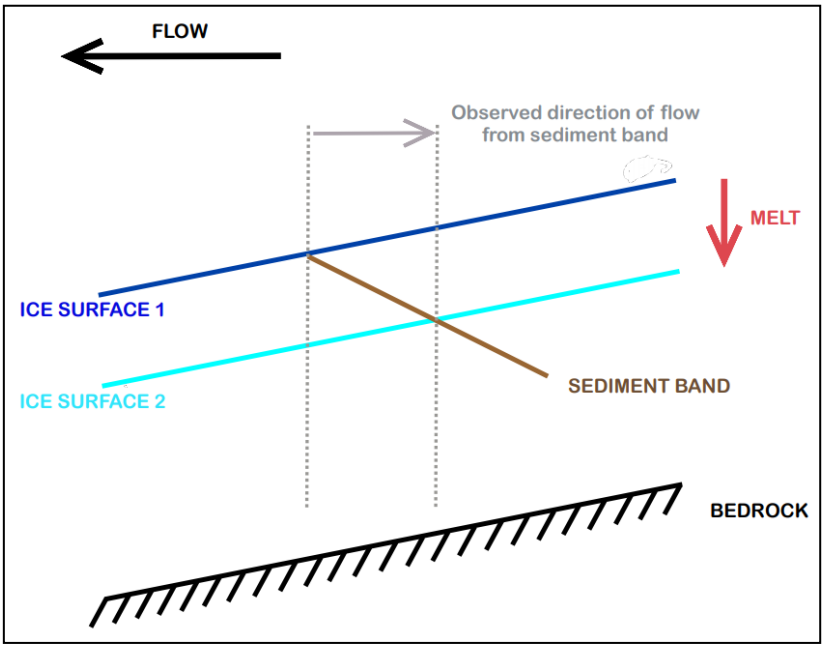

Figure 6.6: *Cartoon showing how mass loss can affect the accuracy of flow direction and velocity.*

6.2.3 Residual Data

6.2.3.1 Winter Velocity 2016/17

Hydrologically derived velocity (i.e., sliding) will have a much smaller influence on the flow of the glacier. For example, localised velocity increases due to meltwater channels are not noticeable here, whereas their effects can be noted in Spring and Summer velocities (covered in the next section) where increased glacial velocities are noted at close proximity to larger meltwater channels. Indeed, the negative residuals seen in Figure 5.6 in the central section (AOI3) and the southern section near the portal (AOI5) of up to -20 m yr^{-1} are thought to be due to a lack presence of a channelised drainage system, that, as discussed in Section 3.4.3, develops over the course of the melt season and flows through both of these sections, skirting

the up-glacier extent of the overdeepening. The closing up of meltwater channels in the winter and late summer via the process of viscous deformation (Vieli *et al*., 2004) would further reduce any meltwater still present to flow in larger individual channels.

The limited amount of meltwater over the winter months is the cause of, and explanation as to why residuals of up to -35 m yr^{-1} are seen in the most easterly area (AOI8). This area processes high concentrations of meltwater during the time of year that was used for the baseline velocities model, and the lack of this meltwater is why the velocity differences are so stark in the wintertime. Looking at percentage change from the baseline velocities for winter (Figure 5.6), it can be seen that the areas displaying positive change are also areas where the greatest ice thicknesses are present (Figure 4.4) in the northern section of AOI3 and AOI7. This suggests that during winter velocity movement by internal deformation plays a more significant role than it does during the melt season, as it changes very little across a year (Hewitt & Fowler, 2008) whereas velocity via sliding is largely reduced over the winter due to the scarcity of melt water.

6.2.3.2 Spring Velocity 2017

Velocity patterns in Figure 5.7 show some interesting results for the orthomosaic representing the Spring, or early melt season, period. Several circular features can be seen in the centre of the glacier which align with the area around the collapsed cauldron feature to the north of the portal, the two early-stage cauldron features highlighted in (Figure 3.17). Two other features further up valley align well with the subglacial flow paths from Figure 3.22. The south of the glacier along the lateral extent also shows three similar features.

These circular areas of higher velocities are believed to be due to englacial and subglacial processes and from ice dynamics (Stocker-Waldhuber *et al*., 2016). More specifically in these locations the velocity increases are indicative of channelised meltwater pathways developing beneath the glacier. Nienow *et al.* (2005) suggests these increases in surface velocities are intrinsically linked to hydrological forcing in the proximity of a subglacial channel. Tsutaki *et al.* (2011) found similar features at Rhonegletscher that displayed high velocities also. Velocities outside of these circular features in this region are very low by comparison. It is believed that these high velocity 'spots' denote 2 main flow paths that, as of 5th-7th July when the UAV flights were conducted, are on their way to developing into a more channelised system (Figure 6.7). These pathways funnel large amounts of water to the main egress portal, one through the centre of the glacier cutting south to the portal, and one to the south of the glacier running parallel to the southern glacier border (see Figure 3.24).

A small area containing high velocities was also located at the terminus of the glacier. This area consists of a lot of deposited material from the glacier next to the meltwater stream that runs along, and at times over, the front edge of the glacier terminus. By comparing the images of the orthomosaic pair that makes up the Spring sampling period, the meltwater stream exiting the glacier is higher in the original image than in the secondary image. It is likely the perceived movement of the glacier was that of the differences in the extent of the stream (Figure 6.8).

The circular horizontal velocity features may be affected by the vertical elevation change during this period in the form of melt. The collapsed cauldron in Figure 6.8 displays very high velocity and shows how ice melt can produce misleading horizontal velocities that aren't accurate of glacier flow. Whilst seasonal ice loss will be discussed in full detail later in this

chapter, it should be noted here that spring ice loss occurs in a fairly uniform way (see Figure 5.21) which indicates that there isn't a great deal of variability in vertical elevation change and this is unlikely to be a significant factor in these circular features.

The area immediately down glacier of the ice fall, known as AOI8 shows the highest velocities due to the increased meltwater from winter snow at this location. In addition, there are a couple of other high velocity features further up glacier. This additional available water source is an important factor in why usually spring velocities are high (Kenner *et al*., 2017) and spring events can occur (see Section 1.3.3.1). Due to the patterns of velocity found here it is believed that at this point the glacier is moving towards a more channelised system from the localised high velocity spots, however as velocities are still so high, a channelised system is not quite yet fully evolved.

The percentage change to average ice flow velocity shows fairly consistent increases in velocity across the study area of 40-80% (Figure 5.7). However, there are considerable differences in velocity within AOI4 and AOI5 which suggests that a great deal of change is present in these areas which is likely related to the development of the drainage system in this area when compared to the baseline which is right at the end of the melt season. Also, of note from the percentage change residual data from the spring period (Figure 5.7), is the lower levels of velocity change from spring to baseline data (taken right at the end of the melt season) at the adverse slope of the overdeepening. This suggests that here velocities aren't decreasing to the extent as the areas around them such as AOI3 and that velocities are remaining closer to Spring levels at the overdeepening late into the melt season which supports the notion of a less channelised system being in place at this location.

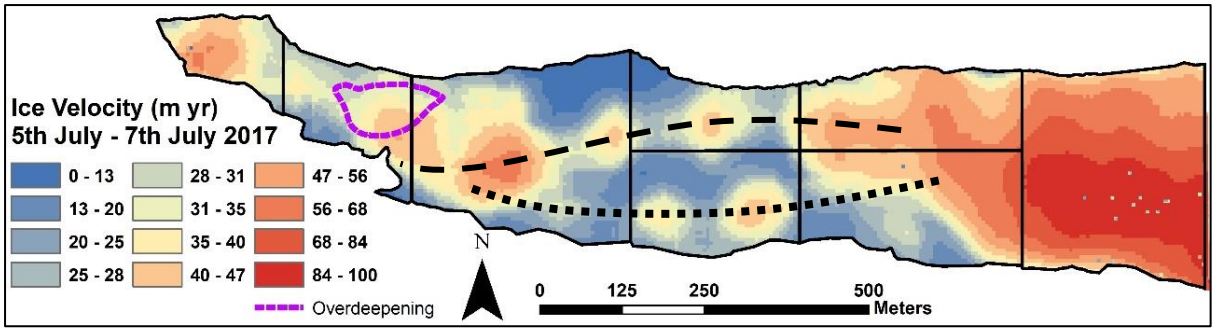

Figure 6.7: *Non-residual ice flow velocities for the Spring (F6F7) orthomosaic pair. Dashed and dotted line represent potential subglacial flow paths creating localised melt.*

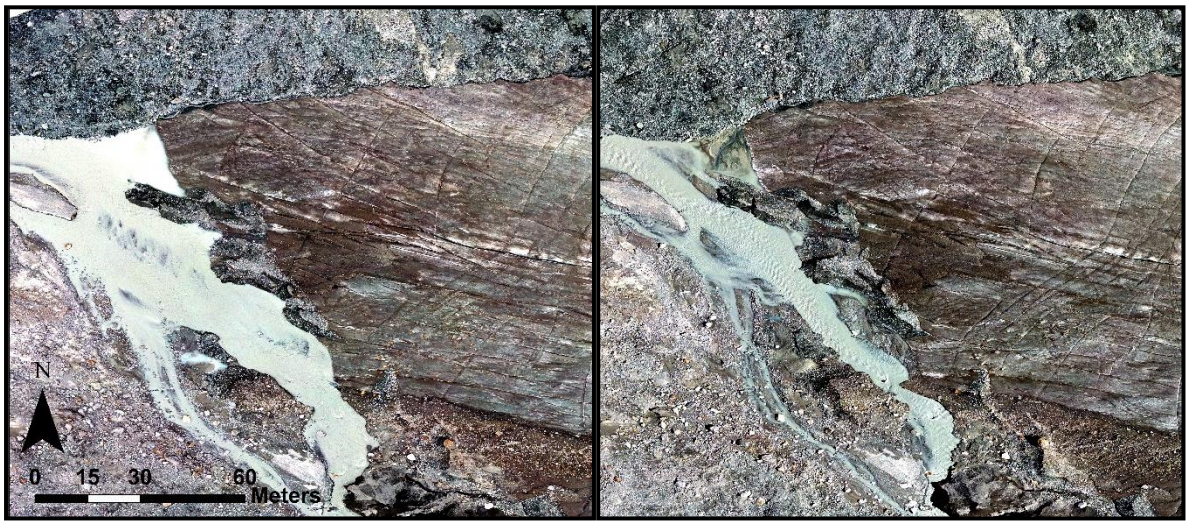

Figure 6.8: *Differences in proglacial stream extents. Left – 5th July 2017, Right – 7th July 2017.*

6.2.3.3 Summer Velocity 2017

A significant subglacial flow channel is situated 200 m East of the cauldron collapse (see Figure 3.17 circles labelled '2017') residual data across the summer time-period suggests that velocities are between 40-70 m yr^{-1} higher at this location likely due to the increased efficiency of the drainage system at this location in summer and therefore higher levels of meltwater being channelled through this area leading to an increase in localised basal sliding.

From Figure 5.8 it can be seen that velocities are generally around 200-400% higher over the summer when compared to the Autumn (baseline) velocities. The cauldron collapse in AOI2

gives a false reading of velocity, however the area around the outside of where this cauldron has collapsed shows that velocities are still high at the overdeepening, and immediately up glacier of the overdeepenings velocities are up to 700% higher. It is possible that this is due to a more distributed pattern at and around the overdeepening with a channelised drainage system being in place up glacier as suggested by Cook & Swift (2012) and Swift *et al.,* (2021), however the noise from the cauldron collapse makes it difficult to tell.

6.3 HYDROLOGY PATTERNS

As outlined in Chapters 3, 4 and 5, hydrology has an important part to play in affecting glacier dynamics at Findelengletscher. The use of GPR enabled a bed model to be made and likely hydrological flow paths postulated. The hydrology within a glacier is in a constant state of flux as it adjusts to changes in atmospheric conditions such as temperature, precipitation, and melt. Topography has a big effect on both spatial and temporal development of the hydrological system, and it is not possible to talk about its development without mentioning topography.

6.3.1 Hydrological routing

At a 'uniform' glacier, by that meaning a straight glacier in length on a steady downslope bed with no undulations, all meltwater would reach the bed and flow in a straight line along the central flow line of the glacier, never having to be rerouted due to topography, but possibly rerouted englacially due to high water pressures during high melt events (Roberts *et al*., 2000; Walter *et al*., 2008). The channelised hydrology at Findelengletscher follows two distinct paths as shown in Figure 6.7. By joining the circular velocity features travelling up-glacier – which have been found to align with flow routes by GPR trace evidence (Figure 3.26; 3.27)

and subglacial flow routing estimates (Figure 3.25; 3.29) – these two routes can be hypothesised. This can also be backed up by field observations (Figure 3.24; 5.21) and recent satellite imagery (Figure 3.30). Clues to the development of hydrological system from previous melt seasons were noticeable in the form of late-stage cauldron features (see Figure 3.16).

It can be seen here from the bed models, and indeed all GPR surveys conducted (Feiger et al., 2018; Grab et al., 2021), that the bed on the south side of the glacier tongue is significantly less steep than that of the north side. Therefore, it would make sense for water to drain downhill with the effects of gravity, into the deeper northern channel area before being evacuated. However, the major portal for the meltwater is situated on the south side of the snout of the glacier. It is therefore likely that either the majority of meltwater is not able to reach this deeper area, or that the water travels englacially instead to reach this egress point, possibly due to some feature in the bed, which according to bed models would be an overdeepening. February GPR transects did not show any clear evidence of subglacial channels which is likely due to the refreezing of most of the water due to environmental temperatures and the effects of creep closure. However, transects taken in the middle of the melt season (July) show the presence of features believed to be meltwater channels (Figure 3.27). Which gives us an idea of where the meltwater is being routed, again, around this overdeepened feature.

From Figure 2.15, at some point between 2012 and 2015 the main egress point flipped from draining from a more northerly location to where it is now at the true south of the snout. It is possible that this may have been due to changes in this overdeepening feature. The diversion of water around this obstacle could be a factor in the change of main egress portal location.

The dimensions of the overdeepening are unlikely to have changed all that much since 2012, it is much more likely that this change in egress point is due to changes in the ice geometry.

6.3.2 Temporal evolution of the drainage system at Findelengletscher

The hydrology of valley glaciers varies across the melt season, becoming more efficient at processing meltwater as the season progresses (Cook & Swift, 2012) (see Section 1.2.2). Findelengletscher is no different in this regard. Evidence for this comes from three sources: GPR findings, Ice loss (through DEM comparisons) and surface velocity. Comparisons of GPR traces recorded in February and July (Figures 3.11, 3.14, 3.15, 3.17) show significantly more reflectors in July; this is due to the abundance of meltwater within the glacier at this time. From the GPR traces, the bed topography was ascertained and used to predict where channelised drainage may develop (see Figure 3.22). Once this predicted flow routing was available, the GPR traces, particularly those from the early melt season (6th July), could be analysed to see whether any signs of the hydrological system could be found. Figure 3.20 shows how a specific GPR transect can be looked at directly over where a predicted hydrological channel is located. Figure 3.26 and 3.27 show how a channel can be seen to be present. Whether this is an englacial or subglacial channel is not clear, however the reflectors above and to the side of the channel are crevasses that have opened in the glacier, caused by melt at the channel. The polarity of these crevasses suggests that within them there is a material denser than ice (water or sediment) (see section 2.3.3.3).

The bed model also highlighted the presence of an overdeepening which will influence the hydrological system. The effect that this overdeepening has on the glacial dynamics will be covered in the following section (6.2.3), however the effect it has on the hydrology at Findelengletscher can be covered here. The overdeepening causes water pressure and basal

sliding to remain high due to the energy that water requires to escape the overdeepening being dissipated in order to flow up the adverse slope. Conduit re-freezing may occur if the adverse slope is steep enough (Hooke & Pohjola, 1994) and therefore the enlargement of conduit sizes by melting is restricted, leading to high water pressures. This varies from the 'standard model' of channel formation in spring and summer whereby a reduction in subglacial water pressures occurs. Therefore, at the overdeepening the summer slowdown of ice velocities may not occur (Cook and Swift, 2012). This is shown succinctly in Figure 1.10. Comparisons of the ice flow velocity above the overdeepened area at various times in the late summer for 2016 and 2017 suggests that a more distributed system may be present (Figure 5.13) with all but one (3rd – 6th September (F4-F5)) showing an area of high velocity over where overdeepening is located. It can be concluded therefore that the overdeepening causes localised velocities to remain high longer into the summer melt season by enabling a more distributed system to be prevalent for longer into the melt season. These findings are supported by Swift *et al.* (2021) who found that subglacial drainage at the terminus of Findelengletscher was dominated by distributed flow during the 2016 summer.

6.4 THE EFFECTS OF OVERDEEPENINGS

Overdeepenings are an important feature of bedrock topography, specifically due to the unique behavioural changes that they create in subglacial drainage hydrology. As mentioned in the previous section, overdeepenings can enable water pressures and basal sliding to remain high for longer due to their ability to resist the typical development of the hydrological regime across a melt season. The overdeepening at Findelengletscher can be compared to that of other overdeepenings from the literature to see if there are any similarities in dynamics between them.

6.4.1 The effects of overdeepenings on glaciers and ice sheets

Overdeepenings at the beds of ice sheets may respond in a slightly different way to that of valley glaciers. The diminished influence of the ice-surface slope at larger glacial bodies can encourage the presence of ponding at overdeepenings. Due to the steeper ice surface slopes of valley glaciers, this is much rarer. The ponding of water within an overdeepening can cause variations in velocity to occur in the opposite manner to what is expected and found at overdeepenings where ponding isn't present. For example, Hooke *et al.* (1989) found that, for an overdeepening showing no evidence of ponding, velocities are high up-glacier and diminish to ~50% of their velocity as the glacier travels over them slowing the most at the adverse slope. However, Ross *et al.* (2011) found that ice flow velocities sped up to around twice the velocity when ice travelled over a subglacial lake at what would be the adverse slope if no lake was present (Figure 6.9).

Overdeepenings are considered to lower the ice surface slope which would encourage additional sedimentation and a more efficient ice flow (Cook & Swift, 2012). The flattening of the surface slope should in theory, encourage supercooling by enabling the supercooling ratio to be met. Bed morphology has a significant influence on sediment evacuation and deposition patterns as subglacial drainage is heavily controlled by it. (Alley *et al*., 2003; Cook & Swift, 2012). For bed topography sloping down-glacier, meltwater in the summer alters the hydrology present within the glacier into a highly efficient system of channelised drainage paths (Seaberg *et al*., 1998, Nienow *et al*., 1998; Section 1.2.2). Conversely, distributed and less efficient drainage systems should endure longer through the melt season where an adverse slope is present (Hooke, 1991; Alley *et al*., 2003a). Therefore, overdeepenings in the bedrock topography at glaciers and ice sheets will accumulate sedimentary deposits at these

locations. Overdeepenings are widespread in ablations areas at temperate glaciers (Hooke *et al.,* 1989; Cook *et al.,* 2006) where, due to an increased amount of surface meltwater available, bedrock erosion is more prevalent (Hooke 1991; Herman *et al.,* 2011). Creyts *et al.* (2013) theorised that the presence of overdeepenings encourage less efficient drainage systems and works at Storglaciären, Sweden, suggest that englacial routing of surface melt is occurring (Fountain *et al*., 2005). More recently Church *et al.* (2019) found GPR traces and borehole imagery that suggest similar processes at Rhonegletscher (Figure 6.10).

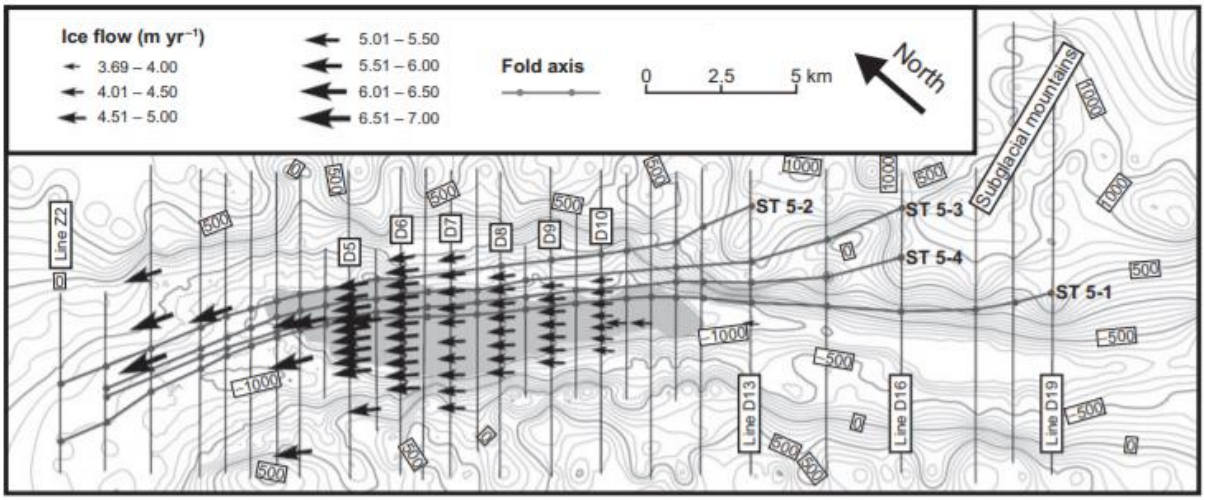

Figure 6.9: *Ice flow velocities over a subglacial lake, Western Antarctica (Ross et al., 2011).*

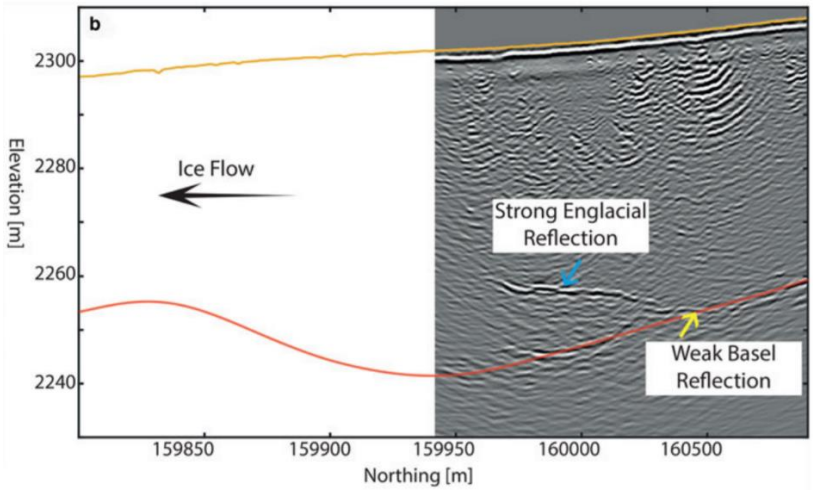

Figure 6.10: *Englacial conduits across an overdeepening at Rhonegletscher (Church et al., 2019).*

6.4.2 Basal sediment and supercooling at Findelengletcher

During the GPR data collections in both February and July 2017 respectively, transects 12 (Feb) and 14 (July), both showed a clear reflector above where the bed was located (see Figure 3.11). It was believed that this was a seam of sediment travelling up out of the overdeepening. Secondary evidence for this comes from the sediment deposits further down-glacier as seen in Figure 3.12 where sediment is being deposited on the surface of the glacier.

As discussed in Section 3.3.2.1, Boulton (1970) observed debris rich planes considered to be thrusts at angles of 20-85°, whilst Gulley & Benn (2007) found that thrusts occur at slope angles approximately eleven times that of the overlying ice. The angle of this reflector in transects 12 and 14 was calculated not to be within these limits. Both of these transects returned a slope angle of ~10° and a slope angle comparison with the surface slope came back at approximately 1.5 times. Based on these criteria, the trace is believed to be basal ice overlaying subglacial sediment, similar to that of the work carried out by Alley *et al.* (2003a). They found what appears to be a similar englacial feature which they hypothesised as basal ice overlaying subglacial sediment at Muir Glacier, Alaska (Figure 6.11). It was suggested that the basal ice at this feature had a slope angle ratio to the ice surface of 2:1 and was therefore considered to meet the supercooling threshold (Hooke and Pohjola, 1994; Alley *et al*., 1998; Cook and Knight, 2009). Locations where the supercooling threshold is met can be seen in Figure 4.7 and shows that it is likely that the supercooling threshold is being met in at least one location at the terminus.

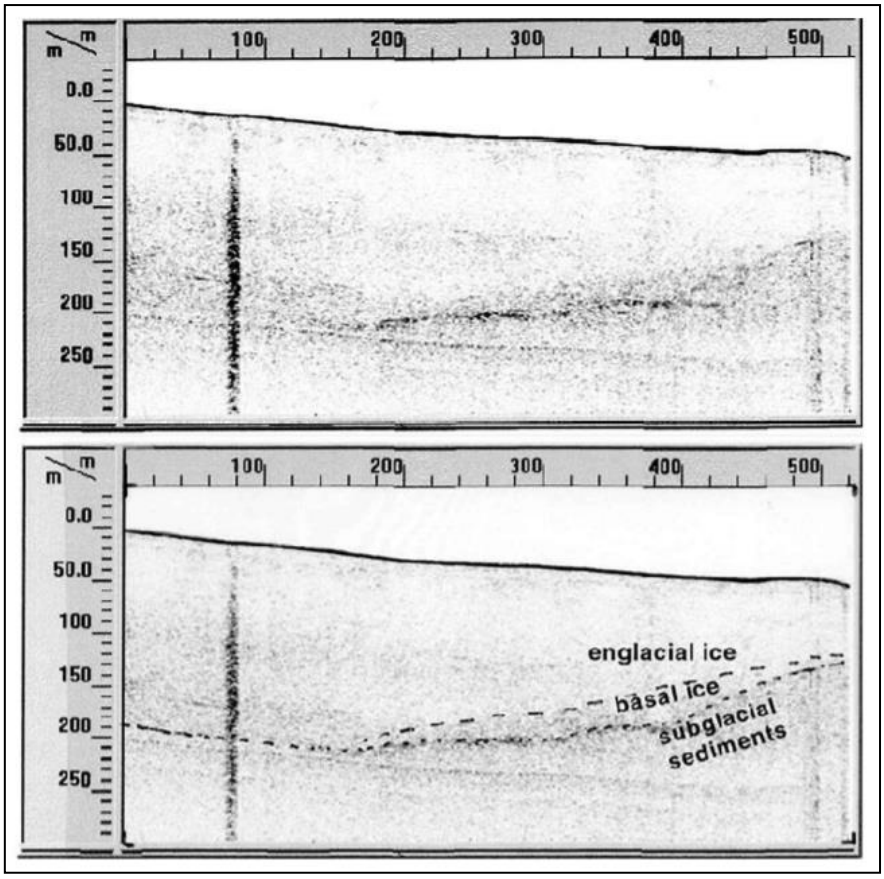

Figure 6.11: *Basal ice and subglacial sediments found on an adverse slope at Muir Glacier, Alaska (Alley et al., 2003a).*

Silt-rich basal ice has been found to be common where supercooling occurs (Cook *et al*., 2010; Swift *et al*., 2018), particularly if the slopes greater than 1.2x the ice surface slope. However, as the melt season develops and channelised drainage becomes more prevalent, basal sediment flushing rates increase (Swift *et al*., 2005b). Rates of quarrying of the bedrock was considered too small to be noticeable based on the time between surveys, the resolution of the traces, and error levels inherent in the recording of this data (see Section 3.4.2.2).

Stratified silt-rich basal sediment was found on site (Cook, S.J., pers. comm.) and had characteristics that suggested supercooling was and/or is occurring within the glacier as can be seen in Figure 6.12. According to Cook *et al.* (2006; 2009) a high silt content in the

entrained sediment is indicative of supercooling processes. As discussed in Section 1.4.3, supercooling occurs where the adverse slope angle reaches 1.2 to 1.7 times the ice surface slope. Evidence therefore points towards the overdeepening highlighted in Section 3.2.4 fulfilling the supercooling ratio threshold. Further support for this can be seen by observations of frazil ice exiting the glacier (Figure 6.12) which is an indicator of supercooling occurring (Yde et al. 2005; Larson et al. 2010). Swift *et al.* (2021) suggested that an inefficient subglacial flow morphology is present at Findelengletscher which is backed up by the steepness of the relation between discharge and suspended sediment concentration in fieldwork carried out at the main egress point in summer 2016.

The reflector measured at Findelengletscher (Figure 3.11) had a bed to ice surface ratio of 1.5 and therefore also meets the supercooling threshold. Sediment rich basal ice is considered to make up the area between the two traces. Photos taken from the field show the cauldron collapse ~100 m up-glacier (Figure 6.13). Within this cauldron can be seen a considerable volume of sediment entrained within the ice. Of note are the high levels of sediment being carried englacially, perhaps in basal crevasses, and deposited on the surface which is indicative of high basal water pressures (Alley *et al*., 2003) and is consistent with what is understood to be the effects of supercooling plugging low pressure channels, causing high pressure water that is capable of rising to the surface. The fact that so much sediment is entrained within the glacier here suggests that there is not enough energy to flush this sediment out of the overdeepening. The increase in potential energy from adverse elevations will reduce the generation of heat to below what is needed in order to maintain water on the phase boundary. This water will then supercool to form ice (Lawson *et al*., 1998). This amount of englacial debris would explain why GPR transects in the area were busy and complicated, causing difficulties in ascertaining the bed topography. Supercooling is not the only process

by which sediment can be transported to the surface, regelation (Iverson, 1993), or folding and thrust faulting through compressive stresses (Moore *et al*., 2011) could also be involved. The amount of secondary evidence that suggests that supercooling is occurring here does lend itself to supporting the notion that this process is involved in some form in the transportation of basal sediment to the surface.

The basal sediment at the bed refreezes onto the glacier and is transported englacially until it is deposited at the surface. As posited by Stearns and van der Veen (2018) sediment can cover basal irregularities which reduces the bed roughness to zero, increasing observed surface velocities. Therefore, the refreezing of basal meltwater along with the removal of basal sediment which occur during supercooling would act in the opposite manner causing velocities to be slower here than they would otherwise be. However, Alley *et al*. (2003) suggest that ice creation from regelation will tend to block up or 'plug' areas of preferred hydrological flow which would spread the water flow and reduce the ability of the glacier to first erode, then transport basal sediment. The spreading of water flow would likely make the glacier in the localised area less efficient at dealing with meltwater. The increased lag time between melt and discharge leading to more water within the glacier and therefore a longer period where the effects of sliding are increased due to the lubricative effects of this water. This may increase velocity rates locally. Figure 4.6 shows velocity decreasing over the upslope area of the overdeepening. Based on available evidence from Tweed et al. (2005) and Cook et al. (2007; 2010) supercooling varies considerably both temporally and spatially even when conditions for the process are being met, so the idea of supercooling having an effect on ice velocity is tenuous at best and that the underlying topography is the more important factor. Given the location (travelling out of an overdeepening) This englacial basal laden ice band feature (Figure 3.19) is believed to be related to an injection of sediment-laden supercooled

water associated with an overpressurised overdeepening much in the same way as Figure 6.11 shows at Matanuska Glacier (Ensminger *et al.,* 2001; Alley *et al.,* 2003) and Monz *et al*. (2021) at Storglaciären (Figure 6.14). Sediment desposited at the terminus from this band (Figure 3.12; Figure 3.13) is similar to that at Storglaciären (Monz *et al.,* 2021) due to longitudinal compression of ice at the adverse slope near the glacier terminus.

Figure 6.12*: Top: Field photo of basal debris facies band near the main egress point of Findelengletscher, August 2016. Bottom: Frazil ice in the proglacial zone of Findelengletscher, 1 km from the glacier terminus 28th August 2016.*

Figure 6.13: *Field photo of the collapsed cauldron at the terminus of Findelengletscher facing south, taken 3rd September 2017.*

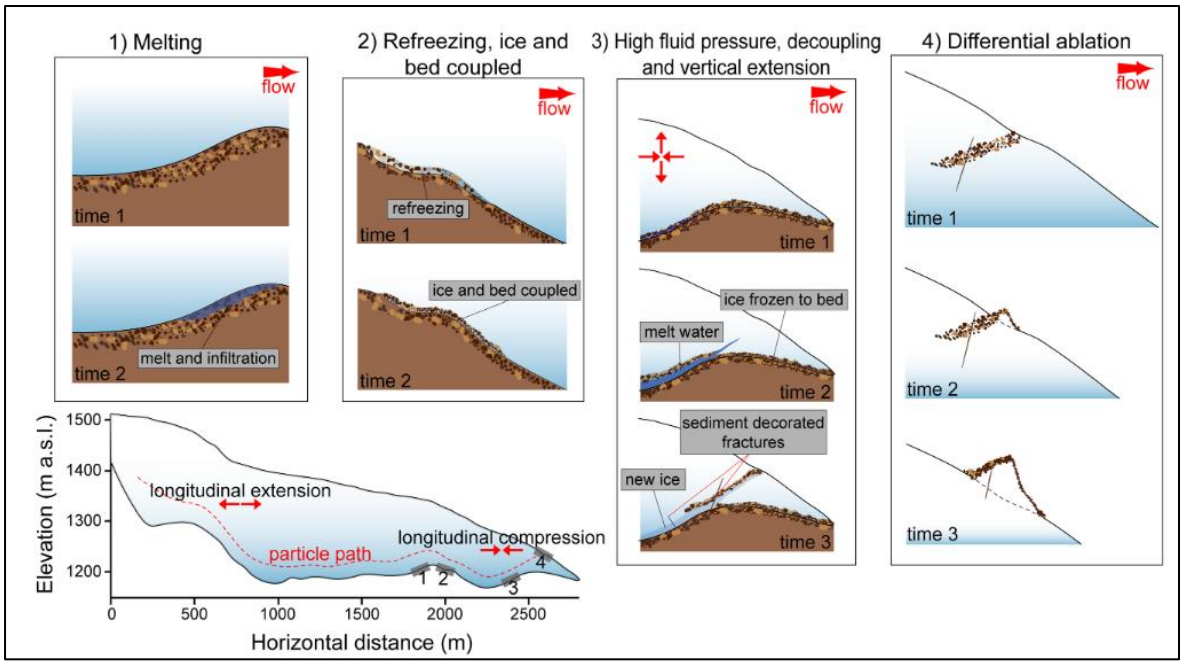

Figure 6.14: *Debris entrainment at a glacier base based on variations in bedrock topography and subsequent transportation to the ice surface (taken from Monz et al.,* 2021*).*

6.4.3 The effects of an overdeepening on Findelengletscher

The overdeepening at Findelengletscher should behave similarly to other observed overdeepenings; resisting the seasonal evolution of the drainage system towards a more efficient channelised hydrology. The drainage system can change over small distances (Jansson, 1996) and therefore the dynamics of this system should also be highly spatially variable. It is therefore possible that the terminus could change spatially from a channelised system to an inefficient distributed one locally over the area of the overdeepening.

There is no obvious flattening of the ice surface above the overdeepening (see Figure 4.7). This is likely because it is situated close to a retreating terminus where the slope angle is typically steep relative to the rest of the glacier.

The work of Hooke *et al.* (1989) at Storglaciären (see Figure 6.15) shows a sharp decrease in velocity as the glacier moves over the maximum depth of the overdeepening, and a slower steadier decrease in velocity as the glacier travels over the adverse slope. A similar pattern was observed at Findelengletscher at the end of the 2016 melt season (Figure 4.7) and at the beginning of the melt season 2017 (Figure 6.7). However, this was not always found to be the case, and spatial changes to the routing of water in the 2017 melt season are believed to have caused less meltwater in the system around the overdeepening. Discharge was significantly higher in the 2017 season (Figure 5.5), including a spring event in late June. The higher level of discharge is likely to have had an effect on the hydrological system, making it more efficient over the course of the melt season when compared to that of 2016. It is believed that this efficiency has caused more of the meltwater to drain through the main portal, slightly up-glacier from the overdeepening and that most meltwater traverses the edge of the overdeepening to reach the portal as this is the most efficient route.

Therefore, much less water is present at the overdeepening generally, causing basal water pressures and sliding rate to be low and a less efficient drainage system to be present in general. However, at times of high discharge englacial conduits will be more active in this area, and this will lead to higher water pressures here later into the melt season. We can see from the Figure 4.7 & Figure 6.5 that velocities are higher over the overdeepening (AOI2) in the summer than the more channelised area up-glacier of this (AOI3). These findings are consistent with those of Cook & Swift, (2012) whereby basal water pressures and sliding velocities continue at higher rates deeper into the melt season. The presence of high quantities of till at the cauldron and immediately down-glacier from the overdeepening would further support this area being inefficient with regard to drainage.

The presence of an overdeepening with adverse slope may alter the main flow route of the subglacial hydrological channel. Hooke & Pohjola (1994) found that over a riegel at Storglaciären, Sweden, hydrology passing through this area moves almost entirely englacially. Overdeepenings have been found to cause substantial lateral deviations in the drainage system (Sharp, 2006) and it believed that this is what is occurring at the Findelengletscher terminus as most of the subglacial water looks to circumvent the overdeepening shown in Figure 3.10 and flow in the most efficient way towards the main egress point to the south around the overdeepening as is shown in Section 3.4.3, Figures 3.22, 3.23 and 3.25 where subglacial flow routing switches from the true north of the glacier to the south across the face of the overdeepening to the main egress portal. Figure 3.30 taken in late summer 2019 after considerable retreat at the terminus shows the route of the now proglacial stream that follows the same route that was predicted subglacially two years before, again flowing across the face of the overdeepening location. It has also been suggested that water will flow

englacially across the top of the overdeepening (Fountain & Walder, 1998; Church *et al*., 2019) traversing the overdeepening completely.

During the melt season we are likely to see an increase in the ice flow velocity at and around the main subglacial meltwater channel due to the effects of basal sliding (covered in Section 1.3). If the overdeepening at Findelengletscher is to behave in a similar way to other temperate valley glacier overdeepenings, it is also likely that ice flow velocities will be high here relative to surrounding ice due to the lubricative effects of basal sediment (more prevalent having been flushed into the overdeepening (Cook & Swift *et al*., 2012; Swift *et al*., 2018; 2021)) and subglacial water.

6.4.4 Velocity changes across the overdeepening

It is expected that at an overdeepening – because of the change in longitudinal stress – the velocity will increase up-glacier of the overdeepening where the downslope is steepest and decrease over the adverse slope as discussed in Section 1.4.1. As can be seen in Figure 6.15, Hooke *et al*. (1989) found exactly this at Storglaciären. Looking at the velocity along the central flow transect at the overdeepening of Findelengletscher over a 10-day period in the melt season of 2016 (27th August – 6th September) shows a similar picture with a rapid increase in velocity moving down-slope towards the centre of the overdeepening followed by a gradual reduction in velocity as the bedrock slope becomes more adverse (Figure 4.6). The inefficient evacuation of sediment on the adverse slope of the overdeepening should increase the amount of subglacial till present which can influence rates of glacier flow, increasing velocities due to greater rates of basal slip due to soft-sediment deformation in this area. Previous studies suggest that the hydrological systems at overdeepened areas would be inclined to favour a less efficient form (Alley *et al*., 2003; Werder *et al*., 2016) i.e., distributed

over channelised. This would support an increase in velocity at the adverse slope as well as for the rest of the glacier downstream from the overdeepening (c.200 m). As has previously been discussed, a channelised drainage system is understood to be present which skirts this overdeepening and exits the glacier via a portal to the south of the overdeepening and much of the remaining water will likely be distributed around or over the overdeepening englacially. The pattern of high velocities within close proximity of the downslope of the overdeepening and lower velocities at the adverse slope is noticeable at many different time periods from this study. For example, Figure 4.5 and 4.6 shows this from 27th August – 6th September 2016, Figure 6.7 shows this for the Spring period (5th – 7th July 2017) and Figure 4.9 shows this for Summer (7th July – 7th September 2017). This is an expected pattern of glacier movement being influenced by topography, where velocities are higher down slope and slower on the adverse slope. However, in order to see whether any hydrological factors might be influencing velocity, the percentage change in velocity vs the interpolated baseline is a better indicator of whether velocities are continuing to stay high later into the melt season indicative of a more distributed system (Swift *et al.,* 2021)

The opposite of what is occurring at Storglaciären and Findelengletscher in terms of a longitudinal velocity profile can be seen in Ross *et al*. (2011) where ice velocities over an overdeepened area appear to increase over the adverse slope. This is likely due to the ponding present subglacially and the reduction in friction this presents as well as with the presence of ponding the glacier technically wouldn't be travelling upslope. It may be possible to estimate whether ponding is present at a site from velocity profiles along known overdeepenings. Whilst this appeared to be the trend over the shorter term (1 month) at both Findelengletcher and Storglaciären, when looking at velocity across an entire melt season such as the 2017 summer, (5th July – 7th September) smaller scale variations in glacier

velocities are less apparent. This may be due to the resolution of the data when taken over longer time periods not accounting for smaller scale fluctuations in velocity due to the larger sampling windows required.

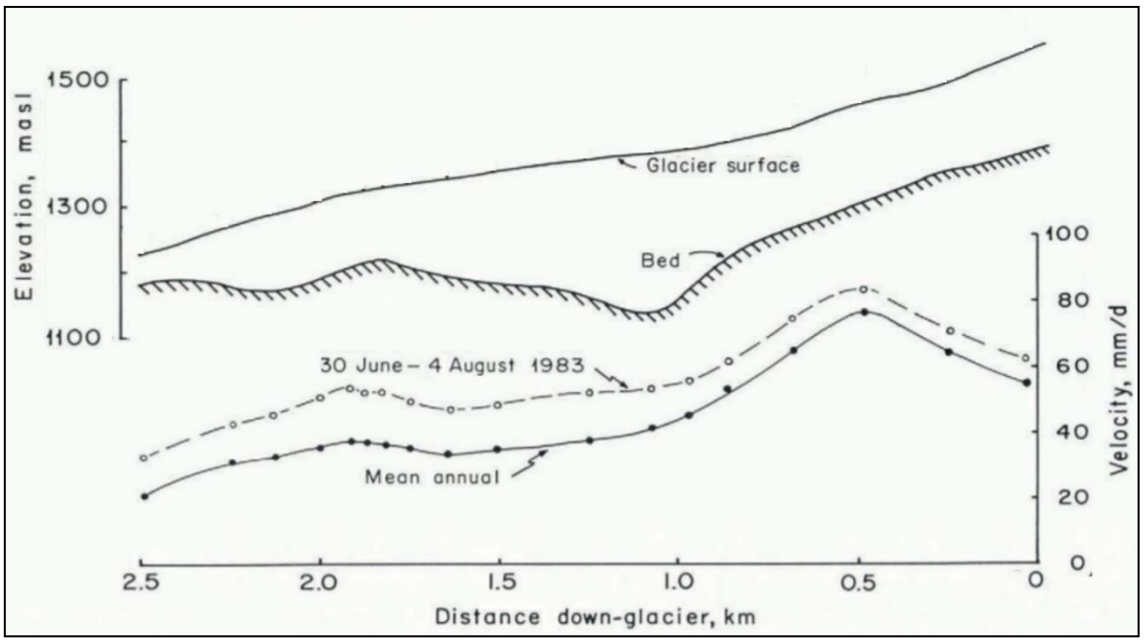

Figure 6.15: *Longitudinal variation of velocity across an overdeepened bed at Storglaciären in July 1983. Taken from Hooke et al. (1989).*

6.5 ICE LOSS

As outlined in Chapters 3 and 5, the patterns of ice loss can tell us a lot about the dynamics of a glacier. Ice loss is predominantly caused by melt, although at tidewater glaciers or glaciers terminating at a body of water, calving can also be a form of ice loss (Bassis & Jacobs, 2013). Ice loss at glaciers is predominantly looked at across regions (Luthcke *et al*., 2008; Paul & Haeberli, 2008; Farinotti *et al*., 2015; Zheng *et al*., 2018); or continents (Brun *et al*., 2016; Braun *et al*., 2019) and the resolution of such findings are low. However, there is significant smaller scale complexity in glacier melt (Arnold *et al*., 2006). A high degree of complexity at

spatial levels is due small-scale topographic features which cause localised high and low ice loss totals (Arnold *et al*., 2006). The difficulty in capturing the mass loss before UAV technology was the relative sparsity of stakes and low resolution of satellite data.

The process of estimating subglacial conditions such as the hydrological system from changes in ice loss has been done before. Immerzeel *et al.* (2014) estimated the locations of englacial conduits based on subsidence patterns calculated by differencing DEMs and Stocker-Waldhuber *et al.* (2017) identified specific localised melt from volcanic activities beneath a glacier.

6.5.1 Patterns of ice loss Findelengletscher

Looking first at ice loss patterns at Findelengletscher, the least ice loss occurred over the winter period, averaging 9.4 m yr^{-1} (Figure 5.23). The amount of ice loss more than doubled during the Spring (19.83 m yr^{-1}), and the summer (23.06m yr^{-1}) represented the period with the most ice loss due to higher atmospheric temperatures. Ice loss was found to be more concentrated as the melt season progressed. Initially in spring, a steady melt across the bottom ~800 m of the ablation area. A small area was evident, situated at AOI6 & 7 where no ice loss appeared to be occurring. One possible explanation could be the capture of a kinematic wave here where the glacier uplift has cancelled out the recording of any potential melt. These kinematic waves usually occur with horizontal velocities of 5-8 times the surrounding ice (Van de Wal & Oerlemans, 1995; Hewitt & Fowler, 2008)). A look at the glacier velocities in this area (Figure 6.7) show that velocities are high here ~50-70 m yr^{-1}, yet they are not quite fast enough to support the hypothesis of a kinematic wave.

Summer ice loss could clearly be seen to be focused around specific areas or features of the field site. Secondly, addressing the ice loss spatially at Findelengletscher, a general pattern of

down wasting at the surface in the ablation area, causing the glacier to retreat over time can be seen (see Figure 2.11 & 3.28). Looking at ice loss in a smaller scale however, show that certain areas are melting at significant rates. The area with the highest ice flow velocities (AOI8) also displays the highest rates of melt with rates during this summer period (7th July – 7th September) of 50 m yr^{-1}. It is understood that this is mostly due to the underlying hydrology present in this area, being down-glacier of an area of considerable crevassing which directs surface melt to the ice-bed interface which would increase local water pressures and water pressure fluctuations (Iverson, 1991; MacGregor *et al*., 2000) and basal sliding in this area. The influx of meltwater into this area along with the high water pressures will have a melting on the drainage channels present at this glacier. This shows how ice loss, and velocities are strongly linked. The collapsing cauldron in AOI2 also shows significant loss as the ice caves in under its own weight having been eroded by the meltwater channel below.

6.5.2 Interpreting Seasonal and annual elevation change

By comparing the differences in elevation changes spatially from both seasonal and temporal timescales, patterns emerge that can help towards explaining what changes might be occurring within the glacier at different stages in the year. The change from a distributed system to a channelized drainage system occurs gradually over the melt season (see Section 1.2.2). By taking a closer look at the ice loss levels we can see how the glacier is displaying this change.

Ice loss comparisons between the early (Spring) and late (Summer) melt season show that loss is more concentrated in specific areas later in the season (see Figure 5.21). Figure 6.16 shows a comparison between early and late melt season mass loss (July 5th - 7th and September 3rd - 7th respectively). It can be seen that mass loss per day is generally higher in

July, likely due to the higher atmospheric temperatures in July averaging of 12 °C across 24 hours compared to 7 °C in September (Figure 6.17), with surface erosion of supraglacial meltwater channel clearly seen. However, ice loss specific to the development of the cauldron features is more prevalent in September (Figure 6.16). This is likely due to a more channelised drainage system having developed by September here and therefore higher subglacial channel erosion caused by the high levels of meltwater flowing through this area leading to internal stresses characterised by the development of the circular crevasses in the surface. The crevasses that develop and the subsequent surface concaving help to channel more surface water into this area which further increases the amount of meltwater available. Just to the north of this zone highlighted in Figure 6.16 two moulins develop over the course of the summer which further helps to deliver surface melt into the internal hydrological structure of the glacier. Closer to the main water egress point can be seen a more developed and older cauldron finally collapse from its centre as the glacier is eroded from below to such an extent that it could no longer support its own weight (the same thing happening to the highlighted area in Figure 6.16 in 2019). Over the course of the 2017 melt season the development of a channelised drainage system encourages localised erosion along and around the main hydrological flow channel and eventually leads to cauldron development and eventual collapse travelling back up along this flow path.

It is not just this area that is noticeable for large amounts of ice loss over the annual and summer timescales. The area immediately preceding the ice fall at the top of the field site shows the highest rates of mass loss from the entire field site except for the cauldron collapse next to the subglacial meltwater portal. It is unclear as to why this is occurring, as due to the heavily crevassed nature of this area, it was not possible to safely carry out a GPR survey. It is likely however, that due to the high mass loss combined with the high velocity of ice flow, a

major subglacial pathway may be present here and a cauldron like feature could develop in the near future as the ice thins and the glacier retreats.

Ice loss comparisons between the early (Spring) and late (Summer) melt season show that loss is more concentrated in specific areas later in the season (see Figure 5.21). This is due to a more channelised (localised) system having developed and supports that the hydrological system was still moving towards a more channelised system after the July orthomosaic data was gathered.

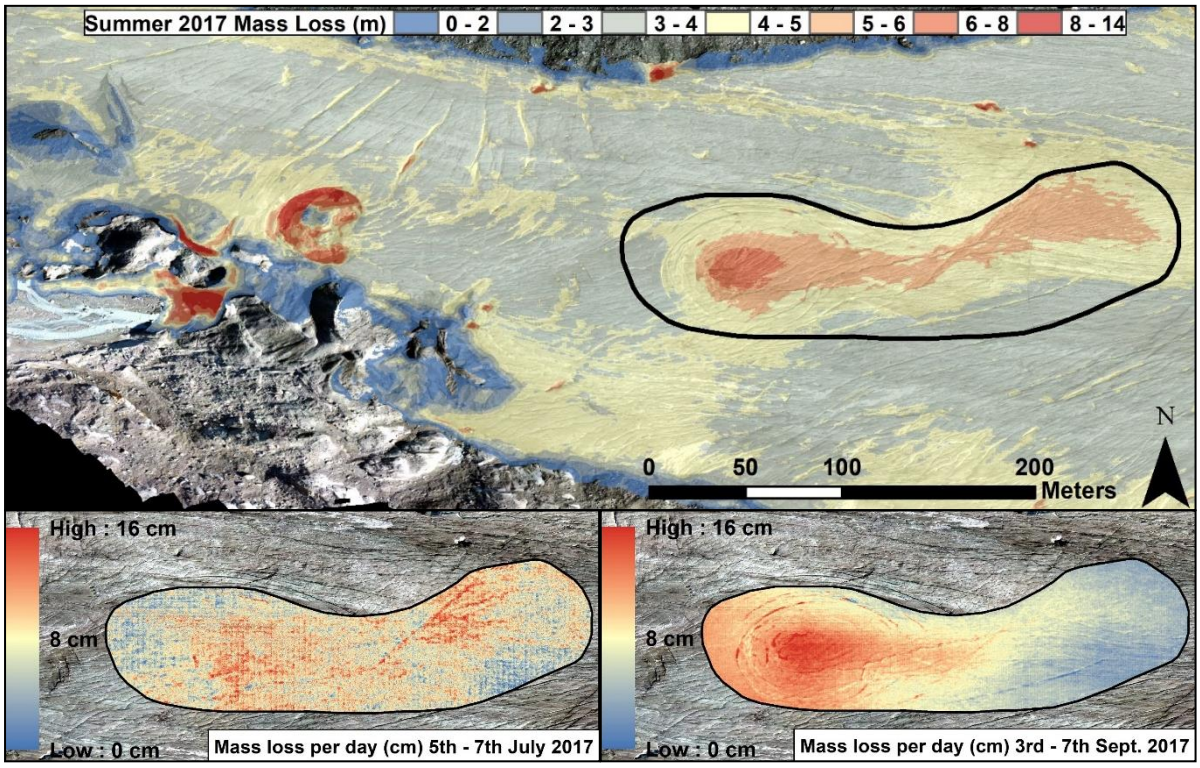

Figure 6.16: *Summer 2017 mass loss across the cauldron feature at Findelengletscher, also considered to be the area of prominent hydrological flow. Above shows mass loss across the entire summer from 5th July to 7th September. Bottom left shows patterns of loss per day at the beginning of the season. Bottom right shows the patterns of loss at the end of the season.*

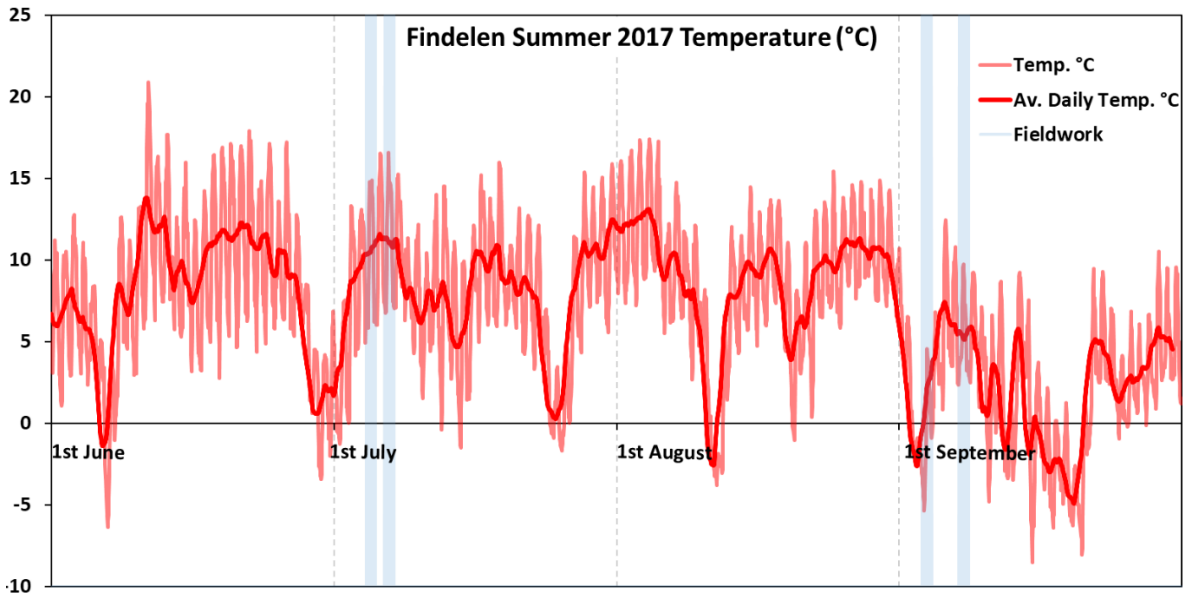

Figure 6.17: *Atmospheric temperatures across the 2017 melt season with highlighted data collection days at Findelengletscher. Weather station is located (lat 46.00036, lon 7.8727036) approx. 2 km up glacier and at an altitude 300 m higher than the field site. Therefore, actual field site temperatures are likely to be underestimated here.*

6.5.3 Ice loss vs ice flow

A link between ice loss and ice dynamics, namely an increase in ice velocity (Li *et al*., 2016), is logical considering meltwater reduces friction with the glacier bed which therefore increases sliding. Therefore generally, the more ice loss (melting) occurring, the faster the glacier will flow. However, this link is more complicated than it first seems as more melt can cause channelisation beneath the glacier which in turn reduces ice flow, or melt might not even reach the bed to provide the reduction in friction. Spatial meltwater location and its method of travel (supraglacial, englacial or subglacial) can vary melt's effect on ice dynamics. When looking at the area immediately downslope of the ice fall, which displays the highest levels of both ice loss and flow velocity (Figure 3.28, Figure 4.9) at the study area, this link does appear to be accurate. It should be considered here whether the ice loss is due to melting or not. Ice

loss and ice flow are consistently high in this area, however percentage change to the velocity of the baseline interpolations shows that acceleration in Spring and summer are similar to that of the rest of the glacier (Figure 5.7; Figure 5.8) despite this area displaying significant ice loss in the summer period (Figure 5.21). However, ice velocities around the cauldron features at or near the main meltwater portal appear to be slower than the surrounding area (Figure 6.18) despite the high levels of elevation change in this area in summer 2016. However, when comparing ice loss and ice velocity in this same area in summer 2017 velocities in Figure 6.18 are significantly higher than surrounding areas which could be in part a response of this collapse, which could impact upon the horizontal feature tracking. It is worth pointing out that Figure 6.18 shows velocity data across a period of 64 days and extrapolates these values to give an annual velocity in m / yr. High velocities of up to 120 m of flow over the course of a year are therefore not realistically what can expected here, but more gives a scale of the short-term displacement of the ice during this high-melt period and is perhaps more indicative of rapid changes around the cauldron features.

The reason for the high levels of both mass loss and flow velocity immediately down valley from the ice fall, may be due to the heavy crevassing occurring in this area. The widening of crevasses in the summer from surface meltwater can give the appearance of extreme elevation change (based on the high relief of crevasses) as well as the high meltwater in the area running off into these deep crevasses causing faster ice flow velocities from less friction at the bed and higher levels of melt from the abundance of warmer meltwater available.

The lining up of areas displaying extreme ice loss and the subglacial water flow routing system directly up glacier from the portal is believed to be linked. The high levels of meltwater running through this area is leading to increased localised subglacial melt. This in turn causes

increased stress from ice above the subglacial flow channel leading to crevassing as the ice collapses in on itself. These stress crevasses can be seen in Figure 3.24 and 3.25 above and around strong reflectors that are located where subglacial channels are located. This ice loss is exacerbated late in the melt season when the channelised system is at its most developed and efficient at routing water through a smaller number of larger conduits.

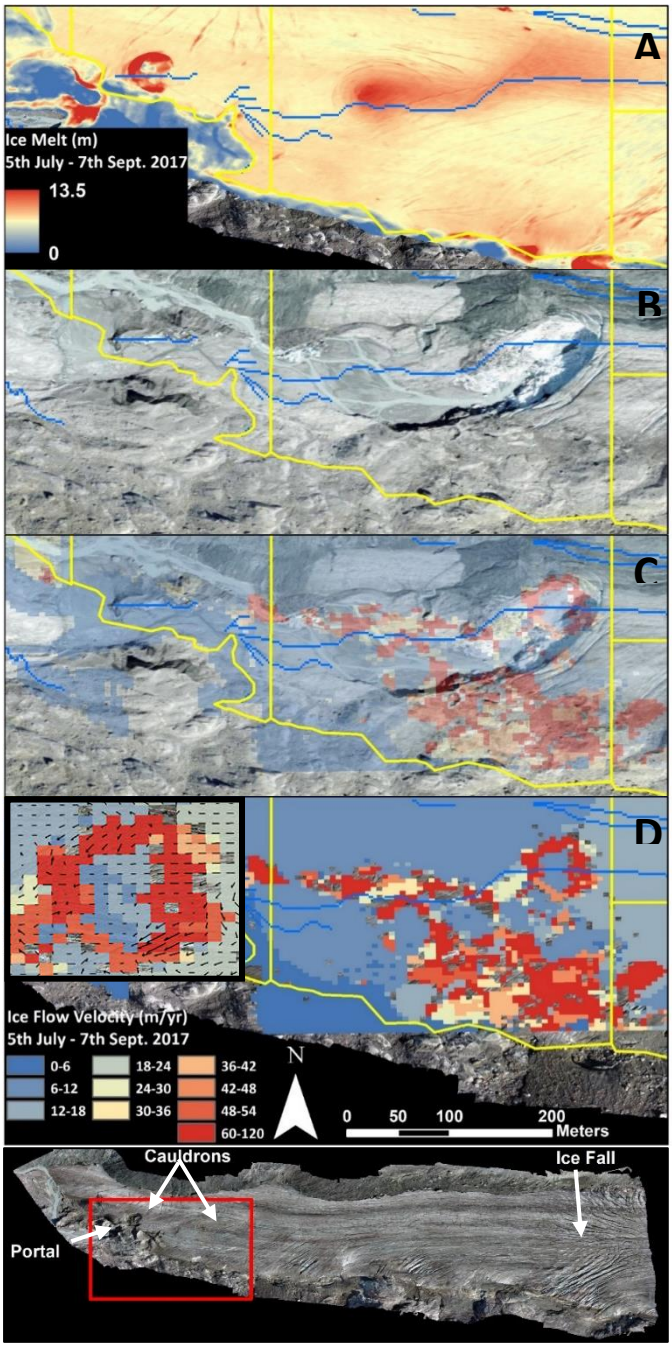

Figure 6.18: *A) Ice loss for summer period between 5th July and 7th September 2017. B) State of the terminus of Findelengletscher, 2019. C & D) Ice flow velocity over same period and comparison with the 2019 glacier extent. Inset in D shows a close up of the cauldron with ice flow velocity and direction. Yellow lines depict AOIs with cauldron development occurring within AOI3.*

From the findings when comparing orthomosaics from 5th July to 7th September across 64 days of the melt season of 2017 a general pattern of the glacier slowing as it reached the

terminus was observed (Figure 6.18). Due to the length of time between the orthomosaics that make up this time period, a considerable amount of background noise is present, and a much larger window size was necessary to capture trends. However, Figure 6.18 shows that within the noise can be seen a circular feature on the end of a long thin shape that looks likely to be related to the cauldron features present at the glacier. Here velocity is greatly increased around the outside of the feature whilst the centre remains consistent with the typical glacier ice velocity in this area. Directionally the ice appears to flow faster around the slower moving centre of the feature and on the immediate lee side of the feature, flow direction appears to travel contradictory to the expected downslope direction (Figure 6.18D). It could be that due to the amount of ice loss, that the expanding of crevasses are giving off the impression of ice moving backwards, or as Figure 6.6 suggests, melt of angular crevasses could give the impression of backwards movement.

The thin line of high velocity data in Figure 6.18 proceeding the cauldron feature follows what has been estimated to be the main subglacial flow pathway right up to the point of egress. It is therefore understood that the high velocities shown surrounding this pathway is due to increased sliding due to high levels of subglacial water.

When compared with ice loss data for the same period (Figure 6.18; Figure 6.19A) and the estimated subglacial flow data (Figure 3.22) spatially a direct pattern can be seen, namely that the noise directly follows both the mass loss and the flow path with the circular feature highlighting where the next cauldron collapse will take place. By referring to Figure 3.16 we can see that this feature is located where an extensive cauldron collapse occurred in 2018 however at the time of the orthomosaics being taken there were no signs of crevasse features present on the surface of the glacier. Therefore, in this case it was possible to show where

this cauldron feature would occur from micro-scale ortho-comparisons across a matter of 64 days. By using this velocity data combined with GPR feature data and bedrock surface estimations it has been possible to show future glacial features at least a year before they become evident on the surface. The clues for the development of these cauldron features present themselves subglacially at first and by using techniques such as GPR and orthomosaic DEM comparisons, the development of these features can be located much earlier than when they become noticeable to the human eye, in this example, at least a year before.

6.6 CAULDRONS AT FINDELENGLETSCHER

During the fieldwork certain glacial features were observed that warranted special attention. Whilst not directly a finding aligned with the first two research questions, these features may provide clues as to the conditions beneath Findelengletscher such as from a hydrological and glacial dynamics standpoint. A very clear feature at Findelengletscher noted from the site visits in 2016 and 2017 was the development and subsequent collapse of a cauldron-like feature close to the main meltwater portal. This feature is very distinct given its circular crevassing and 'bowl-like' shape. Since this original cauldron (Figure 6.18; Figure 6.19), multiple future cauldrons have begun to form.

Figure 6.19: *Field image of collapsed cauldron and distinctive circular crevassing at Findelengletscher looking south (3rd September 2017).*

6.6.1 Development and Analysis of Cauldrons

Cauldrons in the literature have been widely observed with Stocker-Waldhuber *et al.* (2017) identifying four different glaciers in the Austrian Alps and Egli *et al*. (2021b) studying 22 glaciers within the Swiss Alps. Magnusson *et al.* (2007) also discusses cauldron formation at Vatnajökull where a subglacial lake leads to the surface depression. At all four glaciers discussed by Stocker-Waldhuber *et al.* (2017), the collapses ended with the formation of subglacial lakes. It is likely therefore that the presence of significant meltwaters plays a significant role in their formation and development, indeed, Kellerer-Pirklbauer *et al.* (2019) suggest that the amount of water travelling these channels causes ablation rates to substantially increase. Cauldrons are predominantly found close to the terminus in rapidly

retreating glaciers where surface velocities are decreasing (Stocker-Waldhuber *et al.*, 2017; Kellerer-Pirklbauer *et al.,* 2019).

From imagery and GPR measurements of the cauldrons at Findelengletscher, before surface crevasses become apparent with naked eye, they can be identified via circular subsidence (Figure 6.18A), and englacial crevassing, usually around what appears to be a subglacial channel (see Figures 3.14, 3.15). The presence of a subglacial hydrological channel beneath shallow ice can instigate a collapse due to upwards melting from meltwater (Egli *et al.* 2021b). This cauldron formation above the subglacial channel has also been seen to occur at d'Otemma glacier, Switzerland in Figure 6.20 (Egli *et al.* 2021b). In this instance down-wasting of ice above the subglacial channel has been found to stretch back up-glacier 600 m, which supports the findings at Findelengletscher in Figure 3.16 and Figure 6.7. The development of cauldron features at Findelengletscher appear to form moving back from the terminus approximately one year apart. These findings are consistent with that of Stocker-Waldhuber *et al.* (2017) who found that these features develop in the immediate proximity of the first one within a year. They go on to suggest that they form at an elevation change of ~20-30 m with a diameter of upwards of 125 m which again is in keeping with the characteristics of cauldrons at Findelengletscher.

Once a cauldron is evident at the ice surface, through circular crevasses and ice loss at its centre, it will continue to subside due to thermal heat delivered by meltwater to the base. This continues until the surface ice collapses under its own weight possibly as a result of a sudden heavy precipitation event (Stocker-Waldhuber *et al*., 2017) which have been seen to increase ice velocities by 400 % (Iken, 1974). It is believed that the collapse of the cauldron

closest to the terminus at Findelengletscher (Highlighted as '2016' in Figure 3.16) happened after one of these high precipitation events around early August 2017 (Figure 5.4)

This feature occurs due to the presence of subglacial water flow, which is considered an essential criterion for the development of cauldrons (Figure 6.18B). The linear formation clearly denotes major hydrological pathways generally becoming less obvious with distance travelled up-glacier. High resolution velocity analyses have been shown to accurately locate cauldrons more than a year before they are able to be observed on the surface by crevassing and surface depression. (Figure 6.18C&D).

It can be concluded that the presence of cauldrons hastens glacier retreat. Figure 6.21 shows the significant speed up of glacier retreat over three years from 2016 – 2019 (~500 m) was similar to the retreat of the previous 7 years (also ~500 m). This increased retreat speed is considered to be, in part, due to the development of cauldrons (Egli et al. 2021a; 2021b). However, whether cauldrons can be considered an indicator for extreme retreat cannot be known for certain until further studies have been carried out (Stocker-Waldhuber *et al*., 2017).

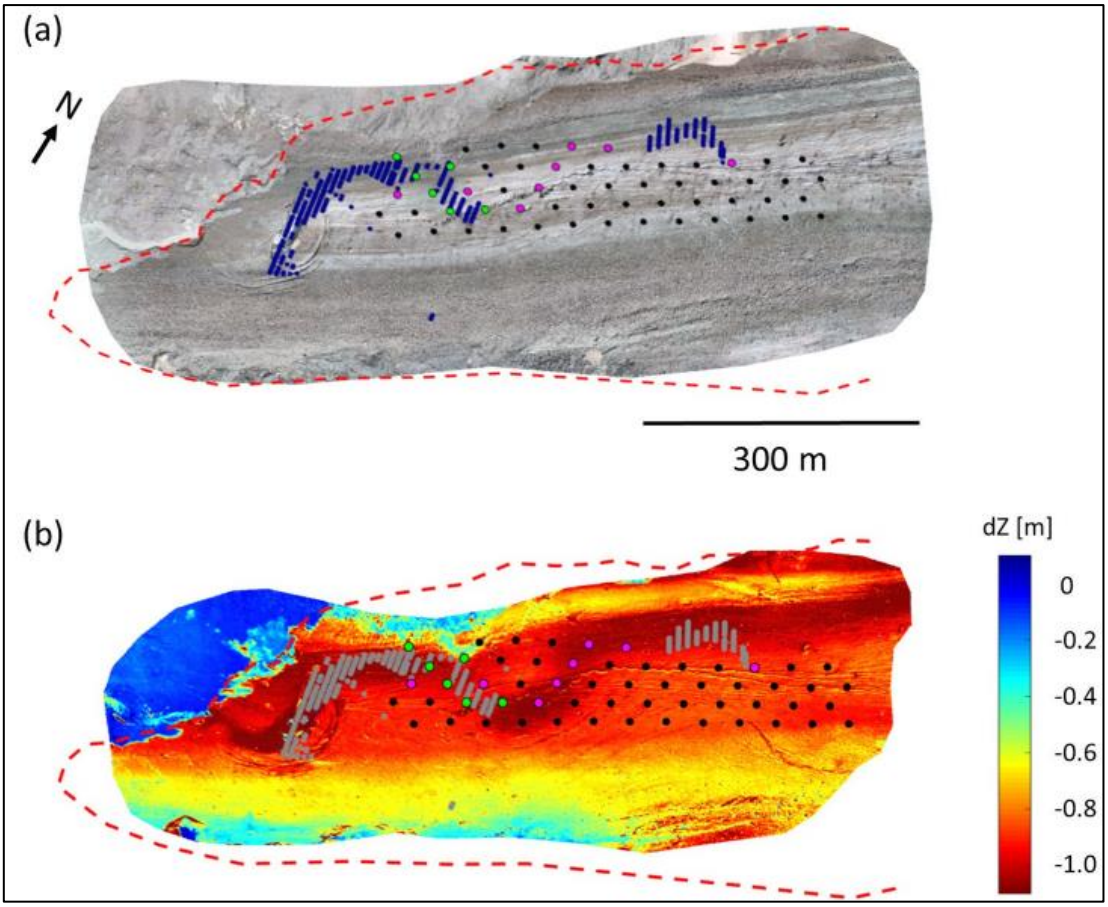

Figure 6.20*: Cauldron collapse and subglacial channel at d'Otemma glacier. a) Orthomosaic with ablation stakes (black dots) and GPR surveys (blue stipples). b) change in surface elevation between 7th – 23rd August 2018 (Taken from Egli et al. 2021a)*

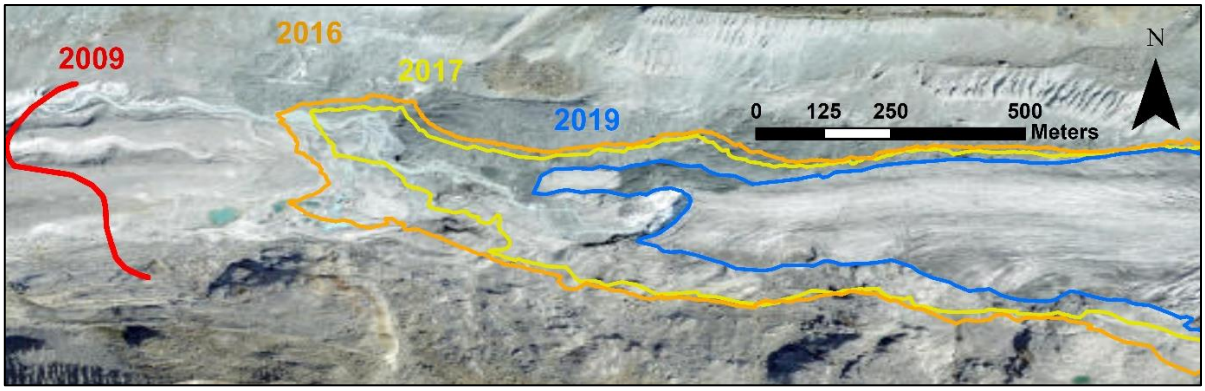

Figure 6.21: *Retreat of Findelengletscher from 2009 to 2019.*

6.6.2 Future Cauldron development at Findelengletscher

Looking forward, as the glacier continues to retreat, it is believed that a string of cauldrons will develop up glacier over the main subglacial flow path (Egli *et al*. 2021a). Figure 6.7 shows how this is happening, with UAV images from the summer melt season of 2019 displaying further cauldron collapses along this main flow line (D) where evidence was not visible from the surface during the fieldwork of this study. However, looking at transect 21 that was taken from summer 2017 fieldwork (Figure 3.26), we can see some englacial voids likely to be the beginnings of the cauldrons tell-tale circular surface crevassing located above a feature believed to be either water and debris filled englacial conduits caused by a subglacial channel, or the subglacial channel itself (Figure 3.26). Looking even further up glacier and therefore further forward in time, transects 22 & 16 shows the beginning of this process occurring 350 m and 1000 m up-glacier respectively (Figure 3.27; 3.17), in much the same way that this pattern is evident in the work of Egli *et al*., (2021a). From the GPR traces of transect 16 a feature believed to be a subglacial channel - albeit smaller than that observed in transect 22 – is present, above which is a void likely caused by the stresses of channel melt and expansion beneath. Figure 3.17 shows the reversed polarity, or 'negative-positive-negative' trace believed to be the englacial crevasse and the channel. Whereas the bedrock displays a 'positive-negative-positive' trace. It is likely, based on the current rate of retreat that this cauldron feature will begin to show on the surface in the 2020 melt season with a collapse the following year. From the temporal evidence of the development of these features, it has been shown that cauldron features develop above subglacial channels where ice loss is occurring at a faster rate than surrounding ice as seen in Figure 6.18A (Egli et *al.* 2021b) (covered in more detail in Section 3.5). Englacial crevasses present first before surface crevasses open up. Once surface crevasses have developed, supraglacial melt is channelled

into these crevasses - aided by the rapid lowering of ice surface in these cauldrons relative to the rest of the glacier (Kellerer-Pirklbauer & Kulmer 2019) – further accelerating melt. Subglacial melt and crevasses will expand to the point of cauldron collapse from below. To summarise, cauldron features can be identified before they are evident to the naked eye at least one year in advance through a number of methods. Within this work alone, indicators for these features developing have been through small scale velocity changes through feature tracking analysis, circular areas of ice loss through DEM differencing, englacial crevassing and subglacial channel traces through GPR surveys. These features have been shown to cause drastic localised ice loss until collapse, likely hastening the rates of glacial retreat.

6.7 SUMMARY OF DISCUSSION

A summary of the discussion, including some of the key findings of this thesis can now be made. How this study met its aims will be discussed in the concluding chapter.

7. CONCLUSION AND WIDER IMPLICATIONS

7.1 Introduction

This thesis has taken steps toward understanding how glacier bed morphology influence many facets of the glacial system such as hydrology, ice flow velocity, ice loss and sediment entrainment and storage. It answers the call for more in-depth study on the influence of overdeepenings on glacial behaviour over both spatial and temporal scales. The findings produced by the various methods within this thesis give insight into the internal workings and interplay between different variables at a valley glacier. This chapter concludes the major findings of the thesis and briefly discusses the wider implications of this research and future suggestions for avenues of research.

7.2 Answering the Research Questions of the Thesis

In this section we will look at the research questions initially covered in Section 1.5 and consider whether they have been addressed suitably.

7.2.1 Research Question 1

How is the seasonal development of a drainage system influenced by subglacial topography, namely due to the presence of an overdeepening?

Multiple data sources were successfully collected from Findelengletscher that showed the bed surface shape beneath the glacier and therefore the presence of overdeepened

topography. The overdeepening was analysed and found to present bed to ice surface ratios (1.2 to 1.7 times the ice surface slope (Alley *et al*., 1998) suitable for supercooling to be occurring. Basal ice was identified from GPR and debris-rich subglacially derived facies were observed. The amount of sediment examined within the glacier from a cauldron collapse strongly suggests that meltwater is struggling to 'flush' out sediment within the glacier, a good indicator of supercooling. The drainage system was seen to support the assertions of Swift *et al.* (2021), in that a distributed system dominated at the terminus late into the melt season believed to be due to the localised overdeepened topography.

7.2.2 Research Question 2

How does the drainage system influence glacial dynamics such as flow velocities and elevation change?

As mentioned for Research Question 1, the drainage system influenced glacial dynamics by velocities remaining high in terminal areas into the late melt season due to a more distributed system being in place. Additionally, further up-glacier, seasonal velocity profiles suggested that a more channelised system had formed from the summer slow-down of ice velocity. Negative elevation change data showed early cauldron formation which overlayed areas where subglacial flow routing was calculated to be occurring. This was further backed up by alignment with feature tracking data and GPR trace analysis. The channelised system development was seen to exacerbate localised ice loss subglacially which was demonstrated from comparisons of DEM differencing from the early and late melt season. Ice flow velocities were also able to identify these main channelised pathways.

7.2.3 Research Question 3

Is it possible to identify cauldron features before they present on the ice surface and what influences do these features have on elevation change and glacial retreat?

Cauldron features were able to be identified at least a year before they began to present concentric crevasses on the surface. DEM differencing as well as feature tracking led to the identification of cauldron development locations that linked up with estimated subglacial meltwater routing which is a key requirement in the formation of cauldrons (Kellerer-Pirklbauer *et al.* 2019)). GPR analysis also provided evidence in the form of identification of englacial crevasses that were found to form long before surface crevassing. Cauldrons displayed significant negative elevation changes and eventual collapse hastens glacial retreat as seen in satellite imagery of the site in 2019.

7.3 Limitations

Like any project, a range of limitations on the scope and accuracy obtained were apparent. Firstly, the range of temporal resolutions used was fairly limited due to the financial costs and time associated with repeated travel to the field site. This led to long gaps in the temporal data of ice velocities such as the time window 'winter' being averaged from 6th September 2016 to 5th July 2017 and 'Spring' being represented by two orthomosaics two days apart (5th – 7th July). Time windows being too long led to 'noisy' data whilst time windows being shorter made findings not necessarily indicative of the entire season they were representing. Ideally, numerous UAVs, consistent days apart would be done to improve the reliability of the velocity results so that a clear picture of the development of the glacier over the course of at least one melt season could be acquired.

The size of the study area was confined by the area that could be covered before the batteries ran out of power, a fixed wing UAV with flight planning software would have increased the scope of the study but was deemed too expensive an investment.

Furthermore, the availability of borrowed equipment such as GPR was also limited. In the case of this study, GPR was only available for one day in February and one day in July with no prior field experience. The bed DEM had limitations in its accuracy in the form of uncertainly from GPR measurements and limited transects due again to the scarcity of availability.

7.4 Wider implications

This thesis represents an in-depth analysis of spatial and temporal patterns in ice flow velocity and ice loss in response to topography, atmospheric climate and inferred hydrology, with a focus on how these interact at an overdeepened bed. The results of this study support the idea that overdeepenings significantly affect seasonal drainage routings. Whilst this was carried out at only one valley glacier in Switzerland, the findings can be applied to similar topography but on larger ice sheet scales such as Greenland. Glacier modelling of mass balance is important in estimating sea level rises and future climate. It is important that the role of overdeepenings in glacier or ice sheet dynamics is considered.

7.5 Further Research Suggestions

The benefits of further study into this area of glacial hydrology and geomorphology include increasing knowledge and incidences whereby the influence of overdeepenings on glacier hydrology and sediment transport are better understood. Understanding these temporal patterns of sediment storage and transport at overdeepenings, not just on intra-annual scales

but at decadal scales is necessary to fully understand the effect this might have on the export rates of sediments, and glacial erosion and retreat dynamics. Within this thesis, several areas where additional research would be beneficial are as follows:

1. Borehole measurements testing water pressures at the overdeepening and nearby would be beneficially to run alongside any future data. This would give a good idea of how developed the drainage system is spatially across the terminus.
2. The same methodology could be used again to build up the validity of the findings, perhaps at ice sheet level to also show similarities and differences between the effects of overdeepenings at different scales.
3. With regard to UAV surveys, full glacier coverage, rather than just the terminus would offer a better understanding as to processes across the glacier as a whole and mass balance estimates could be included in analysis. A greater number of flights across multiple melt seasons would also be advantageous in capturing glacier response to specific high discharge events and evidence for the development of the drainage system at finer resolutions.

8. REFERENCES

Agisoft 2018, 'Agisoft PhotoScan User Manual professional edition, version 1.2' http://www.agisoft.com/pdf/photoscan-pro_1_2_en.pdf [Accessed 21st September 2018]

Agisoft PhotoScan., 2018a. Densecloud and mesh generation 'http://www.agisoft.com/pdf/tips_and_tricks/PhotoScan_Memory_Requirements.pdf' [Accessed 21st September 2018]

Agisoft PhotoScan., 2018b. How to Get an Image Dataset that Meets PhotoScan Requirements. http://www.agisoft.com/pdf/tips_and_tricks/Image%20Capture%20Tips%20-%20Equipment%20and%20Shooting%20Scenarios.pdf [Accessed 21st September 2018]

Ai, S., Wang, Z., E, D., Holmen, K., Tan, Z., Zhou, C. and Sun, W., 2014. Topography, ice thickness and ice volume of the glacier Pedersenbreen in Svalbard, using GPR and GPS. *Polar Research*, *33*(1), p.18533.

Alley, R.B., Cuffey, K.M. and Zoet, L.K., 2019. Glacial erosion: status and outlook. *Annals of Glaciology*, *60*(80), pp.1-13

Alley, R.B., 1993. In search of ice-stream sticky spots. *Journal of Glaciology*, *39*(133), pp.447-454

Alley, R.B., Cuffey, K.M., Evenson, E.B., Strasser, J.C., Lawson, D.E. and Larson, G.J., 1997. . *Quaternary Science Reviews*, *16*(9), pp.1017-1038

Alley, R.B., Lawson, D.E., Evenson, E.B., Strasser, J.C. and Larson, G.J., 1998. Glaciohydraulic supercooling: a freeze-on mechanism to create stratified, debris-rich basal ice: II. Theory. *Journal of Glaciology*, *44*(148), pp.563-569.

Alley, R.B., Lawson, D.E., Evenson, E.B. and Larson, G.J., 2003a. Sediment, glaciohydraulic supercooling, and fast glacier flow. *Annals of Glaciology*, *36*(1), pp.135-141.

Alley, R.B., Lawson, D.E., Larson, G.J., Evenson, E.B. and Baker, G.S., 2003b. Stabilizing feedbacks in glacier-bed erosion. *Nature*, *424*(6950), pp.758-760.

Amundson, J.M. and Burton, J.C., 2018. Quasi-static granular flow of ice mélange. *Journal of Geophysical Research: Earth Surface*, *123*(9), pp.2243-2257.

Anandakrishnan, S. and Alley, R.B., 1997. Stagnation of ice stream C, West Antarctica by water piracy. *Geophysical Research Letters*, *24*(3), pp.265-268.

Andreasen, J.O., 1985. Seasonal surface-velocity variations on a sub-polar glacier in West Greenland. *Journal of Glaciology*, *31*(109), pp.319-323.

Andrews, L.C., Catania, G.A., Hoffman, M.J., Gulley, J.D., Lüthi, M.P., Ryser, C., Hawley, R.L. and Neumann, T.A., 2014. Direct observations of evolving subglacial drainage beneath the Greenland Ice Sheet. *Nature*, *514*(7520), p.80.

Antoniazza, G. and Lane, S.N., 2021. Sediment yield over glacial cycles: A conceptual model. *Progress in Physical Geography: Earth and Environment*, *45*(6), pp.842-865

Anurogo, W., Lubis, M.Z., Khoirunnisa, H., Hanafi, D.S.P.A., Rizki, F., Surya, G. and Dewanti, N.A., 2017. A simple aerial photogrammetric mapping system overview and image acquisition using uncrewed aerial vehicles (UAVs). *Geospatial Information*, *1*(1), pp.11-18

Arcone, S.A., 1996. High resolution of glacial ice stratigraphy: a ground-penetrating radar study of Pegasus Runway, McMurdo Station, Antarctica. *Geophysics*, *61*(6), pp.1653-1663.

Armstrong, W.H., Anderson, R.S. and Fahnestock, M.A., 2017. Spatial patterns of summer speedup on south central Alaska glaciers. *Geophysical Research Letters*, *44*(18), pp.9379-9388.

Ayoub, F., Leprince, S. and Keene, L., 2009. User's guide to COSI-CORR co-registration of optically sensed images and correlation. *California Institute of Technology: Pasadena, CA, USA*, *38*

Bælum, K. and Benn, D.I., 2011. Thermal structure and drainage system of a small valley glacier (Tellbreen, Svalbard), investigated by ground penetrating radar. *The Cryosphere*, *5*(1), pp.139-149.

Baird, T., Bristow, C.S. and Vermeesch, P., 2019. Measuring sand dune migration rates with COSI-Corr and landsat: Opportunities and challenges. *Remote Sensing*, *11*(20), p.2423

Baker, G.S., Strasser, J.C., Evenson, E.B., Lawson, D.E., Pyke, K. and Bigl, R.A., 2003. Near-surface seismic reflection profiling of the Matanuska Glacier, Alaska. *Geophysics*, *68*(1), pp.147-156.

Baojuan, H., Zhongqin, L., Feiteng, W., Wenbin, W., Puyu, W. and Kaiming, L., 2015. Glacier volume estimation from ice-thickness data, applied to the Muz Taw glacier, Sawir Mountains, China. *Environmental Earth Sciences*, *74*(3), pp.1861-1870

Bartholomaus, T.C., Anderson, R.S. and Anderson, S.P., 2008. Response of glacier basal motion to transient water storage. *Nature Geoscience*, *1*(1), p.33

Bartholomaus, T.C., Anderson, R.S. and Anderson, S.P., 2011. Growth and collapse of the distributed subglacial hydrologic system of Kennicott Glacier, Alaska, USA, and its effects on basal motion. *Journal of Glaciology*, *57*(206), pp.985-1002

Bartholomew, I., Nienow, P., Mair, D., Hubbard, A., King, M.A. and Sole, A., 2010. Seasonal evolution of subglacial drainage and acceleration in a Greenland outlet glacier. *Nature Geoscience*, *3*(6), p.408

Bartholomew, I.D., Nienow, P., Sole, A., Mair, D., Cowton, T., King, M.A. and Palmer, S., 2011. Seasonal variations in Greenland Ice Sheet motion: Inland extent and behaviour at higher elevations. *Earth and Planetary Science Letters*, *307*(3-4), pp.271-278

Bash, E.A., Moorman, B.J. and Gunther, A., 2018. Detecting short-term surface melt on an Arctic Glacier using UAV surveys. *Remote Sensing*, *10*(10), p.1547.

Bassis, J.N. and Jacobs, S., 2013. Diverse calving patterns linked to glacier geometry. *Nature Geoscience*, *6*(10), pp.833-836.

Beaud, F., Flowers, G.E. and Venditti, J.G., 2018. Modeling sediment transport in ice-walled subglacial channels and its implications for esker formation and proglacial sediment yields. *Journal of Geophysical Research: Earth Surface*, *123*(12), pp.3206-3227

Bell, R.E., 2008. The role of subglacial water in ice-sheet mass balance. *Nature Geoscience*, *1*(5), p.297.

Benn, D., Gulley, J., Luckman, A., Adamek, A. and Glowacki, P.S., 2009. Englacial drainage systems formed by hydrologically driven crevasse propagation. *Journal of Glaciology*, *55*(191), pp.513-523.

Benn, D.I., Bolch, T., Hands, K., Gulley, J., Luckman, A., Nicholson, L.I., Quincey, D., Thompson, S., Toumi, R. and Wiseman, S., 2012. Response of debris-covered glaciers in the Mount Everest region to recent warming, and implications for outburst flood hazards. *Earth-Science Reviews*, *114*(1-2), pp.156-174.

Benn, D.I., Thompson, S., Gulley, J., Mertes, J., Luckman, A. and Nicholson, L., 2017. Structure and evolution of the drainage system of a Himalayan debris-covered glacier, and its relationship with patterns of mass loss. *Cryosphere*

Berthier, E., Arnaud, Y., Kumar, R., Ahmad, S., Wagnon, P. and Chevallier, P., 2007. Remote sensing estimates of glacier mass balances in the Himachal Pradesh (Western Himalaya, India). *Remote Sensing of Environment*, *108*(3), pp.327-338.

Binder, D., Brückl, E., Roch, K.H., Behm, M., Schöner, W. and Hynek, B., 2009. Determination of total ice volume and ice-thickness distribution of two glaciers in the Hohe Tauern region, Eastern Alps, from GPR data. *Annals of Glaciology*, *50*(51), pp.71-79

Bindschadler, R.A. and T.A. Scambos. 1991. Satellite-imagederived velocity field of an Antarctic ice stream. Science, 252(5003), 242–246.

Bingham, R.G., Nienow, P.W., Sharp, M.J. and Copland, L., 2006. Hydrology and dynamics of a polythermal (mostly cold) High Arctic glacier. *Earth Surface Processes and Landforms: The Journal of the British Geomorphological Research Group*, *31*(12), pp.1463-1479.

Bjornsson, H.E.L.G.I., 2009. Jokulhlaups in Iceland: sources, release, and drainage. *Megaflooding on Earth and Mars. Cambridge University Press, Cambridge*, pp.50-64

Bolch, T., Menounos, B. and Wheate, R., 2010. Landsat-based inventory of glaciers in western Canada, 1985–2005. *Remote sensing of Environment*, *114*(1), pp.127-137.

Boulton, G.S., 1970. On the origin and transport of englacial debris in Svalbard glaciers. *Journal of Glaciology*, *9*(56), pp.213-229.

Boulton, G.S., Dobbie, K.E. and Zatsepin, S., 2001. Sediment deformation beneath glaciers and its coupling to the subglacial hydraulic system. *Quaternary International*, *86*(1), pp.3-28

Bowling, J.S., Livingstone, S.J., Sole, A.J. and Chu, W., 2019. Distribution and dynamics of Greenland subglacial lakes. *Nature communications*, *10*(1), pp.1-11

Bradford, J.H., Nichols, J., Mikesell, T.D. and Harper, J.T., 2009. Continuous profiles of electromagnetic wave velocity and water content in glaciers: an example from Bench Glacier, Alaska, USA. *Annals of Glaciology*, *50*(51), pp.1-9.

Brædstrup, C.F., Egholm, D.L., Ugelvig, S.V. and Pedersen, V.K., 2016. Basal shear stress under alpine glaciers: insights from experiments using the iSOSIA and Elmer/Ice models. *Earth Surface Dynamics*, *4*(1), pp.159-174.

Braun, M.H., Malz, P., Sommer, C., Farías-Barahona, D., Sauter, T., Casassa, G., Soruco, A., Skvarca, P. and Seehaus, T.C., 2019. Constraining glacier elevation and mass changes in South America. *Nature Climate Change*, *9*(2), pp.130-136

Brun, F., Berthier, E., Wagnon, P., Kääb, A. and Treichler, D., 2017. A spatially resolved estimate of High Mountain Asia glacier mass balances from 2000 to 2016. *Nature geoscience*, *10*(9), pp.668-673

Brzozowski, J. and Hooke, R.L., 1981. Seasonal variations in surface velocity of the lower part of Storglaciären, Kebnekaise, Sweden. *Geografiska Annaler: Series A, Physical Geography*, *63*(3-4), pp.233-240

Buechi, M.W., Frank, S.M., Graf, H.R., Menzies, J. and Anselmetti, F.S., 2017. Subglacial emplacement of tills and meltwater deposits at the base of overdeepened bedrock troughs. *Sedimentology*, *64*(3), pp.658-685

Burke, M.J., Brennand, T.A. and Perkins, A.J., 2012. Transient subglacial hydrology of a thin ice sheet: insights from the Chasm esker, British Columbia, Canada. *Quaternary Science Reviews*, *58*, pp.30-55

Burns, P. and Nolin, A., 2014. Using atmospherically-corrected Landsat imagery to measure glacier area change in the Cordillera Blanca, Peru from 1987 to 2010. *Remote Sensing of Environment*, *140*, pp.165-178

Burschil, T., Tanner, D.C., Reitner, J.M., Buness, H. and Gabriel, G., 2019. Unravelling the shape and stratigraphy of a glacially-overdeepened valley with reflection seismic: the Lienz Basin (Austria). *Swiss Journal of Geosciences*, *112*(2), pp.341-355

Butcher, F.E., Balme, M.R., Conway, S.J., Gallagher, C., Arnold, N.S., Storrar, R.D., Lewis, S.R., Hagermann, A. and Davis, J.M., 2021. Sinuous ridges in Chukhung crater, Tempe Terra, Mars: Implications for fluvial, glacial, and glaciofluvial activity. *Icarus*, *357*, p.114131

Carlson, A.E., Jenson, J.W. and Clark, P.U., 2007. Modeling the subglacial hydrology of the James Lobe of the Laurentide Ice Sheet. *Quaternary Science Reviews*, *26*(9-10), pp.1384-1397.

Cathala, M., Magnin, F., Linsbauer, A., Haeberli, W., Ravanel, L. and Deline, P., 2020, May. Modelling glaciers bed overdeepenings and possible future lakes in deglaciating landscapes of the French Alps. In *EGU General Assembly Conference Abstracts* (p. 21229)

Chandler, D.M., Wadham, J.L., Lis, G.P., Cowton, T., Sole, A., Bartholomew, I., Telling, J., Nienow, P., Bagshaw, E.B., Mair, D. and Vinen, S., 2013. Evolution of the subglacial drainage system beneath the Greenland Ice Sheet revealed by tracers. *Nature Geoscience*, *6*(3), p.195

Christoffersen, P. and Tulaczyk, S., 2003. Response of subglacial sediments to basal freeze-on 1. Theory and comparison to observations from beneath the West Antarctic Ice Sheet. *Journal of Geophysical Research: Solid Earth*, *108*(B4).

Church, G., Bauder, A., Grab, M., Rabenstein, L., Singh, S. and Maurer, H., 2019. Detecting and characterising an englacial conduit network within a temperate Swiss glacier using active seismic, ground penetrating radar and borehole analysis. *Annals of Glaciology*, *60*(79), pp.193-205.

Church, G., Grab, M., Schmelzbach, C., Bauder, A. and Maurer, H., 2020. Monitoring the seasonal changes of an englacial conduit network using repeated ground-penetrating radar measurements. *The Cryosphere*, *14*(10), pp.3269-3286.

Claesson Liljedahl, L., Kontula, A. and Harper, J., 2016. *The Greenland analogue project. Final report* (No. NWMO-TR--2016-12). Nuclear Waste Mangement Organization (NWMO)

Clark, C.D., 1997. Reconstructing the evolutionary dynamics of former ice sheets using multi-temporal evidence, remote sensing, and GIS. *Quaternary Science Reviews*, *16*(9), pp.1067-1092.

Clarke, G.K., 2005. Subglacial processes. *Annu. Rev. Earth Planet. Sci.*, *33*, pp.247-276

Clason, C.C., Coch, C., Jarsjö, J., Brugger, K.A., Jansson, P. and Rosqvist, G., 2015. Dye tracing to determine flow properties of hydrocarbon-polluted Rabots glaciär, Kebnekaise, Sweden. *Hydrology and Earth System Sciences*, *19*(6), p.2701.

Clerc, S., Buoncristiani, J.F., Guiraud, M., Vennin, E., Desaubliaux, G. and Portier, E., 2013. Subglacial to proglacial depositional environments in an Ordovician glacial tunnel valley, Alnif, Morocco. *Palaeogeography, Palaeoclimatology, Palaeoecology*, *370*, pp.127-144

Clyne, E., Alley, R.B., Vore, M., Gräff, D., Anandakrishnan, S., Walter, F. and Sergeant, A., 2022. Glacial hydraulic tremor on Rhonegletscher, Switzerland. *Journal of Glaciology*, pp.1-11

Conyers, L.B., 2015. Analysis and interpretation of GPR datasets for integrated archaeological mapping. *Near Surface Geophysics*, *13*(6), pp.645-651

Cook, S.J., Waller, R.I. and Knight, P.G., 2006. Glaciohydraulic supercooling: the process and its significance. *Progress in Physical Geography*, *30*(5), pp.577-588.

Cook, S.J., Knight, P.G., Waller, R.I., Robinson, Z.P. and Adam, W.G., 2007. The geography of basal ice and its relationship to glaciohydraulic supercooling: Svínafellsjökull, southeast Iceland. *Quaternary Science Reviews*, *26*(19-21), pp.2309-2315.

Cook, S.J. and Knight, P.G., 2009. Glaciohydraulic supercooling. *Progress in Physical Geography*, *33*(5), pp.705-710.

Cook, S.J., Robinson, Z.P., Fairchild, I.J., Knight, P.G., Waller, R.I. and Boomer, I.A.N., 2010. Role of glaciohydraulic supercooling in the formation of stratified facies basal ice: Svínafellsjökull and Skaftafellsjökull, southeast Iceland. *Boreas*, *39*(1), pp.24-38

Cook, S.J. and Swift, D.A., 2012. Subglacial basins: Their origin and importance in glacial systems and landscapes. *Earth-Science Reviews*, *115*(4), pp.332-372.

Copland, L., Sharp, M.J. and Nienow, P.W., 2003. Links between short-term velocity variations and the subglacial hydrology of a predominantly cold polythermal glacier. *Journal of Glaciology*, *49*(166), pp.337-348

Copland, L., Pope, S., Bishop, M.P., Shroder, J.F., Clendon, P., Bush, A., Kamp, U., Seong, Y.B. and Owen, L.A., 2009. Glacier velocities across the central Karakoram. *Annals of Glaciology*, *50*(52), pp.41-49

Cowton, T., Nienow, P., Sole, A., Wadham, J., Lis, G., Chandler, D., Bartholomew, I. and Mair, D., 2012, April. Drainage system structure and evolution at a Greenland outlet glacier. In *EGU General Assembly Conference Abstracts* (Vol. 14, p. 1030).

Cowton, T., Nienow, P., Sole, A., Wadham, J., Lis, G., Bartholomew, I., Mair, D. and Chandler, D., 2013. Evolution of drainage system morphology at a land-terminating Greenlandic outlet glacier. *Journal of Geophysical Research: Earth Surface*, *118*(1), pp.29-41

Cowton, T., Nienow, P., Sole, A., Bartholomew, I. and Mair, D., 2016. Variability in ice motion at a land-terminating Greenlandic outlet glacier: the role of channelized and distributed drainage systems. *Journal of Glaciology*, *62*(233), pp.451-466

Creyts, T.T. and Clarke, G.K., 2010. Hydraulics of subglacial supercooling: theory and simulations for clear water flows. *Journal of Geophysical Research: Earth Surface*, *115*(F3).

Cruzan, M.B., Weinstein, B.G., Grasty, M.R., Kohrn, B.F., Hendrickson, E.C., Arredondo, T.M. and Thompson, P.G., 2016. Small unmanned aerial vehicles (micro-UAVs, drones) in plant ecology. *Applications in plant sciences*, *4*(9), p.1600041.

Cuffey, K.M. and Paterson, W.S.B., 2010. *The physics of glaciers*. Academic Press.

Dahlke, H.E., Williamson, A.G., Georgakakos, C., Leung, S., Sharma, A.N., Lyon, S.W. and Walter, M.T., 2015. Using concurrent DNA tracer injections to infer glacial flow pathways. *Hydrological Processes*, *29*(25), pp.5257-5274.

Damsgaard, A., Suckale, J., Piotrowski, J.A., Houssais, M., Siegfried, M.R. and Fricker, H.A., 2017. Sediment behavior controls equilibrium width of subglacial channels. *Journal of Glaciology*, *63*(242), pp.1034-1048

Das, S., 2021. Glacier Surface Velocities in the Chandrabhaga Massif, Western Himalaya (India) Derived Using COSI-Corr From Landsat Images

Davison, B.J., Sole, A.J., Livingstone, S.J., Cowton, T.R. and Nienow, P.W., 2019. The influence of hydrology on the dynamics of land-terminating sectors of the Greenland ice sheet. *Frontiers in Earth Science*, *7*, p.10

Davison, B.J., Sole, A.J., Cowton, T.R., Lea, J.M., Slater, D.A., Fahrner, D. and Nienow, P.W., 2020. Subglacial drainage evolution modulates seasonal ice flow variability of three tidewater glaciers in southwest Greenland. *Journal of Geophysical Research: Earth Surface*, *125*(9), p.e2019JF005492

Degenhardt Jr, J.J., 2009. Development of tongue-shaped and multilobate rock glaciers in alpine environments–Interpretations from ground penetrating radar surveys. *Geomorphology*, *109*(3-4), pp.94-107

DJI. 2016. *Phantom Comparison.* [ONLINE] Available at: http://www.dji.com/products/compare-phantom. [Accessed 20 May 2016]

DJI., 2016. – Phantom 4 User Manual 1.4, <https://www.dji.com/uk/downloads/products/phantom-4> [Accessed 20 May 2016]

Dobhal, D.P., Mehta, M. and Srivastava, D., 2013. Influence of debris cover on terminus retreat and mass changes of Chorabari Glacier, Garhwal region, central Himalaya, India. *Journal of Glaciology*, *59*(217), pp.961-971.

Dou, Q, Wei, L, Magee, D *et al*. (1 more author) (2017) Real-Time Hyperbolae Recognition and Fitting in GPR Data. IEEE Transactions on Geoscience and Remote Sensing, 55 (1). pp. 51-62. ISSN 0196-2892

Dow, C.F., Kavanaugh, J.L., Sanders, J.W., Cuffey, K.M. and MacGREGOR, K.R., 2011. Subsurface hydrology of an overdeepened cirque glacier. *Journal of Glaciology*, *57*(206), pp.1067-1078.

Dow, C.F., Kavanaugh, J.L., Sanders, J.W. and Cuffey, K.M., 2014. A test of common assumptions used to infer subglacial water flow through overdeepenings. *Journal of Glaciology*, *60*(222), pp.725-734.

Dugdale, S.J., 2007. *An evaluation of imagery from an unmanned aerial vehicle (UAV) for the mapping of intertidal macroalgae on Seal Sands, Tees Estuary, UK* (Doctoral dissertation, Durham University).

Durand, G., Gagliardini, O., De Fleurian, B., Zwinger, T. and Le Meur, E., 2009. Marine ice sheet dynamics: Hysteresis and neutral equilibrium. *Journal of Geophysical Research: Earth Surface (2003–2012)*, *114*(F3).

Echelmeyer, K. and Zhongxiang, W., 1987. Direct observation of basal sliding and deformation of basal drift at sub-freezing temperatures. *Journal of Glaciology*, *33*(113), pp.83-98.

Egan, G.K., Cooper, R.J. and Taylor, B., 2005, February. Unmanned aerial vehicle research at Monash University. In *AIAC-11 Eleventh Australian International Aerospace Congress*

Egholm, D.L., Pedersen, V.K., Knudsen, M.F. and Larsen, N.K., 2012. Coupling the flow of ice, water, and sediment in a glacial landscape evolution model. *Geomorphology*, *141*, pp.47-66.

Egli, P.E., Irving, J. and Lane, S.N., 2021a. Characterization of subglacial marginal channels using 3-D analysis of high-density ground-penetrating radar data. *Journal of Glaciology*, pp.1-14

Egli, P.E., Belotti, B., Ouvry, B., Irving, J. and Lane, S.N., 2021b. Subglacial channels, climate warming, and increasing frequency of Alpine glacier snout collapse. Geophysical Research Letters, 48(21), p.e2021GL096031.

Einarsson, B., Magnússon, E., Roberts, M.J., Pálsson, F., Thorsteinsson, T. and Jóhannesson, T., 2016. A spectrum of jökulhlaup dynamics revealed by GPS measurements of glacier surface motion. *Annals of Glaciology*, *57*(72), pp.47-61

Embleton, C. and King, C. A. M. 1968. *Glacial and Periglacial Geomorphology.* Edward Arnold Ltd., London, UK.

Engel, M., Andreoli, A., Coviello, V., Frentress, J., Buter, A., Vignoli, G., Nadalet, R., Dinale, R. and Comiti, F., 2018, April. Analysing runoff and sediment dynamics at different spatial and temporal scales in a glacierized Alpine catchment (Eastern Italian Alps). In *EGU General Assembly Conference Abstracts* (Vol. 20, p. 14674)

Engelhardt, H. and Kamb, B., 1997. Basal hydraulic system of a West Antarctic ice stream: constraints from borehole observations. *Journal of Glaciology*, *43*(144), pp.207-230.

Evans, D.J., 2009. Controlled moraines: origins, characteristics and palaeoglaciological implications. *Quaternary Science Reviews*, *28*(3-4), pp.183-208.

Ensminger, S.L., Alley, R.B., Evenson, E.B., Lawson, D.E. and Larson, G.J., 2001. Basal-crevasse-fill origin of laminated debris bands at Matanuska Glacier, Alaska, USA. *Journal of Glaciology*, *47*(158), pp.412-422.

Evans, D.J., Ewertowski, M., Orton, C. and Graham, D.J., 2018. The glacial geomorphology of the Ice Cap piedmont lobe landsystem of east Mýrdalsjökull, Iceland. *Geosciences*, *8*(6), p.194

Fan, L., Zhang, F., Fan, H. and Zhang, C., 2019. Brief review of image denoising techniques. *Visual Computing for Industry, Biomedicine, and Art*, *2*(1), pp.1-12.

Farinotti, D., Huss, M., Bauder, A. and Funk, M., 2009a. An estimate of the glacier ice volume in the Swiss Alps. *Global and Planetary Change*, *68*(3), pp.225-231

Farinotti, D., Huss, M., Bauder, A., Funk, M. and Truffer, M., 2009b. A method to estimate the ice volume and ice-thickness distribution of alpine glaciers. *Journal of Glaciology*, *55*(191), pp.422-430.

Farinotti, D., Longuevergne, L., Moholdt, G., Duethmann, D., Mölg, T., Bolch, T., Vorogushyn, S. and Güntner, A., 2015. Substantial glacier mass loss in the Tien Shan over the past 50 years. *Nature Geoscience*, *8*(9), pp.716-722

Farinotti, D., Brinkerhoff, D.J., Clarke, G.K., Fürst, J.J., Frey, H., Gantayat, P., Gillet-Chaulet, F., Girard, C., Huss, M., Leclercq, P.W. and Linsbauer, A., 2017. How accurate are estimates of glacier ice thickness? Results from ITMIX, the Ice Thickness Models Intercomparison eXperiment. *Cryosphere*, *11*(2), pp.949-970

Farinotti, D., Round, V., Huss, M., Compagno, L. and Zekollari, H., 2019. Large hydropower and water-storage potential in future glacier-free basins. *Nature*, *575*(7782), pp.341-344

Feiger, N., Huss, M., Leinss, S., Sold, L. and Farinotti, D., 2018. The bedrock topography of Gries-and Findelengletscher. *Geographica Helvetica*, *73*(1), pp.1-9.

Feinstein, D.T., Hart, D.J., Gatzke, S., Hunt, R.J., Niswonger, R.G. and Fienen, M.N., 2020. A simple method for simulating groundwater interactions with fens to forecast development effects. *Groundwater*, *58*(4), pp.524-534

Felix, D., Albayrak, I., Abgottspon, A. and Boes, R.M., 2016, November. Optimization of hydropower plants with respect to fine sediment focusing on turbine switch-offs during floods. In *IOP Conference Series: Earth and Environmental Science* (Vol. 49, No. 12, p. 122011). IOP Publishing

Fenn, C.R. and Gomez, B., 1989. Particle size analysis of the sediment suspended in a proglacialstream: Glacier de Tsidjiore Nouve, Switzerland. *Hydrological Processes*, *3*(2), pp.123-135

Fiebig, M., Preusser, F., Decker, K. and Schlüchter, C., 2010. Preface: special section of papers dealing with overdeepened basins and valleys in the alpine realm. *Swiss Journal of Geosciences*, *103*(3), pp.327-328.

Fiore, J., Pugin, A. and Beres, M., 2002. Sedimentological and GPR studies of subglacial deposits in the Joux Valley (Vaud, Switzerland): backset accretion in an esker followed by an erosive jökulhlaup. *Géographie physique et Quaternaire*, *56*(1), pp.19-32

Fischer, A., 2009. Calculation of glacier volume from sparse ice-thickness data, applied to Schaufelferner, Austria. *Journal of Glaciology*, *55*(191), pp.453-460

Fischer, M., Huss, M. and Hoelzle, M., 2015. Surface elevation and mass changes of all Swiss glaciers 1980–2010. *The Cryosphere*, *9*(2), pp.525-540

Flowers, G.E., Marshall, S.J., Björnsson, H. and Clarke, G.K., 2005. Sensitivity of Vatnajökull ice cap hydrology and dynamics to climate warming over the next 2 centuries. *Journal of Geophysical Research: Earth Surface (2003–2012)*, *110*(F2).

Flowers, G.E., 2015. Modelling water flow under glaciers and ice sheets. *Proceedings of the Royal Society A: Mathematical, Physical and Engineering Sciences*, *471*(2176), p.20140907

FOCA., 2018. Federal Office of Civil Aviation. 'Rules and general questions about drones' https://www.bazl.admin.ch/bazl/de/home/gutzuwissen/drohnen-und-flugmodelle/allgemeine-fragen-zu-drohnen.html [Accessed on 12 May 2018]

Fonstad, M.A., Dietrich, J.T., Courville, B.C., Jensen, J.L. and Carbonneau, P.E., 2013. Topographic structure from motion: a new development in photogrammetric measurement. *Earth Surface Processes and Landforms*, *38*(4), pp.421-430

Fountain, A.G. and Walder, J.S., 1998. Water flow through temperate glaciers. *Reviews of Geophysics*, *36*(3), pp.299-328.

Frey, H., Haeberli, W., Linsbauer, A., Huggel, C. and Paul, F., 2010. A multi-level strategy for anticipating future glacier lake formation and associated hazard potentials. *Natural Hazards and Earth System Sciences*, *10*(2), pp.339-352.

Fudge, T.J., Harper, J.T., Humphrey, N.F. and Pfeffer, W.T., 2005. Diurnal water-pressure fluctuations: timing and pattern of termination below Bench Glacier, Alaska, USA. *Annals of Glaciology*, *40*, pp.102-106

Fudge, T.J., Humphrey, N.F., Harper, J.T. and Pfeffer, W.T., 2008. Diurnal fluctuations in borehole water levels: configuration of the drainage system beneath Bench Glacier, Alaska, USA. *Journal of Glaciology*, *54*(185), pp.297-306

Fyffe, C.L., Brock, B.W., Kirkbride, M.P., Mair, D.W.F., Arnold, N.S., Smiraglia, C., Diolaiuti, G. and Diotri, F., 2019. Do debris-covered glaciers demonstrate distinctive hydrological behaviour compared to clean glaciers?. *Journal of Hydrology*.

Gaffey, C. and Bhardwaj, A., 2020. Applications of unmanned aerial vehicles in cryosphere: Latest advances and prospects. *Remote Sensing*, *12*(6), p.948

Gainullin, I.I., Khomyakov, P.V. and Usmanov, B.M., 2018, January. Study of medieval fortified settlements destruction under natural and anthropogenic factors using remote sensing data. In *IOP Conference Series: Earth and Environmental Science* (Vol. 107, No. 1, p. 012006). IOP Publishing.

Garmin eTrex series., 2016. https://www8.garmin.com/manuals/webhelp/eTrex_10_20x_30x/EN-US/eTrex_10_20_20x_30_30x_OM_EN-US.pdf [Accessed 15th January 2017]

Gärtner-Roer, I., Nussbaumer, S.U., Hüsler, F. and Zemp, M., 2019. Worldwide assessment of national glacier monitoring and future perspectives. *Mountain Research and Development*, *39*(2), pp.A1-A11

Gerbaux, M., Genthon, C., Etchevers, P., Vincent, C. and Dedieu, J.P., 2005. Surface mass balance of glaciers in the French Alps: distributed modeling and sensitivity to climate change. *Journal of Glaciology*, *51*(175), pp.561-572.

Gerber, R., Felix-Henningsen, P., Behrens, T. and Scholten, T., 2010. Applicability of ground-penetrating radar as a tool for nondestructive soil-depth mapping on Pleistocene periglacial slope deposits. *Journal of Plant Nutrition and Soil Science*, *173*(2), pp.173-184

Gergan, J.T., Dobhal, D.P. and Kaushik, R., 1999. Ground penetrating radar ice thickness measurements of Dokriani bamak (glacier), Garhwal Himalaya. *Current Science*, pp.169-173

Gimbert, F., Tsai, V.C., Amundson, J.M., Bartholomaus, T.C. and Walter, J.I., 2016. Subseasonal changes observed in subglacial channel pressure, size, and sediment transport. *Geophysical Research Letters*, *43*(8), pp.3786-3794

Gindraux, S., Boesch, R. and Farinotti, D., 2017. Accuracy assessment of digital surface models from unmanned aerial vehicles' imagery on glaciers. *Remote Sensing*, *9*(2), p.186

Glaciological reports (1881-2017). "The Swiss Glaciers", Yearbooks of the Cryospheric Commission of the Swiss Academy of Sciences (SCNAT) published since 1964 by the Labratory of Hydraulics, Hydrology and Glaciology (VAW) of ETH Zürich. No. 1-136, (http://www.glamos.ch).

Glasser, N.F., 1995. Modelling the effect of topography on ice sheet erosion, Scotland. *Geografiska Annaler: Series A, Physical Geography*, *77*(1-2), pp.67-82.

GlaThiDa Consortium W., 2019. Glacier Thickness Database 3.0.1. *World Glacier Monitoring Service. Zurich, Switzerland*. doi: 10.5904/wgms-glathida-2019-03.

Glen, J.W., 1955. The creep of polycrystalline ice. *Proceedings of the Royal Society of London. Series A. Mathematical and Physical Sciences*, *228*(1175), pp.519-538.

Google Maps., 2018. Findelengletscher, Switzerland, 46.00954110099102, 7.8331075967253865, elevation 100M. 2D map, viewed 8 February 2018, <https://www.google.co.uk/maps >.

Gordon, S., Sharp, M., Hubbard, B., Smart, C., Ketterling, B. and Willis, I., 1998. Seasonal reorganization of subglacial drainage inferred from measurements in boreholes. *Hydrological Processes*, *12*(1), pp.105-133.

Gordon, S., Sharp, M., Hubbard, B., Willis, I., Smart, C., Copland, L., Harbor, J. and Ketterling, B., 2001. Borehole drainage and its implications for the investigation of glacier hydrology: experiences from Haut Glacier d'Arolla, Switzerland. *Hydrological Processes*, *15*(5), pp.797-813

Grab, M., Mattea, E., Bauder, A., Huss, M., Rabenstein, L., Hodel, E., Linsbauer, A., Langhammer, L., Schmid, L., Church, G. and Hellmann, S., 2021. Ice thickness distribution of all Swiss glaciers based on extended ground-penetrating radar data and glaciological modeling. *Journal of Glaciology*, pp.1-19

Grabiec, M., Jania, J., Puczko, D., Kolondra, L. and Budzik, T., 2012. Surface and bed morphology of Hansbreen, a tidewater glacier in Spitsbergen.

Greenwood, S.L., Clason, C.C., Helanow, C. and Margold, M., 2016. Theoretical, contemporary observational and palaeo-perspectives on ice sheet hydrology: processes and products. *Earth-Science Reviews*, *155*, pp.1-27.

Grove, J.M., 1958. Some structures associated with rotational flow in compound and composite cirque glaciers. *IAHS Publication*, *47*, pp.306-31.

Gudmundsson, G.H., 2003. Transmission of basal variability to a glacier surface. *Journal of Geophysical Research: Solid Earth*, *108*(B5)

Gulley, J. and Benn, D.I., 2007. Structural control of englacial drainage systems in Himalayan debris-covered glaciers. *Journal of Glaciology*, *53*(182), pp.399-412

Gulley, J., 2009. Structural control of englacial conduits in the temperate Matanuska Glacier, Alaska, USA. *Journal of Glaciology*, *55*(192), pp.681-690

Gulley, J.D., Benn, D.I., Müller, D. and Luckman, A., 2009. A cut-and-closure origin for englacial conduits in uncrevassed regions of polythermal glaciers. *Journal of Glaciology*, *55*(189), pp.66-80

Gulley, J.D., Benn, D.I., Screaton, E. and Martin, J., 2009. Mechanisms of englacial conduit formation and their implications for subglacial recharge. *Quaternary Science Reviews*, *28*(19-20), pp.1984-1999

Hackney, C. and Clayton, A., 2015. 2.1. 7. Unmanned Aerial Vehicles (UAVs) and their application in geomorphic mapping.

Haeberli, W. and Hohmann, R., 2008, June. Climate, glaciers and permafrost in the Swiss Alps 2050: scenarios, consequences and recommendations. In *Proceedings Ninth International Conference on Permafrost* (Vol. 1, pp. 607-612). Institute of Northern Engineering, University of Alaska Fairbanks.

Haeberli, W., 2013. New lakes in deglaciating high-mountain areas: climate-related development and challenges for sustainable use (NELAK) http://www.nfp61.ch/en/projects/project-nelak

Haeberli, W., Buetler, M., Huggel, C., Friedli, T.L., Schaub, Y. and Schleiss, A.J., 2016a. New lakes in deglaciating high-mountain regions–opportunities and risks. *Climatic change*, *139*(2), pp.201-214

Haeberli, W., Linsbauer, A., Cochachin, A., Salazar, C. and Fischer, U.H., 2016b. On the morphological characteristics of overdeepenings in high-mountain glacier beds. *Earth Surface Processes and Landforms*, *41*(13), pp.1980-1990

Hagen, J.O., Kohler, J., Melvold, K. And Winther, J. G., 2003. Glaciers in Svalbard: mass balance, runoff and freshwater flux. *Polar Research, 22(2). pp.145-159.*

Hall, A.M. and Glasser, N.F., 2003. Reconstructing the basal thermal regime of an ice stream in a landscape of selective linear erosion: Glen Avon, Cairngorm Mountains, Scotland. *Boreas*, *32*(1), pp.191-207

Hannah, D.M., Gurnell, A.M. and McGregor, G.R., 1999. A methodology for investigation of the seasonal evolution in proglacial hydrograph form. *Hydrological Processes*, *13*(16), pp.2603-2621.

Harbor, J.M., 1992. Application of a general sliding law to simulating flow in a glacier cross-section. *Journal of Glaciology*, *38*(128), pp.182-190

Harbor, J., Sharp, M., Copland, L., Hubbard, B., Nienow, P. and Mair, D., 1997. Influence of subglacial drainage conditions on the velocity distribution within a glacier cross section. *Geology*, *25*(8), pp.739-742

Harper, J.T., 1993. Glacier terminus fluctuations on Mount Baker, Washington, USA, 1940–1990, and climatic variations. *Arctic and Alpine Research*, *25*(4), pp.332-340

Harper, J.T., Bradford, J.H., Humphrey, N.F. and Meierbachtol, T.W., 2010. Vertical extension of the subglacial drainage system into basal crevasses. *Nature*, *467*(7315), p.579

Harrison, S., Kargel, J.S., Huggel, C., Reynolds, J., Shugar, D.H., Betts, R.A., Emmer, A., Glasser, N., Haritashya, U.K., Klimeš, J. and Reinhardt, L., 2018. Climate change and the

global pattern of moraine-dammed glacial lake outburst floods. *The Cryosphere*, *12*(4), pp.1195-1209.

Heid, T. and Kääb, A., 2012. Evaluation of existing image matching methods for deriving glacier surface displacements globally from optical satellite imagery. *Remote Sensing of Environment*, *118*, pp.339-355.

Heilig, A., Eisen, O. and Schneebeli, M., 2010. Temporal observations of a seasonal snowpack using upward-looking GPR. *Hydrological processes*, *24*(22), pp.3133-3145.

Herman, F., Beaud, F., Champagnac, J.D., Lemieux, J.M. and Sternai, P., 2011. Glacial hydrology and erosion patterns: a mechanism for carving glacial valleys. *Earth and Planetary Science Letters*, *310*(3), pp.498-508.

Heuff, F.A.W., 2015. *Assessing mass change and surface velocity of the debris-covered tongue of the Lirung Glacier, Nepal, over the winter period between October 2013 and May 2014 by means of Unmanned Airborne Vehicle imagery* (Master's thesis)

Hewitt, I.J. and Fowler, A.C., 2008. Seasonal waves on glaciers. *Hydrological processes*, *22*(19), pp.3919-3930

Hirano, M. and Aniya, M., 1988. A rational explanation of cross-profile morphology for glacial valleys and of glacial valley development. *Earth Surface Processes and Landforms*, *13*(8), pp.707-716

Hock, R. and Wangler, A., 1999. Tracer experiments and borehole observations in the over-deepening of Aletschgletscher, Switzerland. *Annals of Glaciology*, *28*, pp.253-260

Hock, R., Jansson, P. and Braun, L.N., 2005. Modelling the response of mountain glacier discharge to climate warming. In *Global Change and Mountain Regions* (pp. 243-252). Springer Netherlands

Hodge, S.M., 1974. Variations in the sliding of a temperate glacier. *Journal of Glaciology*, *13*(69), pp.349-369

Hoffman, M. and Price, S., 2014. Feedbacks between coupled subglacial hydrology and glacier dynamics. *Journal of Geophysical Research: Earth Surface*, *119*(3), pp.414-436.

Hooke, R.L., Miller, S.B. and Kohler, J., 1988. Character of the englacial and sub glacial drainage system in the upper part of the ablation area of Storglaciaren, Sweden. *Journal of Glaciology. 34(117).*

Hooke, R.L., 1989. Englacial and subglacial hydrology: a qualitative review. *Arctic and Alpine Research*, *21*(3), pp.221-233

Hooke, R.L., Calla, P., Holmlund, P., Nilsson, M. and Stroeven, A., 1989. A 3 year record of seasonal variations in surface velocity, Storglaciären, Sweden. *Journal of Glaciology*, *35*(120), pp.235-247.

Hooke, R.L., Laumann, T. and Kohler, J., 1990. Subglacial water pressures and the shape of subglacial conduits. *Journal of Glaciology*, *36*(122), pp.67-71.

Hooke, R.L., 1991. Positive feedbacks associated with erosion of glacial cirques and overdeepenings. *Geological Society of America Bulletin*, *103*(8), pp.1104-1108

Hooke, R.L. and Pohjola, V.A., 1994. Hydrology of a segtnent of a glacier situated overdeepening, Storglaciaren, Sweden. *Journal of Glaciology*,*40*(134).

Hooke, R.L., 2005. *Principles of glacier mechanics*. Cambridge university press.

How, P., Benn, D.I., Hulton, N.R., Hubbard, B., Luckman, A., Sevestre, H., Van Pelt, W.J., Lindbäck, K., Kohler, J. and Boot, W., 2017. Rapidly changing subglacial hydrological pathways at a tidewater glacier revealed through simultaneous observations of water pressure, supraglacial lakes, meltwater plumes and surface velocities. *The Cryosphere*, *11*(6), pp.2691-2710.

Howat, I.M., Tulaczyk, S., Waddington, E. and Björnsson, H., 2008. Dynamic controls on glacier basal motion inferred from surface ice motion. *Journal of Geophysical Research: Earth Surface*, *113*(F3).

Hubbard, B.P., Sharp, M.J., Willis, I.C., Nielsen, M. and Smart, C.C., 1995. Borehole water-level variations and the structure of the subglacial hydrological system of Haut Glacier d'Arolla, Valais, Switzerland. *Journal of Glaciology*, *41*(139), pp.572-583.

Hubbard, B. and Nienow, P., 1997. Alpine subglacial hydrology. *Quaternary Science Reviews*, *16*(9), pp.939-955

Hubbard, A., Blatter, H., Nienow, P., Mair, D. and Hubbard, B., 1998. Comparison of a three-dimensional model for glacier flow with field data from Haut Glacier d'Arolla, Switzerland. *Journal of Glaciology*, *44*(147), pp.368-378

Hubbard, A., Lawson, W., Anderson, B., Hubbard, B. and Blatter, H., 2004. Evidence for subglacial ponding across Taylor Glacier, Dry Valleys, Antarctica. *Annals of Glaciology*, *39*(1), pp.79-84.

Hudleston, P.J., 2015. Structures and fabrics in glacial ice: A review. *Journal of Structural Geology*, *81*, pp.1-27.

Huss, M., Farinotti, D., Bauder, A. and Funk, M., 2008. Modelling runoff from highly glacierized alpine drainage basins in a changing climate. *Hydrological processes*, *22*(19), pp.3888-3902.

Hutter, K., 2017. *Theoretical glaciology: material science of ice and the mechanics of glaciers and ice sheets* (Vol. 1). Springer

Huybrechts, P., 2002. Sea-level changes at the LGM from ice-dynamic reconstructions of the Greenland and Antarctic ice sheets during the glacial cycles. *Quaternary Science Reviews*, *21*(1), pp.203-231.

Ignéczi, Á., Sole, A.J., Livingstone, S.J., Ng, F.S. and Yang, K., 2018. Greenland Ice Sheet surface topography and drainage structure controlled by the transfer of basal variability. *Frontiers in Earth Science*, *6*, p.101

Iken, A., 1974. *Velocity fluctuations of an arctic valley glacier: a study of the White Glacier, Axel Heiberg Island, Canadian Arctic Archipelago* (Doctoral dissertation, ETH Zurich).

Iken, A., 1981. *The effect of the subglacial water pressure on the sliding velocity of a glacier in an idealized numerical model.* Versuchsanst. Für Wasserbau, Hydrologie u. Glaziologie an d. Eidg. Techn. Hochsch.

Iken, A., Röthlisberger, H., Flotron, A. and Haeberli, W., 1983. The uplift of Unteraargletscher at the beginning of the melt season–a consequence of water storage at the bed. *J. Glaciol*, *29*(101), pp.28-47.

Iken, A. and Bindschadler, R.A., 1986. Combined measurements of subglacial water pressure and surface velocity of Findelengletscher, Switzerland: conclusions about drainage system and sliding mechanism. *Journal of Glaciology*, *32*(110), pp.101-119.

Iken, A. and Truffer, M., 1997. The relationship between subglacial water pressure and velocity of Findelengletscher, Switzerland, during its advance and retreat. *Journal of Glaciology*, *43*(144), pp.328-338

Immerzeel, W.W., Petersen, L., Ragettli, S. and Pellicciotti, F., 2014. The importance of observed gradients of air temperature and precipitation for modeling runoff from a glacierized watershed in the Nepalese Himalayas.*Water Resources Research*, *50*(3), pp.2212-2226.

Irvine-Fynn, T.D.L., Moorman, B.J., Williams, J.L.M. and Walter, F.S.A., 2006. Seasonal changes in ground-penetrating radar signature observed at a polythermal glacier, Bylot Island, Canada. *Earth Surface Processes and Landforms: The Journal of the British Geomorphological Research Group*, *31*(7), pp.892-909.

Iverson, N.R., 1991. Morphology of glacial striae: implications for abrasion of glacier beds and fault surfaces. *Geological Society of America Bulletin*,*103*(10), pp.1308-1316.

Iverson, N.R., 1993. Regelation of ice through debris at glacier beds: Implications for sediment transport. *Geology*, *21*(6), pp.559-562

Iverson, N.R., Cohen, D., Hooyer, T.S., Fischer, U.H., Jackson, M., Moore, P.L., Lappegard, G. and Kohler, J., 2003. Effects of basal debris on glacier flow. *Science*, *301*(5629), pp.81-84

Jacob, J.D., Chilson, P.B., Houston, A.L. and Smith, S.W., 2018. Considerations for atmospheric measurements with small unmanned aircraft systems. *Atmosphere*, *9*(7), p.252

James, M.R. and Robson, S., 2014. Mitigating systematic error in topographic models derived from UAV and ground-based image networks. *Earth Surface Processes and Landforms*, *39*(10), pp.1413-1420.

Jansson, P., Hock, R. and Schneider, T., 2003. The concept of glacier storage: a review. *Journal of Hydrology*, *282*(1-4), pp.116-129

Jarvis, A., Rubiano, J., Nelson, A., Farrow, A. and Mulligan, M., 2004. Practical use of SRTM data in the tropics–comparisons with digital elevation models generated from cartographic data. *Working document*, *198*, p.32

Jawak, S.D., Kumar, S., Luis, A.J., Bartanwala, M., Tummala, S. and Pandey, A.C., 2018. Evaluation of geospatial tools for generating accurate glacier velocity maps from optical remote sensing data. In *Multidisciplinary Digital Publishing Institute Proceedings* (Vol. 2, No. 7, p. 341)

Jiroušek, T., Kapica, R. and Vrublová, D., 2014. The testing of photoscan 3D object modelling software. *Geodesy and Cartography*, *40*(2), pp.68-74

Johnston, R.R., Fountain, A.G. and Nylen, T.H., 2005. The origin of channels on lower Taylor Glacier, McMurdo Dry Valleys, Antarctica, and their implication for water runoff. *Annals of Glaciology*, *40*, pp.1-7

Jol, H.M. ed., 2008. *Ground penetrating radar theory and applications*. elsevier.

Jol, H.M., 1995. Ground penetrating radar antennae frequencies and transmitter powers compared for penetration depth, resolution and reflection continuity. *Geophysical prospecting*, *43*(5), pp.693-709

Jordan, T.A., Ferraccioli, F., Corr, H., Graham, A., Armadillo, E. and Bozzo, E., 2010. Hypothesis for mega-outburst flooding from a palaeo-subglacial lake beneath the East Antarctic Ice Sheet. *Terra Nova*, *22*(4), pp.283-289

Joughin, I., Das, S.B., King, M.A., Smith, B.E., Howat, I.M. and Moon, T., 2008. Seasonal speedup along the western flank of the Greenland Ice Sheet. *Science*, *320*(5877), pp.781-783.

Kamb, B. and LaChapelle, E., 1964. Direct observation of the mechanism of glacier sliding over bedrock. *Journal of Glaciology*, *5*(38), pp.159-172

Kamb, B., Raymond, C.F., Harrison, W.D., Engelhardt, H., Echelmeyer, K.A., Humphrey, N., Brugman, M.M. and Pfeffer, T., 1985. Glacier surge mechanism: 1982-1983 surge of Variegated Glacier, Alaska. *Science*, *227*(4686), pp.469-479

Kamb, B. and Echelmeyer, K.A., 1986. Stress-gradient coupling in glacier flow: IV. Effects of the "T" term. *Journal of Glaciology*, *32*(112), pp.342-349

Kamb, B., 1987. Glacier surge mechanism based on linked cavity configuration of the basal water conduit system. *Journal of Geophysical Research: Solid Earth*, *92*(B9), pp.9083-9100.

Kääb, A. and Funk, M., 1999. Modelling mass balance using photogrammetric and geophysical data: a pilot study at Griesgletscher, Swiss Alps. *Journal of Glaciology*, *45*(151), pp.575-583.

Kääb, A., 2005. Combination of SRTM3 and repeat ASTER data for deriving alpine glacier flow velocities in the Bhutan Himalaya. *Remote Sensing of Environment*, *94*(4), pp.463-474.

Kaushik, S., Singh, T., Bhardwaj, A. and Joshi, P.K., 2022. Long-term spatiotemporal variability in the surface velocity of Eastern Himalayan glaciers, India. *Earth Surface Processes and Landforms*

Kehew, A.E., Piotrowski, J.A. and Jørgensen, F., 2012. Tunnel valleys: Concepts and controversies—A review. *Earth-Science Reviews*, *113*(1-2), pp.33-58 Turner, D., Lucieer, A.

and De Jong, S.M., 2015. Time series analysis of landslide dynamics using an unmanned aerial vehicle (UAV). *Remote Sensing*, *7*(2), pp.1736-1757

Kellerer-Pirklbauer, A. and Kulmer, B., 2019. The evolution of brittle and ductile structures at the surface of a partly debris-covered, rapidly thinning and slowly moving glacier in 1998–2012 (Pasterze Glacier, Austria). Earth Surface Processes and Landforms, 44(5), pp.1034-1049

Kim, J.H., Cho, S.J. and Yi, M.J., 2007. Removal of ringing noise in GPR data by signal processing. *Geosciences Journal*, *11*(1), pp.75-81

Knight, P. G. 2003. Classics in physical geography revisited – Kamb, B. and LaChapelle, E. 1964: Direct observation of the mechanism of glacier sliding over bedrock. Progress in Physical Geography 27, 107–11.

Kraaijenbrink, P., Meijer, S.W., Shea, J.M., Pellicciotti, F., De Jong, S.M. and Immerzeel, W.W., 2016. Seasonal surface velocities of a Himalayan glacier derived by automated correlation of unmanned aerial vehicle imagery. *Annals of Glaciology*, *57*(71), pp.103-113

Krabbendam, M., 2016. Sliding of temperate basal ice on a rough, hard bed: creep mechanisms, pressure melting, and implications for ice streaming. *The Cryosphere*, *10*(5), pp.1915-1932

Kulkarni, A.V., Bahuguna, I.M., Rathore, B.P., Singh, S.K., Randhawa, S.S., Sood, R.K. and Dhar, S., 2007. Glacial retreat in Himalaya using Indian Remote Sensing satellite data. *Current science*, *92*(1), pp.69-74.

Kyrke-Smith, T.M., Gudmundsson, G.H. and Farrell, P.E., 2018. Relevance of detail in basal topography for basal slipperiness inversions: a case study on Pine Island Glacier, Antarctica. *Frontiers in Earth Science*, *6*, p.33.

Langhammer, L., Rabenstein, L., Bauder, A. and Maurer, H., 2017. Ground-penetrating radar antenna orientation effects on temperate mountain glaciers. *Geophysics*, *82*(3), pp.H15-H24.

Langhammer, L., Rabenstein, L., Schmid, L., Bauder, A., Grab, M., Schaer, P. and Maurer, H., 2019. Glacier bed surveying with helicopter-borne dual-polarization ground-penetrating radar. *Journal of Glaciology*, *65*(249), pp.123-135

Langley, E.S., Leeson, A.A., Stokes, C.R. and Jamieson, S.S., 2016. Seasonal evolution of supraglacial lakes on an East Antarctic outlet glacier. *Geophysical Research Letters*, *43*(16), pp.8563-8571.

Larson, G.J., Lawson, D.E., Evenson, E.B., Knudsen, O., Alley, R.B. and Phanikumar, M.S., 2010. Origin of stratified basal ice in outlet glaciers of Vatnajökull and Öræfajökull, Iceland. *Boreas*, *39*(3), pp.457-470

Lawson, D. E., Strasser, J. C., Evenson, E. B., Alley, R. B., Larson, G. J., and Arcone, S. A., 1998, Glaciohydraulic supercooling: a mechanism to create stratified, debris-rich basal ice: I. Field evidence: J. Glaciology, 44, 547–562

Le Gall, A., Ciarletti, V., Berthelier, J.J., Reineix, A., Guiffaut, C., Ney, R., Dolon, F. and Bonaime, S., 2008. An imaging HF GPR using stationary antennas: Experimental validation over the Antarctic ice sheet. *IEEE Transactions on Geoscience and Remote Sensing*, *46*(12), pp.3975-3986

Le Meur, E., Gagliardini, O., Zwinger, T. and Ruokolainen, J., 2004. Glacier flow modelling: a comparison of the Shallow Ice Approximation and the full-Stokes solution. *Comptes Rendus Physique,* 5(7), pp.709-722.

Lee, V., Cornford, S.L. and Payne, A.J., 2015. Initialization of an ice-sheet model for present-day Greenland. *Annals of Glaciology*, *56*(70), pp.129-140

Leon, J.X., Roelfsema, C.M., Saunders, M.I. and Phinn, S.R., 2015. Measuring coral reef terrain roughness using 'Structure-from-Motion'close-range photogrammetry. *Geomorphology*, *242*, pp.21-28.

Leprince, S., Barbot, S., Ayoub, F. and Avouac, J.P., 2007a. Automatic and precise orthorectification, coregistration, and subpixel correlation of satellite images, application to ground deformation measurements. *IEEE Transactions on Geoscience and Remote Sensing*, *45*(6), pp.1529-1558.

Leprince, S., Ayoub, F., Klinger, Y. and Avouac, J.P., 2007b, July. Co-registration of optically sensed images and correlation (COSI-Corr): An operational methodology for ground deformation measurements. In *2007 IEEE International Geoscience and Remote Sensing Symposium* (pp. 1943-1946). IEEE

Li, X., Rignot, E., Mouginot, J. and Scheuchl, B., 2016. Ice flow dynamics and mass loss of Totten Glacier, East Antarctica, from 1989 to 2015. *Geophysical Research Letters*, *43*(12), pp.6366-6373.

Lindbäck, K., Pettersson, R., Hubbard, A.L., Doyle, S.H., As, D., Mikkelsen, A.B. and Fitzpatrick, A.A., 2015. Subglacial water drainage, storage, and piracy beneath the Greenland ice sheet. *Geophysical Research Letters*, *42*(18), pp.7606-7614.

Linsbauer, A., Paul, F. and Haeberli, W., 2012. Modeling glacier thickness distribution and bed topography over entire mountain ranges with GlabTop: Application of a fast and robust approach. *Journal of Geophysical Research: Earth Surface*, *117*(F3)

Linsbauer, A., Frey, H., Haeberli, W., Machguth, H., Azam, M.F. and Allen, S., 2016. Modelling glacier-bed overdeepenings and possible future lakes for the glaciers in the Himalaya—Karakoram region. *Annals of Glaciology*, *57*(71), pp.119-130.

Livingstone, S.J., Clark, C.D., Piotrowski, J.A., Tranter, M., Bentley, M.J., Hodson, A., Swift, D.A. and Woodward, J., 2012. Theoretical framework and diagnostic criteria for the identification of palaeo-subglacial lakes. *Quaternary Science Reviews*, *53*, pp.88-110

Livingstone, S.J., Clark, C.D. and Tarasov, L., 2013. Modelling North American palaeo-subglacial lakes and their meltwater drainage pathways. *Earth and Planetary Science Letters*, *375*, pp.13-33

Liu, Y., Wang, N., Zhang, J. and Wang, L., 2019. Climate change and its impacts on mountain glaciers during 1960–2017 in western China. *Journal of Arid Land*, *11*(4), pp.537-550

Lliboutry, L., 1983. Modifications to the theory of intraglacial waterways for the case of subglacial ones. *Journal of Glaciology*, *29*(102), pp.216-226.

Lucieer, A., de Jong, S. and Turner, D., 2013. Mapping landslide displacements using Structure from Motion (SfM) and image correlation of multi-temporal UAV photography. *Progress in Physical Geography*, p.0309133313515293.

Luckman, A., Quincey, D. and Bevan, S., 2007. The potential of satellite radar interferometry and feature tracking for monitoring flow rates of Himalayan glaciers. *Remote Sensing of Environment*, *111*(2), pp.172-181.

Lundberg, A., Thunehed, H. and Bergström, J., 2000. Impulse radar snow surveys–influence of snow density. *Hydrology Research*, *31*(1), pp.1-14

Luthcke, S.B., Arendt, A.A., Rowlands, D.D., McCarthy, J.J. and Larsen, C.F., 2008. Recent glacier mass changes in the Gulf of Alaska region from GRACE mascon solutions. *Journal of Glaciology*, *54*(188), pp.767-777

Maanya, U.S., Kulkarni, A.V., Tiwari, A., Bhar, E.D. and Srinivasan, J., 2016. Identification of potential glacial lake sites and mapping maximum extent of existing glacier lakes in Drang Drung and Samudra Tapu glaciers, Indian Himalaya. *Current Science*, pp.553-560

MacGregor, K.R., Anderson, R.S., Anderson, S.P. and Waddington, E.D., 2000. Numerical simulations of glacial-valley longitudinal profile evolution.*Geology*, *28*(11), pp.1031-1034

Machguth, H., Eisen, O., Paul, F. and Hoelzle, M., 2006. Strong spatial variability of snow accumulation observed with helicopter-borne GPR on two adjacent Alpine glaciers. *Geophysical Research Letters*, *33*(13).

MacKie, E.J., Schroeder, D.M., Caers, J., Siegfried, M.R. and Scheidt, C., 2020. Antarctic topographic realizations and geostatistical modeling used to map subglacial lakes. *Journal of Geophysical Research: Earth Surface*, *125*(3), p.e2019JF005420

Magnússon, E., Pálsson, F., Björnsson, H. and Guðmundsson, S., 2012. Removing the ice cap of Öræfajökull central volcano, SE-Iceland: mapping and interpretation of bedrock topography, ice volumes, subglacial troughs and implications for hazards assessments. *Jökull*, *62*, pp.131-150.

Magrani, F., Valla, P.G. and Egholm, D., 2022. Modelling alpine glacier geometry and subglacial erosion patterns in response to contrasting climatic forcing. *Earth Surface Processes and Landforms*, *47*(4), pp.1054-1072

Mair, D., Nienow, P., Willis, I. and Sharp, M., 2001. Spatial patterns of glacier motion during a high-velocity event: Haut Glacier d'Arolla, Switzerland. *Journal of Glaciology*, *47*(156), pp.9-20.

Mair, D., Nienow, P., Sharp, M., Wohlleben, T. and Willis, I., 2002. Influence of subglacial drainage system evolution on glacier surface motion: Haut Glacier d'Arolla, Switzerland. *Journal of Geophysical Research: Solid Earth*, *107*(B8), pp.EPM-8.

Mair, D., Willis, I., Fischer, U.H., Hubbard, B., Nienow, P. and Hubbard, A., 2003. Hydrological controls on patterns of surface, internal and basal motion during three''spring events'': Haut Glacier d'Arolla, Switzerland. *Journal of Glaciology*, *49*(167), pp.555-567.

Maizels, J., 1997. Jökulhlaup deposits in proglacial areas. *Quaternary Science Reviews*, *16*(7), pp.793-819.

Malard, F., Tockner, K. and Ward, J.V., 1999. Shifting dominance of subcatchment water sources and flow paths in a glacial floodplain, Val Roseg, Switzerland. *Arctic, Antarctic, and Alpine Research*, *31*(2), pp.135-150

Marcer, M., Stentoft, P.A., Bjerre, E., Cimoli, E., Bjørk, A., Stenseng, L. and Machguth, H., 2017. Three decades of volume change of a small Greenlandic glacier using ground penetrating radar, Structure from Motion, and aerial photogrammetry. *Arctic, Antarctic, and Alpine Research*, *49*(3), pp.411-425

Marshall, S.J., Björnsson, H., Flowers, G.E. and Clarke, G.K.C., 2005. Simulation of Vatnajökull ice cap dynamics. *Journal of Geophysical Research: Earth Surface (2003–2012)*, *110*(F3)

Marston, R.A., 1983. Supraglacial stream dynamics on the Juneau Icefield. *Annals of the Association of American Geographers*, *73*(4), pp.597-608

Martin, F.M., Müllerová, J., Borgniet, L., Dommanget, F., Breton, V. and Evette, A., 2018. Using single-and multi-date UAV and satellite imagery to accurately monitor invasive knotweed species. *Remote Sensing*, *10*(10), p.1662

Marziali, S. and Dionisio, G., 2017. Photogrammetry and macro photography. The experience of the MUSINT II Project in the 3D digitizing process of small size archaeological artifacts. *Studies in Digital Heritage*, *1*(2), pp.298-309

McGrath, D., Steffen, K., Scambos, T., Rajaram, H., Casassa, G. and Lagos, J.L.R., 2012. Basal crevasses and associated surface crevassing on the Larsen C ice shelf, Antarctica, and their role in ice-shelf instability. *Annals of glaciology*, *53*(60), pp.10-18

Meierbachtol, T., Harper, J. and Humphrey, N., 2013. Basal drainage system response to increasing surface melt on the Greenland ice sheet. *Science*, *341*(6147), pp.777-779.

Mejía, J.Z., Gulley, J.D., Trunz, C., Covington, M.D., Bartholomaus, T.C., Xie, S. and Dixon, T.H., 2021. Isolated cavities dominate Greenland Ice Sheet dynamic response to lake drainage. *Geophysical Research Letters*, *48*(19), p.e2021GL094762

Mernild, S.H. and Hasholt, B., 2009. Observed runoff, jökulhlaups and suspended sediment load from the Greenland ice sheet at Kangerlussuaq, West Greenland, 2007 and 2008. *Journal of Glaciology*, *55*(193), pp.855-858.

Meteoblue, ”Weather history download Zermatt”, can be accessed in: https://www.meteoblue.com/en/weather/archive/export/zermatt_switzerland_2657928

Meyer, C.R., Fernandes, M.C., Creyts, T.T. and Rice, J.R., 2016. Effects of ice deformation on Röthlisberger channels and implications for transitions in subglacial hydrology. *Journal of Glaciology*, *62*(234), pp.750-762

Miles, K.E., Hubbard, B., Quincey, D.J., Miles, E.S., Irvine-Fynn, T.D. and Rowan, A.V., 2019. Surface and subsurface hydrology of debris-covered Khumbu Glacier, Nepal, revealed by dye tracing. *Earth and Planetary Science Letters*, *513*, pp.176-186

Minchew, B. and Joughin, I., 2020. Toward a universal glacier slip law. *Science*, *368*(6486), pp.29-30.

Moon, T., Joughin, I., Smith, B., Van Den Broeke, M.R., Van De Berg, W.J., Noël, B. and Usher, M., 2014. Distinct patterns of seasonal Greenland glacier velocity. *Geophysical research letters*, *41*(20), pp.7209-7216.

Moore, P.L., Iverson, N.R., Brugger, K.A., Cohen, D., Hooyer, T.S., Jansson, P., 2011. Effect of a cold margin on ice flow at the terminus of Storglaciaren, Sweden: implications for sediment transport. Journal of Glaciology 57, 7787.

Moorman, B.J. and Michel, F.A., 1998, May. The application of ground-penetrating radar to the study of glacial hydrology. In *GPR ‘98: Seventh International Conference on Ground-Penetrating Radar, University of Kansas, Lawrence, KS, USA* (pp. 27-30).

Morgan, J.A., Brogan, D.J. and Nelson, P.A., 2017. Application of Structure-from-Motion photogrammetry in laboratory flumes. *Geomorphology*, *276*, pp.125-143.

Moya Quiroga, V., Mano, A., Asaoka, Y., Udo, K., Kure, S. and Mendoza, J., 2013. Probabilistic estimation of glacier volume and glacier bed topography: the Andean glacier Huayna West. *The Cryosphere Discussions*, *7*(4), pp.3931-3967.

Mulac, B.L., Tschudi, M.A., Maslanik, J.A. and Holland, G.J., 2004, December. Using Digital Imagery from a Small Unmanned Aerial Vehicle (UAV) to Estimate Arctic Melt Pond Coverage on Sea Ice. In *AGU Fall Meeting Abstracts* (Vol. 2004, pp. C42A-07).

Murray, T., Booth, A. and Rippin, D.M., 2007. Water-content of glacier-ice: limitations on estimates from velocity analysis of surface ground-penetrating radar surveys. *Journal of Environmental and Engineering Geophysics*, *12*(1), pp.87-99.

Murray, T., Booth, A.D., 2010. Imaging glacial sediment inclusions in 3-D using ground-penetrating radar at Kongsvegen, Svalbard. Journal of Quaternary Science 25, 754-761.

Muthyala, R., Rennermalm, A.K., Leidman, S.Z., Cooper, M.G., Cooley, S.W., Smith, L.C. and van As, D., 2020. Seasonal Variability in In-situ Supraglacial Streamflow and Drivers in Southwest Greenland in 2016. *The Cryosphere Discussions*, pp.1-28

Nanni, U., Gimbert, F., Vincent, C., Gräff, D., Walter, F., Piard, L. and Moreau, L., 2020. Quantification of seasonal and diurnal dynamics of subglacial channels using seismic observations on an Alpine glacier. *The Cryosphere*, *14*(5), pp.1475-1496

NASA., 2009. https://earthobservatory.nasa.gov/images [Accessed 6th June 2019]

Nex, F. and Remondino, F., 2019. Preface: Latest developments, methodologies, and applications based on uav platforms

Ng, F.S., Ignéczi, Á., Sole, A.J. and Livingstone, S.J., 2018. Response of surface topography to basal variability along glacial flowlines. *Journal of Geophysical Research: Earth Surface*, *123*(10), pp.2319-2340

Nick, F.M., Vieli, A., Howat, I.M. and Joughin, I., 2009. Large-scale changes in Greenland outlet glacier dynamics triggered at the terminus. *Nature Geoscience*, *2*(2), pp.110-114.

Nienow, P., Sharp, M. and Willis, I., 1996a. Temporal switching between englacial and subglacial drainage pathways: dye tracer evidence from the Haut Glacier d'Arolla, Switzerland. *Geografiska Annaler: Series A, Physical Geography*, *78*(1), pp.51-60

Nienow, P.W., Sharp, M. and Willis, I.C., 1996b. Velocity–discharge relationships derived from dye tracer experiments in glacial meltwaters: implications for subglacial flow conditions. *Hydrological Processes*, *10*(10), pp.1411-1426.

Nienow, P., Sharp, M. and Willis, I., 1998. Seasonal changes in the morphology of the subglacial drainage system, Haut Glacier d'Arolla, Switzerland. *Earth Surface Processes and Landforms: The Journal of the British Geomorphological Group*, *23*(9), pp.825-843

Nienow, P.W., Sole, A.J., Slater, D.A. and Cowton, T.R., 2017. Recent advances in our understanding of the role of meltwater in the Greenland ice sheet system. *Current Climate Change Reports*, *3*(4), pp.330-344

Nobes, D.C., 2015. Discussion of 'Geomorphology, internal structure, and successive development of a glacier foreland in the semiarid Chilean Andes (Cerro Tapado, upper Elqui Valley, 30° 08' S, 69° 55' W.)', by S. Monnier, C. Kinnard, A. Surazakov and W. Bossy, Geomorphology 207 (2014), 126–140. *Geomorphology*, *250*, pp.459-460

Nye, J.F., 1951. The flow of glaciers and ice-sheets as a problem in plasticity. *Proceedings of the Royal Society of London. Series A. Mathematical and Physical Sciences*, *207*(1091), pp.554-572

Nye, J.F., 1959. The motion of ice sheets and glaciers. *Journal of Glaciology*, *3*(26), pp.493-507.

Nye, J.F., 1960. The response of glaciers and ice-sheets to seasonal and climatic changes. *Proc. R. Soc. Lond. A*, *256*(1287), pp.559-584.

Nye, J.F., 1965. The flow of a glacier in a channel of rectangular, elliptic or parabolic cross-section. *Journal of glaciology*, *5*(41), pp.661-690.

Oderwald, R.G. and Boucher, B.A., 2003. GPS after selective availability: How accurate is accurate enough?. *Journal of Forestry*, *101*(4), pp.24-27

Oerlemans, J. and Fortuin, J.P.F., 1992. Sensitivity of Glaciers and Small Ice Caps to Greehouse Warming. *Science*, *258*(5079), pp.115-117.

Oerlemans, J., 1994. Quantifying global warming from the retreat of glaciers.*Science-AAAS-Weekly Paper Edition-including Guide to Scientific Information*, *264*(5156), pp.243-244.

Oerlemans, J., 2005. Extracting a climate signal from 169 glacier records. *Science*, *308*(5722), pp.675-677.

Overeem, I., Hudson, B.D., Syvitski, J.P., Mikkelsen, A.B., Hasholt, B., Van Den Broeke, M.R., Noël, B.P.Y. and Morlighem, M., 2017. Substantial export of suspended sediment to the global oceans from glacial erosion in Greenland. *Nature Geoscience*, *10*(11), pp.859-863

Pälli, A., Kohler, J.C., Isaksson, E., Moore, J.C., Pinglot, J.F., Pohjola, V.A. and Samuelsson, H., 2002. Spatial and temporal variability of snow accumulation using ground-penetrating radar and ice cores on a Svalbard glacier. *Journal of Glaciology*, *48*(162), pp.417-424.

Palmer, S.J., Dowdeswell, J.A., Christoffersen, P., Young, D.A., Blankenship, D.D., Greenbaum, J.S., Benham, T., Bamber, J. and Siegert, M.J., 2013. Greenland subglacial lakes detected by radar. Geophysical Research Letters, 40(23), pp.6154-6159.

Patton, H., Swift, D.A., Clark, C.D., Livingstone, S.J., Cook, S.J. and Hubbard, A., 2015. Automated mapping of glacial overdeepenings beneath contemporary ice sheets: Approaches and potential applications. *Geomorphology*, *232*, pp.209-223

Patton, H., Swift, D.A., Clark, C.D., Livingstone, S.J. and Cook, S.J., 2016. Distribution and characteristics of overdeepenings beneath the Greenland and Antarctic ice sheets: Implications for overdeepening origin and evolution. *Quaternary Science Reviews*, *148*, pp.128-145

Pattyn, F., De Smedt, B. and Souchez, R., 2004. Influence of subglacial Vostok lake on the regional ice dynamics of the Antarctic ice sheet: a model study. Journal of Glaciology, 50(171), pp.583-589.

Pattyn, F., Delcourt, C., Samyn, D., De Smedt, B. and Nolan, M., 2009. Bed properties and hydrological conditions underneath McCall Glacier, Alaska, USA. *Annals of glaciology*, *50*(51), pp.80-84

Paul, F. and Haeberli, W., 2008. Spatial variability of glacier elevation changes in the Swiss Alps obtained from two digital elevation models. *Geophysical Research Letters*, *35*(21)

Paul, F. and Linsbauer, A., 2012. Modeling of glacier bed topography from glacier outlines, central branch lines, and a DEM. *International Journal of Geographical Information Science*, *26*(7), pp.1173-1190

Pedersen, V.K., Huismans, R.S., Herman, F. and Egholm, D.L., 2014. Controls of initial topography on temporal and spatial patterns of glacial erosion. *Geomorphology*, *223*, pp.96-116

Pelto, M., 2016. *Recent climate change impacts on mountain glaciers*. John Wiley & Sons.

Persson, B.N.J., 2015. Ice friction: Role of non-uniform frictional heating and ice premelting. *The Journal of chemical physics*, *143*(22), p.224701

Pettersson, R., Jansson, P. and Holmlund, P., 2003. Cold surface layer thinning on Storglaciären, Sweden, observed by repeated ground penetrating radar surveys. *Journal of Geophysical Research: Earth Surface*, *108*(F1)

Pfeffer, W. and Welch, B., 1996. Short wavelength variations in the horizontal velocity field of a valley glacier. *Glaciers, Ice Sheets and Volcanoes: A Tribute to Mark F. Meier*, *96*(27), p.41

Pimentel, S. and Flowers, G.E., 2010. A numerical study of hydrologically driven glacier dynamics and subglacial flooding. *Proceedings of the Royal Society A: Mathematical, Physical and Engineering Sciences*, *467*(2126), pp.537-558

Planet imagery., 2020. from late summer 2019. World Imagery - Source: Esri, Maxar, GeoEye, Earthstar Geographics, CNES/Airbus DS, USDA, USGS, AeroGRID, IGN, and the GIS User Community

Poinar, K., Dow, C.F. and Andrews, L.C., 2019. Long-term support of an active subglacial hydrologic system in Southeast Greenland by firn aquifers. *Geophysical Research Letters*, *46*(9), pp.4772-4781

Preusser, F., Reitner, J.M. and Schlüchter, C., 2010. Distribution, geometry, age and origin of overdeepened valleys and basins in the Alps and their foreland. *Swiss Journal of Geosciences, 103(3). pp.407-426.*

Puppala, A.J. and Congress, S.S.C., 2019, September. A holistic approach for visualization of transportation infrastructure assets using UAV-CRP technology. In *International Conference on Inforatmion technology in Geo-Engineering* (pp. 3-17). Springer, Cham

Purdie, H.L., Brook, M.S. and Fuller, I.C., 2008. Seasonal variation in ablation and surface velocity on a temperate maritime glacier: Fox Glacier, New Zealand. *Arctic, Antarctic, and Alpine Research*, *40*(1), pp.140-147

Rada, C. and Schoof, C.: Channelized, distributed, and disconnected: subglacial drainage under a valley glacier in the Yukon, The Cryosphere, 12, 2609–2636, https://doi.org/10.5194/tc-12-2609-2018, 2018

Rango, A., Laliberte, A., Herrick, J.E., Winters, C., Havstad, K., Steele, C. and Browning, D., 2009. Unmanned aerial vehicle-based remote sensing for rangeland assessment, monitoring, and management. *Journal of Applied Remote Sensing*, *3*(1), pp.033542-033542.

Reinardy, B.T., Booth, A.D., Hughes, A.L., Boston, C.M., Åkesson, H., Bakke, J., Nesje, A., Giesen, R.H. and Pearce, D.M., 2019. Pervasive cold ice within a temperate glacier–implications for glacier thermal regimes, sediment transport and foreland geomorphology. *The Cryosphere*, *13*(3), pp.827-843

Rignot, E., Mouginot, J. and Scheuchl, B., 2011. Ice flow of the Antarctic ice sheet. *Science*, *333*(6048), pp.1427-1430

Rippin, D., Willis, I., Arnold, N., Hodson, A., Moore, J., Kohler, J. and Björnsson, H., 2003. Changes in geometry and subglacial drainage of Midre Lovénbreen, Svalbard, determined from digital elevation models. *Earth Surface Processes and Landforms: The Journal of the British Geomorphological Research Group*, *28*(3), pp.273-298

Rippin, D.M., Vaughan, D.G. and Corr, H.F., 2011. The basal roughness of Pine Island Glacier, West Antarctica. *Journal of Glaciology*, *57*(201), pp.67-76.

Rippin, D.M., 2013. Bed roughness beneath the Greenland ice sheet. *Journal of Glaciology*, *59*(216), pp.724-732

Roberts, M.J., Russell, A.J., Tweed, F.S. and Knudsen, Ó., 2000. Ice fracturing during jökulhlaups: implications for englacial floodwater routing and outlet development. *Earth surface processes and landforms*, *25*(13), pp.1429-1446.

Roberts, M.J., Tweed, F.S., Russell, A.J., Knudsen, Ó., Lawson, D.E., Larson, G.J., Evenson, E.B. and Björnsson, H., 2002. Glaciohydraulic supercooling in Iceland. *Geology*, *30*(5), pp.439-442

Robleda Prieto, G. and Pérez Ramos, A., 2015. Modeling and accuracy assessment for 3d-virtual reconstruction in cultural heritage using low-cost photogrammetry: surveying of the "santa maría azogue" church's front. *3D-ARCH 2015 "3D virtual reconstruction and visualization of complex architecture*, pp.263-270

Robson, B.A., Nuth, C., Nielsen, P.R., Girod, L., Hendrickx, M. and Dahl, S.O., 2018. Spatial variability in patterns of glacier change across the Manaslu Range, Central Himalaya. *Frontiers in Earth Science*, *6*, p.12.

Ross, N., Siegert, M.J., Woodward, J., Smith, A.M., Corr, H.F., Bentley, M.J., Hindmarsh, R.C., King, E.C. and Rivera, A., 2011. Holocene stability of the Amundsen-Weddell ice divide, West Antarctica. *Geology*, *39*(10), pp.935-938

Rossi, P., Mancini, F., Dubbini, M., Mazzone, F. and Capra, A., 2017. Combining nadir and oblique UAV imagery to reconstruct quarry topography: methodology and feasibility analysis. *European Journal of Remote Sensing*, *50*(1), pp.211-221

Röthlisberger, H., 1972. Water pressure in intra-and subglacial channels. *Journal of Glaciology*, *11*(62), pp.177-203

Russell, A.J., Roberts, M.J., Fay, H., Marren, P.M., Cassidy, N.J., Tweed, F.S. and Harris, T., 2006. Icelandic jökulhlaup impacts: implications for ice-sheet hydrology, sediment transfer and geomorphology. *Geomorphology*, *75*(1-2), pp.33-64

Rutishauser, A., Maurer, H. and Bauder, A., 2016. Helicopter-borne ground-penetrating radar investigations on temperate alpine glaciers: A comparison of different systems and their abilities for bedrock mapping Helicopter GPR on temperate glaciers. *Geophysics*, *81*(1), pp.WA119-WA129.

Ryan, J.C., Hubbard, A.L., Box, J.E., Todd, J., Christoffersen, P., Carr, J.R., Holt, T.O. and Snooke, N., 2015. UAV photogrammetry and structure from motion to assess calving dynamics at Store Glacier, a large outlet draining the Greenland ice sheet. *The Cryosphere*, *9*(1), pp.1-11.

Saintenoy, A., Friedt, J.M., Booth, A.D., Tolle, F., Bernard, E., Laffly, D., Marlin, C. and Griselin, M., 2013. Deriving ice thickness, glacier volume and bedrock morphology of Austre Lovénbreen (Svalbard) using GPR. *Near Surface Geophysics*, *11*(2), pp.253-262.

Sanders, J.W., Cuffey, K.M., MacGregor, K.R., Kavanaugh, J.L. and Dow, C.F., 2010. Dynamics of an alpine cirque glacier. *American Journal of Science*, *310*(8), pp.753-773.

Sandmeier, K. J. Reflexw manual, version 4.5. www.sandmeier-geo.de, July 2007.

Scambos, T.A., Berthier, E. and Shuman, C.A., 2011. The triggering of subglacial lake drainage during rapid glacier drawdown: Crane Glacier, Antarctic Peninsula. *Annals of Glaciology*, *52*(59), pp.74-82

Scheidt, S.P. and Lancaster, N., 2013. The application of COSI-Corr to determine dune system dynamics in the southern Namib Desert using ASTER data. *Earth Surface Processes and Landforms*, *38*(9), pp.1004-1019

Schellenberger, T., Dunse, T., Kääb, A., Kohler, J. and Reijmer, C.H., 2015. Surface speed and frontal ablation of Kronebreen and Kongsbreen, NW Svalbard, from SAR offset tracking. *The Cryosphere*, *9*(6), pp.2339-2355.

Scherler, D., Bookhagen, B. and Strecker, M.R., 2011. Hillslope-glacier coupling: The interplay of topography and glacial dynamics in High Asia. *Journal of Geophysical Research: Earth Surface*, *116*(F2).

Scherler, D. and Strecker, M.R., 2012. Large surface velocity fluctuations of Biafo Glacier, central Karakoram, at high spatial and temporal resolution from optical satellite images. *Journal of Glaciology*, *58*(209), pp.569-580

Schneeberger, C., Albrecht, O., Blatter, H., Wild, M. and Hock, R., 2001. Modelling the response of glaciers to a doubling in atmospheric CO2: a case study of Storglaciären, northern Sweden. *Climate Dynamics*, *17*(11), pp.825-834

Schoof, C., 2004. Bed topography and surges in ice streams. *Geophysical research letters*, *31*(6).

Schoof, C., 2005. The effect of cavitation on glacier sliding. *Proceedings of the Royal Society A: Mathematical, Physical and Engineering Sciences*, *461*(2055), pp.609-627

Schoof, C., 2007. Ice sheet grounding line dynamics: Steady states, stability, and hysteresis. Journal of Geophysical Research-Earth Surface 112 (F3), F03S28.

Schoof, C., 2010. Ice-sheet acceleration driven by melt supply variability. *Nature*, *468*(7325), pp.803-806.

Schreiber, J., 2016, October. Antenna pattern reconstitution using unmanned aerial vehicles (UAVs). In *2016 IEEE Conference on Antenna Measurements & Applications (CAMA)* (pp. 1-3). IEEE

Schuler, T., Fischer, U.H. and Gudmundsson, G.H., 2004. Diurnal variability of subglacial drainage conditions as revealed by tracer experiments. *Journal of Geophysical Research: Earth Surface*, *109*(F2)

Seaberg, S.Z., Seaberg, J.Z., Hooke, R.L. and Wiberg, D.W., 1988. Character of the englacial and subglacial drainage system in the lower part of the ablation area of Storglaciären, Sweden, as revealed by dye-trace studies. *Journal of Glaciology*, *34*(117), pp.217-227.

Seddik, H., Greve, R., Sakakibara, D., Tsutaki, S., Minowa, M. and Sugiyama, S., 2019. Response of the flow dynamics of Bowdoin Glacier, northwestern Greenland, to basal lubrication and tidal forcing. *Journal of Glaciology*, *65*(250), pp.225-238

Sharp, M., Gemmell, J.C. and Tison, J.L., 1989. Structure and stability of the former subglacial drainage system of the Glacier de Tsanfleuron, Switzerland. *Earth Surface Processes and Landforms*, *14*(2), pp.119-134.

Sharp, M., Richards, K., Willis, I., Arnold, N., Nienow, P., Lawson, W. and Tison, J.L., 1993. Geometry, bed topography and drainage system structure of the Haut Glacier d'Arolla, Switzerland. *Earth Surface Processes and Landforms*, *18*(6), pp.557-571

Sharp, M., 2006. Subglacial drainage. *Encyclopedia of Hydrological Sciences*.

Sharp, M. and Tranter, M., 2017. 4. The First Haut Glacier D'arolla Project (MT). *Geochemical Perspectives*, *6*(2), pp.201-214

Shilts, W.W., 1984. *Applications of techniques of glacial geology to radioactive waste disposal modelling* (No. AECL--7822)

Shreve, R.L., 1972. Movement of water in glaciers. *Journal of Glaciology*,*11*, pp.205-214.

Shukla, A., Arora, M.K. and Gupta, R.P., 2010. Synergistic approach for mapping debris-covered glaciers using optical–thermal remote sensing data with inputs from geomorphometric parameters. *Remote Sensing of Environment*, *114*(7), pp.1378-1387.

Siegert, M.J., 2018. A 60-year international history of Antarctic subglacial lake exploration. *Geological Society, London, Special Publications*, *461*(1), pp.7-21

Simkins, L.M., Greenwood, S.L., Munevar Garcia, S., Eareckson, E.A., Anderson, J.B. and Prothro, L.O., 2021. Topographic controls on channelized meltwater in the subglacial environment. *Geophysical Research Letters*, *48*(20), p.e2021GL094678

Slater, D., Nienow, P., Sole, A., Cowton, T.O.M., Mottram, R., Langen, P. and Mair, D., 2017. Spatially distributed runoff at the grounding line of a large Greenlandic tidewater glacier inferred from plume modelling. *Journal of Glaciology*, *63*(238), pp.309-323.

Slater, J.A., Garvey, G., Johnston, C., Haase, J., Heady, B., Kroenung, G. and Little, J., 2006. The SRTM data "finishing" process and products.*Photogrammetric Engineering & Remote Sensing*, *72*(3), pp.237-247.

Smith, B. and Sandwell, D., 2003. Accuracy and resolution of shuttle radar topography mission data. *Geophysical Research Letters*, *30*(9).

Smith, D.G. and Jol, H.M., 1995. Ground penetrating radar: antenna frequencies and maximum probable depths of penetration in Quaternary sediments. *Journal of Applied Geophysics*, *33*(1-3), pp.93-100

Sold, L., Huss, M., Machguth, H., Joerg, P.C., Leysinger Vieli, G., Linsbauer, A., Salzmann, N., Zemp, M. and Hoelzle, M., 2016. Mass balance re-analysis of Findelengletscher, Switzerland; benefits of extensive snow accumulation measurements. *Frontiers in Earth Science*, *4*, p.18

Stearns, L.A. and Van der Veen, C.J., 2018. Friction at the bed does not control fast glacier flow. *Science*, *361*(6399), pp.273-277

Steinemann, O., Ivy-Ochs, S., Hippe, K., Christl, M., Haghipour, N. and Synal, H.A., 2021. Glacial erosion by the Trift glacier (Switzerland): Deciphering the development of riegels, rock basins and gorges. *Geomorphology*, *375*, p.107533

Stevens, L.A., Nettles, M., Davis, J.L., Creyts, T.T., Kingslake, J., Ahlstrøm, A.P. and Larsen, T.B., 2021. Helheim Glacier diurnal velocity fluctuations driven by surface melt forcing. *Journal of Glaciology*, pp.1-13

Stocker-Waldhuber, M., Fischer, A., Keller, L., Morche, D. and Kuhn, M., 2017. Funnel-shaped surface depressions—Indicator or accelerant of rapid glacier disintegration? A case study in the Tyrolean Alps. *Geomorphology*, *287*, pp.58-72

Stokes, C.R., Clark, C.D., Lian, O.B. and Tulaczyk, S., 2007. Ice stream sticky spots: a review of their identification and influence beneath contemporary and palaeo-ice streams. *Earth-Science Reviews*, *81*(3-4), pp.217-249

Stone, D.B., Clarke, G.K. and Blake, E.W., 1993. Subglacial measurement of turbidity and electrical conductivity. *Journal of Glaciology*, *39*(132), pp.415-420

Strasser, J. C., Lawson, D. E., Larson, G. J., Evenson, E. B., and Alley, R. B., 1996, Preliminary results of tritium analyses in basal ice, Matanuska Glacier, Alaska, USA: Evidence for subglacial ice accretion: Annals of Glaciology, 22, 126–133

Stumpf, A., Malet, J.P., Allemand, P. and Ulrich, P., 2014. Surface reconstruction and landslide displacement measurements with Pléiades satellite images. *ISPRS Journal of Photogrammetry and Remote Sensing*, *95*, pp.1-12.

Sugiyama, S. and Hilmar Gudmundsson, G., 2004. Short-term variations in glacier flow controlled by subglacial water pressure at Lauteraargletscher, Bernese Alps, Switzerland. *Journal of Glaciology*, *50*(170), pp.353-362.

Sugiyama, S., Navarro, F.J., Sawagaki, T., Minowa, M., Segawa, T., Onuma, Y., Otero, J. and Vasilenko, E.V., 2019. Subglacial water pressure and ice-speed variations at Johnsons Glacier, Livingston Island, Antarctic Peninsula. *Journal of Glaciology*, *65*(252), pp.689-699

Sundal, A.V., Shepherd, A., Van Den Broeke, M., Van Angelen, J., Gourmelen, N. and Park, J., 2013. Controls on short-term variations in Greenland glacier dynamics. *Journal of Glaciology*, *59*(217), pp.883-892

Süsstrunk , AE Unpublished. Report on the seismic soundings of Findelen Glacier, made in October 1959 . [Written for Great Dixence SA , Sion, Switzerland .]

Swift, D.A., Nienow, P.W. and Hoey, T.B., 2005a. Basal sediment evacuation by subglacial meltwater: suspended sediment transport from Haut Glacier d'Arolla, Switzerland. *Earth Surface Processes and Landforms*, *30*(7), pp.867-883

Swift, D.A., Nienow, P.W., Hoey, T.B. and Mair, D.W., 2005b. Seasonal evolution of runoff from Haut Glacier d'Arolla, Switzerland and implications for glacial geomorphic processes. *Journal of Hydrology*, *309*(1-4), pp.133-148.

Swift, D.A., Cook, S.J., Graham, D.J., Midgley, N.G., Fallick, A.E., Storrar, R., Rodrigo, M.T. and Evans, D.J.A., 2018. Terminal zone glacial sediment transfer at a temperate overdeepened glacier system. *Quaternary Science Reviews*, *180*, pp.111-131

Swift, D.A. and Jones, A.H., 2018. Going against the flow: testing the hypothesis of pulsed axial glacier flow. *Earth Surface Processes and Landforms*, *43*(13), pp.2754-2761

Swift, D.A., Tallentire, G.D., Farinotti, D., Cook, S.J., Higson, W.J. and Bryant, R.G., 2021. The hydrology of glacier-bed overdeepenings: sediment transport mechanics, drainage system morphology, and geomorphological implications. *Earth Surface Processes and Landforms*

Swisstopo., 2018. https://www.swisstopo.admin.ch/en/maps-data-online/maps-geodata-online.html [Accessed May 2017]

Swisstopo (2019) Bundesamt für Landestopografie swisstopo-swissALTI3D, Ausgabebericht 2019.

Szymczyk, M. and Szymczyk, P., 2013. Preprocessing of GPR data. *Image Processing & Communications*, *18*(2-3), pp.83-90.

Tallentire G., 2016. Unpublished. 'Sediment discharge data at Findelengletscher fieldwork', University of Sheffield.

Tiwari, R.K., Gupta, R.P. and Arora, M.K., 2014. Estimation of surface ice velocity of Chhota-Shigri glacier using sub-pixel ASTER image correlation. *Current Science*, pp.853-859.

Tonkin, T.N. and Midgley, N.G., 2016. Ground-control networks for image-based surface reconstruction: An investigation of optimum survey designs using UAV derived imagery and structure-from-motion photogrammetry. *Remote Sensing*, *8*(9), p.786

Trusel, L.D., Frey, K.E. and Das, S.B., 2012. Antarctic surface melting dynamics: Enhanced perspectives from radar scatterometer data. *Journal of Geophysical Research: Earth Surface*, *117*(F2)

Tsutaki, S., Nishimura, D., Yoshizawa, T. and Sugiyama, S., 2011. Changes in glacier dynamics under the influence of proglacial lake formation in Rhonegletscher, Switzerland. *Annals of Glaciology*, *52*(58), pp.31-36

Turner, D., Lucieer, A. and Watson, C., 2012. An automated technique for generating georectified mosaics from ultra-high resolution unmanned aerial vehicle (UAV) imagery, based on structure from motion (SfM) point clouds. *Remote sensing*, *4*(5), pp.1392-1410

Tweed, F.S. and Russell, A.J., 1999. Controls on the formation and sudden drainage of glacier-impounded lakes: implications for jökulhlaup characteristics. *Progress in Physical Geography*, *23*(1), pp.79-110.

Tweed, F.S., Roberts, M.J. and Russell, A.J., 2005. Hydrologic monitoring of supercooled meltwater from Icelandic glaciers. *Quaternary Science Reviews*, *24*(22), pp.2308-2318.

UAVphoto (2014) https://sourceforge.net/projects/uavphoto/ Accessed 8 October 2021

Urbini, S., Vittuari, L. and Gandolfi, S., 2001. GPR and GPS data integration: examples of application in Antarctica.

Van de Wal, R.S.W. and Oerlemans, J., 1995. Response of valley glaciers to climate change and kinematic waves: a study with a numerical ice-flow model. *Journal of Glaciology*, *41*(137), pp.142-152

Van der Veen, C.J., 1998. Fracture mechanics approach to penetration of surface crevasses on glaciers. *Cold Regions Science and Technology*, *27*(1), pp.31-47.

van der Veen, C.J., Leftwich, T., Von Frese, R., Csatho, B.M. and Li, J., 2007. Subglacial topography and geothermal heat flux: Potential interactions with drainage of the Greenland ice sheet. *Geophysical research letters*, *34*(12).

van Wynsberghe, E. and Turak, A., 2016. Station-keeping of a high-altitude balloon with electric propulsion and wireless power transmission: A concept study. *Acta Astronautica*, *128*, pp.616-627

Viani, C., Giardino, M., Christian, H., Perotti, L. and Mortara, G., 2017. Morphodynamics of glacier lakes in the Western Italian Alps resutling form continued glacier shrinkage: past

evidences and future scenarios. In *VII Young Geomorphologists' Day* (pp. 73-75). Associazione Italiana di Geografia Fisica e Geomorfologia.f

Vieli, A., Jania, J., Blatter, H. and Funk, M., 2004. Short-term velocity variations on Hansbreen, a tidewater glacier in Spitsbergen. *Journal of Glaciology*, *50*(170), pp.389-398

Vincent, C., 2002. Influence of climate change over the 20th Century on four French glacier mass balances. *Journal of Geophysical Research: Atmospheres*, *107*(D19).

Vincent, C., Gilbert, A., Walpersdorf, A., Gimbert, F., Gagliardini, O., Jourdain, B., Roldan Blasco, J.P., Laarman, O., Piard, L., Six, D. and Moreau, L., 2022. Evidence of seasonal uplift in the Argentière glacier (Mont Blanc area, France). *Journal of Geophysical Research: Earth Surface*, *127*(7), p.e2021JF006454

Vijay, S., King, M.D., Howat, I.M., Solgaard, A.M., Khan, S.A. and Noël, B., 2021. Greenland ice-sheet wide glacier classification based on two distinct seasonal ice velocity behaviors. *Journal of Glaciology*, *67*(266), pp.1241-1248

Wächter , H.-P. Unpublished. Radio-Echolotungen auf dem Findelengletscher . *Versuchsanstalt für Wasserbau, Hydrologie und Glaziologie an der Eidgenössischen Technische Hochschule (Zürich)*.

Walder, 1. S. 1982. Stability of sheet flow of water beneath temperate glaciers and implications for glacier surging. Journal oJGlaciology, Vol. 28, No. 99, p. 273-93.

Walder, J.S. and Fowler, A., 1994. Channelized subglacial drainage over a deformable bed. *Journal of glaciology*, *40*(134), pp.3-15

Walter, F., Deichmann, N. and Funk, M., 2008. Basal icequakes during changing subglacial water pressures beneath Gornergletscher, Switzerland. *Journal of Glaciology*, *54*(186), pp.511-521

Walter, F., Chaput, J. and Lüthi, M.P., 2014. Thick sediments beneath Greenland's ablation zone and their potential role in future ice sheet dynamics. *Geology*, *42*(6), pp.487-490.

Wang, X., Shangguan, D., Li, D. and Anjum, M.N., 2021. Spatiotemporal Variability of Velocity and Influence of Glacier Thickness Using Landsat Imagery: Hunza River Basin, Karakoram Range. *IEEE Access*, *9*, pp.72808-72819

Ward, A.B. and Newman, J.K., 2019. *Assessment of LiDAR and Photogrammetry based Airfield Roughness Profiling Techniques*. ERDC Vicksburg United States

Weertman, J., 1958. Travelling waves on glaciers. *IASH*, *47*, pp.162-168

Weertman, J. 1972. General theory of water flow at the base of a glacier or ice sheet. Rev. Geophys. Space Phys., 10(1), 287–333

Weertman, J. and Birchfield, G.E., 1983. Stability of sheet water flow under a glacier. *Journal of Glaciology*, *29*(103), pp.374-382.

Wendleder, A., Friedl, P. and Mayer, C., 2018. Impacts of climate and supraglacial lakes on the surface velocity of Baltoro Glacier from 1992 to 2017. *Remote Sensing*, *10*(11), p.1681

Werder, M.A. and Funk, M., 2009. Dye tracing a jökulhlaup: II. Testing a jökulhlaup model against flow speeds inferred from measurements. *Journal of Glaciology*, *55*(193), pp.899-908.

Werder, M.A., 2016. The hydrology of subglacial overdeepenings: a new supercooling threshold formula. *Geophysical Research Letters*, *43*(5), pp.2045-2052.

Werder, M.A., Schuler, T.V. and Funk, M., 2010. Short term variations of tracer transit speed on alpine glaciers. *The Cryosphere*, *4*(3), pp.381-396

WGMS., 1989.: World glacier inventory – Status 1988. Haeberli, W., Bösch, H., Scherler, K., Østrem, G. and Wallén, C. C. (eds.), IAHS (ICSI) / UNEP / UNESCO, World Glacier Monitoring Service, Zurich, Switzerland: 458 pp.

Wigmore, O., and Mark, B., 2016. UAV mapping of debris covered glacier change, Llaca Glacier, Cordillera Blanca, Peru. In *Proceedings of the 73rd Annual Meeting of the Eastern Snow Conference.*

Willis, I.C., 1995. Intra-annual variations in glacier motion: a review. *Progress in Physical Geography*, *19*(1), pp.61-106.

Willis, I.C., Richards, K.S. and Sharp, M.J., 1996. Links between proglacial stream suspended sediment dynamics, glacier hydrology and glacier motion at Midtdalsbreen, Norway. *Hydrological Processes*, *10*(4), pp.629-648

Willis, I., Mair, D., Hubbard, B., Nienow, P., Fischer, U.H. and Hubbard, A., 2003. Seasonal variations in ice deformation and basal motion across the tongue of Haut Glacier d'Arolla, Switzerland. *Annals of Glaciology*, *36*, pp.157-167

Wingham, D.J., Siegert, M.J., Shepherd, A. and Muir, A.S., 2006. Rapid discharge connects Antarctic subglacial lakes. *Nature*, *440*(7087), pp.1033-1036

Winkler, K., 2014, March. Hydro-abrasive erosion: Problems and solutions. In *IOP Conference Series: Earth and Environmental Science* (Vol. 22, No. 5, p. 052022). IOP Publishing

Wójcik-Długoborska, K.A. and Bialik, R.J., 2021. The influence of shadow effects on the spectral characteristics of glacial meltwater. *Remote Sensing*, *13*(1), p.36

Xu, S., Fu, P., Quincey, D., Feng, M., Marsh, S. and Liu, Q., 2022. UAV-based geomorphological evolution of the Terminus Area of the Hailuogou Glacier, Southeastern Tibetan Plateau between 2017 and 2020. *Geomorphology*, *411*, p.108293

Yang, W., Wang, Y., Wang, Y., Ma, C. and Ma, Y., 2020. Retrospective deformation of the Baige landslide using optical remote sensing images. *Landslides*, *17*(3), pp.659-668.

Young, T.J., Christoffersen, P., Bougamont, M., Tulaczyk, S.M., Hubbard, B., Mankoff, K.D., Nicholls, K.W. and Stewart, C.L., 2022. Rapid basal melting of the Greenland Ice Sheet from surface meltwater drainage. *Proceedings of the National Academy of Sciences*, *119*(10), p.e2116036119

Zang, W., Lin, J., Wang, Y. and Tao, H., 2012, June. Investigating small-scale water pollution with UAV remote sensing technology. In *World Automation Congress (WAC), 2012* (pp. 1-4). IEEE.

Zechmann, J.M., Truffer, M., Motyka, R.J., Amundson, J.M. and Larsen, C.F., 2021. Sediment redistribution beneath the terminus of an advancing glacier, Taku Glacier (T'aakú Kwáan Sít'i), Alaska. *Journal of Glaciology*, *67*(262), pp.204-218

Zekollari, H., Huss, M. and Farinotti, D., 2019. Modelling the future evolution of glaciers in the European Alps under the EURO-CORDEX RCM ensemble. *The Cryosphere*, *13*(4), pp.1125-1146

Zemp, M., Frey, H., Gärtner-Roer, I., Nussbaumer, S.U., Hoelzle, M., Paul, F., Haeberli, W., Denzinger, F., Ahlstrøm, A.P., Anderson, B. and Bajracharya, S., 2015. Historically unprecedented global glacier decline in the early 21st century. *Journal of Glaciology*, *61*(228), pp.745-762.

Zemp, M., Huss, M., Thibert, E., Eckert, N., McNabb, R., Huber, J., Barandun, M., Machguth, H., Nussbaumer, S.U., Gärtner-Roer, I. and Thomson, L., 2019. Global glacier mass changes and their contributions to sea-level rise from 1961 to 2016. *Nature*, *568*(7752), pp.382-386.

Zhan, Z., 2019. Seismic noise interferometry reveals transverse drainage configuration beneath the surging Bering Glacier. *Geophysical Research Letters*, *46*(9), pp.4747-4756.

Zhang, Y., Fujita, K., Liu, S., Liu, Q. and Wang, X., 2010. Multi-decadal ice-velocity and elevation changes of a monsoonal maritime glacier: Hailuogou glacier, China. *Journal of Glaciology*, *56*(195), pp.65-74.

Zheng, W., Pritchard, M.E., Willis, M.J., Tepes, P., Gourmelen, N., Benham, T.J. and Dowdeswell, J.A., 2018. Accelerating glacier mass loss on Franz Josef Land, Russian Arctic. *Remote Sensing of Environment*, *211*, pp.357-375.

Zhang, D., Watson, R., Dobie, G., MacLeod, C., Khan, A. and Pierce, G., 2020. Quantifying impacts on remote photogrammetric inspection using unmanned aerial vehicles. *Engineering Structures*, *209*, p.109940.

Zhang, J., Jia, L., Menenti, M. and Ren, S., 2021. Interannual and seasonal variability of glacier surface velocity in the parlung zangbo basin, tibetan plateau. *Remote Sensing*, *13*(1), p.80.

Zirizzotti, A., Cafarella, L., Baskaradas, J.A., Tabacco, I.E., Urbini, S., Mangialetti, M. and Bianchi, C., 2010. Dry–wet bedrock interface detection by radio echo sounding measurements. *IEEE Transactions on Geoscience and Remote Sensing*, *48*(5), pp.2343-2348.

Zoet, L.K., Carpenter, B., Scuderi, M., Alley, R.B., Anandakrishnan, S., Marone, C. and Jackson, M., 2013. The effects of entrained debris on the basal sliding stability of a glacier. *Journal of Geophysical Research: Earth Surface*, *118*(2), pp.656-666.